UNIVERSIDAD DE LA LAGUNA

Center to lim variation of solar pjotospheric stuctures

Autor: Sánchez Cuberes, Mónica

Directores: José Antonio Bonet Navarro
y Manuel Vázquez Abeledo

Departamento de Astrofísica

Als meus pares,
i a l'àvia

Resumen

Hemos realizado el estudio de dos estructuras fotosféricas solares diferentes, la granulación y las fáculas, combinando observaciones fotométricas y simulaciones numéricas. La herramienta usada para obtener observacionalmente información acerca de su estructura vertical ha sido la adquisición de datos a diferentes ángulos heliocentricos y rangos espectrales.

Durante un eclipse parcial solar, se obtuvieron imágenes en $\lambda 6708$ Åen diferentes posiciones en el disco. La presencia del borde lunar en cada una de las imágenes nos ha permitido estimar la degradación debida a la atmósfera terrestre. Se ha construido un filtro de ruido basado en los mismos datos, y las imágenes han sido reconstruidas. Además, se han realizado observaciones de la granulación en los extremos de la distribución de la opacidad con la longitud de onda, esto es en $\lambda 8000$ Å y $\lambda 15500$ Å, a diferentes ángulos heliocéntricos. Se han realizado estudios de las propiedades estadísticas y morfológicas que caracterizan a la granulación sobre estos datos.

Este estudio observacional se ha complementado con simulaciones numéricas. Un código de transporte radiativo tridimensional se ha aplicado a cajas de datos que simulan la granulación solar. Ello nos ha permitido probar la influencia de condiciones de observación variables y la bondad de diversos modelos, teóricos y semi-empiricos.

Observaciones de varias regiones activas en diferentes posiciones en el disco se han llevado a cabo en $\lambda 8000$ Å y $\lambda 15500$ Å. Se ha usado técnicas de fotometría diferencial para identificar las fáculas. Se ha estudiado su intensidad relativa y propiedades dependientes del tamaño facular, y se ha propuesto un escenario físico para explicar las tendencias observadas. Además, se ha realizado un primer intento de simular la variación centro a borde de la intensidad facular. Se presentan resultados preliminares sobre la influencia de condiciones de observación variables, diferentes geometrias y varias atmósferas magnéticas y no-magnéticas. La presencia de algunos poros en los campos de visión usados

ha permitido extender el estudio a estas estructuras, las cuales comparten el mismo mecanismo físico que las fáculas.

Abstract

We have approached the study of two different solar photospheric structures, granulation and faculae, by means of combining photometric observations and numerical simulations. The tool used to obtain observationally information about their vertical structure has been the acquisition of data at different heliocentric angles and spectral ranges.

Images of the solar granulation at λ6708 Å were obtained at different disk positions during a partial solar eclipse. The presence of the lunar limb in every frame has allowed to estimate the degradation caused by the terrestrial atmosphere. A noise filter based on the data themselves has been constructed and the images have been restored. Besides, observations of the granulation at the extremes of the distribution of the continuum opacity with wavelength, this is at λ8000 Å and λ15500 Å, have also been obtained at various heliocentric angles. On these data, studies of the different morphological and statistical properties characterizing the solar granulation have been performed.

This observational study has been complemented with numerical simulations. A three dimensional radiative transfer code has been applied to boxes of data simulating the solar granulation. This has allowed to test the influence of variable observing conditions and the goodness of different theoretical and semi-empirical models.

Observations of various active regions at different disk positions have been performed at λ8000 Å and λ15500 Å. Differential photometry has been used to identify faculae. Their relative brightness and size dependent properties have been studied and a physical scenario to explain the observed trends outlined. Moreover, a first attempt to simulate the center to limb variation of the brightness of facular regions has been made. Preliminary results about the influence of various observing conditions, geometries and magnetic and non-magnetic atmospheres are presented. The presence of some pores in the observing field has allowed to extend the study to these structures, which share a common physical

mechanism with faculae.

Contents

1

Introduction

1.1 Introduction: The Sun

The Sun, our star, is the fundamental source of energy for the majority of life processes on Earth. This energy reaches us as radiation, which emerges at the surface of the Sun after tracing a complex path during millions of years.

The thermonuclear reactions of hydrogen burning that take place in the Sun's nucleus generate great quantities of energy over long periods of time. The gamma rays produced during these reactions interact with the surrounding matter, are absorbed and reemitted continuously, and finally emerge into the so-called radiative zone. In this region, the temperature and the density are smaller, allowing the atomic nuclei and electrons to recombine and form ions. The increase in opacity of matter in this state complicates the transit of the radiation through this region of the atmosphere. The photons follow an intricate path, are absorbed and and reemitted in random directions, and in each absorption and reemission energy is lost. After millions of years, when the photons finally reach the solar surface, most of them are no longer gamma rays but have become transformed into ultraviolet or visible radiation. However, not all the energy transported from the nucleus to the surface is performed in a radiative manner.

The temperature gradient is smooth in the deep layers of the Sun smooth. Nevertheless, when the temperature drops below 2 000 000 K the opacity increases considerably, blocking the transport of energy by radiation. As a consequence, the temperature gradient becomes more abrupt and the medium becomes unstable to convection. This region of the atmosphere is called the convective envelope. Bubbles of hot gas ascend, expand and finally fragment, thus transporting their internal energy.

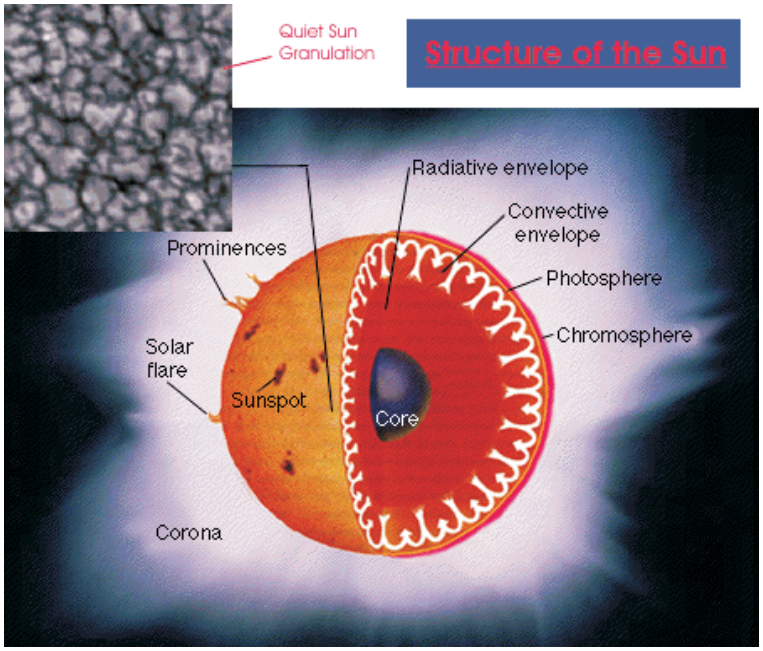

FIGURE 1.1— The structure of the Sun.

It is now believed that in the intermediate layer between the radiative and convective zones the Sun's magnetic field is maintained and amplified by a magnetic dynamo. The changes in fluid flow velocities across the layer (shear flows) can stretch magnetic field lines of force and make the field intensity stronger. The magnetic ropes are lighter than their surroundings and therefore emerge at the surface.

Temperature diminishes with height and, in parallel, the degree of ionization of the main element, hydrogen, also decreases. This decrease causes a decrease in the opacity and, at a certain height, the matter again becomes transparent to radiation. The light escapes freely from the Sun, forming the so called photosphere or 'sphere of light'. In this region the energy is again transported by radiation and not by convection. In Fig. (1.1) a sketch of the structure of the Sun is presented.

To the naked eye, the photosphere seems to be the 'surface' of the Sun although, strictly speaking, a gaseous body like the Sun has no surface. The photosphere looks like a solid body because of its lower temperature as compared to that of the interior. In reality, the difference in temperature generates a difference in opacity which creates the illusion of a well-defined solar limb.

This opacity makes it impossible to perform direct observations of the interior of the Sun. Therefore, the phenomena that take place there have their most direct sign in the effects that they induce in the photosphere or in outer layers of the Sun. In this sense, the photosphere is a highly active and irregular region. When observed with high enough resolution, a wide variety of magnetic and non-magnetic structures can be appreciated.

The regions of the solar photosphere where magnetic structures are not predominant are called 'quiet regions'. In these, a structure of irregular bright quasi-polygonal cells (granules) separated by darker narrower regions (intergranular lanes) can be observed. These structures have sizes close to the resolution limit of present-day telescopes and are of fundamental interest since they occupy most of the surface of the photosphere. They also offer a unique chance to study how the variation from a convective to a radiative regime occurs in stars. Apart from the granular structures, the photosphere also has convective patterns of larger sizes such as meso- and supergranulation, a summary of whose properties is given in Table (1.1).

TABLE 1.1— Convective structures

	sizes [km]	lifetimes	$V_{vertical}[km \cdot s^{-1}]$	$V_{horizontal}[km \cdot s^{-1}]$
Granulation	1500	8 min	1.5	2.2
Mesogranulation	10000	$\geq$30 min	0.3	0.75
Supergranulation	30000	$\geq$24 hours	0.2	0.3-0.5

Spread over the solar disc, dark and bright structures of magnetic origin such as sunspots, pores, faculae and network bright points can also be seen. These magnetic structures have a wide range of sizes and magnetic strengths, and understanding their physics is crucial for clarifying the mechanisms that produce the solar cycle and give rise to the nature of magnetic structures. Figure (1.2) shows an image of the full solar disc in which several structures of magnetic origin can be seen.

1.2 The quiet Sun: granulation

1.2.1 Historical overview

Granulation, which forms the basic structure of the quiet Sun, has caused interest among the scientific community since it was discovered. Understanding its basic nature has required a lot of research, which, combining different approaches to the problem, has finally led to an agreement among the community

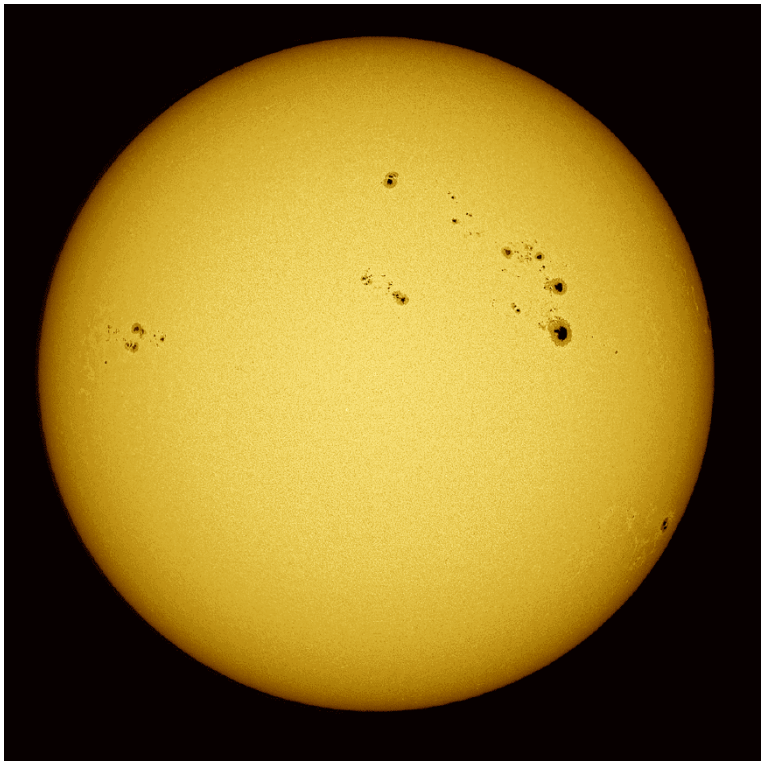

FIGURE 1.2— Image of the full solar disc [courtesy of J. A. Bonet (IAC)].

concerning the main physical processes involved in this phenomenon. Nevertheless, the increase in the accuracy of the measurements and models available nowadays have also revealed details of granular structures that are still not completely understood.

The first to observe irregularities in the intensity of the surface of the quiet Sun was Sir William Herschel, who in 1801 described them as 'small rice grains'. Nasmyth, in 1862, confirmed this observations and suggested the existence of a structure of 'willow leaves'. This description was contradicted by Dawes, who in 1864 described the surface as granulated and introduced the word 'granule' to describe the basic elements of this texture. Dawes did not find any evidence that granules had an elongated shape and estimated their typical size at between 1 and 1.5 arcseconds.

Most of the discussion about granular shape, based on observations performed ocularly, ended in 1896 when Janssen succeeded in photographing the solar granulation. These pictures showed that granules were not elongated and

had typical sizes of 1 to 2 arcsec. Hansky (1908), using temporal sequences of images of granulation, estimated the mean lifetime of granules to be 5 minutes. In 1933 Strebel obtained good spatial resolution pictures that revealed the polygonal shape of granules.

The theory that states that the origin of granulation is convection was established in 1930 by Unsöld, who showed that, as a consequence of the increase in the ionization of hydrogen with depth, a zone of instability to convection must exist below the photosphere. He related the origin of granulation to convective fluxes, but did not study its mechanism in further detail. In 1933 Siedentopf, continuing Unöld's work, suggested that granules were bubbles of hot ascending gas embedded in a colder medium of descending matter. He remarked that the Reynolds number in the convection zone exceeds the critical value of turbulent instability, and that therefore the convective flows must have a turbulent character. Siedentopf based his ideas on the theory of the mixing length of turbulence. This theory assumes that the convective energy is transported by turbulent cells, which split after ascending a distance equal to the mixing length, in this way transporting their energy and momentum.

The study of solar granulation experienced a considerable impulse with the improvements achieved in the design and production of new diffraction gratings. With these it was possible to resolve individual granules with short exposure times, thus allowing high resolution spectra to be obtained relatively free of the degradation owing to the earth atmosphere. In 1933 Richardson obtained spectra in which, for the first time, individual granules could be resolved. Taking into account the convective nature of granulation, a strong correlation between brightness and velocity variations was expected, with hot granules moving upwards and cold intergranular lanes moving downwards. Nevertheless, Richardson and Schwarzchild (1950), performing studies of Doppler shifts on these spectra, found no such correlation since it was masked by the 5 minute oscillations (which they ignored). These authors interpreted the measured granular velocities as the statistical effect produced by the higher velocities of unresolved turbulent cells. They predicted that granules had much smaller sizes than 1 arcsecond, a greater brightness than observed until then, and a Kolmogorov spectrum for their size distribution. Following this work, Skumanich (1955) and Uberoi (1955) concluded that the brightness fluctuations in the photosphere were random, and that the granular cell pattern did not exist.

These predictions led to the launch of balloon-borne stratospheric telescopes to check the turbulent origin of solar granulation. Nevertheless, although great efforts were made, no conclusive evidence was ever found. But high resolution diffraction-limited images of the granulation were obtained and were of great importance for characterizing the granulation observationally.

In 1963 Leighton et al., on the basis of the quasi-polygonal shape of granulation, defended the cellular nature of granulation, in contradiction to the isotropic turbulence hypothesis supported by other authors. Leighton and coworkers observed also that the whole photosphere oscillated with a period of about 5 minutes and concluded that the velocity field on a small spatial scale was created by the shaking produced by granules in the atmosphere. The study of maps of vertical velocities led them to observe the existence of a supergranular structure of larger scale ($\approx$ 30 Mm)

At the beginning of the 1980s most astronomers believed that granulation had a convective rather than a turbulent origin. It was considered that most of its observable properties were correctly characterized, although the nature of the convection and how it penetrated into the photosphere was not well understood.

In the last few decades, the observational data on solar granulation have improved considerably, partly because of the construction of more powerful telescopes, the more powerful computational capabilities of computers, and the use of image correlatorcorrelation trackers capable of stabilizing the images. The creation of interactive systems with large memory and the development of digital processing techniques have led to new methods of acquisition and selection of images and to codes for their reconstruction and analysis. All of this is relevant in the study of solar granulation since it reveals structures at the limit of resolution and because to investigate them it is of crucial importance to have high resolution data. Also, to perform dynamical or statistical studies is necessary to deal with large amounts of data, which is possible nowadays thanks to technological improvements.

The increase of computational capabilities has also allowed the development of numerical simulation codes for solar granulation in which realistic physical conditions are incorporated. Comparison of the properties of solar granulation derived from numerical simulations with those derived from observations has contributed to physical interpretation of the data, although in some cases it has also shown that the nature of some structures is not correctly understood.

Methods have also been developed that allow us to build semi-empirical models of the physical parameters of the photosphere from the observational data. These are the so-called inversion methods.

Therefore, several techniques can currently be used to study the structure of the quiet Sun photosphere, namely, observations, numerical modelling and semi-empirical modelling. These have led to great advances in the study of photospheric structures, which are now understood in a deeper sense with information about detailed physical mechanisms that explain the fine structure inside the granulation. In summary, it can be stated that the combination of

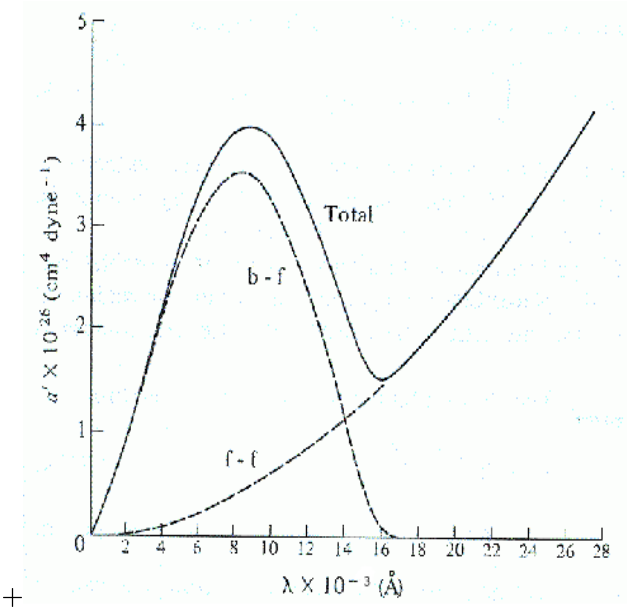

FIGURE 1.3— Absorption coefficient of the H^- ion at a temperature of 6300 K due to bound–free transitions (b–f) and free–free transitions (f–f). From *Introduction to Stellar Atmospheres and Interiors*, Eva Novotny, 1973.

these three techniques offers a powerful tool for gaining a deeper insight into the physics of the phenomenon. The aim of this thesis is to perform a study of solar granulation by using a combination of these different methods.

1.2.2 How to scan the solar photosphere in height

The observational characterization of granulation is necessary in order to proceed towards its understanding; comparison with the predictions derived from the theoretical models allows us to validate them. Observations are the raw material for inversion codes that obtain semi-empirical models of the photosphere; also, observations sometimes show previously unknown details of the structure of granulation. Several observing techniques can be used and each of them appropriate for studying different aspects of granular phenomena.

Of prime interest is the study of the vertical thermal structure of granulation. To obtain information about the stratification of physical quantities two resorts can be used. First, different wavelengths carry information coming from different layers of the Sun because of the wavelength dependence of the absorption coefficient of the continuum. Fig (1.3) shows the dependence of the

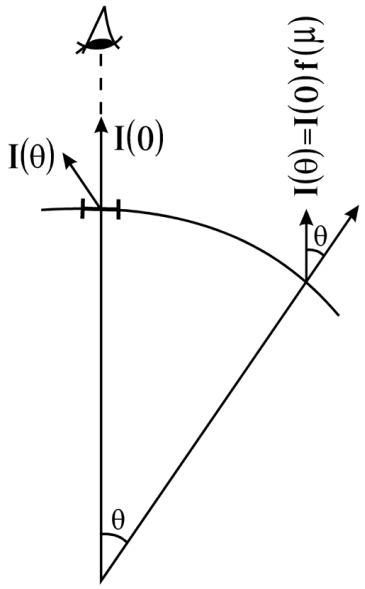

FIGURE 1.4— Perspective effect caused by an oblique angle of view in the solar atmosphere.

absorption coefficient of the H^- ion oon wavelength. Note that the curve shows a minimum at $\lambda 16000$Å which is the infrared region where the lower layers of the photosphere can be observed. Second, images coming from different heliographic positions contain information coming from different layers of the solar atmosphere. From simple geometric considerations, in the photosphere the radiation comes from deeper layers at the disc centre than near the limb. To a first approximation, the optical depth that is observed at a certain disc position is $\tau = cos\theta$, where θ is the angle that the line of sight forms with the normal to the surface ($\tau = 1$ at disc centre). Fig (1.4) illustrates this perspective effect.

Spectroscopy is a very powerful tool for obtaining detailed information about the vertical structure by studying the detailed shape of the spectral lines. This technique is fundamental for the study of velocities and dynamics (through the Doppler shift), the penetration height of granules, their intensity–velocity relation, etc. However, it is usually difficult to achieve high spatial and spectral resolution at the same time. Furthermore, spectroscopy usually obtains one-dimensional scans of the photosphere, which are obviously of limited use. Two-dimensional spectroscopy has also been used recently, but achieves spatial and/or spectral resolution that is not always as high as might be wished.

Photometric images offer a unique chance to obtain high spatial resolution

two-dimensional data of the Sun's atmosphere because of the short exposure times. The layers of the photosphere that contribute to continuum formation have a wide range of heights; therefore, the information is mixed in photometric observations. Nevertheless, by using different heliocentric angles and taking wavelength into account, information about the vertical structure can be obtained. However, it is unavoidable that the information concerning a wide range of layers in the solar photosphere is mixed.

In this thesis we have chosen to use photometric techniques since they offer the chance to achieve high spatial resolution and perform morphological and statistical studies. Moreover, we will use observations at different heliocentric angles and observing wavelengths which, as explained above, will allow us to characterize the vertical structure of the temperature, the main contributor to the photometric observations.

1.2.3 Photometry of solar granulation

Different kinds of studies can be performed with photometrical data. Here we present a summary of the most relevant for this thesis.

Granular sizes

When performing morphological studies of solar granulation it is important to take into account that still images of a dynamical process are analysed. Therefore, the information about size and shape obtained are those resulting from the process of birth, growth and disappearance of granules.

Approximately 60% of the granules evolve by fragmentation; a granule grows, divides typically into 3 or 4 pieces, each piece growing and fragmenting in its turn. Other granules appear spontaneously in the intergranular lanes or disappear diluting into them, although their appearance through the union of two adjacent granules is also possible. But the most spectacular mechanism is occurs in the form of explosive granules, which expand radially and develop a dark region at their centre.

The shape and size of granules therefore depends on the evolutionary status they have reached.

To perform a statistical study of the distribution of granular sizes it is necessary to define the border of each individual granule. But the dynamical effects mentioned above make this task difficult. In an attempt to overcome these difficulties, different methods for automatic detection of the granular borders have been developed, although the results depend on the chosen algorithm.

Namba & Diemel (1969) performed a morphological study to identify granules visually. They obtained a narrow range of granular sizes, which they in-

terpreted as proof of the convective origin of granulation.

Roudier & Muller (1987) and Hirzberger et al. (1997), using an intensity threshold algorithm that identifies the granules automatically, found that the number of small granules grows considerably for granular sizes close to the resolution limit. A histogram of this kind is more characteristic of turbulent than of convective cells. These authors also found a change in the slope of the histogram of areas when it was presented on a log–log scale, which they interpreted as proof of the existence of two different regimes of granulation.

Nevertheless, not all scientists coincide in this finding. Title et al. (1989) analysed data obtained with the SOUP instrument in the Spacelab2 experiment on board the *Challenger* Shuttle using two different algorithms. One identified the local intensity minima as the borders of granular cells (a granular cell is defined as a granule and its corresponding intergranular lane portion). This method infers the centre of the granule in the central part of the closed area obtained. The other algorithm localized directly the granular centres as the local intensity maxima. These authors found no evidence for the existence of the change of slope in the size histogram previously mentioned.

The numerical models of granulation are able to reproduce partially the distribution of areas observed, although generally they do not generate enough small granules as compared to what is observed in the Sun (Muller 1999). Besides, the maximum size of granules is controlled in the models by a parameter of numerical diffusion introduced arbitrarily to stabilize the hydrodynamical equations.

Studies of granular size allow us to investigate the physical origin of the appearance, scale and structure of the granulation. Nevertheless, it is known that similar structures can appear under very different conditions, and therefore only knowing the structure it is difficult to infer information about the forces involved in a given process. But the parameters derived from this kind of studies can be directly compared to those derived from the numerical models. Also, the analysis of the distribution of granular sizes allows us to perform phenomenological investigations like the one by Schrijver et al. (1997).

These authors characterized the cellular structure of granulation and supergranulation using an identification algorithm based on the local slope of the intensity. They showed that the granular structure is reproduced by tessellating a surface with a generalized Voronoi model (this model is explained in greater detail in section 5.1.2, chapter 5). This kind of model determines zones of dominance, or cells from a group of 'source' points. Each of these points has an associated 'force' that determines which points of its surroundings belong to its dominant area. Scrjiver et al. (1997), studying the parallelism existing between granulation and a model of Voronoi, concluded that it is possible to reproduce

the convective structure only if the range of 'forces' of the 'source' points is relatively small. They identified these points as those with a maximum ascending flux, suggesting that the range of 'forces' of the ascending fluxes must be small. They also inferred that the 'source' points should have some correlation in their positions and that the spatial density of these points or fluxes is what determines the scale of the granular cellular structure.

It seems interesting, then, to study the granular size distribution in high spatial resolution photometric images in order to put further constraints on the theoretical models and get deeper information about the processes of emergence, scale and structure of granulation.

Area–perimeter relation

In the literature, it can be found that by plotting the granular area versus perimeters on a log–log scale, a low dispersion and two different slopes for two ranges of granular areas are obtained. It seems suitable, thanks to the low dispersion, to fit straight lines to each range of granular areas. This allows us to express the granular perimeter as $P_{\rm g} \propto A_G^{D_f/2}$, where D_f is the fractal dimension. The fractal dimension describes the morphological complexity of the borders of two- and three-dimensional objects. The values published in the literature are of about $D_f = 1.34$ for small granules, specifically: $D_{\rm f} = 1.34$ (Darvann & Kusoffsky 1989), $D_{\rm f} = 1.31$ (Brandt et al. 1991), $D_{\rm f} = 1.3$ (Hirzberger et al. 1997). For large granules the values are around $D_{\rm f} = 2$: $D_{\rm f} = 1.9$ (Darvann & Kusoffsky 1989), $D_{\rm f} = 1.99$ (Brandt et al. 1991), $D_{\rm f} = 2.1$ (Hirzberger et al. 1997). The fact that two different ranges can be distinguished in the graph, and that the value of D_f is near 4/3, the value predicted by the Kolmogorov theory of isotropic homogeneous turbulence for the isobars, have been often interpreted as a sign of the turbulent nature of small granules. Nevertheless, since these studies are performed in white-light images, it seems reasonable that the isophotes coincide with isotherms rather than with isobars, and for the isotherms the value predicted by the Kolmogorov theory is D_f=1.67. Brandt et al. (1991) claim that the differentiation of the fractal dimension for two ranges of granular areas is is owing to the method used to analyse the data. They argue that the difference found is due to the finite pixel size, which favours values of the fractal dimension near $D_{\rm f} = 1.3$ for small granules. However, they also show the good agreement found among different studies on the determination of the fractal dimension for large granules, although they remark that these values are only upper limits.

Therefore, the question of what the fractal dimension of granules really is is still unresolved.

Area–intensity relation

Maximum and mean granular intensities grow linearly with granular size for granules smaller than $\approx 1\farcs4$, while for larger granules it is, on average, constant. On the contrary, intergranular lanes have constant mean and maximum intensities over the whole range of observed sizes (Hirzberger et al. 1997).

This result is interesting since, from a thermodynamical point of view, the larger a convective element, the larger intensity it should have. This is because, according to mixing-length theory, larger convective cells extend to deeper layers in the convective zone (Simon & Weiss 1968) and therefore carry hotter gas to the surface. This energy cannot be dissipated in the horizontal direction because of radiative losses since the higher temperature causes the opacity also to increase. Thus, the large granules observed by Hirzberger et al. (1997) do not seem to be large convective cells because their intensity remains constant, independently of their size.

The three-dimensional models of Nordlund (1985) show that the intensity structure observed in the solar photosphere is caused by the adiabatic expansion (compression) of gas upflows (downflows) and the loss of energy through radiation. This implies a strong correlation between the vertical velocities and the emergent intensities. This correlation has been observed (Wiehr & Kneer 1988; Hanslmeier, Nesis & Mattig 1993). Nevertheless, it also implies an increase of brightness with size, which Hirzberger et al. (1997) observe only for small granules. They proposed as a solution to the problem the possibility that large granules are clumps of smaller fundamental granules that appear as local intensity maxima.

Steffen et al. (1989) simulated solar granulation with a two-dimensional code in which the granular cell size was the input. They analysed the dependence of granular properties with granular size and found that the fluctuations in intensity increase with cell size for sizes smaller than 1000 km. For larger cells the fluctuations saturate because of the thermal isolation between hot and cold regions. In these simulations, the condition was imposed that, independently of cell size, the mean emergent radiative flux at the higher boundary of the simulation had to match the effective temperature of the Sun. Thus, small cells that lose more energy by radiative cooling arrive in this simulation at $\tau = 1$ with higher temperatures than those of larger cells.

A similar study to that performed by Hirzberger et al. (1997) was recently done by Berrili et al. (1999), who analysed simultaneous observations in white light and two different narrow band spectral ranges representing different heights in the photosphere. Segmenting the white-light images, they determined the contours of individual granules and investigated the dependence

of their photometric properties on granular size. These authors identified 400 granules of sizes between 0 ".4 and 1 ".4. The general trend found for the lower layers of the photosphere was an increase in the intensity with granular size. For higher layers, they found an inverse correlation. These authors explain the observed correlation in the lower layers with thermodynamical arguments already mentioned, i.e. larger cells penetrate deeper into the convection zone. For the higher layers they explain the observed correlation as a consequence of supercooling and lower radiative loss.

It is thus not clear how the granular intensity varies with granular size. This is a really interesting topic since this dependence has a lot of implications for the physics of granular theoretical models.

Intensity fluctuations

The study of the intensity contrast gives information on the associated temperature fluctuations. But a direct interpretation of the contrast in terms of temperature is not possible since an increase in the intensity produced by a rise in the temperature is partially eaten up by the corresponding increase in the H^- opacity. Many scientists have measured the granular contrast and many techniques have been used. The results vary widely because of the different reconstruction techniques used and the different wavelengths selected. Even normalizing all the values to a unique wavelength, no clear correspondence is found between the different wavelengths, the different studies or the contrast values found (see Table (2.2) for details).

It is important to take into account that approximately 30% of the contrast in a granulation image is caused by the 5 minute oscillation. Title et al. (1989), analysing data obtained with a space telescope free from the degradation due to the Earth's atmosphere, found a contrast of 15.5% for the granulation observed at λ6000 Å. After processing the images with a subsonic filter to eliminate solar oscillations, the resulting contrast was of 10.2%. These values are in good agreement with those predicted by the computations of Stein & Nordlund (1998), who computed a contrast of 16% in the centre of the disc for λ6000 Å. Convolving these results with a synthetic PSF to simulate the effects due to the earth atmosphere, they obtained a value of the granular contrast of 10%, similar to the value measured by these authors at the SVST. Nevertheless, the values resulting from a simulation are, in general, much larger than those observed on the Sun. At λ5000Å, the contrast obtained by Nordlund (1985) and Gadun & Pikalov (1996) are $\approx$25–30%, and for λ6000 Å, $\approx$20–25% (Gadun & Pikalov 1996). The different intensity fluctuations obtained by different authors reflect the differences in their temperature structures. In the models, a higher

temperature in the higher layers of the photosphere may give rise to smaller intensity fluctuations, while lower temperatures may mean larger intensity fluctuations (Astroschenko & Gadun 1994). Since values obtained from models are, in general, larger than those observed in the Sun, it is usual to convolve the results with a PSF to simulate the effects of the Earth's atmosphere, a process that also reduces the intensity fluctuations. But Nordlund (1984) showed how the specific shape of the PSF significantly affects the obtained intensity fluctuations.

It is usual to study the variations of the contrast through the position on the solar disc since this gives information about its variation in the photosphere with height. Many studies have been performed on this topic and many different CLV curves have been obtained. There is no clear correlation between the different observed curves and wavelength. Nevertheless, two different trends can be distinguished between the different authors. Most of the curves show a monotonic decrease in the contrast from the centre to the limb, although the slope and the exact shape of the curve varies from one author to another (Wilken et al. 1997; Pravdjuk et al. 1974). On the other hand, some studies present contrasts that increase for positions near the disc centre and then decrease near the limb (Rodríguez Hidalgo et al. 1992b; Schmidt et al. 1979). The study of the response functions to the temperature in the solar photosphere show that the first kind of curve implies a more steep slope of the mean temperature gradient (Kneer 1984).

The variation of the intensity fluctuations with height in the photosphere can also be studied from the statistical analysis of spectroscopic data. Espagnet et al. (1995), performing studies on data of this kind obtained with a MSDP (Mein 1977), found that the intensity fluctuations decrease rapidly with height, reach a minimum at a height of ≈ 60 km and increase again for all granular sizes in higher layers of the photosphere.

Nelson (1978) performed numerical simulations of solar granulation in which they assumed a unique cell size and determined the horizontal fluctuations of temperature, density and pressure. With this model, the author computed the CLV curves of the intensity fluctuations in solar granulation and reproduced the general observed trend.

Power spectra of intensity fluctuations

The power spectrum is a good tool for studying the average geometric properties and intensity fluctuations of granulation, even though its interpretation is not straightforward since the information about size and relative position is mixed up. It is of especial interest to compare power spectra obtained observationally

with those derived from the models.

The theory of turbulent fluids predicts a power spectrum that decreases as $k^{-5/3}$, where k is the horizontal wavenumber, down to scales corresponding to a Peclet number of P_e=1. For smaller scales, it predicts a steeper slope proportional to $k^{-17/3}$. It is usual to find in the literature fits of straight lines with these slopes to the power spectrum since the upper layers of the convection zone must be highly turbulent (Bray et al. 1984). Many authors have interpreted the good fit of this kind of line as a proof of the turbulent origin of granulation. Nevertheless, Nordlund et al. (1997) proved that it is not necessary to have turbulence to explain the shape of the granular power spectrum because such a shape can be obtained simply by the sharp edges existing between granules and intergranular lanes.

The study of the variation of the power spectrum with position on the solar disc provides information on the variation of the scales of granulation with height in the photosphere. Since, statistically, the photometric properties of granulation are isotropic, it is usual to average the power spectrum azimuthally and analyse the resulting one-dimensional power spectrum, which has a maximum around a certain spatial frequency that could be considered as the characteristic frequency of granulation at that determined disc position. The observed tendency is that, for positions closer to the solar limb, the characteristic frequencies correspond to larger spatial scales. It is possible to interpret this result as evidence for the existence of larger spatial scales in the higher layers of the photosphere (Durrant et al. 1983).

Wilken et al. (1997) performed a study of the centre-to-limb variation (hereafter CLV) of the sections, parallel and perpendicular to the limb, of the two-dimensional power spectra of granulation. They compared the obtained sections with those derived from power spectra at disc centre extrapolated to other disc positions by assuming that only perspective affects the spectra. They found, in positions near to limb, a higher than expected power in high frequencies and interpreted this as a manifestation of the penetration of hot material into the higher layers of the photosphere. These authors argue that this result supports the explanation given by Steffen et al. (1994) for the bright rims of granules. This view maintains that the low pressure existing in the interface between granular upflows and intergranular downflows permits the enhanced transport of hot material into the higher layers.

Stein & Nordlund (1998) compared power spectra at disc centre generated with observed and simulated granules. They smoothed the synthetic spectra with a PSF that simulated the degradation caused by the Earth's atmosphere and obtained good agreement between both spectra. Nevertheless, as mentioned above, the specific shape of the power spectrum depends on the shape of the

chosen PSF. Therefore, it would be of interest to compare the data obtained without atmospheric degradation with those derived from models.

Vertical structure of the photosphere

The granules generated in the upper layers of the convection zone penetrate into the photosphere because of their inertia. The study of this penetration as well as of the vertical structure of the photosphere has been the main topic of much work in recent decades.

The analysis of the height dependence of statistical properties of one-dimensional spectra has been the most frequent tool used for these kinds of investigations. Many articles have been published (e.g. Komm et al. 1990; Hanslmeier et al. 1991; Nesis et al. 1993), and the obtained results can be summarized as follows. The photosphere is divided in two layers with different physical properties: in the deeper layers granules, which transport the convective energy, decay in a turbulent cascade because of the strong existing stratification. This decay is completed at a geometrical height of 170 km, a height reached only by granules of sizes larger than 1000 km. Both intensity and velocity fluctuations vanish at this height. In the upper layers of the photosphere, above 170 km, secondary motions of non-convective origin induced by granule penetration predominate.

Keil & Canfield (1978), Keil (1980) and Kneer et al. (1981) performed similar studies to those described above and obtained similar results, although a much more abrupt decay of the intensity fluctuations was found. According to these authors, the fluctuations vanish at a height of 60 km.

Salucci et al. (1994), analysing filtergrams obtained with a narrow band Fabry–Perot found a model atmosphere in which two different layers above and below 170 km also exist. However, in their model this is true only for granules of sizes smaller than 1000 km since larger granules show coherent velocities throughout the entire photospheric range studied, that is, from 100 km to 400 km.

An interesting result is that obtained by Bendlin & Volkmer (1993) who, using data similar to those of Salucci et al. (1994), observed the formation of granules at a height of 290 km.

However, it must be taken into account that in all the studies mentioned above the 5 minute oscillation, which can perturb the results, was not filtered correctly. In order to reduce the disturbing influence of the 5 minute oscillations it is necessary to have time series, and to filter them out in the wavenumber (k)–frequency (ω) space.

Espagnet et al. (1995) performed statistical and morphological studies on

temporal series obtained with an MSDP spectrogram. These authors correctly filtered the solar oscillations, and the results obtained agree with the existence of two different layers in the photosphere. In this study the intensity fluctuations vanish at a height of 65–90 km, although the velocity fluctuations remain coherent throughout the photosphere. The large granules are those that penetrate higher into the photosphere. Nevertheless, the small spatial resolution of this work (1 arcsec) does not allow a conclusive resultto be reached with respect to small granular and inner granular structures. The numerical models (Steffen et al. 1989; Stein & Nordlund 1989) predict a reversal of sign in the temperature fluctuations in the higher layers of granular penetration; that is, lower temperatures on the granular upflows and higher temperatures on the intergranular downflows. Espagnet et al. (1995) observed in the convective downflows this correspondence between the intensity structures visible in the upper photospheric layers and the continuum granulation. However, they observed neither downflows associated with granules nor an inversion of contrast above them.

Rodríguez Hidalgo et al. (1995), applied an inversion code to each point of a spectrogram, obtaining the temperature fluctuations, which showed a change of sign at 140 km. That is, for higher layers they obtained granules with smaller temperatures than those of the intergranules.

In all the studies presented above, except that of Rodíguez Hidalgo et al. (1995), points in the spectral lines have been directly associated with geometrical heights by mean of the 'formation heights'. This is a misleading concept since there exist no heights that can be directly associated with a point in the spectral line. In fact, the information coming from different atmospheric layers is mixed in the spectral lines. Therefore, it is more suitable to study the response functions to the temperature, which show the variation of the emergent intensity at a given wavelength produced by a differential change in the temperature at a given photospheric depth.

Krieg et al. (1999) analysed data obtained with a Fabry–Perot interferometer performing a study of the height variation of granular structures. Their data are reconstructed by means of 'speckle' techniques, and the different heights in the photosphere are assigned by means of linear combinations of images at different wavelengths, following the corresponding linear combinations of the response functions. These authors observed a decay in granular intensity fluctuations with height and the formation of secondary structures at 150 km. They also found the formation of dark zones above intergranules, which extended to $z \sim$ 200–300 km in the photosphere. However, they found no evidence of the contrast inversion predicted by the numerical models.

Therefore, some observations point to the existence of a contrast inversion at

a given atmospheric layer, while others do not confirm it. It would be important to clarify this point, since it has great implications for our understanding of the solar photosphere.

1.2.4 Numerical modelling of solar granulation

In order to arrive at a deeper understanding of solar granulation, it is interesting to study numerical models and the observational predictions derived from them. Knowledge of the physical scenario in which the numerical simulations generate granulation enables observational results to be interpreted and also allows us to test the degree of precision of the models.

The models also simulate atmospheric layers where direct observation is impossible, and give information about the convective layer.

There are two kinds of models, those which include more realistic physical conditions, in which it is difficult to interpret the physics behind a determined feature (i.e. Stein & Nordlund 1998), and those that simplify the physics in order to study in detail the influence of a certain parameter or process on the whole phenomenon (i.e. Steffen et al. 1989).

But it is fundamental to study in detail the observables derived from the models in order to validate them or constrain them if a certain observable is not reproduced. Nevertheless, this is not always straightforward since it sometimes happens that the same observables are deduced from two completely different physical scenarios.

In this thesis we aim to test different theoretical models by deducing the observable parameters derived from them and comparing these with the observables that we find in the Sun. Comparison of the two results will help us to clarify which model better explains our observations and thus possibly distinguish between the different physical scenarios that the models propose.

In the following subsections we present a summary of current explanations for the different aspects of granular phenomena, together with recent open questions.

General structure

The compressible convection has been understood for decades as a cascade of energy that is transferred from large driving eddies to small dissipative eddies. The 'mixing length theory' considers that the movement is divided into characteristic cells generated by convective instabilities of larger scale. These cells move independently of each other and are a uniquely effective method of energy transport. This theory states also that a cell of size l ascends a distance

H in the atmosphere; it then expands and fragments, releasing its energy and momentum, where $l = H$.

Nevertheless, more recent numerical simulations that use realistic physical conditions have modified our comprehension of this phenomenon (Stein & Nordlund 1989; Spruit, Nordlund & Title 1990; Nordlund & Stein 1990; Spruit 1997; Stein &Nordlund 1998). Convection is considered as a non-local phenomenon driven by the thermal superficial layer. The upflow, hot and of low density, expands when it penetrates into layers of lower density. When it reaches the surface it loses its energy and entropy by radiative cooling. Dense material is then produced and attracted to lower layers by gravity, in this way forming filamentary downflows that reach very deep layers. These currents are responsible for producing both large scale cellular upflows and turbulent small scale movements. The shear flow that takes place at the edges of the downflows generates vortices and turbulence. In contrast, upflows have fewer fluctuations since their divergence smoothes out all the perturbations. As a consequence, upflows have a laminar look, while downflows look turbulent. The horizontal velocity field has a hierarchic cell pattern, with small cells at the surface and larger cells for deeper layers, all of them generated by the fusion of filamentary downflows. Only the small cells are visible on the surface (the granules) due to their large temperature contrast.

According to this view, the granules have horizontal sizes an order of magnitude larger than their vertical sizes, which is quite different from the assumptions made from the mixing length theory. Nevertheless, the qualitative predictions derived from this theory maintain their validity.

Cattaneo et al. (1991) performed simulations of a three-dimensional compressible turbulent convection. They found that, in the turbulent regime, the convection presents local and non-local properties, although the non-local ones do not contribute to the total transport of energy. Therefore, the transport of turbulent energy can be described by the simple ideas underlying the mixing length theory.

Alternatively, Rast (1995) proposed that the dynamics of solar granulation can be explained in terms of processes of local cooling that generate downflows. According to this view, the granulation can be considered as a process of advection–fragmentation if we take as the basic dynamical unit the thermal descending plumes. Despite their dynamical importance, the studies on the stability of compressible downflow plumes lead to a limited vertical coherence, which means that granulation is a surface phenomenon. This model proposes that the granulation is essentially unperturbed by the passive convective motions existing in the lower layers, and that it is mainly generated by the surface radiative cooling.

Granular evolution

The granules evolve by buffeting the surrounding granules. When granules expand, the pressure at their centre grows because the input of flow given by the lower layers must increase in order to maintain the horizontal flow. The increase in pressure, preferentially at the centre of the granule, produces a deceleration in the upflow that diminishes the heat input at the surface and produces stagnation in the granule. This allows the atmosphere above the granule to cool radiatively, increasing its density and attracting it downwards by gravity, in this way forming a new intergranular lane that fragments the granule (Stein & Nordlund 1989; Rast 1995).

Temperature structure

The temperature gradient is much larger in the ascending flux ($\approx$100 K km^{-1}) than in the mean structure ($\approx$ 30 K km^{-1}). This smaller value is produced because the decrease in the temperature of the upflows happens at different heights for different granules and the increase in the temperature of the downflows is produced at deeper layers and is more gradual than for upflows.

The energy transport passes from a convective to a radiative regime. This produces a gradient of temperature caused by the increase of radiative flux, which takes place as a consequence of the decrease in opacity. Since the H^- depends strongly on the temperature, a small increase in temperature produces a large increase in opacity and hence a large increase in optical depth over a very small geometrical depth range. Therefore, the range of temperatures in a given geometric layer is much larger (from$\approx$5000 K to $\approx 10^4$ K) than at a given optical depth. This wide range of temperatures is not observed in the radiation since hot granules reach $\tau = 1$ in higher layers than the cold intergranules. The surface of the Sun is therefore corrugated, with a variation of approximately 30 km.

Above the surface, Stein & Nordlund (1994) predicted an inversion of the temperature structure. In their model, the granules cool because of the adiabatic expansion of the diverging upflow in a subadiabatic region. The intergranules heat up owing to adiabatic compression.

Granulation topology

The size of individual granules is influenced by the interactions and instabilities produced by small surrounding granules. The limited resolution of numerical models makes the small scale flows show up as laminar flows. But the solar plasma is, in fact, less viscous than those produced in the simulations, and this probably causes the interactions between expanding granules in the Sun to

generate disorder and turbulence. The number of small granules produced by the simulations is generally much less than observed in the Sun.

The maximum granular size produced by the models is influenced by the boundary conditions and the numerical diffusivity introduced to stabilize the hydrodynamical equations. But this size is also limited by mass conservation. The excess of pressure that generates the horizontal expansion of the granules also reduces the upflows in their centres. This diminishes the heat flow to the surface and, as a consequence, decelerates the granular expansion. Stein & Nordlund (1989) make a qualitative argument which leads to the conclusion that the maximum granular size is approximately 2 Mm. They assumed that the scale height of the vertical flow mass is of the same order as the density scale height, and that the vertical ascending velocities are of the order of 2 $km \cdot s^{-1}$, which is the necessary value to compensate the loss of energy by radiation. With these assumptions, they found that sonic velocities in the horizontal direction cannot maintain radii larger than 10 density scale heights, which corresponds approximately to 2 Mm.

Steffen et al. (1989) performed simulations in two dimensions of the solar granulation in which cell size was an input. They found that the models with diameters greater than 2000 km were unstable and non-stationary, suggesting that this could be the maximum cell size in the solar photosphere.

1.2.5 Empirical modelling

Observations allow us to determine the dependence of the intensity on the heliocentric angle, the spatial position and the atmospheric depth depending on the kind of studies performed. One of the main aims of the solar scientist is to determine in an accurate way the stratification of physical quantities in the solar photosphere. This can be done through different techniques. One procedure is to assume a certain atmospheric model and through forward modelling to obtain synthesized observable parameters that can be then directly compared with real observations. An alternative way is to perform an inversion of the observations that obtains as output a model of the atmosphere through iteratively comparing synthetic with real observables. Fig (1.5) shows a sketch of possible techniques available for performing these studies. Semi-empirical models can also be obtained by mixing a theoretical model with physical quantities derived from empirical observations.

As mentioned, inversion methods address the problem of determining the stratification of physical quantities by simultaneously varying all (or at least many) relevant physical quantities in a parameterized model of the atmosphere in order to obtain iteratively the best fit to the observed profiles. The devel-

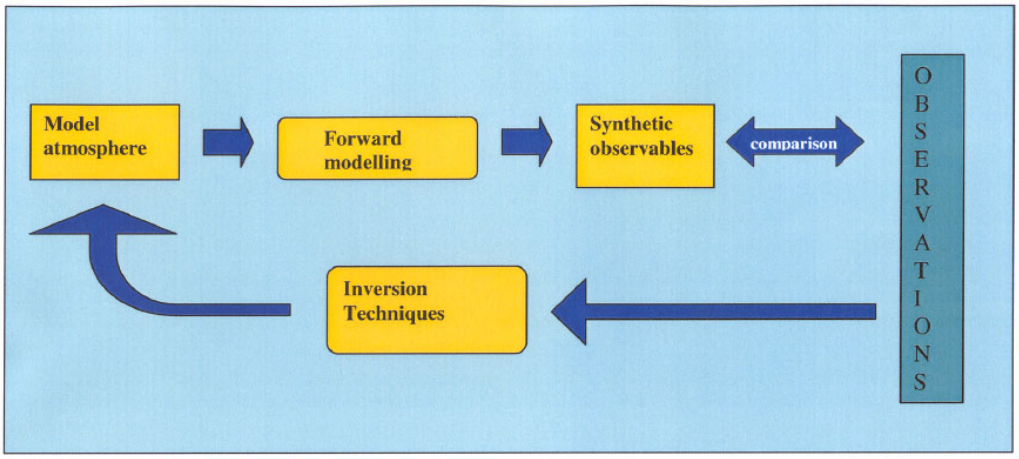

FIGURE 1.5— Possible techniques available for performing studies on the stratification of physical quantities in the Sun.

opment of inversion models has been possible thanks to the availability of high quality data (usually spectral or spectro–polarimetric observations are used for this purpose) and the development of powerful computers.

The main idea of inversion methods is to use the misfit between synthetic and observed profiles to modify a guess atmosphere until the misfit is minimized, usually by means of a least-squares fitting procedure. But this process is not easy to perform since the radiative transfer equation is non-linear and many free parameters appear in the computations. Different iteration schemes have been proposed that differ in the number of free parameters, the specific physical assumptions used in order to simplify the problem, etc.

The first to construct a semi-empirical two-dimensional model of the solar atmosphere including a physical model of granulation was Nelson (1978), who showed the importance of including the horizontal inhomogeneities in order to obtain the right vertical structure for the temperature. Later, Skumanich & Lites (1987) constructed a model which assumed a Milne–Eddington atmosphere in their inversion code. During the last decade several inversion methods have been developed at the IAC. Ruiz Cobo & del Toro Iniesta (1992) presented an inversion code named SIR (Stokes Inversion based on Response functions) capable of dealing with arbitrary stratifications of the physical parameters in the photosphere. The problem was solved using response functions, which are computed at the same time as the radiative transport equations are solved.

Assuming local thermodynamic equilibrium (LTE) and making a first-order approximation, this code is able to obtain the full stratification of all the relevant physical quantities in the atmosphere studied.

Allende Prieto et al. (1998) have developed an inversion code named MISS, which is an adaptation of the SIR code to recover 1D LTE model photospheres for late-type stars from very high spectral resolution, high signal-to-noise ratio stellar line profiles.

The SIR code has also been extended to non-local thermodynamic equilibrium (NLTE). Socas-Navarro et al. (1998 a,b) presented an inversion code of spectral lines that combined SIR with robust and efficient solution methods for the NLTE multilevel radiative transfer problem.

An automatic inversion code to recover MIcroStructured Magnetic Atmospheres (MISMAs) by fitting Stokes profiles has also been developed at the IAC (Sánchez Almeida 1997). These solar model atmospheres incorporate small scale fluctuations of the magnetic field vector, the velocity, the temperature, etc., which this code assumes as an intrinsic property of the magnetic photosphere.

These codes have been successfully applied to deduce the structure of the granules and intergranules in the Sun (Rodríguez Hidalgo et al. 1995), of a mean granule (Ruiz Cobo et al. 1996) and to deduce the 1D model photosphere for the Sun's (Allende Prieto et al. 1998), or the photospheric stratification of granules and intergranular lanes obtained from low spatial resolution but high signal to noise ratio spectra (Frutiger et al. 2000).

Nowadays, numerical modelling offer a very good insight into the physical structure of the photosphere, but it costs a big computational effort. The advantage of inversion techniques is that they complement numerical simulations since they do not rely on the same assumptions and besides are computationally much cheaper. It should also be noted that, to a certain extent, the inversion methods allow us to interpret better the information content of the observations. This is because models can often reproduce the observation by having a wrong physical scenario if the specific data used to test the model are not sensitive to that particular physical scenario.

In this thesis, it is intended to perform forward modelling from several theoretical and semi-empirical models of the quiet photosphere, which will allow us to test their validity and to study independently the effect of different physical parameters on the resulting emergent intensity.

1.3 Faculae and small magnetic fields

1.3.1 Hierarchy of solar magnetic structures

As mentioned above, the surface of the Sun offers a unique opportunity to resolve magnetic features. The most evident such features in the photosphere are sunspots, which since their telescopic observation in the XVII century have constituted one of the structures of prime interest in solar research. In the XVIII century S. Schwabe stated that their number changes following an 11 year cycle and, in the XX century, G. E. Hale detected magnetic fields in them. But it was necessary to wait several more years to discover that the magnetic fileds are also concentrated in small scale structures outside sunspots. We now know that sunspots, pores, faculae and network bright points, among others features, have a common magnetic origin despite their differences in sizes and magnetic field strengths. Solar magnetic fields show up in the photosphere in these varied structures, all of which have something in common: their magnetic fields are filamented in magnetic flux tubes. These magnetic structures have diameters ranging from below the best current spatial resolution limit of about 200 km to over 50000 km. Table(1.2) summarizes the basic properties of the different magnetic structures in the solar photosphere.

TABLE 1.2— Photospheric magnetic structures

	Large Sunspots	Small Sunspots	Pores	Active faculae	Network Faculae
Flux [10^{18}Mx]	$3 \cdot 10^4$	500	250-25	20	0.5
Radius [Mm]	28	4	-	-	-
B [Gauss]	2900 $\pm$400	2400 $\pm$200	2200 $\pm$200	1500-2000	1500
Contrast	Dark	Dark	Dark	Bright	Bright
Location	Active regions	Active regions	Active regions	Active regions	Photospheric network
Filling factor	1	1	1	0.1-0.3	0.05-0.1

The study of solar magnetic elements is of crucial importance for several reasons. The Sun is a unique laboratory in which plasma physics can be studied in conditions attainable in terrestrial laboratories. In parallel, the Sun is the only star in which the magnetic structures are resolved, and thus the mechanisms that can be identified there are an invaluable tool for interpreting stellar physics, quite apart from which, understanding the magnetic structures is a challenge *per se* for solar scientists. Moreover, as stated below, the study of the CLV of the facular contrast has great implications in the determination of the total solar irradiance variations with the solar cycle.

In this thesis we will perform a complete study of the CLV of facular structures by means of combining different photometric observations at various wavelengths and heliocentric angles, and forward modelling and numerical tests.

1.3.2 Photometric observations

The most common tool used for studying magnetic features are spectro–polarimetric observations, which give the whole Stokes spectrum and thus carry all the relevant information about the structures being investigated. Nevertheless, this technique in general gives lower spatial resolution and has smaller field coverage than photometry. In contrast, photometry does not give any quantitative information about the magnetic field.

In the visible range, faculae are observed close to the solar limb as bright structures, generally associated with sunspots, forming the active regions. Their contrast decreases clearly towards the disc centre, which in the past made their photometric detection in these zones extremely difficult. The use of narrow band filters centred on temperature-sensitive molecular bands (e.g. CH 3883 Å or CN 4308 Å) made this detection possible. Nowadays, the improvement in high spatial resolution techniques allows us to detect them directly in white-light images.

We present a summary of the most relevant observing techniques and results obtained for the research work we intend to perform.

Contrast of small magnetic elements at the disc centre

For low spatial resolution observations (about a couple of arcsec), a good correlation is found between magnetic field and continuum brightness; regions with small magnetic filling factors are associated with small continuum brightenings while larger filling factors correlate with continuum darkenings (Frazier 1971). But for higher spatial resolution observations the situation gets more complicated, although it seems quite clear that the smallest magnetic features have sizes that still fall below the resolution limit of current observations.

Some authors find values of the brightness excess of faculae at disc centre (I_f/I_q where I_f is the intensity of the facula and I_q is the intensity of the quiet regions) in the range 1.3–1.5 in λ 5750 $\AA$ (Muller & Keil 1983) and up to 2 in H_α (Koutchmy 1977). In general, a correlation can be found between this studies; for higher spatial resolutions, the values of the intensity excess are greater. Nevertheless, other authors find different correlations. For example, Keller (1992) finds that features with diameters smaller than 300 km appear bright at disc centre, while larger ones appear dark. This author finds a maximum contrast of 1.3.

Moreover, authors such as del Toro Iniesta (1990), Title et al. (1992) and Topka et al. (1992) find no correlation between magnetic field and continuum brightening. On the contrary, they find an associated darkening for regions of large magnetogram signals. It has been claimed that these results cannot be straightforwardly interpretedas being caused by the loss of resolution caused by the telescope and the atmosphere.

Foukal et al. (1981) found that the magnetic features are in fact darker than the quiet Sun in the true continuum and explained this in terms of a lower temperature gradient in faculae as compared to the quiet Sun's atmosphere.

The studies by Worden (1975), Foukal et al. (1989) and Moran et al. (1992) show that in the infrared, near the opacity minimum at the lower observable layers, the plage regions continuum intensity is smaller than the quiet Sun intensity.

The brightness of individual flux tubes is a strong function of facular size (see Solanki 1999); nevertheless, the manner in which the excess brightness depends on the flux tube size, and how it depends on the observing wavelength are still matters of controversy. The upper panel of Fig. (1.6) shows the dependence of the continuum brightness of magnetic features versus their area as computed by Solanki (1999). The solid line represents the brightness averaged over the whole flux tube, i.e. over both umbrae and penumbrae of sunspots. The dotted–dashed line represents the brightness of the umbrae only.

Another basic parameter in flux tubes is their magnetic field strength, which, when averaged over the cross-section of the flux tubes over the entire size range, remains notably constant (Solanki 1999). The lower panel of Fig. (1.6) reflects this relation. The solid line roughly encloses the observed range of values of the field strength averaged over the whole flux tube, including both umbrae and penumbrae for sunspots. The dotted–dashed line represents the maximum filed strength in the umbra. Note that for a wide range of flux tube areas (except the very small ones) the curve stays mainly constant.

Centre-to-limb variation of small scale magnetic features contrast

The first observations of the CLV of the small magnetic features contrast showed that the contrast in faculae increased from the centre out to $\mu = 0.3$–0.4 and then decreased again for higher heliocentric angles (Ten Bruggencate 1940; Waldmeier 1940). But of course these observations were performed with a low spatial resolution as compared with the resolution achievable nowadays.

With the increasing precision of observations, a heterogeneous scenario of results has appeared, where no correlation is found among the different authors, spatial resolutions or observing wavelengths.

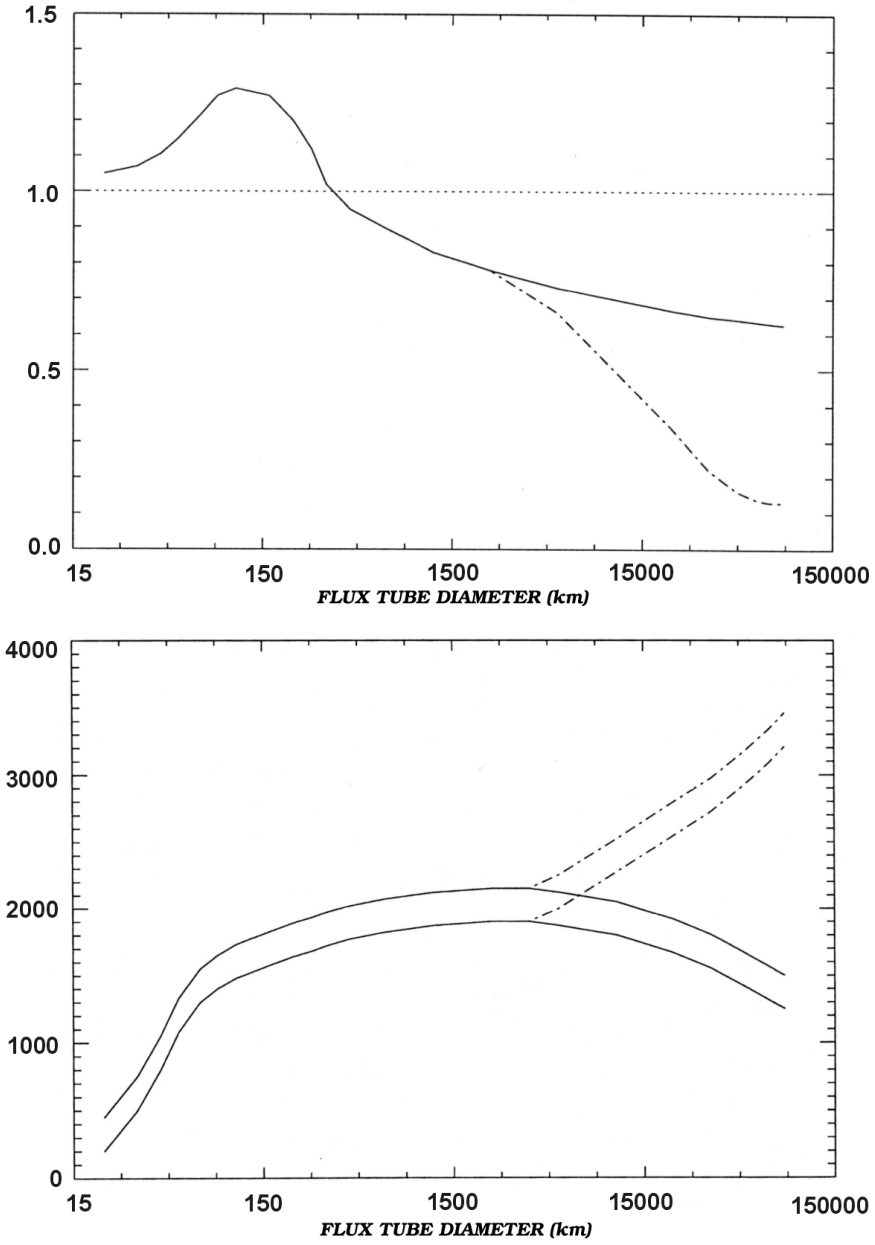

FIGURE 1.6— Upper panel: White-light brightness of magnetic features relative to 'quiet' Sun brightness vs. the diameter of magnetic features. Lower panel: intrinsic field strength, B, of magnetic features vs. their diameter (see text for further explanations). Adapted from Solanki (1999).

Some authors find an increase in facular contrast from the disc centre out to a certain μ and then a decrease. Libbrecht & Khun (1985) found a decrease in facular contrast from $\mu = 0.2$ to μ=0.08 while Auffret & Muller (1991) found that the contrast of small magnetic features peaks somewhere arround $\mu = 0.3$. Wang & Zirin (1987) find that the contrast peaks somewhere around $\mu = 0.15$ at 5250 Å and at $\mu = 0.1$ for 3860 Å.

Other studies find a continuous increase in facular intensity out to the very limb (e.g. Chapman & Klabunde 1982; Lawrence & Chapman 1988; Akimov et al. 1987).

Wang & Zirin (1987), on the other hand, find that the contrast in faculae for shorter wavelengths ($\leq 5000\mathring{A}$) increases out to $\mu = 0.09$ while for longer wavelengths the contrast peaks somewhere around $\mu = 0.1$–0.15.

De Boer et al. (1997) performed a study of the contrast in limb faculae in three different colour bands. They found that the contrast difference between different faculae is larger than the variation with μ. They used images obtained with the Vacuum Tower Telescope (VTT, at the Observatorio del Teide, Tenerife) and with the Gregory Coudé Telescope (GCT, at the Observatorio del Teide, Tenerife). These last observations were corrected for atmospheric degradation by means of speckle reconstruction. The authors found that the GCT data show an increase in facular contrast towards the blue, in agreement with the results of Keller & Koutchmy (1991). For the GCT data they find the opposite behaviour; an increase in the contrast for shorter wavelengths, in agreement with Wang & Zirin (1987) and Lawrence (1988). De Boer et al. interpret this difference as a bias in the VTT data owing to the scattered light. They conclude that faculae radiate like black bodies even near the solar limb. They argue that this means that the temperature stratification of faculae must be steeper than the temperature stratification of the quiet photosphere, in agreement with the results found by Stellmacher & Wiehr (1973) for sunspot umbrae, but in contradiction to many previous studies (e.g. Foukal et al. 1981).

Thus, the exact shape of the CLV of facular contrast is still a matter of controversy and probably depends on the specific type of magnetic feature. Besides, the exact value of the brightness excess depends critically on the spatial resolution of the observations, on the amount of stray light and on the observing constraints imposed by the instrument and the terrestrial atmosphere.

It is an aim of this thesis to study the variation of the CLV of faculae with wavelength and with different types of faculae (i.e. with size). This, together with other diagnostic tools (comparison with the models, deduced emergent intensity by means of a 3D radiative transfer code, etc.), will allow us to obtain information about the facular atmosphere stratification and help to clarify their structure.

1.3.3 Variations in solar irradiance

During the past two decades, satellite observations have revealed that the total solar irradiance, $S_\odot$, changes both on short time scales (Willson et al. 1981; Willson 1982) and on the time scale of the solar cycle (Willson et al. 1986). Figure (1.7) shows a composite view of the irradiance variations prepared by Frölich & Lean (1998) after individual measurement of different radiometers on board of spacecraft.

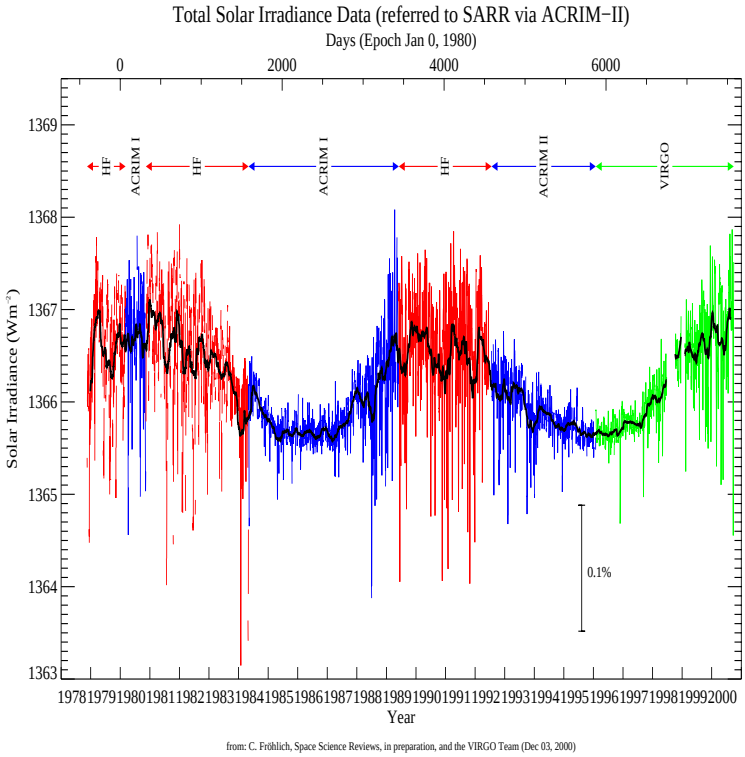

FIGURE 1.7— Total solar irradiance variations. From: C. Fröhlich. Space Science Reviews, in preparation, and the VIRGO team (2000 December 3).

Simulating modern observations by a suitable combination of different kinds of proxies, it might be possible to extrapolate the irradiance changes back in time to periods for which no satellite measurements are available. In other words, *the present could be the key to the past*. What we learn from the past could be applied to the forecasting of future behaviour: *the past could be the key for the future*. Simulated modern observations can be compared with the

corresponding records of surface temperatures to test the validity of a connection between changes in $S_\odot$ and variations in the surface temperature, T_s, of the Earth. This is especially timely in the context of the problem of global warming; i.e. the increase in T_s by $\approx 0.5^\circ$C during the present century.

The irradiance fluctuations, can be expressed as the sum of various components which probably change over different time scales

$$\frac{\Delta S_\odot}{S_\odot} = \frac{\Delta S_{\rm S}}{S_\odot} + \frac{\Delta S_{\rm F}}{S_\odot}, \tag{1.1}$$

where $S_\odot$ is the total solar irradiance, $S_{\rm S}$ the sunspot irradiance and $S_{\rm F}$ the facular irradiance. The $\frac{\Delta S_{\rm S}}{S_\odot}$ is the so-called *Photometric Sunspot Index*, and $\frac{\Delta S_{\rm F}}{S_\odot}$ is the *Photometric Facular Index*. These components can be described in more detail as:

$$\frac{\Delta S_{\rm S}}{S_\odot} = \sum \alpha\, \mu A_{\rm s} \frac{3\mu + 2}{2}, \tag{1.2}$$

α being the bolometric sunspot contrast, $A_{\rm S}$ the sunspot area and μ the cosine of the heliocentric angle, θ, and

$$\frac{\Delta S_{\rm F}}{S_\odot} = \sum A_{\rm f}\, \mu\, f(\mu)\, L_{\rm F}(\mu), \tag{1.3}$$

where $A_{\rm f}$ is the area of the photospheric plage, $f(\mu)$ the limb darkening law of the quiet Sun and $L_{\rm F}(\mu)$ the centre-to-limb variation (CLV) of the facular contrast.

Because of the intrinsic difficulties in measuring the global photospheric contribution of faculae, the areas of chromospheric plages, $A_{\rm P}$, are used in most cases; then a calibration factor, $C_{\rm P}$, is introduced in the formula so that $A_{\rm f} = A_{\rm P} C_{\rm P}$.

However, the worst known factor is the CLV of facular contrast; its measurement and possible dependence on facular size are much sought after for these crucial evaluations of the solar contribution to terrestrial climate. Therefore, it is interesting to determine the dependence of facular photometric properties on facular size and heliocentric angle, which we shall do in this thesis.

1.3.4 Theoretical models for facula

The first models that took into account convective and radiative energy transfer in the calculation of small flux tubes were those of Spruit (1976, 1977) who

showed the importance of the 'hot wall' of the tubes, especially for explaining the observed CLV of facular contrast.

The view Spruit introduced can be summarized as follows. The magnetic concentration inside the flux tube suppresses the convective transport of energy, thus making the total energy flux smaller in flux tubes than outside them. Nevertheless, the walls are hotter than the interior due to the increase of temperature with depth (the non-magnetic stratification is superadiabatic). These hot walls radiate into the tube, heating it, and, if the tube is thin enough, this produces a hot bottom in the flux tube at the level of $\log \tau = 1$ (Spruit 1976; Deinzer et al. 1984; Ferrari et al 1985; Kalkofen et al. 1986). But if the tube is not completely optically thin this heating is not enough to equal the temperatures inside and outside the flux tube; therefore, at an equal geometrical height, the tube is cooler than the warm walls. At disc centre, larger tubes have smaller contrast because of the less efficient heating of the bottom. Similarly as when approaching the limb, the bottom begins to be obscured by the wall on the side of the disc centre, and the wall on the side of the solar limb begins to appear in the observer's field of view, enlarging the contrast of the facula. At sufficiently large μ, one wall blocks the other and the contrast of the small magnetic element decreases. Obviously, this decrease takes place at smaller μ the larger the flux tube is.

However, as mentioned above, it is supposed that most small flux tubes have diameters smaller than it is possible to resolve at present ($\leq$ 300 km), and all observations agree in the increase in facular contrast at least out to $\mu = 0.2$–0.3. For such small flux tubes, the hot-wall mechanism would produce a peak in the facular intensity at larger μ. Without an additional heating mechanism in the flux tube this behaviour cannot be explained for the smallest flux tubes, while for larger magnetic structures the hot wall works correctly (Spruit 1976; Caccin & Severino 1979; Chapman & Gingell 1984; Deinzer et al. 1984). A 'hot cloud' model has been proposed that works best if a number of small flux tubes are present in the line of sight and their hot cloud overlap. Note that these two models have different predictions for the continuum contrast of small flux tubes at disc centre; the hot wall predicts dark contrast at disc centre, while the hot cloud predict positive contrast (Knölker et al. 1991; Schussler 1987).

Since the bottom of the flux tube and the walls are hot, the upper and middle parts of the flux tube are illuminated by the radiation coming from below, thus increasing their temperature. This can partially explain the hot cloud effect, although not completely. The observed CLV of the facular contrast of small features is best fitted when this 'warm wall' effect is taken into account but still cannot be completely fitted by considering only this effect (Grossman-Doerth et al. 1989; Steiner 1990; Steiner & Stenflo 1990). When comparing the

model atmospheres deduced from theoretical computations with semi-empirical atmospheres obtained by inverting Stokes V profiles, it is clear that a heating mechanism is still missing in the theoretical models for the higher layers of the atmosphere. Several effects could play an important role in the CLV of the facular contrast that have so far not been properly taken into account when performing theoretical computations. This is the case for NLTE effects, for taking a non-grey radiative transfer, for the specific geometry of the flux tubes, for including waves inside the tubes, or for the necessity of introducing flux tubes of different sizes into the computations.

In this thesis we will study the observational CLV of faculae at different wavelengths that will allow us to test the validity of the different models and the influence of different mechanisms by comparing the results obtained with those predicted by the models.

1.3.5 Empirical modelling

One of the main aims of the empirical study of solar magnetic features is to determine their temperature stratification. Inversion of observations gives information about the temperature stratification. When empirical stratifications are compared to theoretical models, information about the heating and cooling mechanisms can be derived.

One-component models invert only the facular atmosphere, without taking into account the surrounding quiet atmosphere by using the Stokes I spectrum. In general these models reveal what is seen in low spatial resolution observations, i.e. no facular contrast at disc centre and a brightness excess near the limb. This appears in the models as a temperature equal to the quiet photosphere in low facular layers, but higher than that of the photosphere in middle and upper layers (e.g. Fontnela et al. 1993; Ayres et al. 1986).

On the other hand, two-component models take into account both the magnetic atmosphere and the surrounding quiet photosphere; they also use the Stokes I spectrum. In general these models show, in the higher layers, higher temperatures than 1-component models. Nevertheless, in the lower layers 2-component the models deduced by different authors are discrepant. This is mainly bacause of the different values of the observed facular contrast at disc centre. Generally, models inverted from data with high facular contrast at disc centre obtain high facular temperatures at the lower layers, and those with small facular contrast at disc centre obtain lower temperatures in the lower layers. In addition, differences in the surrounding quiet atmosphere assumed by the different authors can also explain the different atmospheres obtained (e.g. Chapman, 1970, 1977, 1979; Ayres et al. 1986; Walton 1987; Koutchmy &

Stellmacher 1978; Stellmacher & Wiehr 1979).

There are authors who have also obtained model atmospheres by inverting the Stokes V profiles. These kinds of models have shown that the temperature inside the magnetic elements is very dependent on the magnetic filling factor; that is, for larger filling factors the temperature in the layers of formation of the observed line decreases. These models overcome some of the limitations of the 1- and 2-component models based on Stokes I, since a different observed contrast at disc centre does not necessarily lead to different temperatures in deeper layers. Moreover, different models obtained from Stokes V show very similar temperature stratifications. Nevertheless, NLTE effects should be included in future calculations, since it has been proved that they have an important influence (e.g. Solanki & Stenflo 1985; Zayer et al. 1990).

Recently, Bellot Rubio et al. (2000b) have inverted Stokes I and V spectra in a self consistent way. They deduced an empirical model of the interior atmosphere of the flux tube and of the surrounding non-magnetic atmosphere.

In this thesis we intend to apply a 3-dimensional radiative transfer code to different geometries and filling factors of plage regions derived from the different semi-empirical models. We intend in this way to check the degree of agreement between the observed CLV curves of the facular contrast and those derived from the semi-empirical models.

1.4 Thesis overview

In this introduction we have presented the current knowledge and open questions concerning two different photospheric structures: granulation and small magnetic features. The importance of studying these phenomena has been stated and the way we are going to approach this problem has been outlined. Here, for the sake of clarity, we summarize the aims of this thesis.

The object of study of this thesis is the solar photosphere, which is a region of special interest since a change occurs in it from a convective to a radiative regime. Two structures have been selected for study in this layer of the Sun because of their importance and implications in solar physics. One the one hand, granular phenomenon offers the opportunity to study how overshooting convective cells change with height in the photosphere until they disappear. On the other hand, the faculae provide us with the chance to understand the small magnetic structures in the photosphere whose brightness CLV is particularly important in determining the total solar irradiance variation with the solar cycle.

It is also interesting to study these two different structures together since, when observing near the limb, the light comes from both granular and mag-

netic structures in active regions, and near disc centre it cannot be ensured that the magnetic structures are fully resolved; therefore, a mixing of information could also exist. Nevertheless, in active regions granulation suffers some alterations, and in this case the granulation is called *abnormal granulation*. On the other hand, network bright points appear outside active regions, where the granulation is *quiet granulation*.

We will approach this study by means of combining different techniques; namely, observations and forward modelling.

Specifically, concerning quiet granulation, a complete photometric study at different wavelengths and heliocentric angles will be performed. This will allow us to characterize different granular properties, such as size distribution, area–intensity relations, power spectra, fractal dimension, CLV of the contrast, etc. The characterization at different wavelengths and heliocentric angles will allow us to obtain information about the vertical structure of the granular properties, but will also allow us also to confirm, or put further constraints on, existing models of the solar granulation. This is interesting since recently CLV studies have not been widely used to test the validity of the modern models that have been developed in the last decades taking advantage of the advances in computing capabilities.

To this end, the observational work will be complemented by forward modelling studies. We will mainly apply a three-dimensional radiative code to different models of granulation obtained by different authors by means of hydrodynamic codes. This will allow us to test the degree of adjustment between the observations and the models, opening up the possibility of interpreting the observations in greater detail and stating the limitations of the models. These studies will be complemented by forward modelling performed from semi-empirical atmospheres.

Concerning small magnetic features, a similar scheme will be followed. First, a deep photometric study will be performed for different wavelengths and heliocentric angles. This will allow us to characterize the facular properties and their variation with height in the solar photosphere. Statistical and morphological studies will be made, and the dependence of different facular properties on facular size will be obtained. This is important by itself since there is still considerable debate about what the CLV of facular brightness is, and how it depends on the observing wavelength. Besides, as mentioned above, these kinds of studies have great implications in the study of total solar irradiance variations with the solar cycle.

A study of forward modelling will then be performed using different facular atmospheres in different conditions, geometries, etc. In all these studies, the effect of the surrounding 'quiet' photosphere will be included, which will allow

us to establish a bridge between studies on quiet granulation and those on small magnetic features.

Since pores have the same magnetic origin as faculae, and since many of the photometric properties change gradually from small magnetic features to larger ones, a study of the CLV of the brightness of pores will also be made.

Finally we wish to mention that the following papers have been published as a consequence of the work of this thesis:

- 'Center-to-limb variation of solar granulation from partial eclipse observations', M. Sánchez Cuberes, J.A. Bonet, M. Vázquez , A.D. Wittmann: 2000, Astrophysical Journal, 538, 940-959
- 'Center-to-limb variation of the Solar Granulation', M. Sánchez Cuberes, J.A. Bonet, M. Vázquez , A.D. Wittmann: 1998, in Astrophysics and Space Science, Vol. 263, Edited by Kluwer, p. 343-346
- 'Implementation of a Filter for the Restoration of solar Granulation images', M. Sánchez Cuberes, J.A. Bonet, M. Vázquez , A.D. Wittmann: 1999 in High Resolution Solar Physics: Theory, Observations, and Techniques, ASP Conference Series, Vol. 183. Edited by T. R. Rimmele, K. S. Balasubramaniam, and R. R. Radick, p. 515
- 'Infrared photometry of solar photospheric structures. I Active regions at the center of the disk', M. Sobotka, M. Vázquez, M. Sánchez Cuberes, J.A. Bonet: 2000, Astrophysical Journal, 544, 1155-1168
- ' Infrared photometry of solar active regions', M. Sobotka, M. Vázquez, M. Sánchez Cuberes, J.A. Bonet: 2000 in Journal of Astrophysics and Astronomy, 21, 289
- 'Infrared photometry of solar photospheric structures. II Center-to-limb variation of active regions', M. Sánchez Cuberes, M. Vázquez, J.A. Bonet, M. Sobotka, Astrophysical Journal, 570, 886
- 'Center to limb variation of quiet granulation in the infrared', M. Sánchez Cuberes, M. Vázquez, J.A. Bonet, M. Sobotka, 2002, Astronomy and Astrophysics, in press

2

CLV of solar granulation at λ 6708 Å

As explained in the introduction, we will do observational studies of the center-to-limb variation of solar granulation properties at different wavelengths. In this chapter we present the investigation performed on images obtained at λ 6708 Å during a partial solar eclipse visible from the Canary Islands on 1994 May 10. Several factors were combined to obtain an observational set of good quality: first, the use of an excellent telescope installed at a very good site, where high-resolution observations are frequently obtained, and secondly the good atmospheric conditions prevailing during the eclipse, even though it was close to sunset.

Granulation contrast is severely attenuated by the degradation caused by atmospheric turbulence and telescope instrumental profile and aberrations. Several procedures have been developed to compensate for these effects (see Bonet, 1999 for a recent review). Solar partial eclipses offer an opportunity to get an estimate of the Point Spread Function (hereafter PSF) representing the degradation produced by the telescope and the atmosphere. In this chapter we present the implementation of a filter based on an estimate of the PSF from solar partial eclipse observations, to restore images of granulation at different positions on the solar disk.

Then, granular properties are deduced from this high quality reconstructed images. This observational data, together with the ones presented in the following chapters, will allow us to achieve the objectives of the present thesis.

An important test for any theoretical model of the granulation is the observed temperature variation. This is usually measured by rms fluctuations of the continuum intensity. The distributions of other statistical properties (sizes and velocities) are also useful for comparing the output of numerical models

with observations (e.g., Wöhl & Nordlund 1985; Gadun & Pikalov 1996).

The definition of the geometrical boundaries of a physical process is a necessary ingredient for its modeling. This is also the case for the convective overshoot producing solar granulation. It is well known that granulation is a very shallow phenomenon observable only at the surface layers of the Sun, and the determination of its upper boundary is of crucial importance.

The CLV of different photometric and spectroscopic parameters is a good diagnostic tool for modeling the physical parameters with altitude in the photosphere. We measure variations of the continuum intensity contrast and, therefore, the related physical parameter will be the temperature contrast between the granular and intergranular regions. Close to the limb, observations are handicapped by the effect of geometrical foreshortening and the effects of a oblique line of sight crossing several individual granular cells. However, we can use this fact to extract information about the 3D structure of the solar granulation.

The horizontal temperature fluctuations associated with the granulation, decrease rapidly with height above optical depth unity (at $\approx$ 500 nm). Druesne et al. (1989) using speckle techniques found a decrease in power in the highest spatial frequencies near the limb. They attribute this to the expansion of granules with height as well as to the loss of the smallest granules. Wilken et al. (1997) have also made use of speckle techniques. They find an increase in small structures towards the limb, which they identify with the bright structures appearing sometimes at the granular borders (de Boer, Kneer, & Nesis 1992).

Different shapes of the CLV have been obtained by different authors and not all these changes can be attributed to the observing technique used or to the image processing applied. Time and spatial variability could also play a role. The so-called *quiet Sun*, including the solar granulation, changes with the solar cycle (see, for example, Muller 1990 for a summary). Rodríguez Hidalgo, Collados, & Vázquez (1992b) found, in quiet regions, a lower contrast, a larger mean size and a steeper CLV of the granulation contrast along the central meridian than along the equator.

A determination of the distance from the limb to which the temperature fluctuations, ΔT, associated with the granulation, are detectable is of great importance for knowing its variation with altitude in the solar atmosphere. This in turn is important for understanding the properties of convective overshooting into the stable solar atmosphere. Results by different authors, based on spectroscopic observations, vary widely. Keil & Canfield (1978), Keil (1980), and Kneer et al. (1981) obtained a rapid decrease with altitude, which terminates at a geometrical height of 60 km. Komm et al. (1990), Hanslmeier et

al. (1991), and Nesis et al. (1993) obtained a less steep decrease, in which the fluctuations vanish at an altitude of 170 km, although only granules larger than 1000 km were observed to reach this level. On the other hand, Salucci et al. (1994) observed granules larger than 1000 km that were coherent all through the atmosphere, that is, from 100 km to 400 km. Information about this can be obtained with the aforementioned photometric measurements.

2.1 Observations

Images of solar granulation at different heliocentric positions on the disk, $\mu = \cos\theta$, were obtained at the Swedish Vacuum Solar Telescope (SVST, Observatorio del Roque de los Muchachos, La Palma; see Scharmer et al. 1985) of $\approx$50 cm of aperture, during the 1994 May 10 solar eclipse. This annular solar eclipse (see Espenak & Anderson 1993 for general information) was observable as a partial eclipse from the Canary Islands and began at 17:53 UT, reaching mid-eclipse at 19:05 UT. Ephemerides for El Roque de los Muchachos were calculated using precise determinations of the local weather conditions (air temperature, barometric pressure, and relative humidity) which allowed to determine the apparent positions of the Sun and the Moon (see Sánchez Cuberes et al. 2000).

Image acquisition was carried out with a KODAK Megaplus 8-bit CCD camera (1360 $\times$ 1035 pixel) with an exposure time of 13 ms. An interference filter at $\lambda 6708 \pm 20$ Å selected a spectral range with a small number of spectral lines. This spectral range is of spetial interest since in the literature few works on the granular properties at this wavelength exist. The frames were taken by using an automatic selection system (the best two images within selection periods of 10 s were recorded). The image scale was $0\farcs124$/pixel.

The selected images are grouped into 18 series. Each series consists of a few images taken within a short time range (typically 3 minutes), at essentially the same heliographic coordinates on the solar disk. In all images a portion of the lunar limb was captured. See Table 2.1 for a census of the series and positions studied.

In addition, a set of 21 images at $\lambda 5425$ Å recorded on 1995 June 29 with the same telescope and similar observing parameters (except for the eclipse event and the pixel size which is now $0\farcs062$) have also been considered. These images include the solar limb oriented parallel to the y-axis of the camera and are analyzed in §2.3.4, devoted to the study of the penetration of convective motions into the higher photospheric layers.

The images were pre-treated with dark-current subtraction and flatfielding division. Only the best 181 images (good and uniform quality over the whole

TABLE 2.1— Census of the observations

Series	Position-μ	No. boxes
1	0.5/0.6	804/527
2	0.6/0.7	418/193
3	0.7	750
4	0.7/0.8	411/537
5	0.8/0.85	204/624
6	0.85/0.9	563/435
7	0.9/0.95	701/561
8	0.9/0.95	764/591
9	0.95/1.0	543/770
10	1.0	1305
11	1.0	1492
12	1.0	1584
13	1.0	1135
14	0.95	643
15	0.85/0.90	664/469
16	0.75/0.80/0.85	363/401/593
17	0.2/0.3/0.4/0.5	105/187/520/340
18	0.85/0.9	194/524

field) out of the 504 recorded during the eclipse, were selected for further processing .

Figure 2.1 shows a field of solar granulation partially covered by the Moon's limb during the solar eclipse. This image is only for illustration purposes and in this case our restoration method, presented in the following sections, has been applied to a box of $23\overset{''}{.}0 \times 23\overset{''}{.}0$. Left panel shows the unrestored image, and right panel the restored one.

2.2 Image processing techniques

2.2.1 Determination of positions on the solar disk

We located the position of each frame to within $1\overset{''}{.}0$ by using the eclipse ephemeris and lunar limb geometry.

An ephemeris of the eclipse was calculated to determine very precisely the relative position of the Sun and the Moon for every given time. Differential atmospheric refraction was included in the calculation, considering the local atmospheric conditions simultaneously measured from the Northern Optical Telescope also operating on the Roque de los Muchachos, to describe their

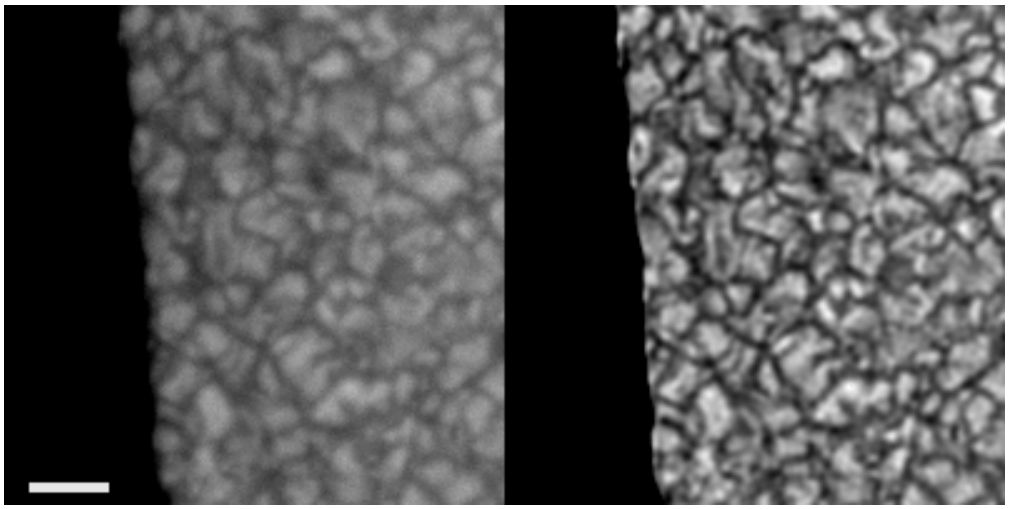

FIGURE 2.1— Image of the Moon's limb covering a filed of solar granulation close to the center of the solar disk. The image on the right is the same as that on the left but after applying our restoration method to correct for instrumental and atmospheric degradation (see section 2.2). The white mark in the lower left corner represents a length of $4\,''.0$.

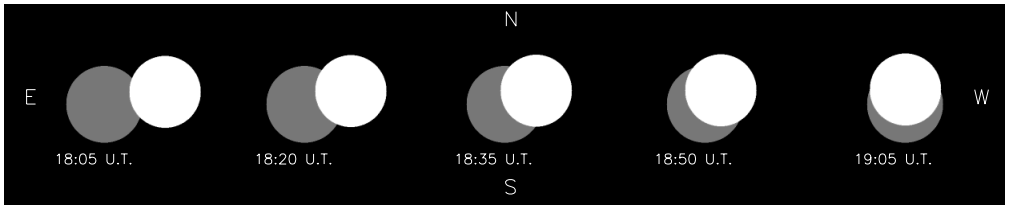

FIGURE 2.2— Relative positions of the Sun and the Moon for different times during our observations as seen from the Roque de los Muchachos.

apparent relative positions. Figure 2.2 shows the relative positions of the Sun and the Moon during the partial eclipse.

The basic idea of the method that we have applied to determine the position of a granular field on the solar disk, is to match the lunar limb present in each frame to the numerical simulation of the eclipse geometry.

Because of the altazimuthal mounting of the SVST, the image rotates in the focal plane, so all the images were de-rotated before applying the matching algorithm. The de-rotation process produces images with equal relative orientation but there exists an offset with respect to the absolute orientation on the sky. This absolute rotation angle was obtained by matching to the simulation of the eclipse those frames where the limbs of both the Sun and the Moon were

present.

The accuracy of the method was checked by using a group of pores close to the solar disk center, at $\mu = 0.96$ according to the Solar Geophysical Data. Our matching method reproduces this value of μ for the pores. Apart from the pores, the only relevant structure on the solar disk was a sunspot near the limb, but we could not use it for calibration due to the insufficient accuracy for our purposes of the Solar Geophysical Data, which is more crucial near the limb (see Steinegger et al. 1996).

A more detailed expalanation of the method used can be found in Sánchez Cuberes et al. (2000)

2.2.2 Image reconstruction

The process of formation of solar granulation images at the focal plane of the telescope can be described by the expression

$$i(x, y) = i_{\rm o}(x, y) * s(x, y) + n(x, y)\,, \tag{2.1}$$

where $*$ denotes convolution, $i(x, y)$ is the recorded image, $i_{\rm o}(x, y)$ is the object (or "true" intensity distribution), and $s(x, y)$ is the PSF at the moment of the exposure, describing the degradation effects from both the telescope and the atmosphere. The additive term, $n(x, y)$, represents the noise. In images taken with a good CCD camera the noise is predominantly photon noise, and because of the low contrast in solar granulation the correlation between signal and noise can be considered as negligible. Accordingly, the latter is well represented in formula (2.1) as an additive contribution to the signal.

The retrieval of the object $i_{\rm o}(x, y)$ can be performed from the inversion of equation (2.1) in the Fourier domain

$$\hat{i}_{\rm o}(x, y) = \mathcal{F}^{-1}\left[\frac{I(u_x, u_y) \cdot \Phi(u_x, u_y)}{S(u_x, u_y)}\right], \tag{2.2}$$

where $\mathcal{F}^{-1}$ stands for the inverse Fourier transform, u_x and u_y for the spatial frequencies in the x and y axis respectively, $I(u_x, u_y)$ and $S(u_x, u_y)$ are the Fourier transforms of $i(x, y)$ and $s(x, y)$ respectively—$S(u_x, u_y)$ is also called optical transfer function (OTF) of the imaging system. $\hat{i}_{\rm o}(x, y)$ is an estimate of the real object and the circumflex indicates that the restoration will not be complete in any case since the optical system operates as a low-frequency pass-band filter irrecoverably suppressing the spectral information beyond a certain cut-off. $\Phi(u_x, u_y)$ in (2.2) is a noise filter that has to be applied to the observed signal, $I(u_x, u_y)$, prior to the restoration process—division by $S(u_x, u_y)$—to avoid amplification of the noise, which would have a disastrous effect in the restored image.

2.2.3 Determination of the PSF

Solar eclipses are exceptional cases where the Moon's limb crossing the solar disk serves as a reference object to estimate amplitudes of the instantaneous OTF. Thus, an estimate of the perturbing contribution from the atmosphere and the telescope in a portion of the observed field can be inferred from the degradation of the nearby lunar-limb profile. Bonet et al. (1995) show that, if the x-axis is taken to coincide with the direction perpendicular to the Moon's limb, the section of $S(u_x, u_y)$ along the x-frequency-axis in the Fourier domain is given by

$$S(u_x, 0) = \mathcal{F}\Big[s_c(x)\Big], \tag{2.3}$$

where $s_c(x) = \int s(x, y)\, dy$ can be obtained from the expression

$$s_c(x) = \frac{d}{dx}\Big[i^M(x)\Big], \tag{2.4}$$

where $i^M(x)$ represents the intensity profile resulting from a perpendicular scan to the lunar limb. We compute $s_c(x)$ by performing the numerical derivative of $i^M(x)$, resulting in a bell-shaped function with significant oscillations in the wing obtained from the solar side, due to the solar granulation. Therefore, only the wing obtained from the lunar side, which is considerably less noisy, and its symmetric reflection are preserved for further calculations. Moreover, based on the isoplanatic approximation (this is, to assume that the PSF is common in all the studied field), we minimize the noise by averaging in each frame several estimates (typically ≈ 150) of $s_c(x)$ from different intensity profiles selected all along the Moon's limb included in the frame. In the averaging process, individual realizations of $s_c(x)$ have been shifted with sub-pixel accuracy to compensate for the Moon's topography. This smoothing method enabled us to avoid any kind of analytical approximations to the PSF (see, for example, Deubner & Mattig 1975; Collados & Vázquez 1987) that may lead to an unrealistic description of the image degradation. Assuming azimuthal symmetry for $s(x, y)$, it follows that $S(u_x, u_y)$ is also real and azimuthally symmetric so that the complete OTF can be constructed by rotation of $S(u_x, 0)$ and represented by $M(\nu)$, where $\nu = \sqrt{u_x^2 + u_y^2}$. Residual noise effects after averaging several $s_c(x)$ are removed from $S(u_x, 0)$ by least-squares fitting of cubic splines. The resulting rotated function, $M(\nu)$, will substitute $S(u_x, u_y)$ in expression (2.2).

Note that our determination of $s(x, y)$ is influenced by two assumptions. On the one hand, the isoplanatic approximation that could be partially justified by

the above-mentioned uniform quality observed in our selected frames. On the other hand, azimuthal symmetry in $s(x, y)$ is assumed, i.e. isotropic degradation. We are compelled to make such an approximation because our reference object (the lunar limb) is substantially a 1D structure. The symmetrization of $s_c(x, y)$ implies, in addition, a loss of the phases in $S(u_x, 0)$ since the Fourier transform of a symmetric function is real. Hence, we are limited to restoring only amplitudes. We are aware of the weight of these two assumptions. They are essentially equivalent to estimating a sort of average degradation in each frame. Given the excellent quality of our images—our working wavelength favors the quality of the seeing in comparison with other spectral ranges in the visible (see, for example, Roddier 1981)—to our understanding this would mean that the restoration process would not introduce substantial bias in the statistical analysis we intend to do taking advantage of a singular phenomenon offered by the nature (viz., the eclipse) and of the low computational cost of the method.

The stray light caused by scattering in the Earth's atmosphere and by optical surfaces has been estimated by averaging the signal in an area inside the Moon's disk at a distance of $1'.3$ from the lunar limb. At this distance the far wing of the measured PSF is virtually constant. For this purpose we have used images from series No. 9 near the solar disk center. The amount of scattered light determined in this way is $\sim 1\%$ of the mean photospheric intensity. Although the observations were performed shortly before sunset, this level of stray light is plausible because the transparency of the sky was excellent and the amount of atmospheric scattered light is smaller in the red range of the spectrum. Moreover, the influence of stray light may be substantial in measurements close to the solar limb; however, in our case the Moon occulted a significant portion of the Sun ($\geq 70\%$) at the time of the observations close to the limb ($\mu \leq 0.4$), thus drastically diminishing the amount of scattered light.

2.2.4 Noise filtering

Noise filtering is performed by weighting the spectral components of the image at various frequencies in some optimum way. Thus, our filter $\Phi(u_x, u_y)$ used in equation (2.2) is based on the so-called *optimum filter* described by Brault & White (1971), and is derived from the observed images themselves. This filter is constructed by imposing the reasonable condition that, in the measuring domain, the deviation of the image smeared by the PSF and not affected by noise (i.e. $i_o * s$), from the image which results from the filtering, is a minimum in the root-mean-square error sense.

Assuming the noise to be uncorrelated with the signal, this optimum filter

can be formulated as

$$\Phi(u_x, u_y) = \frac{|I(u_x, u_y)|^2 - |N(u_x, u_y)|^2}{|I(u_x, u_y)|^2}, \tag{2.5}$$

where $|I(u_x, u_y)|^2$ stands for the power spectrum of the observed image, and $|N(u_x, u_y)|^2$ for that of the noise. In the practical realization of $\Phi(u_x, u_y)$ it is usually adequate to replace both the signal and the noise power spectra by smooth fitted models.

In the present study the noise has been modeled as a constant power ("white") noise. White noise is typical for the statistical fluctuations in photon flux, which are the most prominent noise source in solar images taken with a good CCD camera. However the construction of a smooth model that fits well the observed power spectrum is much trickier. An accurate fit is increasingly important as the power level of the signal approaches the power level of noise in the high spatial frequency range.

In the paper by Brault & White (1971) simple functional forms to be fitted to the observed power spectra of 1D signals (spectral line profiles) are discussed, depending of their peculiarities. In image restoration, the problem is much more troublesome. The fact that the shape of the power spectra significantly changes depending on the nature of the structures in the considered image is added to the difficulty of dealing with 2D data. Consequently the choice of suitable functional forms to be fitted in each particular case is a very difficult task.

What saves us is the nature of the solar granulation. Brightness fluctuations due to granulation at the center of the solar disk can be considered as a statistically isotropic phenomenon and hence, the corresponding power spectrum is expected to be azimuthally symmetric. Away from the disk center, granular structures become progressively narrower in the direction perpendicular to the solar limb as one moves toward the limb. This effect produces power spectra closely approximating a bell with elliptical horizontal sections, which simplifies the fitting process. Since the shape (the *ellipticity* of the sections, ϵ [1]) of the power spectrum changes with the position in the solar disk, the noise filter has to be specific for each μ-position and this compelled us to deal with small boxes for constructing the filter as well as for performing the restoration process. Based on the stability of parameters such as PS shape, centroid of the 1D azimuthally integrated spectrum and total integrated power, the final decision for the boxsize was $12\farcs4 \times 12\farcs4$ (100×100 pixel).

[1] The term ellipticity is defined as: $\epsilon = 1 - (b/a)$, b and a being the the minor and the major semiaxis of an ellipse, respectively. This parameter intuitively represents how elongated an ellipse is.

Several attempts to fit 2D splines and Gaussian elliptical bells to the power spectra have failed, on the one hand, due to the oscillations obtained in the spline fit (very dependent on the specific node positions) and, on the other hand because the power bells have elliptical sections with variable ellipticity and orientation at different power levels so that they do not match Gaussian bells well. Consequently, we have chosen the fitting procedure described below.

To obtain the power spectrum of the observed signal at a given μ-position on the solar disk, an average of power spectra is performed—the resulting mean power spectrum will hereafter be denoted by PS. To this aim, several boxes placed within a range $\mu \pm \delta\mu$ ($\delta\mu$=0.05 for $\mu \geq 0.75$ and $\delta\mu$=0.1 for $\mu < 0.75$), are taken from the best-quality images that contain such a range of positions. However, for a given μ, images obtained at different solar latitude and longitude are treated separately to prevent the possibility of the properties of the granulation differing as a function of the coordinates on the solar disk. Following Cooley et al. (1970), the boxes are overlapped by 50%. In that way, the number of power spectra included in the average is substantially increased thus reducing the "noise" in PS stemming from the statistical differences between single boxes.

To fit a smooth model to PS, isocontours at various power levels are obtained and ellipses are fitted to them. The power levels have been chosen to have an isocontour representation as dense as possible, only being limited by the overlapping of the ellipse sampled points due to the small box size. No a priori assumptions about ellipticity or orientation of the fitted ellipses are made. The fitting method consist of taking many sets (typically 100000 for the outer iso-contours, and 700 for the inner ones) of three well separated points in an isocountour. Each set of three points defines an ellipse centered on the origin of frequencies. The parameters describing each of these ellipses are represented in the parameter space A-B-Θ, where $A \equiv$ major axis, $B \equiv$ minor axis and $\Theta \equiv$ ellipse orientation. The coordinates of the centroid (A_c, B_c, Θ_c) of the resulting cloud of points, defines the ellipse that is chosen as the best fit to the isocontour. This process has been applied to every isocontour obtaining a series of fitted ellipses at different power levels, all of them centered at the origin of spatial frequencies. Representation of these ellipses in the $12.''4 \times 12.''4$ box—i.e. sampling their analytical expressions—gives the ellipse data points describing PS at those power levels where isocontouring has been performed.

The overall slope of the power spectrum flattens in the high frequency range and the peaks due to the remaining statistical uncertainties cause the isocontours in this region to be disconnected so that an elliptical shape cannot be recognized. Thus, an information gap concerning the PS's shape is found between the lowest isocontour elliptically shaped and the noise level, where the

horizontal section of PS is a circumference of radius equal to the telescope cut-off spatial frequency. We assume an exponential decay of PS in this power range, described in every radial direction by the expression:

$$p = a \cdot e^{-b \cdot \nu} + c\,, \tag{2.6}$$

where ν is the spatial frequency, a and b are determined by forcing the decay to pass through the lowest contour and the cut-off, and c is the free parameter that rules the slope of the decay. The ensemble of data points compounded by the sampling of the ellipses and of the exponential decay, form an irregular grid describing the entire PS. To interpolate these data values a Delaunay triangulation of the set of data points has been performed to obtain a triangular grid structure (cf. Dahlquist & Björck, 1974). Then, linear interpolation has been applied to obtain a regular grid of interpolated surface values. Interpolated values are only computed from nearby points since the circumcircle of any triangle of a Delunay triangulation has the property of containing no other vertices in its interior. A logarithmic scale has been used to perform interpolation of the surface values in order to obtain a much realistic steeper decay between isocontours.

Figure 2.3a shows typical contours of PS at $\mu = 0.5$ and their fitted ellipses. The corresponding global smooth model fitting PS is presented in Figure 2.3b.

The constant power level of the white noise is computed by averaging the values of PS at frequencies higher than the telescope cutoff. Substituting $|I(u_x, u_y)|^2$ in expression (2.5) by the fit to PS described above and $|N(u_x, u_y)|^2$ by the fit to the noise, the optimum noise filter is obtained. Figure 2.3c shows a typical example of a noise filter corresponding to the case also represented in Figures 2.3a,b.

2.2.5 The restoration filter

A glance at equation (2.2) reveals that the restoration process globally consists in multiplying $I(u_x, u_y)$ by the quotient of $\Phi(u_x, u_y)$ and the OTF—$M(\nu)$ in our case. Consequently, this quotient is termed the "restoration filter" and is constructed by dividing the noise filter, calculated in the preceding section, by the specific $M(\nu)$ derived from each particular frame. Note that the optimum noise filter is calculated by averaging power spectra from different frames, affected by different $M(\nu)$s, whereas in the restoration filter the specific $M(\nu)$ for each frame is considered. From numerical simulations of observed spectra, based on real measurements of $M(\nu)$, we conclude that the resulting restoration filters are mainly sensitive to changes of the PS's shape in the high-frequency range ($\nu > 2$ arcsec^{-1}). However, this sensitivity is only remarkable when the

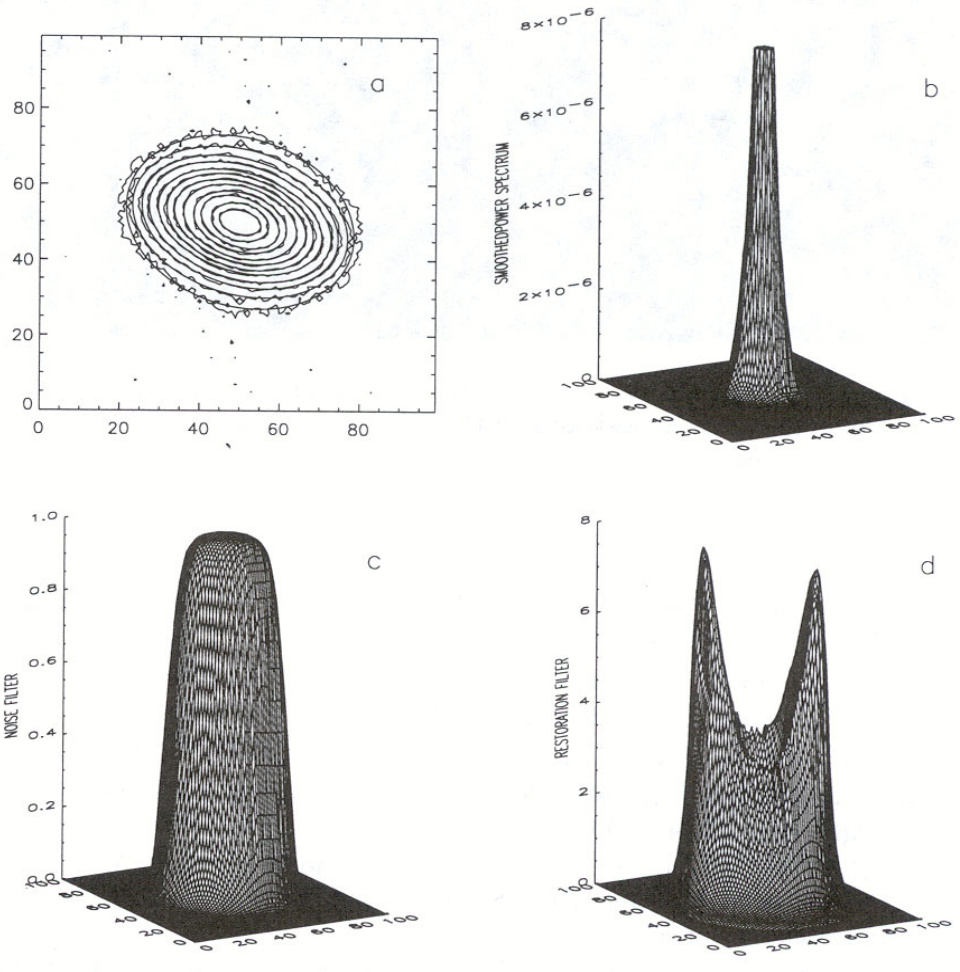

FIGURE 2.3— a) PS iso-contours and the corresponding fitted ellipses; b) Smooth model of PS; c) Noise filter, and d) Restoration filter. All cases correspond to PS at $\mu = 0.5$. The abscissa values are expressed in pixels.

$M(\nu)$s are very close to zero (bad image quality) or when they differ significantly (ample spread of image qualities) in this frequency range. Accordingly, we have selected for restoration only those images with good and similar quality in this frequency range, by analyzing and comparing the corresponding $M(\nu)$ functions.

It is worth commenting that the noise filter is derived from the information contained in the PS, and that the only free parameter is c, which determines the exponential decay from the lowest elliptically shaped isocontour to the noise level. This affects only the highest-frequency part of the filter, beyond the maximum of restoration, so most of the restoration filter is data-based. Another feature to mention is that, although $M(\nu)$ is a symmetric function, the restoration filter for $\mu \neq 1$ is not, as shown in panel d of Figure 2.3. This is because the noise filter is a function of the power level of the observed signal which, away from the disk center, is not azimuthally symmetric (for more details about the restoration filter see Sánchez Cuberes et al. 1999).

Once the restoration filter is ready for a given μ-range and a particular frame, individual boxes of $12\farcs4 \times 12\farcs4$ included in this range and frame are restored following expression (2.2). In this formula $I(u_x, u_y)$ represents the Fourier transform of a particular box. Prior to the calculation of $I(u_x, u_y)$, normalization of the granular intensities to the mean value and simultaneous removal of local gradients (e.g., limb darkening) have been performed by dividing each box by a two-dimensional linear surface least-squares fit. In order to avoid oscillatory behavior at the edges of the restored subfield, the borders of the original box have been apodized by a cosine bell extended over the 10% of the boxsize. Figure 2.4 shows pairs of original and reconstructed images for comparison. The contrast has been adjusted for each original-restored pair and the sub-fields represented are only $9\farcs92 \times 9\farcs92$ since the apodized edges have been removed.

2.3 Results

In the following sections we present the results obtained on the λ6708 Å images (sections 2.3.1, 2.3.2, 2.3.3.) and on the λ5425 Å images (section 2.3.4).

2.3.1 Power spectra of granulation

The power spectrum is a suitable tool for studying the geometrical properties and the intensity fluctuations in the granulation pattern although its interpretation is not straightforward because the information about sizes and relative positions of the granules is mixed. In this section we introduce the wavenumbers k_x and k_y expressed in Mm^{-1} as an alternative to the spatial frequencies

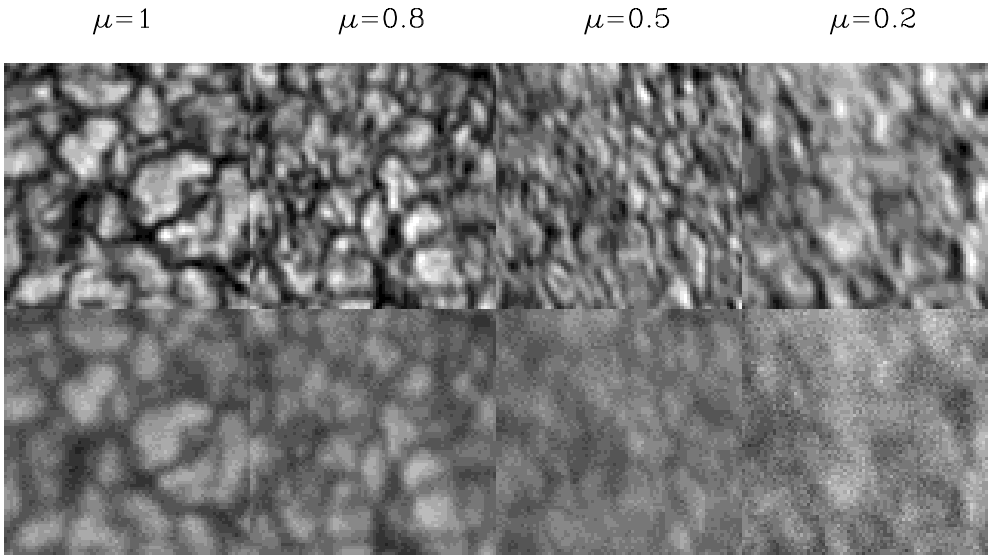

FIGURE 2.4— Pairs of reconstructed (top panel) and original images (bottom panel) at four μ-positions on the solar disk. The boxes cover a field of $9''.92 \times 9''.92$. For each $\mu-$position original and reconstructed images are scaled together.

u_x and u_y in arcsec^{-1}. This is usually done in analogous discussions about power spectra of solar granulation.

Since we are interested in the average properties of solar granulation at each μ-position, we have averaged the power spectra computed from all restored subfields (boxes of $12''.4 \times 12''.4$ overlapped by 50%) within the range $\mu \pm \delta\mu$ (see §2.2.3 for the definition of $\delta\mu$). We have included in the average all boxes with equal μ regardless of whether they belong to different series of images (i.e., different heliographic coordinates). See Table 2.1 for a census of the number of boxes considered at each position. Working with small boxes that moreover have been normalized by dividing by a 2D linear surface fit, favors the suppression of spatial scales larger than those representing the granulation itself (e.g., limb darkening, fluctuations caused by p-modes, meso-granular pattern, etc).

The intensity distribution of quiet solar granulation at the disk center can be considered as a statically isotropic phenomenon so that the expected power spectrum should have azimuthal symmetry. Our results approximate this expectation (see Figure 2.5 upper left panel). Assuming that the granulation pattern does not depend on the z-coordinate (height in the photosphere), and that there is no image degradation at all, the appearance of the granulation away from the disk center should only be affected by foreshortening, i.e., preservation

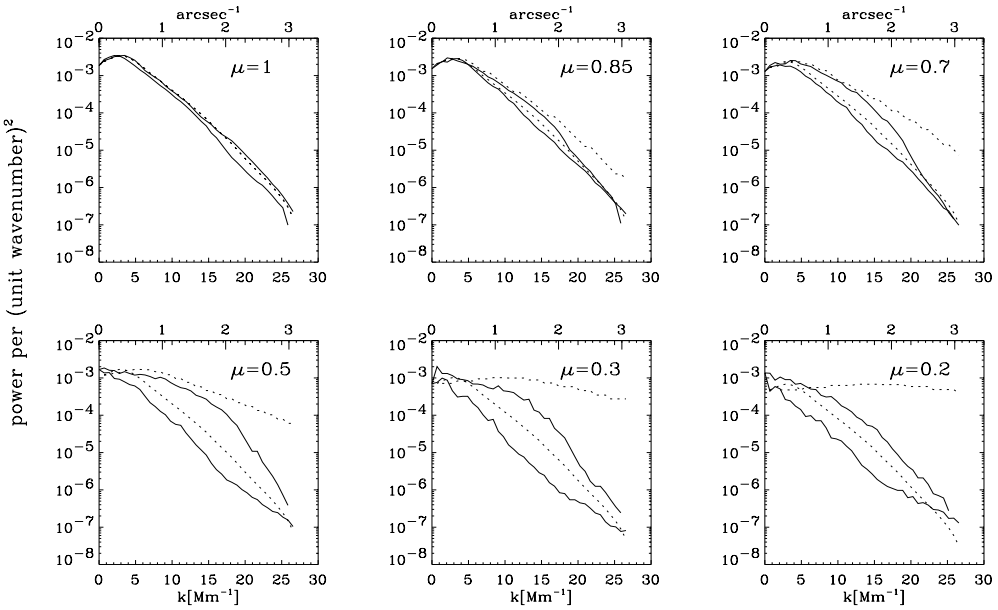

FIGURE 2.5— Mean power spectra along the k_x- and k_y-axes, at different μ-positions on the solar disk. Solid lines: computed from the restored images. Dotted lines: derived from the power at $\mu = 1$ under the assumption of only perspective foreshortening. The upper curve of each pair corresponds to the direction perpendicular to the solar limb. The dotted line at $\mu = 1$ represents the azimuthally averaged power spectrum.

of dimensions parallel to the solar limb (x-axis) and reduction by a factor of μ, of dimensions in the perpendicular direction to the limb (y-axis). The power spectrum of the granulation at position μ, P_μ, would in this case be related to the power at the disk center, P_o, by the expression

$$P_\mu(k_x, k_y) = \mu P_o(k_x, \mu k_y)\,. \tag{2.7}$$

This equation leads to: 1) the integrated power at μ being equal to that at the disk center, and 2) the iso-power lines being ellipses with the major axis coinciding with the k_y-axis, and with an ellipticity equal to $1-\mu$, which we will denote ϵ_μ. In the following we analyze in what extend this assumption of only geometrical foreshortening is realistic.

A crucial ingredient in the discussion on the shape of the power spectra is the image degradation represented in the Fourier domain by a transfer function — $M(\nu)$—monotonically decreasing toward high frequencies (wavenumbers) until a cut-off is reached. Thus, even in the case that such a transfer function be azimuthally symmetric, the isocontours of a power spectrum resulting from

simple geometrical foreshortening at position μ will not have ellipticity equal to ϵ_μ. Higher wavenumbers are more severely attenuated than lower ones, and consequently ellipticities will be smaller than expected (Rodríguez Hidalgo et al. 1992a,b). Hence, a correction for telescopic and atmospheric image degradation is unavoidable if a reliable description of the power spectra is desired.

In Figure 2.5 solid lines represent sections of the resulting mean power spectra along the k_x- and k_y-axes, at different μ-positions, after correction for image degradation. Dotted lines in the figure represent the power along the same axis, derived from the power at $\mu = 1$ (dotted line in the upper left panel of the figure) by means of equation (2.7). In each pair of curves—solid or dotted—the upper one corresponds to the k_y-axis. The measured power in both axes is in general below the expected value from the effect of perspective only. The differences are accentuated as we come close to the solar limb. This result contradicts the conservation of power predicted by the transformation described in (2.7), but it is equivalent, by virtue of Parseval's theorem, to the result presented in the next section that the normalized granulation contrast (i.e., $\Delta I_{\rm rms}$) decreases from the center to the solar limb. At this point the immediate reading that can be made from Figure 2.5 is that there is a loss of contrast at all wavenumbers.

These discrepancies with respect to the expectation for the case of only perspective foreshortening lead to the conclusion that, as a consequence of the three-dimensional structure of the granulation, radiative transfer effects play a role in the construction of the intensity pattern (Kandal & Keil, 1973). As we move toward the solar limb the line of sight goes laterally across more and more adjacent granular structures so that cancellations of their associated intensity fluctuations can be expected. Consequently, the smaller structures will be more affected by such a cancellation.

Figure 2.6 shows ellipticities, ϵ, in horizontal sections of the power spectra, as a function of μ, before and after restoration. Each panel in the figure corresponds to a different power level. Consistent with the above argument, ϵ in our *observed spectra* is smaller than ϵ_μ. However, after the restoration process the ellipticities essentially recover the value expected from foreshortening. Really, a glance to the figure reveals that at higher power levels, except at the very limb, ϵ is very close to ϵ_μ. Thus, radiative transfer effects may force a decrease in the amount of power on all scales but, at least at medium and low wavenumbers, do not alter the cosine law ruling the foreshortening by perspective. However, at lower power levels ϵ deviates noticeably from ϵ_μ. This could reflect the fact that the radiative transfer effects can be more effective at high wavenumbers, although some incomplete compensation for the atmospheric and telescopic degradation cannot be excluded at these spatial scales. In fact these

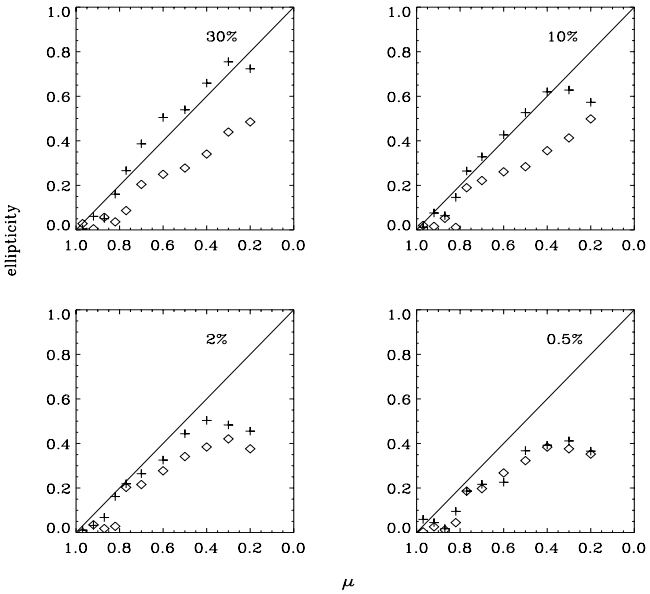

FIGURE 2.6— Ellipticity (ϵ) in horizontal sections of the power spectra, before ($\diamond$) and after (+) image restoration, as a function of μ. Each panel corresponds to a different power level (expressed in % of the maximum power). Thin solid line: ellipticities (ϵ_μ) expected in the case of pure geometrical foreshortening.

power levels correspond to frequencies larger than 2 arcsec^{-1} ($\sim$ 17 Mm^{-1}), approximately the frequency at which the restoration filter becomes more uncertain because it begins to be affected by the exponential decay assumed for the smooth model of the PS. Image degradation may also be mainly responsible for the deviation of ϵ from ϵ_μ at $\mu = 0.2$ or 0.3 since we have a larger contribution of power at high wavenumbers where the degradation is also more severe. Note that, according to expression (2.7), the power contribution shifts along the k_y-axis to frequencies higher by a factor of $1/\mu$. This means that for small μ, a significant amount of power is transferred beyond the cut-off frequency and consequently this information is irretrievable by the restoration process.

Our description of power spectra of solar granulation at different μ-positions agrees quite well with that by Wilken et al (1997) who perform a similar study on the basis of a set of images reconstructed by applying speckle techniques. These authors point out that for positions with small μ the average slope of the power parallel to the solar limb differs from that at $\mu = 1$ so that the corresponding power curves intersect. Thus, the power at large k_x increases at the expense of structures with low k_x. They interpret this result in terms of

the small structures penetrating into photospheric levels higher than the large ones. We arrive at a similar result for $\mu = 0.2$ where the curves corresponding to the power parallel to the limb intersect at $k_x \approx 22$ Mm^{-1}. Nevertheless, it must be kept in mind that this power excess could be caused by the Network Bright Points or by a more uncertain efficiency of the restoration filter at these high frequencies and large heliocentric angle.

The recovery by image restoration, of the ellipticity expected in the power spectrum from simple geometrical foreshortening, at least in the wavenumber region with the larger contribution of power, leads to the conclusion that the distribution of granular structures is isotropic at any position on the solar disk except perhaps for very small spatial scales or at positions very close to the limb ($\mu = 0.2$ or 0.3). This result confirms one of the basic assumptions in the method by Rodríguez Hidalgo et al. (1992a) to determine the degradation of the power spectra; namely, the deviation from ϵ_μ of the measured ϵ in the original mean power spectra is exclusively a consequence of the image degradation.

The isotropy of the granular structures also justifies the azimuthal integration of the 2D spectra over ellipses of ellipticity ϵ_μ to obtain a 1D power spectrum representing the relative power associated with each spatial scale, k. Figure 2.7 presents the 1D mean spectra that we obtain for μ ranging from 1 to 0.4.

The wavenumbers $k_{\max}$ and $\overline{k}$ defining the position of the maximum and of the centroid are standardly referred to in the literature as typical parameters characterizing the 1D spectra of granulation. At $\mu = 1$, $k_{\max}$ is 4 Mm^{-1} and, for decreasing μ, slowly shifts toward smaller wavenumbers. Our values of $k_{\max}$ coincide quite well with those reported by Rodríguez Hidalgo et al. (1992b). The mean wavenumber, $\overline{k}$, corresponds to a spatial scale representing somehow the size of a mean granular cell (see Aime 1978). Figure 2.8 shows the CLV of $\overline{k}$ from the present and previous works. Most of the curves follow a monotonic decrease from the center to the limb—our curve shows the steepest gradient—thus indicating an increase of the mean spatial scale as one moves to higher levels in the photosphere. The results by Rodríguez Hidalgo et al. (1992b) for measurements along the solar equator—they do a comparative analysis of the CLV of $\overline{k}$ and granular contrast along the equator and the central meridian—are an exception to this behavior showing a maximum at $\mu = 0.64$. Our estimates of $\overline{k}$ (~ 6.15 Mm^{-1}) at positions close to the solar center resemble the value reported by Deubner & Mattig (1975) (≥ 6.06 Mm^{-1}) at a near wavelength and also the peak value (6.11 Mm^{-1}) that Rodríguez Hidalgo et al. (1992b) obtained for the equatorial CLV variation of $\overline{k}$. From the figure no clear correlation between the trends of the curves and the wavelength can be derived.

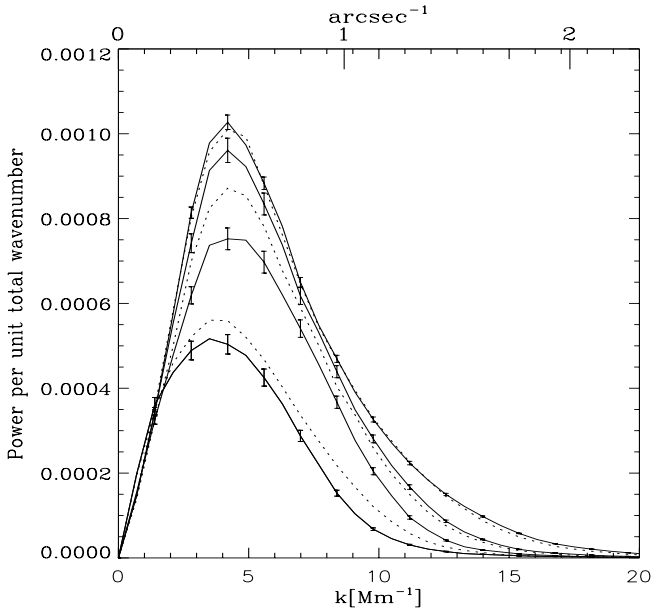

FIGURE 2.7— 1D mean power spectra of solar granulation. The curves correspond to positions μ ranging from 1.0 to 0.4, showing a monotonically decreasing peak with μ. Bars represent the error of the mean value and for the sake of clarity they are only drawn in four of the curves.

2.3.2 Granular contrast

Measurements of the CLV of the granular contrast in the continuum is a suitable input to model temperature inhomogeneities as a function of height in the photosphere. Such measurements have been carried out by many authors along the time (see Bray, Loughhead, & Durrant 1984, and references therein; Pravdjuk, Karpinsky, & Andreiko 1974; Keil 1977; Schmidt et al. 1979; Durrant, Mattig, & Nesis 1983; Druesne et al. 1989; Rodríguez Hidalgo et al. 1992b; Wilken et al. 1997).

Table (2.2) includes the corrected and uncorrected contrast values at the solar disk center from this work and from other authors at several wavelengths. For the sake of comparison we present in the fifth column the contrast value converted to λ 5000 Å. In this conversion we assume that the relative intensity fluctuations vary as the inverse of the wavelength, which seems to be a very good approximation (Wittmann 1979). Again, no agreement is found between different works or between contrasts and wavelengths. However, the power spectra and contrast reported by different authors can also be substantially influenced by factors such as solar cycle variations, observing techniques,

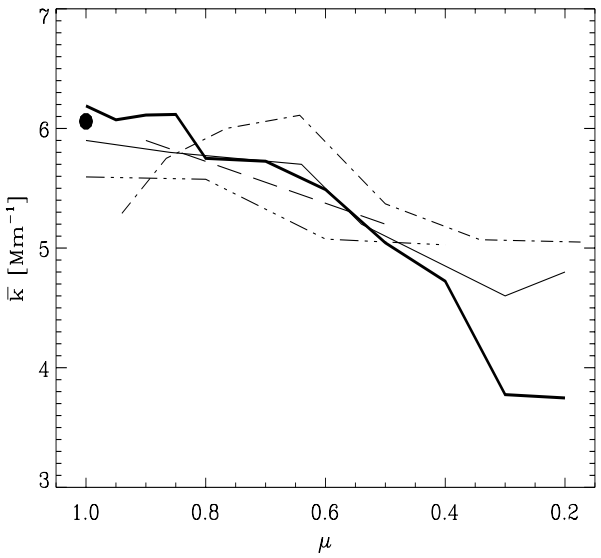

FIGURE 2.8— CLV of the mean wavenumber, $\overline{k}$, of the granular pattern. Thick solid line: this work (λ6708 Å). Dashed-dotted: Rodríguez Hidalgo et al. (1992b) along the solar equator (λ4686 Å). Thin solid line: Schmidt et al. (1979) from Spectro-Stratoskop data (λ5560 Å). Long-dashed: Schmidt et al. (1979) from eclipse data (λ4220 Å). Dashed-three dots: Keil (1977) (λ5520 Å). Filled circle: Deubner & Mattig (1975) (λ6070 Å).

procedures applied for data reduction, etc.

In several previous works dealing with determinations of solar granulation contrasts, only the power spectra of the observed images are restored and from them the contrasts are calculated by integrating the power. Here we compute the contrasts directly from the restored images. Working in the image domain gives the advantage that one can remove the edges of the image affected by the apodization that would lead to an underestimate of the contrast computed from the power spectrum. In addition, the possible appearance of spurious structures originating in defective noise filtering during the restoration process can also be detected.

Figure 2.9 shows the CLV of the granular contrast, $\Delta I_{\rm rms}$, from this and previous works, normalized to the value at the position closer to the disk center. The curves by Schmidt et al. (1979) are multiplied by factor $1/\sqrt{\mu}$ as proposed by Wiesmeier & Durrant (1981). Stray light induces an underestimate of $\Delta I_{\rm rms}$. However, given the small amount of stray light in our images (see §2.2.2), its effect on the data may result in an underestimate of the contrast by 2 or 3%

TABLE 2.2— Summary of $\Delta I_{\rm rms}$ obtained by different authors at μ=1

Authors	λ [Å]	$\Delta I^{\lambda}_{\rm rms}$(obs) [%]	$\Delta I^{\lambda}_{\rm rms}$(corr) [%]	$\Delta I^{5000}_{\rm rms}$ [%]
Keller & Koutchmy (1991)	4451		11.0	9.79
Karpinsky & Pravdjuk (1972)	4650	4.5	14.0	13.02
Krat et al. (1973)	4650	8.8	13.0	12.09
Rodríguez Hidalgo et al. (1992b)	4686	9.4	11	10.30
Ricort & Aime (1979)	5050	1...7	16...19	16.16...19.19
Canfield & Mahltretter (1973)	5170	5.9	8.2	8.47
von der Lühe & Dunn (1987)	5170	3.06	12.7	13.13
Keller & Koutchmy (1991)	5256		10.3...11.0	10.83...11.56
Lévy (1971)	5300	7.0	17.5	18.55
Ricort et al. (1981)	5300		16.5	17.49
Edmonds & Hinkle (1977)	5470	7.9	14.1	15.42
Namba & Diemel (1969)	5490	5.6	9.3	10.21
Schmidt et al. (1981)	5500	6.1	10.5	11.55
Wilken et al. (1997)	5500		13.5	14.85
Mehltretter (1971b)	5520	5.9	10.0	11.04
Keil (1977)	5520	5.7	13.2	14.57
Wittmann & Mehltretter (1977)	5560	5.7	8.7	9.67
Wittmann (1979)	5560	6.6	8.9	9.89
Wiesmeier & Durrant (1981)	5560	4.05	7.2	8.00
Durrant et al. (1983)	5560		11.3	12.56
Karpinsky & Pravdjuk (1972)	6000	3.1	9.6	11.52
Keller & Koutchmy (1991)	6069		9.1	11.04
Deubner & Mattig (1975)	6070	5.0	12.8	15.53
Mehltretter (1971a)	6300	2.6	8.0	10.08
Beckers & Parnell (1969)	6569	1.7	3.9	5.12
This work	6708	4.6	9.6	12.88

of its value at most. No clear correspondence can be concluded between the wavelength and the trends of the curves. Our contrast in the center of the disk amounts to 9.6% and shows a monotonic decrease, slow at the beginning (up to $\mu = 0.9$) and then accentuated up to $\mu = 0.2$. Rodríguez Hidalgo et al. (1992b) find a noticeable increase of the contrast along the equator up to $\mu = 0.64$ and then a rapid decrease. The results of Schmidt et al. (1979) and Durrant et al. (1983), both from the Spektro-Stratoskop data and at the same wavelength, substantially differ one from each other beyond $\mu = 0.6$. The latters' curves present a maximum also located out of the disk center, at μ=0.86 and 0.83, respectively, although much less conspicuous than that obtained by Rodríguez Hidalgo and coworkers.

Many of the curves in Figure 2.9 show a monotonic decrease from the center to the limb in accordance with our results. The observational results of Kneer et al. (1980) and Espagnet et al. (1995) indicate a rapid decrease of ΔT with height, which would lead to a slow monotonic decrease in the CLV of the contrast. This can be understood from the study of the temperature dependence

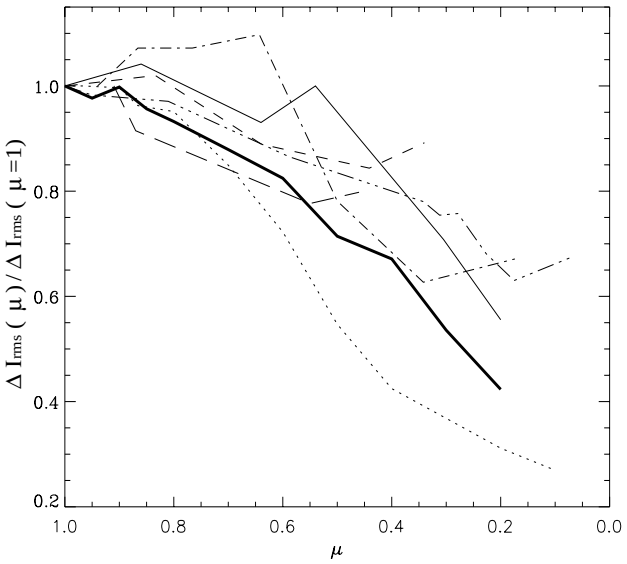

FIGURE 2.9— CLV of the granular contrast, $\Delta I_{\rm rms}$, normalized to the value at the disk center. Thick solid line: this work (λ6708 Å). Dashed-three dots: Wilken at al. (1997) (λ5500 Å). Dashed-dotted: Rodríguez Hidalgo et al. (1992b) along the solar equator (λ4686 Å). Dashed: Durrant et al. (1983) from Spectro-Stratoskop data (λ5560 Å). Thin solid line: Schmidt et al. (1979) from Spectro-Stratoskop data (λ5560 Å). Long-dashed: Schmidt et al. (1979) from eclipse data (λ4220 Å). Dotted: Pravdjuk et al. (1974) (λ4650 Å).

of the source function and of the opacity at the layers in which the continuum is formed. In those layers, where hydrogen is the main electron donor, the opacity is proportional to the electron density which is very temperature sensitive. Thus, an increase in temperature leads to an increase in the source function which is partially canceled by a rise in the opacity, moving the height of formation to higher layers where the temperature fluctuations between granules and intergranular lanes, ΔT, is small (Kneer 1984). In this way, a steep gradient in ΔT leads to a smooth monotonic decrease in the $\Delta I_{\rm rms}$ variation curve. On the other hand, a smaller gradient (Bendlin & Volkmer 1993) would lead the curve to peak somewhere between the disk center and the limb because now in higher layers in the atmosphere ΔT is still significant whereas the counteractive effect of the opacity is not so efficient as in deeper layers. Thus, our results, together with those by Pravdjuk et al. (1974) based on data from the Soviet Stratospheric Solar Observatory (SSSO), although at a quite different wavelength, seem to indicate the steepest gradient of ΔT; the overall slope of both curves represents the upper limit among those considered for comparison.

2.3.3 Distribution of granular Areas and Intensities

The granule-finding algorithm

In previous sections of this chapter we have studied the power spectra at different disk positions, which has given hints about the size distribution and contrast of the granules. Nevertheless, a direct statistical analysis of the restored images can supply invaluable complementary information about the brightness and size distribution, as well as about the morphologies of granular and intergranular areas, as mentioned in the introduction.

In order to get statistically representative data of the granular sizes, an objective and detailed study has been performed by using a granule-finding algorithm. Following Roudier & Muller (1987) a high pass-band filter has been applied to remove large-scale structures other than granulation, such as p-modes and mesogranulation. The filter's analytical expression is

$$F(k) = (1 - e^{-a^2 k^2}), \tag{2.8}$$

where $k = \sqrt{k_{\rm x}^2 + k_{\rm y}^2}$ is the spatial wavenumber and a is a constant proportional to the FWHM of the Gaussian, which in turn defines the width of the band to be filtered. The value of a has been set to have a FWHM $= 3$ Mm^{-1}.

This high pass-band filtering was performed separately in each of the restored sub-fields ($12\farcs4 \times 12\farcs4$) considered above. After filtering, the criterion used to identify the granular structures was an intensity threshold. Since the contrast of granulation varies from the center to the limb, the threshold has been set equal to the average intensity plus 0.1 times the standard deviation in each particular box, thus allowing the use of the criterion shown in equation (2.9) for every disk position.

$$I_g \geq \langle I \rangle + 0.1\sigma_I \tag{2.9}$$

This choice of the filtering and threshold parameters produces the best agreement between the granules identified by the algorithm and those recognized by visual inspection. Nevertheless, the definition of a granule is not trivial since most of them show a complicated inner structure that is sometimes difficult to disentangle from small granules. This effect gets more dramatic when approaching the limb, where radiative transfer effects may produce superpositions of individual granules that are interpreted by the algorithm as large granules with complex inner structure. As a consequence of these reconnections, the area of the granules found by the algorithm gets to unreasonably

high values for positions very near to the limb, where recognition of individual granules is very tricky. Radiative transfer effects may be responsible for the deviation of the ellipticities of the power spectra from the cosine law of foreshortening beyond $\mu = 0.4$. Here we are more conservative and only the results ranging from $\mu = 1$ to $\mu = 0.6$ will be included since in this range none of these reconnection effects is expected to play an important role as verified by visual checking.

Following Hirzberger et al. (1997), the intergranular lanes have been defined by a geometrical law instead of an intensity criterion. That is, granular cells containing the granule and its corresponding part of surrounding intergranular lane have been set to have their perimeters equidistant to the adjacent granules. This way, the intergranular lanes are divided into two halves and each half is assigned to its corresponding granule. By definition, intergranular lanes are those regions not identified as granules by de granule-finding algorithm.

Granular and Intergranular Areas

After applying the granule-finding algorithm to all the boxes of every series, a significant number of granules is obtained for each disk position. Their area distribution at the disk center is represented by the upper curve of Figure 2.10. Following the usual convention an equivalent circular diameter of the granules is defined as $d_{\rm g} = (4A_{\rm g}/\pi)^{1/2}$, where $A_{\rm g}$ is the granular area. Since no peak appears in the curve, no characteristic granular size can be inferred. Note the change in the slope of the histogram at $d_{\rm g} \approx 1\farcs9$, which is in good agreement with the results obtained by Hirzberger et al. (1997). Roudier & Muller (1985) obtained a similar curve shape though with the change of slope at $1\farcs31$. This difference could be caused by the different segmentation technique used for defining the granular contours.

In positions other than the disk center the areas of the granules are affected by foreshortening in the radial direction of the Sun. To compensate for this effect we have divided the measured areas by $\cos\theta$. The corresponding histograms of granular sizes are also shown in Figure 2.10. Since they look quite similar, individual histograms have been plotted with a vertical offset to facilitate individual inspection. Moreover, spline fits to the curves are also overplotted in the lower part of the figure to facilitate their comparison. Note that the change of slope at $d_{\rm g} = 1\farcs9$ gets gradually smoother from $\mu = 1$ up to $\mu = 0.6$, and that the number of larger granules increases in parallel. The minimum observable granular size increases with heliocentric angle due to the foreshortening.

Using the definition of intergranular lanes described above, their area distributions have been computed for different μ-positions. Figure 2.11 shows the

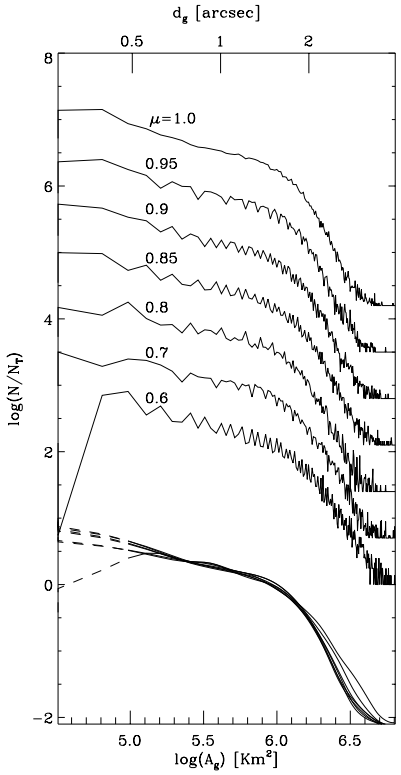

FIGURE 2.10— Normalized histograms of the granular areas from $\mu = 1$ (top curve) to $\mu = 0.6$ (bottom noisy curve). The curves have been plotted with an offset of 0.7 in the vertical direction for the sake of clarity. At the bottom of the figure spline fits to the histograms are overplotted to facilitate comparison. The dashed part of the latter curves shows the range where the fit was not reliable.

results. As in Figure 2.10, an offset has been introduced to enable inspection of individual histograms and the overplot of all of them, but here without fitting of splines, is represented at the bottom of the figure for comparison. In contrast with the results obtained for the granular areas, the intergranular ones have a typical size characterized by the maximum of the histogram, which moves to larger intergranular sizes for positions closer to the limb. This displacement is accompanied by an increase in the number of larger intergranules and a decrease in the number of smaller ones.

Similarly, Figure 2.12 shows the distributions of granular cell areas at different μ (a cell is composed of a granule and its corresponding intergranular area). As expected from the previous results, the general trend observed here

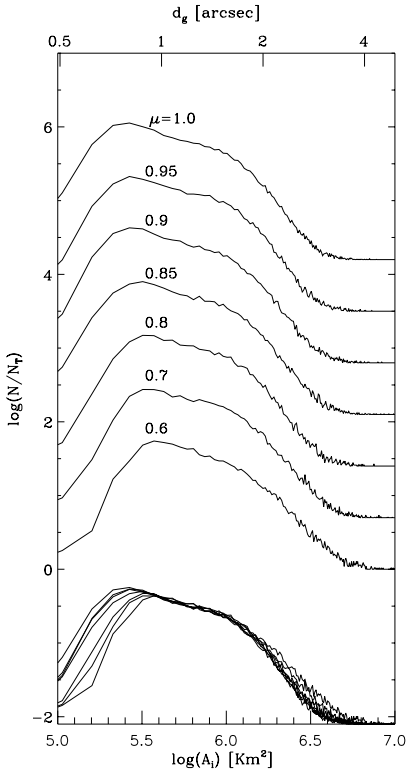

FIGURE 2.11— Histograms of the intergranular areas for different μ-positions. The histograms are overplotted at the lower part of the figure to facilitate their comparison.

is an increase in the cell area when approaching the solar limb. The peaks appearing in these plots can be regarded as the signature of typical sizes for granular cells. Using an intensity threshold in the granular finding algorithm, Roudier & Muller (1986) did not find any peak in the cell areas distribution of granulation. Nevertheless, Schrijver, Hagenaar, & Title (1997) obtained a well-defined peak using a "basin algorithm", and argued that these two apparently fundamental different results merely reflect the different methods used. The mean area of granular cells obtained in the present work ranges from 1.36 Mm^2 at $\mu = 1$ to 2.06 Mm^2 at $\mu = 0.6$. Bray et al. (1984) found an average cell size of 1.67 Mm^2 at the disk center and Schrijver et al. (1997) a value of 1.33 Mm^2, in better agreement with the present work.

To better understand the relation between the granular and the intergranular sizes, the ratio granular/cell area (A_g/A_c) is computed for each cell. The histograms of these ratios at different disk positions are shown in Figure 2.13.

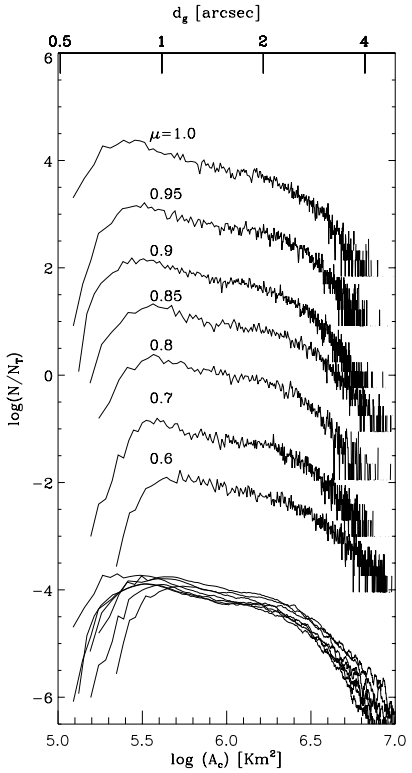

FIGURE 2.12— Histograms of the granular cell areas at different μ-positions. The histograms smoothed by convolving with a boxcar are overplotted at the lower part of the figure to facilitate their comparison.

As in the last three figures, individual curves are arbitrarily displaced in the vertical direction and also overplotted at the bottom to facilitate comparison. Note that the peak characterizing the more frequent value of the ratio $A_{\rm g}/A_{\rm c}$ is located around 0.44. In general terms, one can detect a tendency of the peak to increase slightly in amplitude and shift towards smaller ratios as we move toward the solar limb (i.e., the intergranular lanes become more dominant in the granular cells at positions nearer to the limb).

If the *granular filling factor* (hereafter GFF) is defined as the percentage of area of the image covered by granules, we obtain values decreasing monotonically from 44.2 % at the disk center to 42.8% at $\mu = 0.6$. These values are coherent with the characteristic ratio $(A_{\rm g}/A_{\rm c})$ mentioned above. The decrease in the GFF is equivalent to the displacement of the peak towards smaller values in the $(A_{\rm g}/A_{\rm c})$ histogram. In Figure 2.14 the GFF is plotted against μ from

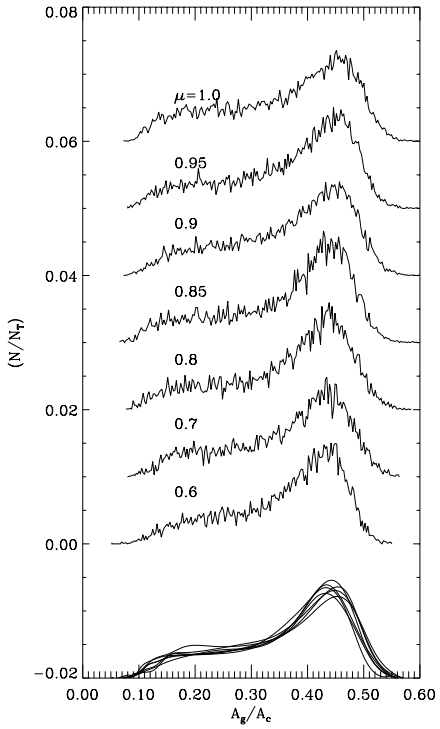

FIGURE 2.13— Histogram of the (A_g/A_c) ratios from $\mu = 1$ (upper curve) to $\mu = 0.6$ (lower noisy curve). Spline fits to the histograms are overplotted in the lower part of the plot.

the disk center to the very limb. The positions close to the limb are included in the plot to show the spectacular increase of the GFF at those positions. Visual inspection of the restored images before applying the granular finding algorithm also leads to the impression that a decrease of the intergranular lanes takes place for positions very near to the limb. Thus, despite the fact that the granular finding algorithm is not suitable for morphological studies near the limb, we interpret this increase of the GFF as a real physical phenomenon, at least qualitatively. However, the origin of this trend in the GFF will be checked in section 5.4, chapter 5.

Dependence of brightness on granular cell area

In the left panel of Figure 2.15, the variation of the mean granular intensity versus the cell area is plotted for $\mu = 1$. Apart from the dispersion of the results, this variation can be described in general terms as an apparently linear

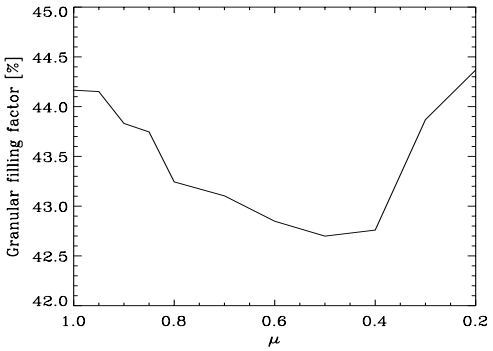

FIGURE 2.14— Granular filling factor for different μ-positions.

increase in the intensity with the cell area up to a certain size, after which the intensity remains constant, on average, for larger cells. The "elbow" defined around $d_g \approx 2\farcs0$ by the change of the mean slope in this variation marks a boundary between two ranges of cell sizes showing different behavior. This singularity was already found by Hirzberger et al. (1997) at the same cell size. The right panel shows similar results for $\mu = 0.6$. The change of slope at $d_g \approx 2\farcs0$ in this plot looks less conspicuous than for $\mu = 1.0$. An analogous behavior is found for the maximum granular intensity versus cell area.

In the upper panels of Figure 2.16 the mean intergranular intensities are plotted versus cell area. Note that the mean intensities of the intergranular lanes are independent of the cell area, although a large dispersion is found for smaller granules. A general increase in the intergranular normalized intensities is observed for positions nearer to the limb. The average of the mean intergranular intensities gives 0.93 at $\mu = 1$ and 0.95 at $\mu = 0.6$.

In the lower panels of Figure 2.16 the minimum intergranular intensity is plotted versus cell area for $\mu = 1$ and $\mu = 0.6$. The smaller cells are those with brighter intergranules. There is also a general increase of the minimum intergranular intensities when approaching the limb. The average values of these peak intensities are: 0.83 at $\mu = 1$ and 0.86 at $\mu = 0.6$

Fractal dimension

In Figure 2.17 granular areas, A_g, are plotted versus their corresponding perimeters, P_g, for $\mu = 1$ and $\mu = 0.6$. Note the different slope of this representation for small and large granules. Because of the small dispersion exhibited in this plot, a linear fit in both ranges seems reasonable. The possibility of fitting

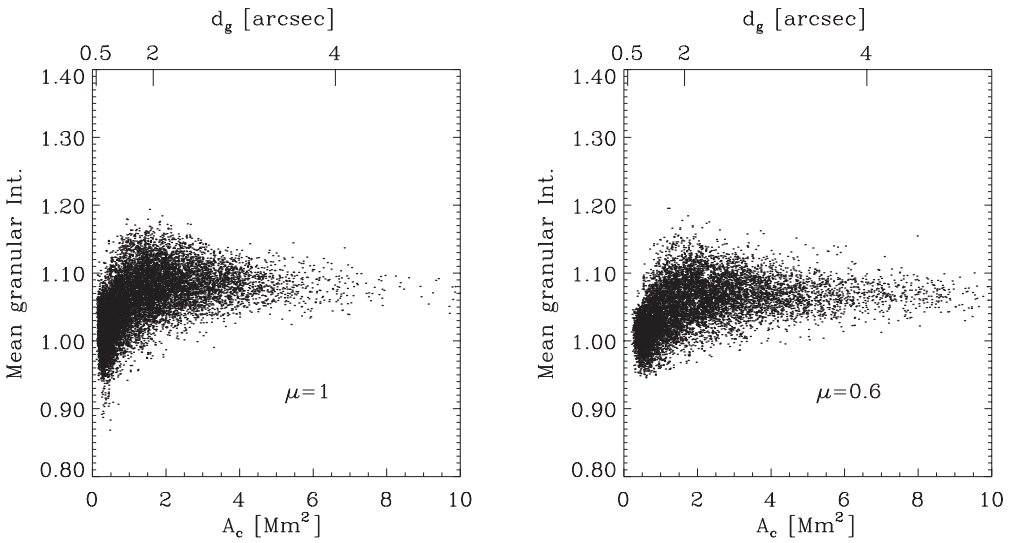

FIGURE 2.15— Mean granular intensities versus granular cell area for $\mu = 1$ and $\mu = 0.6$.

straight lines in this log–log representation means that the perimeter of the granules can be expressed in each size range as $P_{\rm g} \propto A_{\rm g}^{D_{\rm f}/2}$ where $D_{\rm f}$ is the fractal dimension. At the disk center we obtain a fractal dimension $D_{\rm f} = 1.35$ for the small granules. This value is in agreement with those found by other authors (i.e., $D_{\rm f} = 1.34$ by Darvann & Kusoffsky 1989, $D_{\rm f} = 1.31$ by Brandt et al. 1991, $D_{\rm f} = 1.3$ by Hirzberger et al. 1997), and is very near to the value $D_{\rm f} = 4/3$ predicted for isobaric two dimensional cuts in the Kolmogorov theory of isotropic, homogeneous turbulence in three dimensions (Lovejoy 1982). Kolmogorov turbulence theory predicts a fractal dimension of $D_{\rm f} = 1.67$ for isothermal cuts (Mandelbrot 1975). In the present work, the iso-intensity contours are supposed to correspond with isotherms since we are dealing with continuum images. Thus, the expected fractal dimension for a turbulent origin of granulation would be $D_{\rm f} = 1.67$. Although fractal dimension analysis is limited for determining the turbulent origin of granulation (Brandt et al. 1991), our results seem to disagree with a turbulent origin. For large granules we obtain a fractal dimension $D_{\rm f} = 2.16$. This value is an overestimate, since two-dimensional objects cannot have a fractal dimension larger than 2 (Mandelbrot 1977). It must be taken into account that the iso-intensity contours of granulation represent a projection and not a iso-plane cut. The results of laboratory experiments made by Sreenivasan & Meneveau (1986) point to an over-estimate of the fractal dimension due to the thickness of the layers observed. Thus, the fractal dimensions obtained in the present study must be

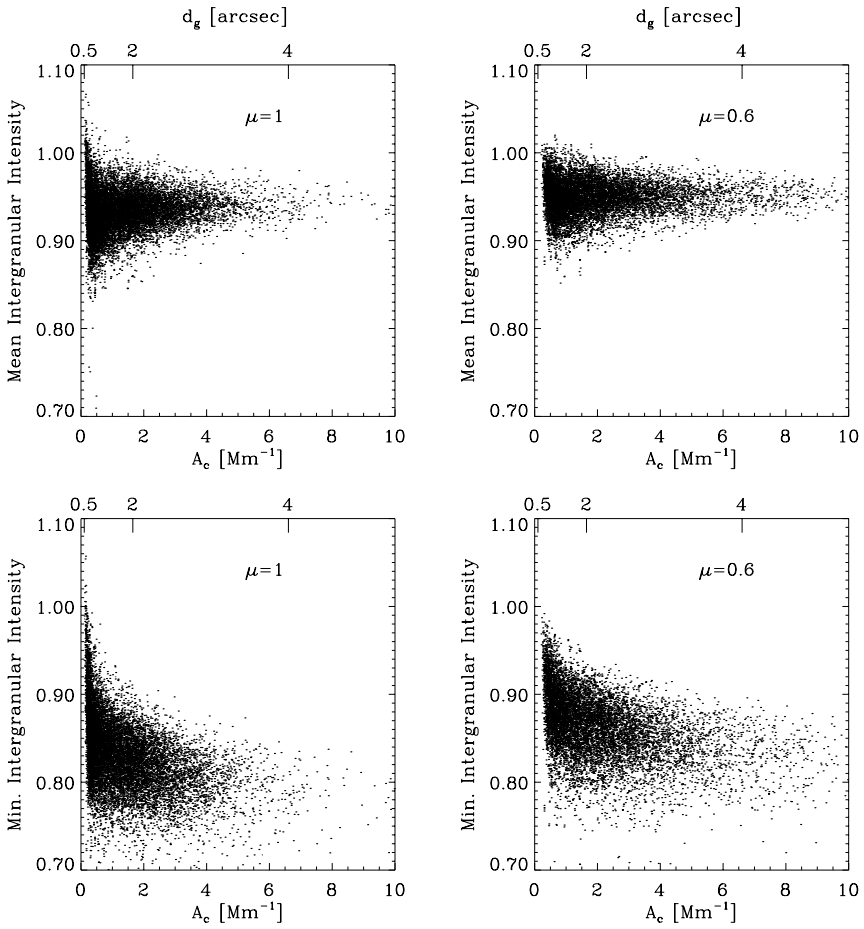

FIGURE 2.16— Mean intergranular intensities and minimum intergranular intensities versus granular cell area for $\mu = 1$ and $\mu = 0.6$.

considered as upper limits. This effect partly explains the overestimation of $D_{\rm f}$ for large granules at the disk center, although the uncertainties due to the finite pixel size and the linear fit cannot be disregarded. In any case, a fractal dimension near two means a complex inner structure, thus indicating that many of the larger granules could already be in a state of fragmentation.

For $\mu = 0.6$ the changing of slope is not so pronounced as at the disk center. The fractal dimensions obtained in this case are $D_{\rm f} = 1.43$ for small granules and $D_{\rm f} = 1.96$ for large ones.

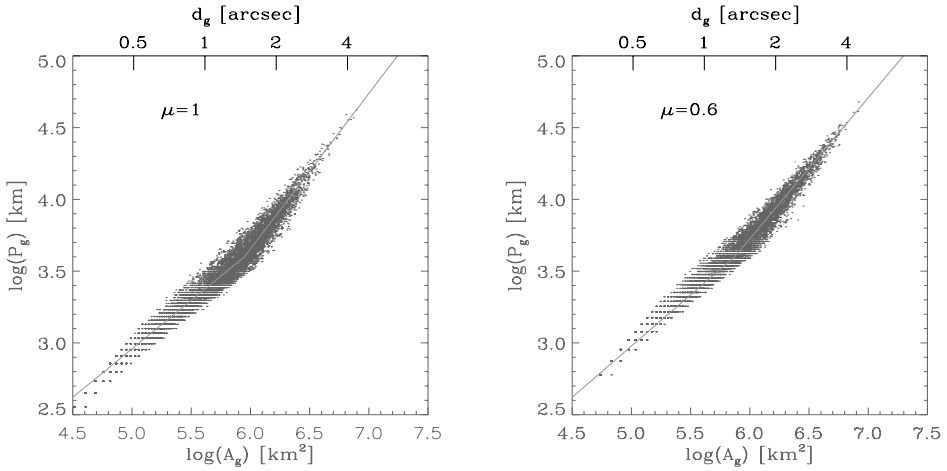

FIGURE 2.17— Area–perimeter relation of granulation for $\mu = 1$ and $\mu = 0.6$.

2.3.4 Penetration of granules

The study of the penetration of the convective phenomenon into the highest photospheric layers requires spectroscopic observations well calibrated in height and/or observations very close to the limb. Bray et al. (1984) summarize the results of this kind of limb observations up till then, at distances to the solar border ranging from $33''$ to $2''$. More recently Rodríguez Hidalgo et al. (1992b) have recognized structures visible out to the very limb.

The analysis of 2D power spectra as performed in previous sections is not feasible at small distances from the limb because the square boxes representing a common μ-position should be extremely small. Instead, we attempt to get information on the spatial scales observed at very small μ from the analysis of 1D photometric profiles parallel to the solar limb.

In all the images of the eclipse that include the solar limb, the latter is not parallel to the x- or y-axis of the CCD camera. To facilitate analysis, the images were rotated by using interpolation algorithms. However, a spurious contribution to the signal, caused by the interpolation, was detected at medium and high spatial frequencies and consequently this procedure was discarded.

Instead, we have analyzed a set of 21 non-restored images taken at λ5425 Å during the campaign of 1995, showing a portion of the solar limb parallel to the y-axis of the camera. In Figure 2.18 a typical image is presented. The solar limb is defined as the inflexion point position in different rows of the frame in the portion analyzed. As a consequence of the image distortion induced by the atmospheric turbulence, these determinations produce a wavy border to which

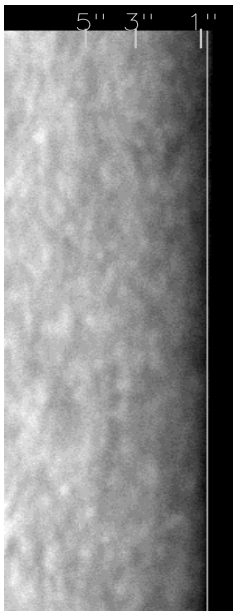

FIGURE 2.18— Unrestored white-light image of the solar limb at λ5425 Å . The white line indicates the position of the solar limb.

a straight line is fitted to be considered as the origin of the distances d to the solar limb. The distances have been measured by means of the pixel size of the CCD camera, which means that they have been oversampled since the pixel size is smaller than the diffraction limit of the telescope. Starting from $d = 0\farcs062$ and at intervals of $\Delta d = 0\farcs062$, scans $15\farcs5$ long, parallel to the limb, have been studied by calculating their 1D power spectra and averaging the results at the same d from the 21 frames. In addition, the resulting mean power spectra have been smoothed by averaging within a running box of 5 points width, in order to reduce the remaining statistical instabilities. The level of noise has been estimated as the mean power beyond the cut-off wavenumber of the telescope at λ5425 Å (36.8 Mm^{-1}).

In Figure 2.20 we present the 1D power spectra, averaged and smoothed as mentioned above, for different limb distances as well as for the disk center. In all spectra the level of the signal decreases with increasing wavenumbers until it merges into the noise level at a wavenumber that will be denoted by k_m. Note that the total power decreases from the center to the limb, as expected from previous results. In parallel, k_m also decreases. This means that less fine structure is seen when approaching the limb. In general terms, the shape

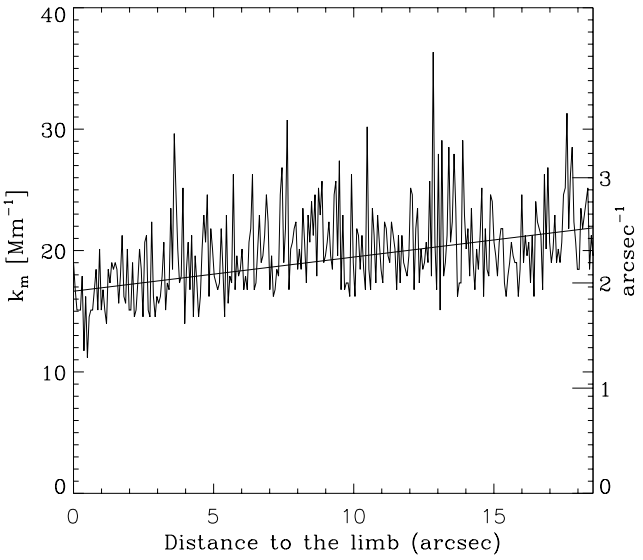

FIGURE 2.19— Variation as a function of the distance to the solar limb of the wavenumber at which the power of the signal merges into the noise level in 1D photometric profiles parallel to the solar border.

of the 1D power spectra is the same near the limb and at the disk center, which suggests that what is seen at the solar limb could be granulation. In any case, the power spectra must be interpreted carefully since different physical phenomena can provide mixed information.

Figure 2.19 shows the variation of k_m as we move toward the solar center as well as the linear fit obtained by recurrently removing the values lying beyond 2σ. From this fit it can be concluded that, very close to the limb, structures as small as ≈ 16.5 Mm^{-1} ($0\farcs53$) can be recognized.

The interpretation of these results regarding the identification of the spatial scales detected has to be carried out with some caution. The Fourier transform of a scan along the y-axis in a 2D intensity distribution, $i(x, y)$, is the "flattening" of the 2D Fourier transform, $I(k_x, k_y)$, against the $k_y I$-plane, that is

$$\mathcal{F}\big[i(0, y)\big] = \int I(k_x, k_y)\, dk_x\,. \tag{2.10}$$

The integral in the second term may produce cancellations because we are

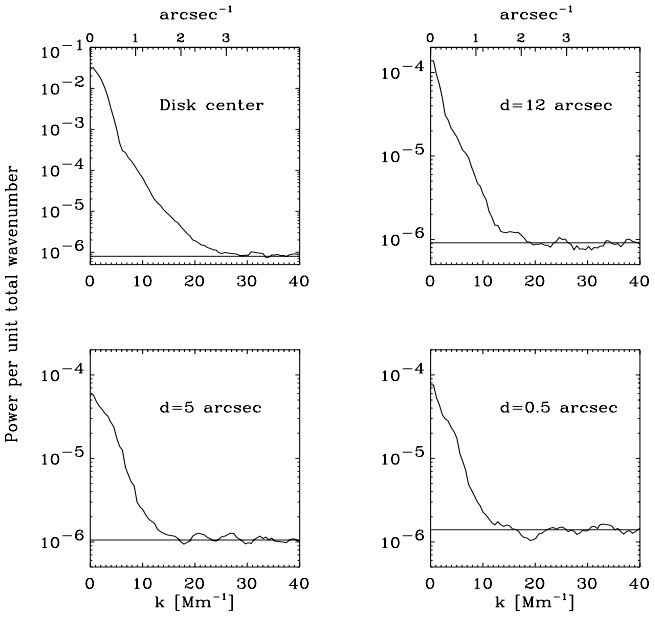

FIGURE 2.20— Smoothed and averaged power spectra of scans parallel to the solar limb at disk center (obtained from λ6708 Å images) and at different limb distances: $d = 12\farcs0, 5\farcs0, 0\farcs5$ (obtained from λ5425 Å images). To enable direct comparison the total contrast of all the power spectra has been converted to λ5000 Å .

summing complex numbers. Then, the power spectrum that we are considering

$$P(k_y) = \left| \int I(k_x, k_y)\, dk_x \right|^2 , \tag{2.11}$$

may not reflect a possible Fourier component beyond a certain wavenumber, k_m. Thus, if we interpret this wavenumber as the minimum spatial scale observed, this is only an upper limit. Similarly, at each wavenumber smaller than k_m the power contains a merging of information stemming from the spectral components with higher k lying on parallel directions to the k_x-axis, which it is impossible to disentangle.

Close to the limb we detect a significant amount of power at low wavenumbers (less than ≈ 3 Mm^{-1}), that rapidly decreases until the position $d \approx 0\farcs5$ where it becomes stable. We interpret these facts as mainly being due to differential seeing and to the undulation of the solar limb caused by local image distortion. In a region of the Sun where the gradient of intensities is so steep both effects can play a substantial role.

At wavenumbers smaller than ≈ 3 Mm^{-1} there is probably a contribution of spatial scales other than solar granulation, such as the mesogranulation pat-

tern. The contribution of the solar oscillations can be neglected near the limb since their intensity contrast diminishes significantly at those disk positions (Schmidt, Stix, & Wöhl 1999). The network bright points (hereafter, NBP) have a contrast which increases from the center to $\mu = 0.3$, and then decreases close to the limb (Auffret & Muller 1991). Since we are performing a spectral analysis, no intensity threshold criterion is useful for disentangling NBP's from the granulation. Thus, the information of granulation and NBP is mixed in the power spectra. Anyway, we expect their contribution not to be too significant because the number of NBP decreases selectively from the center to the limb; only the brightest ones remain up to the limb (Auffret & Muller 1991), and a visual inspection of our limb scans reveals a small amount of these brightest NBP.

In short, we conclude that up to the very limb ($d \sim 0\farcs5$) there may exist spatial scales as small as $0\farcs53$, or perhaps even smaller. By assuming a simple Eddington–Barbier approach for the formation height of the continuum ($\tau = \cos\theta$), and using the conversion of τ to geometrical heights published by Nelson (1978), the structures observed at $d = 0\farcs5$ (i.e., $cos\theta = 0.032$) imply temperature fluctuations until $z \approx 200$ km. This value can be checked with the spectroscopic results mentioned in the introduction.

2.4 Conclusions

The aim of the work presented in this chapter is to study the CLV of the geometric and photometric properties of the solar granulation because of its interest in understanding the physics at different layers of the photosphere. It is based on an excellent set of images taken at the SVST during the solar eclipse of 1994 May 10. The lunar limb profile has been used for estimating the atmospheric and instrumental image degradation. Our working wavelength (λ6708Å), in combination with the good transparency of the terrestrial atmosphere during the observations, favored the low level of stray light detected in our images. Besides, the combination of the results obtained in this chapter with those obtained in the forthcomming ones will allow us to obtain valuable information about the solar granulation.

The determination of the heliocentric position, μ, of different granular subfields studied is based on matching the lunar limb, present in our images, to a numerical model of the eclipse geometry carefully calculated as described in Section 2.2.1. The resulting values of μ are validated by: a) the consistency of the ellipticities measured in the power spectra after the restoration of the images, with the expected values from foreshortening, b) the direct calculation of μ from the distance to the solar limb in those frames where the latter is

included, and c) the identification of topographic details on the Moon's limb.

Measurements of the CLV of the granular contrast in the continuum radiation have been frequently used for checking models in deeper photospheric layers. In this respect one of the strongly disputed aspects is whether or not the CLV curve of $\Delta I_{\rm rms}$ attains its maximum outside the solar disk center (Keil 1977; Durrant et al. 1983). This feature has repercussions on predicting how steep the gradient of $\Delta T(\tau)$ is in the photosphere. Our results, showing a monotonic decrease in contrast toward the limb, point to a steep gradient of ΔT in deeper photospheric layers (Kneer 1984).

From the comparison of the curves of several authors (see Figure 2.9) we cannot conclude any particular trend with λ in the CLV law of the granulation contrast. Our curve shows one of the greatest overall slopes. The contrast that we obtain at the solar disk center (9.6%) is quite high in comparison to other values reported in the literature (see Table (2.2)), considering that our working wavelength, λ6708 Å, is located in the far red spectral range. The same value is reported by Karpinsky & Pravdjuk (1972), based on balloon observations (SSSO), although at a shorter wavelength (λ6000 Å).

We cannot ensure in our measurements that some contribution to the contrast may not be caused by p-modes whose coherence length is not well determined yet and their intensity amplitude is expected to decrease from the center to the limb (e.g., Stix & Wöhl 1974; Schmidt et al. 1999). The removal of these modes would require time series of images at different μ-positions. However, since we are using small sub-fields corrected for linear local gradients we expect this contribution, if any, to be minimized.

The shape of the power spectra of solar granulation has also been examined for different positions on the solar disk. Radiative transfer effects seem not to affect the isotropy of the horizontal intensity pattern of the solar granulation at different μ, at least up to $\mu = 0.4$. This result confirms one of the basic assumptions of the method by Rodríguez Hidalgo et al. (1992a) for estimating the degradation of power spectra of solar granulation. According to Wilken et al. (1997) we also find, very close to the limb, an effective transfer of power from lower to higher wavenumbers in the dimension parallel to the solar limb. These authors interpret this fact as a manifestation of the presence of small granular structures which penetrate into higher photospheric layers than the large ones. Nevertheless, at small μ we cannot discard a possible contribution to the power at large wavenumbers from the quiet network bright points, which are particularly conspicuous at these positions on the disk.

We have also calculated the equivalent 1D power spectra at different μ by azimuthally integrating the 2D spectra along ellipses of ellipticity $1 - \mu$. From these spectra we derive a mean wavenumber, $\overline{k}$, related somehow with the typ-

ical mean granular cell size. Our value near the disk center ($\sim$ 6.15 Mm^{-1}) coincides quite well with that by Deubner & Mattig (1975) at a nearby wavelength, and also with the peak value found by Rodríguez Hidalgo et al. (1992b) along the equator at $\mu = 0.64$. The CLV of $\overline{k}$ shows, similarly to the contrast, a monotonic decrease toward the limb, thus indicating a progressive augmentation of the mean spatial scale with increasing height in the solar photosphere. This sounds somewhat contradictory to the claim that small structures penetrate higher into the upper photosphere. However, both results could be compatible since in the calculation of $\overline{k}$, high wavenumbers have a small weight, i.e., the power is much smaller at these scales.

The size distribution of granular and intergranular areas has also been studied at different positions on the solar disk. A general increase in both granular and intergranular areas is found for positions near to the solar limb, in agreement with the CLV found for $\overline{k}$. For any disk position, no typical granular size is found. In contrast, intergranular areas seem to have a typical size characterized by the maximum of the intergranular area histogram. The mean area of granular cells varies from 1.36 Mm^2 at $\mu = 1$ to 2.06 Mm^2 at $\mu = 0.6$. Together with this increase in granular and intergranular areas, a decrease in the GFF is found from the disk center (44.2%) to $\mu = 0.6$ (42.8%). This just reflects the fact of a larger rise of the intergranular lanes area for positions closer to the solar limb. Appart from possible radiative transfer effects, this could be interpreted as a decrease in the efficiency of the convection with the height.

The dependence of the brightness with the granular cell area, A_c, has also been investigated. The mean and maximum granular intensities of small granules show a linear increase with cell area, and a constant average intensity for granules with equivalent cell diameters larger than $d_g \sim 2\farcs0$. These trends are observed for every disk position studied, although with increasing scattering when approaching to the limb. Intergranular mean and minimum intensities do not show these two differenced slopes in their variation with A_c. The intergranular mean intensity remains constant in average for every cell size while the intergranular minimum intensity decreases almost linearly with cell size, although a larger dispersion is observed for smaller granules. For larger heliocentric angles, a general increase of the intergranular intensities is found.

Another attempt to determine the penetration of granules in high photospheric layers has been performed by analyzing power spectra of 1D photometric profiles parallel and very close to the solar limb. We conclude from this study that spatial scales of $0\farcs53$ or even smaller are detectable up to the very limb (i.e., out to a limb distance of $0\farcs5$). Using a simple Eddington Barbier–approximation, this means that we observe intensity fluctuations up to atmospheric heights of $z \approx 200$ km.

3

CLV of solar granulation in the infrared

As a complement to the previous chapter, in this chapter we present observations of the solar granulation performed in the minimum and maximum of the opacity, this is, in $\lambda 0.8\mu$m and $\lambda 1.55\mu$m. The study at 1.55 μm is especially interesting since it allows us to observe the photosphere at the deepest observable layers, where the 5-minute oscillations contribution to the measured granulation contrast (see Koutchmy & Lebecq 1986) is considerably reduced. In parallel, the effects of atmospheric seeing (see Koutchmy 1994; Keil et al. 1994), and line blocking are reduced, thereby allowing a higher precision in the measurements. Rao et al (2001) studied how the granular contrast is affected by several instrumental and atmospheric parameters.

The difference in formation height of 1.55μ and 0.8μ observations is approximately 30 or 40 km (see section 3.2). However, the temperature fluctuations decrease very rapidly between these two layers, so that the IR observations seem to be useful in setting upper boundary conditions to the models of small-scale solar convection.

On the other hand, IR observations have the disadvantage that granulation shows a smaller contrast and telescopes have less spatial resolution at these wavelengths, constraints that we will keep in mind throughout this chapter.

2-D power spectra of granulation images at the opacity minimum show more power at high spatial frequencies, accompanied by a reduction at the lower ones (Koutchmy, 1990). CLV curves of the r.m.s contrast have been published by Turon & Lena (1973) and Koutchmy (1994), but limited to the spatial range $1.0 > \mu > 0.7$. At IR wavelengths larger than 1.6 μm the radiation is coming from

progresively higher layers. Observations at 12.4 μm show more rapid temporal changes than in the visible and the lack of the cell-like character.

Taking advantage of the good resolution of the images acquired, a photometric study of the CLV of granular sizes is also performed in this chapter. These kinds of studies are useful for understanding the physical scales on which the granulation takes place.

The height penetration of overshooting granules has been extensively studied by means of spectroscopic data, and different authors have obtained different values for the height where the granulation vanishes, with the associated velocities penetrating higher in the photosphere than the corresponding temperature fluctuations. Here, we will perform a photometrical study of granulation at the extreme limb, which can produce new information on this controversial topic.

These studies, when combined with the results presented in the previous chapter, will be very useful for determining properties of the vertical structure of the solar granulation.

3.1 Observations

During the observing campaign 1997 June 17–29 at the SVST images were obtained for different quiet regions at various heliocentric angles. They were taken simultaneously in two channels:

1) $\lambda = 0.8000 \pm 0.0025\,\mu$m (continuum opacity maximum) with a 10-bit 1536×1032 pixel CCD Kodak Megaplus 1.6. The image scale and exposure time were $0\farcs083$ pixel^{-1} and 25 ms, respectively. The camera was working in real-time frame selection mode with selection intervals of 20 s and the instants of exposures of selected frames were recorded.
2) $\lambda = 1.5542 \pm 0.0046\,\mu$m (continuum opacity minimum) using a 16-bit 256×256 pixel Rockwell Nicmos III detector (Collados et al. 1997), with an image scale of $0\farcs362$ pixel^{-1} and an exposure time of 50 ms. The frames were taken at a constant rate of 3 s.

The influence of chromatic aberration of the telescope's lens inside the two observing bands was previously calculated and discarded as a possible source of errors

Bursts of 10 images were obtained at spatial intervals of 10 degrees from the disk center up to the very limb. This process was repeated on 7 different days so that 70 images in each heliocentric angle are available.

The SVST has an accurate system which specifies the heliographic coordinates of each observed disk position, thus allowing the determination of the heliocentric position μ for each set of observations. In addition, for positions near the solar limb (i.e. $\mu < 0.4$) the μ has been derived directly by measuring

the distance from the limb which allows a more precise determination in the range where the position uncertainties are more critical.

Standard flat-field and dark-current correction were applied to all the images. The noise filtering and the correction for the theoretical point spread function (PSF) of the telescope were performed simultaneously by means of a Wiener filter. To eliminate the gradients due to the CLV of the quiet Sun mean intensity, the images were divided by a first-order polynomial fit.

3.2 Response functions

The images analysed are obtained at different heliocentric angles and observing wavelengths. As mentioned above, this implies radiation coming from different layers of the Sun. In order to interpret our observations correctly it is interesting to characterize from which layers of the solar atmosphere the radiation that we observe comes. This has been performed by means of the response functions to the temperature (RFT)(see Beckers & Milkey, 1975; Caccin et al. 1977). The RFTs are computed by changing the temperature value in a given layer of the photosphere and estimating how the emergent intensity changes. This allows us to characterize the relative contribution of each layer to the total emergent intensity for each wavelength and heliocentric angle. We have computed the RFT by applying the three-dimensional radiative transfer code developed by Fabiani Bendicho & Trujillo Bueno (1999) to the mean quiet photosphere HSRA (Gingerich et al. 1971). Figure 3.1 shows the normalized RFTs obtained for $\lambda 0.8$ μm (upper panels) and $\lambda 1.55$ μm (lower panels) at different heliocentric angles: μ = 1, 0.85, 0.7, 0.6, 0.5, 0.4, 0.3, 0.2, and 0.1. In both panels of Figure 3.1 the RFTs with their main contributions in higher layers represent positions nearer the solar limb.

We define the effective formation heights of the continua, $z_{\rm c}$, as the positions of the centroids of the response functions. Table 3.1 shows the $z_{\rm c}$ values obtained, where $z = 0$ corresponds to $\tau_{0.5} = 1$. The last column lists the difference in formation heights: $\Delta z_{\rm c} = z_{\rm c}(0.80) - z_{\rm c}(1.55)$. As shown in the table, for larger heliocentric angles (smaller μ values) the differences in formation heights get larger, which means that the information we obtain comes from more separated layers.

3.3 Results

3.3.1 Center-to-limb variation of quiet granulation contrast

The contrast, ΔI_{rms}, of quiet granulation varies from the center to the limb. As mentioned in previous sections, two tendencies can be found in the results

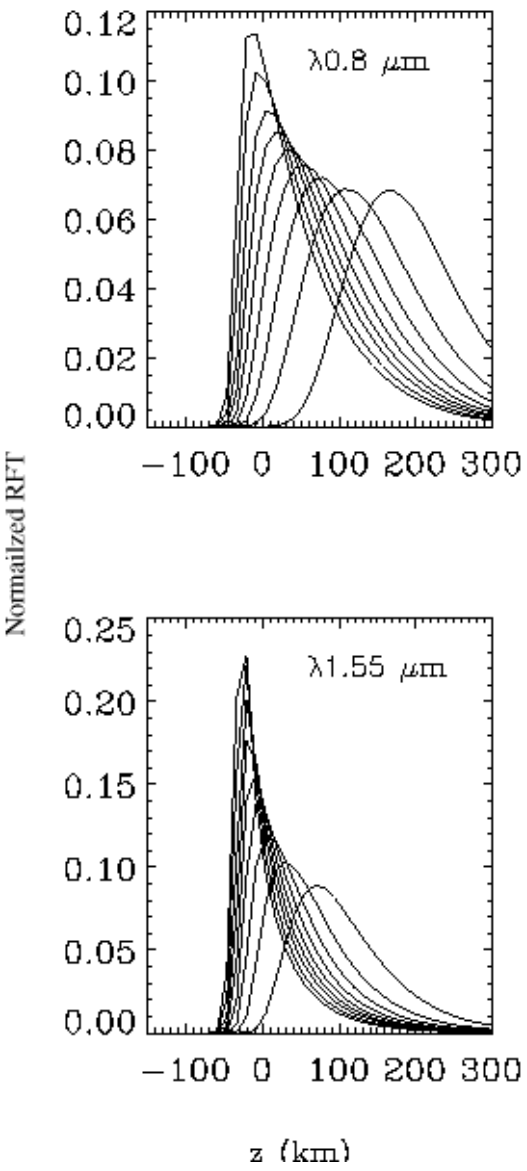

FIGURE 3.1— Normalized response functions to the temperature (RFT) in the model of a mean quiet photosphere HSRA (Gingerich et al. 1971) at $\lambda 0.8$ μm (upper panel) and $\lambda 1.55$ μm (lower panel) at the following disc positions: μ = 1, 0.85, 0.7, 0.6, 0.5, 0.4, 0.3, 0.2, and 0.1.

TABLE 3.1— Effective continuum formation heights z_c (km)

μ	$z_c(0.80\,\mu m)$	$z_c(1.55\,\mu m)$	Δz_c
1	44	4	41
0.85	54	10	44
0.7	66	17	49
0.6	76	23	53
0.5	87	30	57
0.4	102	40	62
0.3	122	53	69
0.2	151	74	77
0.1	201	112	89

of different authors about how this change occures. As reported in the previous chapter, some works find that the contrast increases from the disk center up to a certain μ and then decreases (e.g. Rodríguez Hidalgo et al. 1992 for equatorial CLV) while other studies give a monotonic decrease of the granulation contrast from the center to the limb (e.g. Wilken et al. 1997, Sánchez Cuberes et al. 2000).

In the present work, the CLV of the ΔI_{rms} of the quiet granulation has been computed for the 1.55 μm images and for the 0.8 μm images. The best quality images at each heliocentric angle have been chosen for this purpose, and the resulting CLV curves normalized to the disk center value are shown in Figure (3.2). The solid line corresponds to 0.8 μm images and the dashed line to the 1.55 μm images. For the sake of comparison, the CLV of the quiet granulation contrast at 0.6708 μm obtained in the previous chapter is also included in the figure (dotted-dashed line). The obtained values of the contrast at disk center were 6.1% for 0.8 μm and 2.9% for 1.55 μm. The last value is favourably compared to previous determinations by Turon & Lena (1973): 1.5% and Koutchmy (1994): 2.07% .

It should be kept in mind that, in the present study, the images could not be corrected for the degradation caused by the terrestrial atmosphere, which results in the underestimation of the contrast values. Let us make a simple estimate of this degradation under typical seeing conditions characterized by a mean value of the Fried parameter $r_o = 11$ cm (λ 0.43 μ m), as measured at the Dutch Open Telescope situated near the SVST (Sobotka & Sütterlin, 2001). Since $r_o \propto \lambda^{6/5}$, the $r_o \approx 23$ cm at λ 0.8 μm and $r_o \approx 51$ cm at λ 1.55 μ m. These values characterize high image quality expected in long-exposure frames

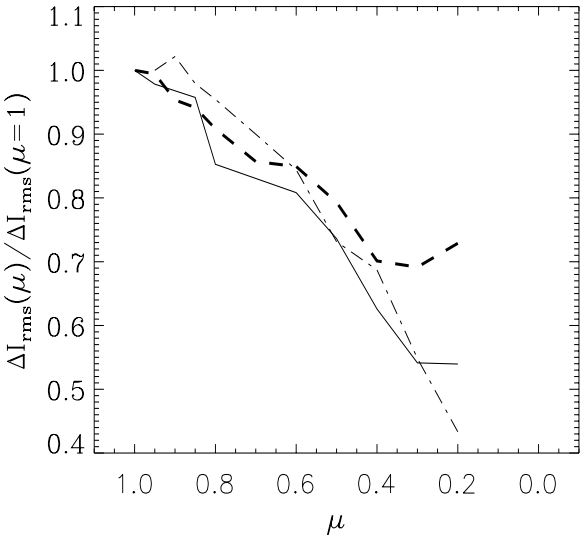

FIGURE 3.2— CLV of the granulation contrast at three different wavelengths normalized to the disk center. 0.8μm solid lines, 1.55μm dashed, 0.6708μm dot-dashed.

taken with an aperture of 48 cm. Because our exposures are short (25 or 50 ms) and only the best frames are selected, the image degradation due to the atmosphere is minor as compared to that caused by the instrument. As a matter of referenece for our image quality let us mention the typical value of r_o=30 at λ1.56 μm reported by Denker et al. (1999) for the Big Bear Observatory.

In Figure (3.2) it can be observed that, on average, the decrease of the CLV curve of the granulation contrast for λ1.55 μm is not as steep as for λ0.8 μm and λ0.6708 μm. It is interesting to know to what extent this behavior is actually a physical phenomenon or is caused by the distinct cutoff frequencies of the telescope for the different observing wavelengths. In order to check it we have performed a simple numerical experiment. A high resolution image of granulation at λ0.4507 μm at disk center obtained in excellent seeing conditions with the SVST during another observing campaign has been chosen. The image has been deconvolved with the instrumental profile of the telescope and denoised with an optimum filter, resulting a restored *reference image* with a granulation contrast of 10.4 % and a cutoff frequency at $\nu_{0.45}$ =5.2 arcsec^{-1}. This image has then been rebinned in one of its axis to different sizes, thus simulating the observed foreshortening (obviously, the radiative effects are not included in this simulation). The foreshortened images have been filtered in the Fourier

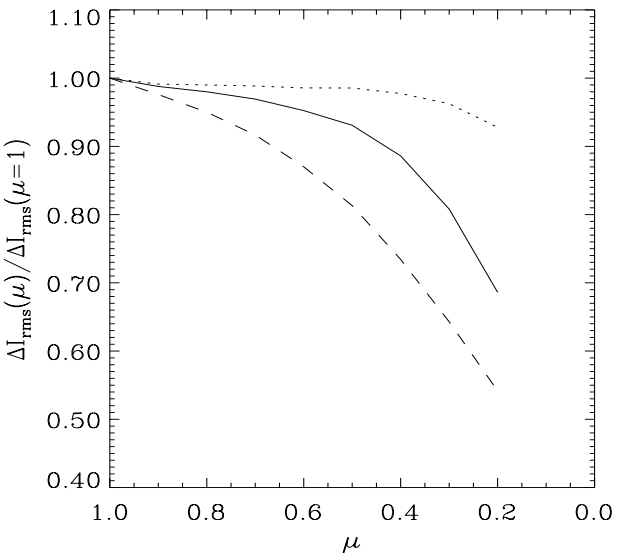

FIGURE 3.3— Computed CLV of granulation contrasts on images at $\lambda 0.4507$ μm artificially foreshortened (dotted line), filtered with a cutoff at $\nu_{0.8}$ (solid line) and with a cutoff at $\nu_{1.55}$ (dashed line) (see the text for a detailed explanation).

domain by means of low passband filters decaying smoothly to zero at the cutoff of the telescope at $\lambda 0.8$ μm ($\nu_{0.8}$ =2.9 arcsec^{-1}) and $\lambda 1.55$ μm ($\nu_{1.55}$ =1.5 arcsec^{-1}), respectively. The smooth transition to zero in the filters prevents spurious oscillations in the images caused by the Gibbs phenomenon, and all the frequencies beyond the respective cutoffs have irrecoverably been lost.

Figure (3.3) shows the resulting CLV of the contrast in the images with the cutoff at $\nu_{0.8}$ (solid line) and at $\nu_{1.55}$ (dashed line), all normalized to the value at the disk center. Dotted line represents the normalized CLV of the contrast in the foreshortened *reference image*. This line reveals that the foreshortening by itself hardly affects the contrast of the *reference image* with a cutoff frequency at $\nu_{0.45}$, far beyond $\nu_{0.8}$ and $\nu_{1.55}$. On the contrary, the images filtered with a cutoff at $\nu_{1.55}$ and $\nu_{0.8}$ do suffer a steep loss of contrast from the center to the limb. Nevertheless, this decrease is more pronounced for images filtered with a cutoff at $\nu_{1.55}$ than for those filtered with a cutoff at $\nu_{0.8}$. The foreshortening produces a power transfer from small to larger spatial frequencies as we approach the solar limb, which together with the different cutoffs of the telescope at different wavelengths causes the cutoff at $\nu_{0.8}$ to preserve more power than that at $\nu_{1.55}$.

In Figure (3.2) it can be seen that the observed CLV curve decreases steeper

for λ0.8 μm than for λ1.55 μm. Thus, we can conclude that the CLV curve of the granulation contrast diminishes at a higher rate for shorter wavelengths, and that this higher rate decrease is underestimated due to the effect of the telescope. The origin of this different contrast tendencies can be understood by looking at the response functions of a HSRA atmosphere, which are presented in Table (3.1). It shows that the difference in formation heights, Δz_c, increases towards the limb. This is due to a larger augment of z_c(0.80 μm) than of z_c(1.55 μm) as approaching to the limb. Since the $\delta\Delta T/\delta\tau$ diminishes with height in the photosphere, and contrast is mainly dependent on $\delta\Delta T/\delta\tau$, the contrast will decrease more for λ0.8 μm than for λ1.55 μm. The difference in formation heights between granules and intergranular lanes is, on average, of 30 km, smaller than the difference of formation height for these two wavelengths near the limb. The fact that the contrast diminishes monotonically from the center to the limb for all the observed wavelengths imply that the gradient of temperature decreases steeply with height in the photosphere. If $\delta T\Delta/\delta\tau$ would diminish less steeply, the observed CLV curve of granulation contrast would peak somewhere between the disk center and the limb (Kneer, 1984).

For μ <0.4 in λ1.55 μm images and for μ <0.3 in λ0.8 μm ones, the granulation contrast shows a tendency to increase. This increase could be caused, at least partially, by the Network Bright Points whose intensity increases towards the limb and peaks around μ=0.2-0.3 (Auffret & Muller, 1991). Other observational effects like the reduced spatial resolution and signal to noise ratio should also be considered.

3.3.2 Granular and intergranular areas

The available photometric data allows to perform a morphologic study of the observed images at the working wavelengths. The statistical determination of granular and intergranular sizes and the dependence of their intensities on the size is of great importance for the characterization of granulation and comparison with the outputs of the theoretical models.

In order to get statistically representative data, all the images obtained at each heliocentric angle have been included in the present study. To identify the granules, a granule-finding algorithm like the one described in section 2.3.3 was used. Similarly, in this chapter the images have been filtered with a high-passband filter in order to remove the large scale structures other than granulation such as p-modes, mesogranulation, etc.

Like in chapter 2, radiative effects make the granule determination uncertain as approaching to the limb. Thus, only the data ranging from $\mu = 1$ to $\mu = 0.6$ will be used in order to study the size distribution of granules and intergranules.

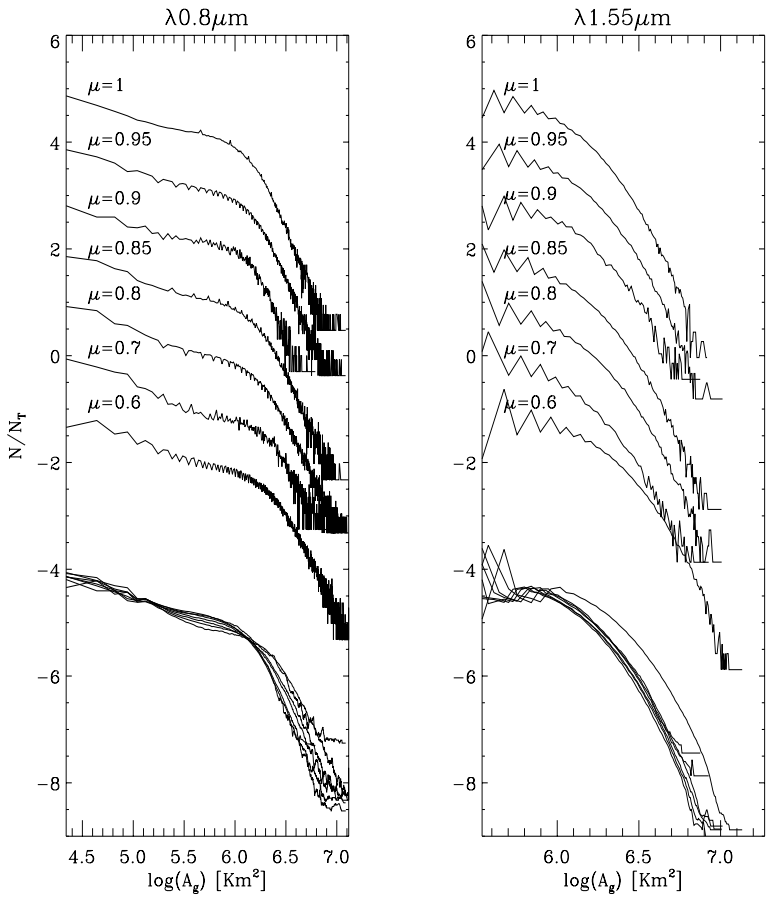

FIGURE 3.4— Histograms of granular areas in $\lambda 0.8\mu$m and $\lambda 1.55\mu$m at different μ positions

Once granules and intergranules are identified, histograms of their areas can be computed. Figure (3.4) shows, for different heliocentric angles, the obtained normalized number of granules for each granular area (left panel for 0.8μm images and right panel for 1.55μm ones). In the upper part of each panel, an offset is introduced between the different curves to enable individual inspection. In the lower part of the panels, a smoothing of the curves with a 5 point boxcar is shown overlapped to facilitate comparison. Note that the scaling in the vertical direction is in arbitrary units. As seen in the figure, smaller granules are detectable in $\lambda 0.8$ μm as compared with $\lambda 1.55$ μm. This is logical, since the resolution of the images decreases considerably for $\lambda 1.55$ μm images. The histograms for each wavelength change also from the disk center to $\mu = 0.6$,

increasing the amount of larger granules for larger heliocentric angles, this is, for higher layers in the photosphere. The mean granular area is found to vary from 1.25 arcsec^2 at disk center to 2 arcsec^2 at $\mu = 0.6$ in λ0.8 μm images and from 1.24 arcsec^2 to 1.85 arcsec^2 in the λ1.55 μm ones. In chapter 2 it was found that the mean area of granular cells ranged from 1.36 Mm^2 at $\mu = 1$ to 2.06 Mm^2 at $\mu = 0.6$ at λ6708 Å. The differences in the absolute values of the mean granular cell sizes found for the distinct wavelengths could reflect, on the one hand, the differences in the spatial resolution of the observations at the various spectral ranges studied, and on the other hand, radiative effects which could change the apparent size of granular cells at different wavelengths. Apart from radiative effects, the fact that mean granular cell sizes increase at all the studied wavelengths with heliocentric angle could be due to the expansion of granules with height in the photosphere. In chapter 2, section 2.3.1, it was found that smaller granules had a larger efficiency in penetrating high into the photosphere. This result seems somewhat contradictory with the increase of the mean granular cell size with heliocentric angle found here. However, both results are compatible. Really, an expansion of all the granules with height in the photosphere would cause the mean granular cell size to increase with heliocentric angle, independnetly of small granules penetrating higher into the photosphere than large ones or not. Besides, in the present chapter data in the infrared is analyzed, and therefore, the layers in the photosphere studied are deeper than those studied in chapter 1, where a higher efficiency of small granules was only found at large heliocentric angles, i.e., high layers.

Figure (3.5) shows the area histograms obtained for intergranular lanes at λ0.8 μm (left panels) and λ1.55 μm (right panels). Similarly, an offset has been introduced between the individual curves in the upper part of each panel, and the smoothed curves are shown overlaped in the lower part. Again, smaller intergranular lanes are detectable in λ0.8 μm than in λ1.55 μm due to the decrease of the diffraction limit with increasing wavelength. Note in figure (3.5) that no characteristic intergranular lane size is found for the observed wavelengths (i.e. no peak appears in the histogram). In the previous chapter intergranular lane area histograms showed a peak around $\log(A_i)\sim$5.3-5.5 km^2. In the present work this is the minimum intergranular lane area detected, and thus the peak is not evident. As for granules, a relative increase of the amount of large intergranular lanes is found for larger heliocentric angles. This suggests that both, granules and intergranular lanes expand with height in the photosphere.

The granular filling factor (GFF) is defined as the percentage of area covered by granules, i.e. the relative amount of granular area in a given region. Figure (3.6) presents the CLV of the GFF at 0.8 μm (upper panel) and 1.55μm (lower panel). The absolute values of the GFF in λ0.8 μm and λ1.55 μm cannot

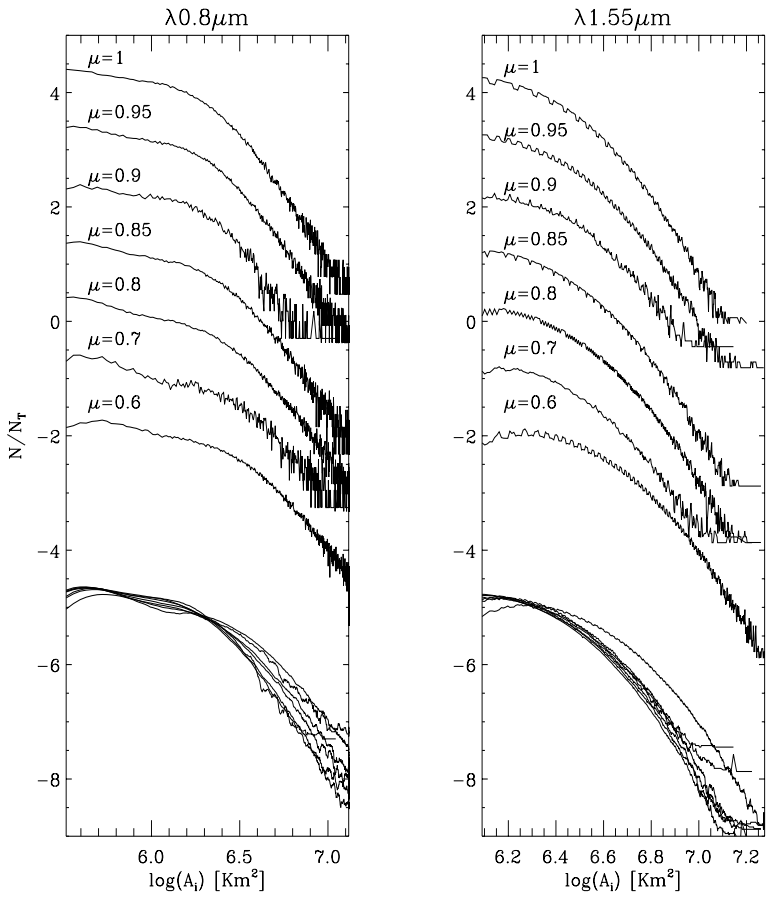

FIGURE 3.5— Histograms of intergranular lane areas in $\lambda 0.8\mu$m and $\lambda 1.55\mu$m at different μ positions

be compared due to the different resolution. Nevertheless, the CLV of the GFF at each wavelength can give valuable information about the variation of the relative amount of granules and intergranular lanes with height in the photosphere. When observing from the center to the limb in $\lambda 0.8$ μm, the relative amount of granular area seems to decrease up to a certain μ and then it increases again. This change occurs at $\mu = 0.5$. In $\lambda 1.55$ μm images the CLV of the GFF is noisier and a minimum of the GFF can not be observed at any disk position. Even though radiative effects difficult the granule identification in positions near to the solar limb, these positions are also included in figure (3.6). The reason is that a relative decrease of the intergranular lanes near the

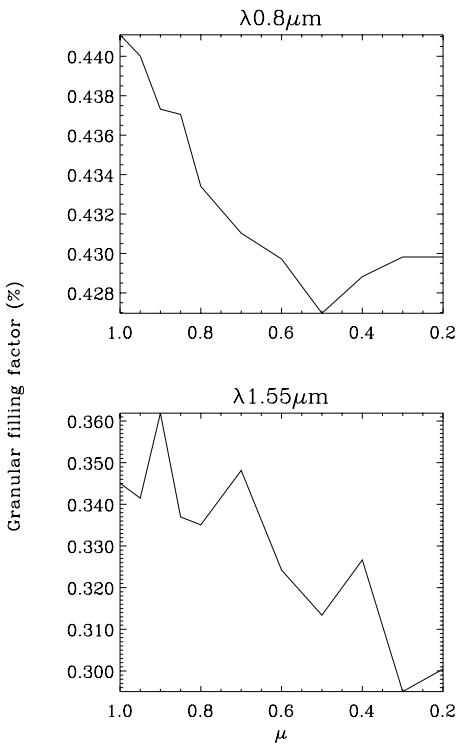

FIGURE 3.6— Variations of granular filling factor with the disk position.

limb is also appreciated by visual inspection of the images. Note that in chapter 2, section 2.3.3, figure 2.13 we found a minimum of the GFF at μ=0.4 in λ6708 Å , in agreement with the trends found in the present chapter. A numerical test will be performed in chapter 5 to try to clarify the origin of this trend in the GFF.

3.3.3 Penetration of granules

Like in section 2.3.4, a study of the penetration of temperature fluctuations associated with granulation across the photosphere has been performed.

In order to perform this study, the best burst of images containing the solar limb parallel to the y-axis of the image was selected. In the 1.55μm images it was impossible to perform a reliable analysis of the data at the very limb due to the low signal to noise ratio. Therefore, in this section only the data at 0.8μm will be analyzed.

The procedure used to detect structures near the solar limb was done as described in section 2.3.4.

The limb, parallel to the y-axis in each frame, was defined as the inflection point in each row of the image. Due to the distortions induced by the terrestrial atmosphere turbulence, the inflection points produced a wavy border to which a straight line was fitted. This line was considered as the origin for measuring distances to the limb. As mentioned above, bursts of 10 images were acquired for each observing position. The 10 images selected were matched to make the limb coincide in all of them and averaged in order to improve the signal to noise ratio. Then, starting from d=0".083 and at intervals of Δd=0".083, scans 34".8 long parallel to the limb were obtained. Similarly as in the previous chapter, the distances have been measured by means of the pixel size of the CCD camera, and therefore they are oversampled since the pixelsize is smaller than the diffraction limit of the telescope. The one-dimensional power spectrum of each individual scan was computed and smoothed by a 5 point width running box. The level of noise of each power spectra was estimated as the mean power beyond the cutoff frequency of the telescope at $\lambda 0.8\mu$m. Then, the frequency k_m at which the signal of the smoothed power spectra merges with the noise level was found for each scan. Figure (3.7) presents the obtained values of k_m as a function of limb distance. The solid straight line is a linear fit to the obtained k_m computed by recurrently removing the values lying beyond 2σ. As seen in the figure, smaller structures (i.e. higher frequencies) are detectable, on average, as moving from the limb towards the disk center.

Since the distances to the limb are measured with an oversampling, we will consider here that the minimum distance at which structures are detectable is the diffraction limit of the telescope at λ8000 Å, this is, d=0".32. We can conclude that frequencies of 1.05 arcsec^{-1} are detectable up to the very limb (d=0".32). This corresponds to spatial scales of 0".96, which sets an upper limit to the smallest structures detectable at the very limb. Smaller structures could exist at this position but not necessarily be revealed in the power spectrum as a consequence of the one dimensional treatment of the data. As discussed in section 2.3.4. it is not probable that the observed structures are due to the solar oscillations neither to the Network Bright Points.

If we take an Eddington-Barbier approximation for the formation height of the continuum (τ=cosθ) and a conversion from τ to geometrical heights as published by Nelson (1978), the structures observed at d=0".32 imply temperature fluctuations up to z$\approx$220 km. In chapter 2, by means of applying the same technique to the observed data at λ5425Å, we obtained that structures as small as 0".53 were detectable up to the very limb, which implied temperature fluctuations until z$\approx$200 km. The heights of penetration of temperature fluctu-

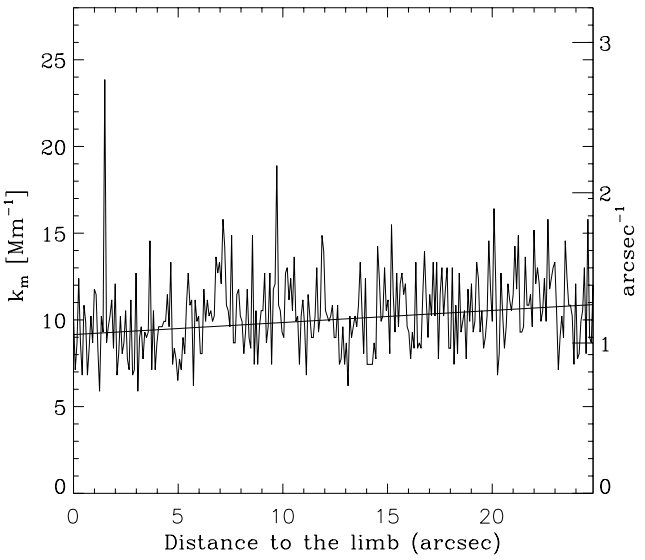

FIGURE 3.7— Variation with the distance to the solar limb of the wavenumber k_m where the unidimensional power spectra join the noise level in $\lambda 0.8\mu$m images.

ations obtained at these two studied wavelength ranges are in good agreement, and the difference in the minimum size of the detectable structures just reflects the difference in resolutions of the two observational data used for the present analysis. These values can be compared with those obtained by other authors using mainly spectroscopic methods (see Table 3.2). Note that the penetration height determined here is among the highest in the literature. However, it must be kept in mind that the method used in the present section is not able to assure that the detected structuires are really granulation.

3.4 Conclusions

A study of the CLV of the granulation contrast in quiet regions has been performed at $\lambda 0.8\mu$m and $\lambda 1.55\mu$m. We found a monotonic decrease of the contrast at both wavelengths from the center to $\mu \approx 0.3$. The decrease is steeper at $\lambda 0.8\mu$m than at $\lambda 1.55\mu$m. The fact that the granulation contrast does not peak somewhere between the disk center and the limb, implies a strong decrease of the temperature fluctuations with the height in the solar atmosphere (Kneer, 1984).

The CLV of granular areas has also been investigated. We find an increase

TABLE 3.2— Height, z, above τ=1, where the temperature fluctuations vanishes or change the sign

Authors	λ [Å]	z (km)	Remark
Altrock & Musman (1976)	5016	40 - 130	Model dependent
Komm et al. (1990)	5172.7	170	
Bendlin & Volkmer (1993)	6302.5	265	
Espagnet et al (1995)	5690	60 - 90	P-modes filtering
Krieg et al. (1999)	5890	100	Speckle reconstruction
Present work	5425	200	
Present work	8000	220	

of the granular area with heliocentric angle. Mean granular sizes are found to vary from 1.25 arcsec^2 at disk center to 2 arcsec^2 at $\mu = 0.6$ in $\lambda 0.8\mu$m images and from 1.24 arcsec^2 to 1.85 arcsec^2 in $\lambda 1.55\mu$m. This increase could be caused by a higher efficiency of the larger granules in penetrating to higher layers in the photosphere. Several authors have found this higher efficiency of the larger granules (e.g. Komm et al. 1990, Nesis et al. 1993), however controversy still exist around this topic. An expansion of the granules with height in the photosphere would also explain the observed effect. Intergranular lanes are also found to increase their area with the heliocentric angle. The granular filling factors (GFF) have also been computed. We find, in the $\lambda 0.8\mu$m images, a decrease of the GFF with heliocentric angle up to μ=0.5 and then an increase of the GFF up to the limb. In the $\lambda 1.55\mu$m images, the CLV curve of the GFF is noisier and a clear minimum is not detected.

Analysis of one dimensional scans at the extreme limb have revealed that structures as small as 0.″96 are detectable up to the very limb. Using a simple Eddington Barbier approximation, this implies that the temperature fluctuations associated with granulation penetrate, at least, until z$\approx$ 220 km above $\tau = 1$ in the solar photosphere.

4

CLV of photospheric faculae and pores

As explained above, in this thesis we use the CLV of photometric properties to study the vertical structure of photospheric features. In the previous chapters a study has been performed on the quiet granulation, here we present the observational work performed to infere information about photosheric small magnetic features.

The study of the CLV of photometric parameters is one of the classical methods for deriving the thermal structure of solar active regions. The photometric characterization of faculae at different disk positions is of crucial importance for setting boundary conditions to different theoretical models of the magnetic structures observed on the surface of the Sun. Moreover, the determination of the CLVs of facular relative intensity has great implications not only for the understanding of the physical nature of these magnetic structures but also for the prediction of the total solar irradiance variations with the solar cycle. The knowledge of the facular CLV is probably the weakest point in simulations of solar irradiance (see recent reviews by Foukal 1998; Vázquez 1999; Solanki & Fligge 2000). Its dependence on facular size makes it complicated to enter it on a daily basis in the calculations.

Since the pioneering works of Richardson (1933), Rogerson (1961) and Schmahl (1967), the CLV of faculae has been studied extensively. The verification that faculae correspond to small-scale magnetic fields and the development of the theory of magnetic flux tubes contributed an adequate physical background to these works (see, for example, Solanki 1999). Nevertheless, individual results show a considerable scatter (e.g., Figure 3 of Unruh et al. 1999).

Some authors find an increase of the facular relative intensity from the center out to the very limb (e.g., Lawrence, Chapman, & Herzog 1988) while others find a peak in the relative intensity around $\mu = 0.3$ (Libbrecht& Kuhn 1984; Auffret & Muller 1991).

Two competing models try to reproduce the CLV of solar faculae by combining geometrical and thermal effects. The "hot wall" model (cf. Spruit 1976; Knölker, Schüssler, & Weisshaar 1985) explains the brightening of faculae from the center to the limb of the solar disk as a consequence of the entrance into the observer's field of view of the "hot wall" behind the evacuated flux tube. From a certain heliocentric angle onwards, only a fraction of the "hot wall" is visible and thus the contrast decreases. This is because, at the extreme limb, one side of the wall blocks the other side. On the other hand, the "hot cloud" model (Rogerson 1961; Chapman & Ingersoll 1972) assumes that faculae are optically thin patches above the top of the photosphere. A continuous increase in contrast is expected in this case.

In a previous work (Sobotka et al. 2000) we have analyzed time series of images at λ 0.8 μ and 1.55 μ of two active regions close to the disk center, corresponding to the minimum and maximum continuum opacities, respectively. The main conclusions of this work, relevant to the topic of this chapter, and the discussion of these results with the literature can be summarized as follows.

Brightness temperatures ($T_{\rm b}$, see section 4.4.3 for the definition) for both wavelength bands were calculated and compared, pixel by pixel, in scatter plots. Pixels belonging to quiet regions are clearly distinguished from those of faculae, where $T_{\rm b}(1.55\,\mu{\rm m})$ is reduced systematically with respect to quiet regions, while pixels belonging to pores extend the cloud of facular pixels smoothly towards low temperatures.

The smooth transition between faculae and pores seen in the temperature scatter plots of Sobotka et al. (2000) manifests a common magnetic origin of these features. Moran et al. (1992) and Wang et al. (1998) presented plots in which the intensity at 1.6 μm decreased smoothly with increasing magnetic field strength from dark faculae to pores and sunspots.

There are two basic mechanisms that determine the thermal structure of magnetic features: the inhibition of convective energy transport and lateral radiative heating, which depends on the size and internal density of the magnetic element. The second mechanism is more efficient in the upper photospheric layers, where the density is lower and the photon mean free path is greater than in the deep layers. In Figure 4.1 we show a simplified comparison of the internal and external temperatures at the depths corresponding to the 0.80- and 1.55-μm continua, for a small, medium, and a large magnetic feature. We should bear in mind that the increase in the sizes of magnetic features is also

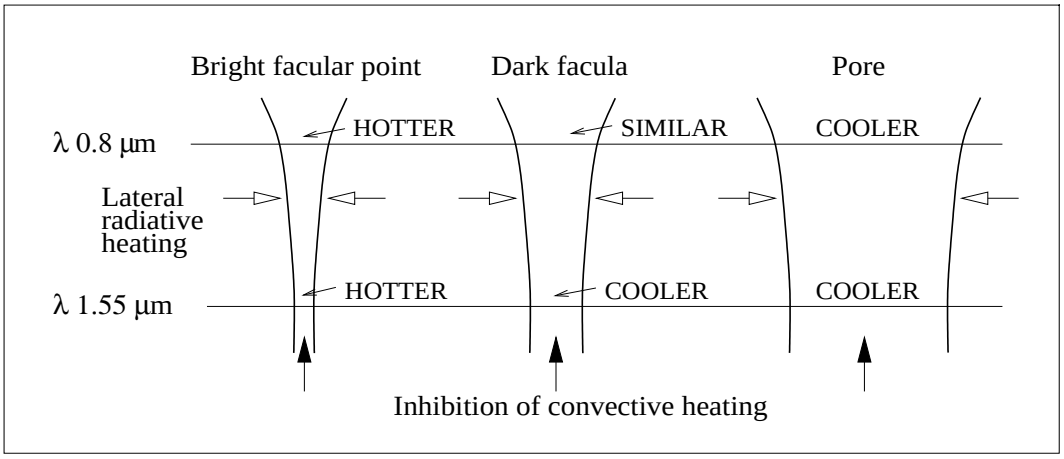

FIGURE 4.1— Schematic view of temperature conditions in magnetic features of different sizes.

accompanied by an increase in their filling factor, which lowers the temperature in the non-magnetic regions between the features and reduces the efficiency of the lateral radiative heating. In the smallest magnetic elements, lateral radiative heating dominates and the elements appear to be brighter than their surroundings. These features, corresponding to bright facular points, cannot be detected in our infrared observations because they are below the resolution limit and their filling factor is very small. With increasing magnetic flux the filling factor and size of magnetic elements increase (Solanki & Brigljević 1992). The convective heating is reduced in the low layers but the lateral radiation balances the temperature deficit in the high layers. So dark faculae, composed of magnetic elements of intermediate sizes, have in their upper layers a temperature similar to that of the undisturbed photosphere and are nearly invisible at 0.80 μm. With further increase in the magnetic flux the lateral radiative heating cannot compensate for the temperature deficit in the upper layers. Magnetic concentrations become cooler than their surroundings at all heights throughout the photosphere and are observed as dark pores or sunspots in both the visible and the infrared.

In Sobotka et al. (2000) we also found that most of the pores were surrounded by ring-like regions of low brightness temperature difference ($\Delta T_\mathrm{b} = T_\mathrm{b}(1.55\ \mu\mathrm{m}) - T_\mathrm{b}(0.8\ \mu\mathrm{m})$) which were identified as the magnetic "sheath" observed beyond the intensity border (Keppens & Martínez Pillet 1996; Martínez Pillet 1997).

In the present chapter we extend these studies to other heliocentric angles to

get more information about the thermal stratification of the different magnetic structures present in the solar photosphere. The observations were performed in the same wavelength ranges as in Sobotka et al. (2000) and as in chapter 3.

4.1 Observations

During the observing campaign 1997 June 17–29 at the SVST single images and time series of broad band images were obtained for different active regions at various heliocentric angles. They were taken simultaneously in two channels, as is described in the previous chapter.

The CLV of the active region NOAA 8056 including a group of pores was observed. This region appeared near the disk center on June 25 and disappeared near the western limb on June 29. In Figure (4.2) the evolution of this active region at the different studied disk positions is shown in both spectral ranges (first column panels for $\lambda 0.8$ μm images and second column panels for $\lambda 1.55$ μm ones). Nevertheless, the studied regions are larger than the fields shown in the figure ($50.6\times$ 55.4 arcsec^2), and images mosaicing all the faculae around were also obtained. We should remark that this region had an important evolution during its passage from the center to the limb. Therefore both, positional and evolutive effects, are mixed together in our data analysis. In order to characterize the evolution of the active region the "Facular Filling Factor" (hereafter FFF) has been computed for every studied disk position. The FFF is defined as the percentage of a given area occupied by facular structures. Figure (4.3) shows the obtained CLV of the FFF of active region NOAA 8056. Facular regions have been identified following the criteria described in section 4.4.1. As seen in the figure, in μ=0.7 and μ=0.35, the filling factor decreases indicating a decrease of the magnetic activity. This FFF will be useful for interpreting the observations.

For completion and comparison purposes, the active regions NOAA 8052 (appearing near the east limb on June 12 and disappearing on June 19) and NOAA 8053 (appearing on June 18 and disappearing on June 21) are also analyzed, although only data corresponding to one heliocentric angle are available for each of these regions. A detailed description of the observed active regions, corresponding μ-position at image center and availability of time series is presented in Table (4.1).

The heliographic coordinates were determined as explained in the previous chapter.

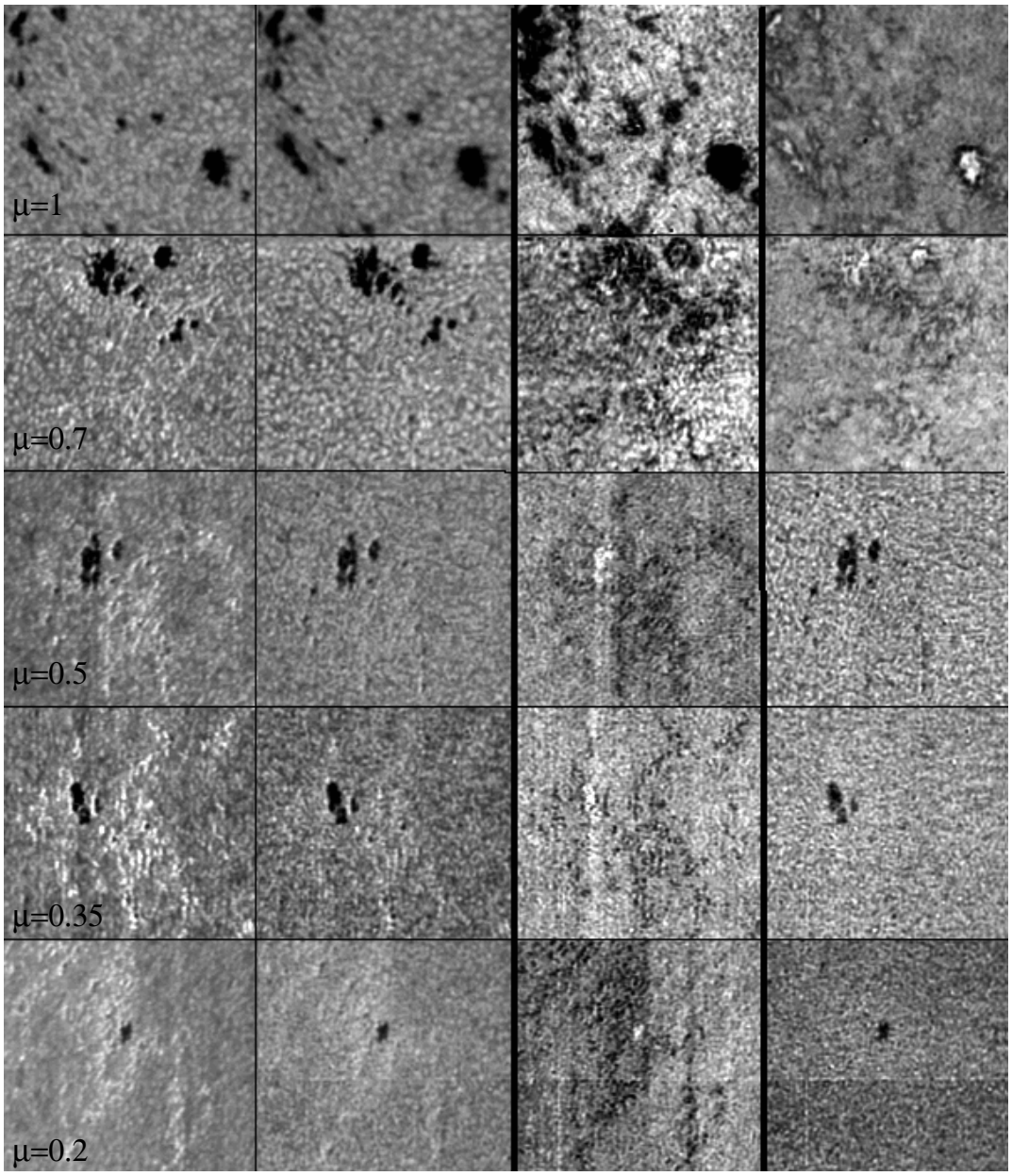

FIGURE 4.2— A composite picture showing the evolution of the active region NOAA 8056 from the center to the limb for $\lambda 0.8 \mu$m and $\lambda 1.55 \mu$m images (first and second column of panels, respectively). The difference images ((see equation 4.1) of the region at the same μ positions (third column of panels), and the maps of temperature differences $T_b(1.55\ \mu\text{m}) - T_b(0.8\ \mu\text{m})$ (forth column of panels). For each panel the field of view is $\approx 50 \times 55$ arcsec^2.

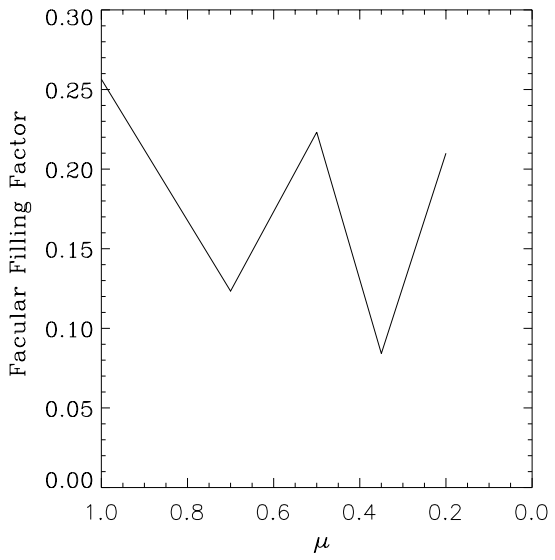

FIGURE 4.3— CLV of the Facular Filling Factor of active region NOAA 8056.

4.2 Response functions

In order to estimate from which layers of the solar atmosphere the radiation that we observe comes from we use the response functions to the temperature (RFT), as in section 3.2, chapter 3. In this case, the 3D radiative transfer code of Fabiani Bendicho & Trujillo Bueno (1999) has been applied to three different models of a: mean quiet photosphere HSRA (Gingerich et al. 1971), facula (Solanki & Steenbock 1988), and small sunspot (Collados et al. 1994). Figure (4.4) shows the height dependence of the temperature values in these three atmospheres. Figure (4.5) shows the obtained normalized RFT for $\lambda 0.8$ μm (upper panels) and $\lambda 1.55$ μm (lower panels). They have been computed for different heliocentric angles: μ=1, 0.85, 0.7, 0.6, 0.5, 0.4, 0.3, 0.2, 0.1. In each panel of Figure (4.5) the RFT with main contributions in higher layers stand for positions closer to the solar limb.

The effective formation heights of the continua, z_c, defined as the positions of the centroids of the response functions are used again. Table (4.2) displays the obtained z_c values, where $z = 0$ corresponds to $\tau_{0.5} = 1$. The last column presents the difference in formation heights: $\Delta z_c = z_c(0.80) - z_c(1.55)$. As shown in the table, for larger heliocentric angles (smaller μ's) the differences in formation heights get larger, which means that the information we observe

TABLE 4.1— Census of the observations in active regions

Region	μ	Time series	Observing period
NOAA 8056	1	Yes	June 25 8:31-10:07 UT
	0.7	Yes	June 27 7:54-9:58 UT
	0.5	No	June 28 8:10 UT
	0.35	No	June 28 15:45 UT
	0.2	No	June 29 8:09 UT
NOAA 8053	0.8	Yes	June 20 8:27-9:10 UT
NOAA 8052	0.6	Yes	June 18 8:20-11:10 UT

comes from more separated layers. Additionally, it can be seen in the table that, for any disk position, Δz_c is larger for spots than for faculae. This is due to the fact that sunspots have smaller mean temperatures atmospheres than faculae and opacity decreases with decreasing temperatures.

4.3 Data reduction

The data reduction was similar to that in Sobotka et al. (2000). In the following we will summarize the main steps, explaining in more detail the differences.

After standard flatfield and dark current correction, all the images were derotated to compensate for the effect of the altazimuthal mounting of the SVST. Following Sobotka, Bonet, & Vázquez (1993) the noise filtering and the correction for the theoretical PSF of the telescope were simultaneously performed by means of a Wiener filter.

In the cases in which time series were available, the images were aligned to remove global image motions, and destretched to minimize the seeing distortions. Solar acoustic waves and residual seeing-induced jitter were removed by means of a sub-sonic filter (cut-off phase velocity 4 km s^{-1}). As shown in Table (4.1), time series of active regions were available at disk positions between $\mu = 1$ and $\mu = 0.6$. Therefore, filtering of the solar acoustic waves was not possible at positions close to the limb. Nevertheless, the power of the solar p-modes of intensity decreases from a normalized value of 1 at the disk center to about 0.3 at $\mu = 0.5$ (Schmidt, Stix & Wöhl, 1999). Thus, it can be assumed that the p-modes are much less significant at the positions where they have not been filtered. A detailed discussion including a test to check the precision of this assumption is shown in the forthcoming sections together with the results.

After the reduction process, all λ0.8 μm images were re-scaled to the λ1.55 μm images pixel size, and their resolution was reduced to the corresponding

TABLE 4.2— Effective continuum formation heights z_c (km)

μ	Model	$z_c(0.80\,\mu m)$	$z_c(1.55\,\mu m)$	Δz_c
1	HSRA	44	4	41
	Facula	35	7	28
	Small spot	27	-37	63
0.85	HSRA	54	10	44
	Facula	43	14	29
	Small spot	35	-31	66
0.7	HSRA	66	17	49
	Facula	52	21	30
	Small spot	45	-24	69
0.6	HSRA	76	23	53
	Facula	59	28	31
	Small spot	52	-18	71
0.5	HSRA	87	30	57
	Facula	68	35	33
	Small spot	61	-12	73
0.4	HSRA	102	40	62
	Facula	78	43	35
	Small spot	72	-3	75
0.3	HSRA	122	53	69
	Facula	92	55	38
	Small spot	84	8	77
0.2	HSRA	151	74	77
	Facula	113	71	42
	Small spot	102	23	79
0.1	HSRA	201	112	89
	Facula	150	99	51
	Small spot	130	49	80

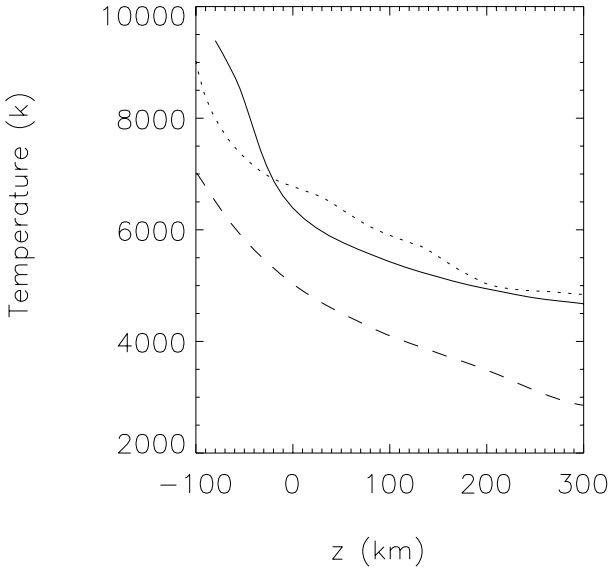

FIGURE 4.4— Height dependence of the temperatures in models of a quiet photosphere HSRA (Gingerich et al. 1971)-solid line, of a facula (Solanki & Steenbock 1988)-dotted line , and of a small sunspot (Collados et al. 1994)-dashed line.

λ1.55 μm resolution. This degradation was performed convolving the λ0.8 μm images, corrected for instrumental profile, with the PSF corresponding to the λ1.55 μm images (see Sobotka et al. 2000 for more details).

Finally, the λ1.55 μm images were correlated to the λ0.8 μm ones using a destreching algorithm, obtaining a very good superposition among them. This procedure ensures that the images are comparable, and allows to obtain, for every structure, simultaneous information coming from different layers of the solar atmosphere.

To eliminate the gradients due to the CLV of the quiet Sun mean intensity, the images were divided by a first order polynomial fit.

4.4 Results

4.4.1 Difference images

Foukal & Duvall (1985) pointed out that differential continuum photometry is a good tool to analyze the differences in internal temperature structure between faculae and photosphere. In particular, they showed that the difference in H^- opacity, and not the mere wavelength difference itself, is the main factor that

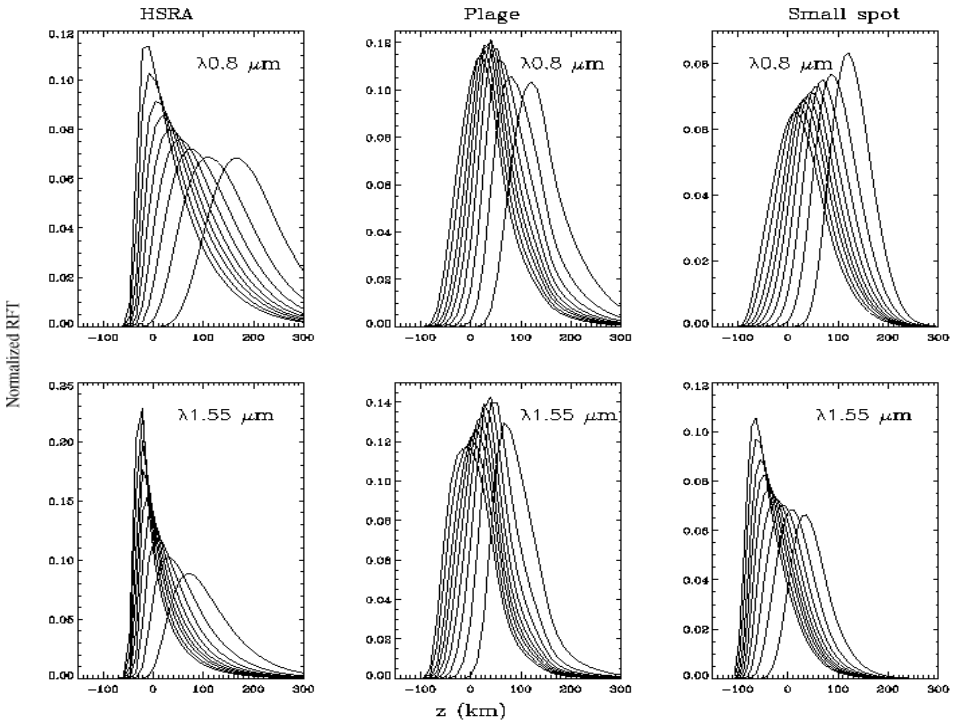

FIGURE 4.5— Normalized response functions to the temperature in the models of a mean quiet photosphere HSRA (Gingerich et al. 1971), of a facula (Solanki & Steenbock 1988), and of a small sunspot (Collados et al. 1994) at $\lambda 0.8$ μm and $\lambda 1.55$ μm in the following disk positions: μ=1, 0.85, 0.7, 0.6, 0.5, 0.4, 0.3, 0.2, 0.1.

makes difference images sensitive to faculae and network. In the present work, data corresponding to the minimum and maximum of opacity are analyzed and their difference images will be particularly sensitive to magnetic structures.

Since the contrast for $\lambda 1.55$ μm images is lower than for $\lambda 0.8$ μm ones, a simple subtraction of the pairs of $\lambda 0.8$ μm/$\lambda 1.55$ μm images would give no significant information. Instead, the difference images have been computed using the following formula:

$$I_{\rm dif} = F \cdot [I(1.55) - \overline{I_{\rm phot}(1.55)}] - [I(0.80) - \overline{I_{\rm phot}(0.8)}] \ , \qquad (4.1)$$

where $\overline{I_{\rm phot}}$ is the mean intensity of the quiet photosphere and F is a factor to put the $\lambda 1.55$ μm contrast on a level with the $\lambda 0.8$ μm one by means of the ratio of the quiet granulation contrast. Quiet regions (QR) have been identified

visually. Factor F is defined as:

$$F = \frac{\Delta I^{\rm QR}_{\rm rms}(0.80)}{\Delta I^{\rm QR}_{\rm rms}(1.55)} \ , \tag{4.2}$$

In Sobotka et al. (2000) the difference images showed, at the disk center, dark structures that were identified as the dark faculae observed in infrared by Foukal et al. (1989) and Foukal et al. (1990). In the present chapter this study is extended to other disk positions and the third column of panels of Figure (4.2) shows the CLV of the obtained difference images of region NOAA 8056. Note that, the changes due to the foreshortening effect and those due to the evolution of the active region are mixed in the figure. For the disk positions where faculae are apparent at $\lambda 0.8 \mu$m and/or $\lambda 1.55 \mu$m, it can be appreciated that the difference images show dark structures resembling in shape the faculae. At positions near disk center these structures are cospatial with the pores and are larger than near the limb, where they are more intermittent and difficult to disentangle from the noise level. Foukal & Duvall (1985), using a simple two component model showed that the dark structures associated with faculae in the difference images could have two distinct origins: a decrease of the temperature difference $\Delta T = T(1.55) - T(0.8)$ in facula relative to the photosphere or a decrease of both $T(1.55)$ and $T(0.8)$ in facula with respect to the photosphere (without requiring any decrease of ΔT). They concluded that, at disk center, faculae are visible in the difference images due to a lower temperature gradient near $\tau_{0.5}$=1 in the facular atmosphere than in the quiet photosphere. Really, as seen in Figure (4.4), the temperatures of the HSRA atmosphere and of the facula have a crossing point near the layers observed at disk center (τ_{5000}=1). Thus, the dark structures that appear in the difference image are caused by a different temperature gradient.

When observing near the solar limb, the information comes from higher layers in the atmosphere, where the temperatures of faculae and photosphere are different (faculae are hotter), although their temperature gradients are more similar than at deeper layers. The fact that faculae appear as dark structures in the difference images for large heliocentric angles is thus probably not only due to the difference in the temperature gradients. Rather, an additional reason can be understood by looking at the temperature response functions of the facular and quiet solar atmospheres. As seen in Figure (4.5), for large heliocentric angles, the information comes from more separated layers between $\lambda 0.8 \mu$m and $\lambda 1.55 \mu$m in the HSRA atmosphere than in the facula atmosphere. Therefore, since the temperature gradients of both atmospheres are similar at these

geometrical heights, the temperature difference will be larger for a quiet atmosphere than for faculae. This makes a decrease of the ΔT in faculae relative to the photosphere, and thus the faculae appear dark in the difference images. Nevertheless, the difference in ΔT is less significant at these heliocentric angles and thus the difference images are less sensitive to magnetic structures, causing the faculae to be less conspicuous in the difference images. In addition, note that the active region NOAA 8056 was decaying when observed near the solar limb. The decay of the region causes the filling factor to decrease, which in general makes the magnetic structures smaller. This, together with the limited resolution of the observations, could also explain the fact that faculae are less conspicuous near the limb.

In order to study in more detail the brightness difference images, the histograms of intensity distributions in QRs and in faculae have been computed. We define faculae as the regions where $I_{\rm dif}$ is smaller than the mean difference intensity in quiet regions minus g-times the standard deviation of the difference images, that is:

$$I_{\rm dif}^{fac} < \overline{I_{\rm dif}^{\rm QR}} - g \cdot \Delta I_{\rm dif}^{\rm rms} \tag{4.3}$$

Empirically g has been set to 1.5. Pores, defined in the λ0.8 μm images by the iso-intensity level of $\overline{I_{phot}(0.8)} - 3 \cdot \Delta I_{\rm QR}^{\rm rms}(0.8)$, have been excluded from these computations.

Figure (4.6) presents the CLV of the resulting histograms. Left panels show the λ0.8 μm intensity histograms of quiet regions (solid line) and faculae (dotted line), and right panels the corresponding λ1.55 μm histograms for the same structures. All the images in every studied heliocentric angle have been used in the computations. Note that various active regions have been included in this figure. Although different regions can have different morphologies and magnetic fluxes, the statistical nature of the performed study plus the fact that the obtained results fit in a general trend have encouraged us to include also regions NOAA 8052 and NOAA 8053 in Figure (4.6).

Inspection of the panels corresponding to disk center leads to the conclusion that the faculae show an intensity deficit in the λ1.55 μm images, which suggests that they can be identified as the dark infrared faculae observed by Foukal et al. (1990). These authors found that the faculae at λ1.63 μm show at μ=1 a brightness deficit of about 2 %. They found that, in the visible continuum, faculae showed no contrast, while Lawrence, Chapman & Herzog (1988) found that at λ0.86 μm faculae have, at disk center, a brightness excess between 0.1 and 1 %. Wang et al.(1998) found that faculae at λ1.6μm at disk center have

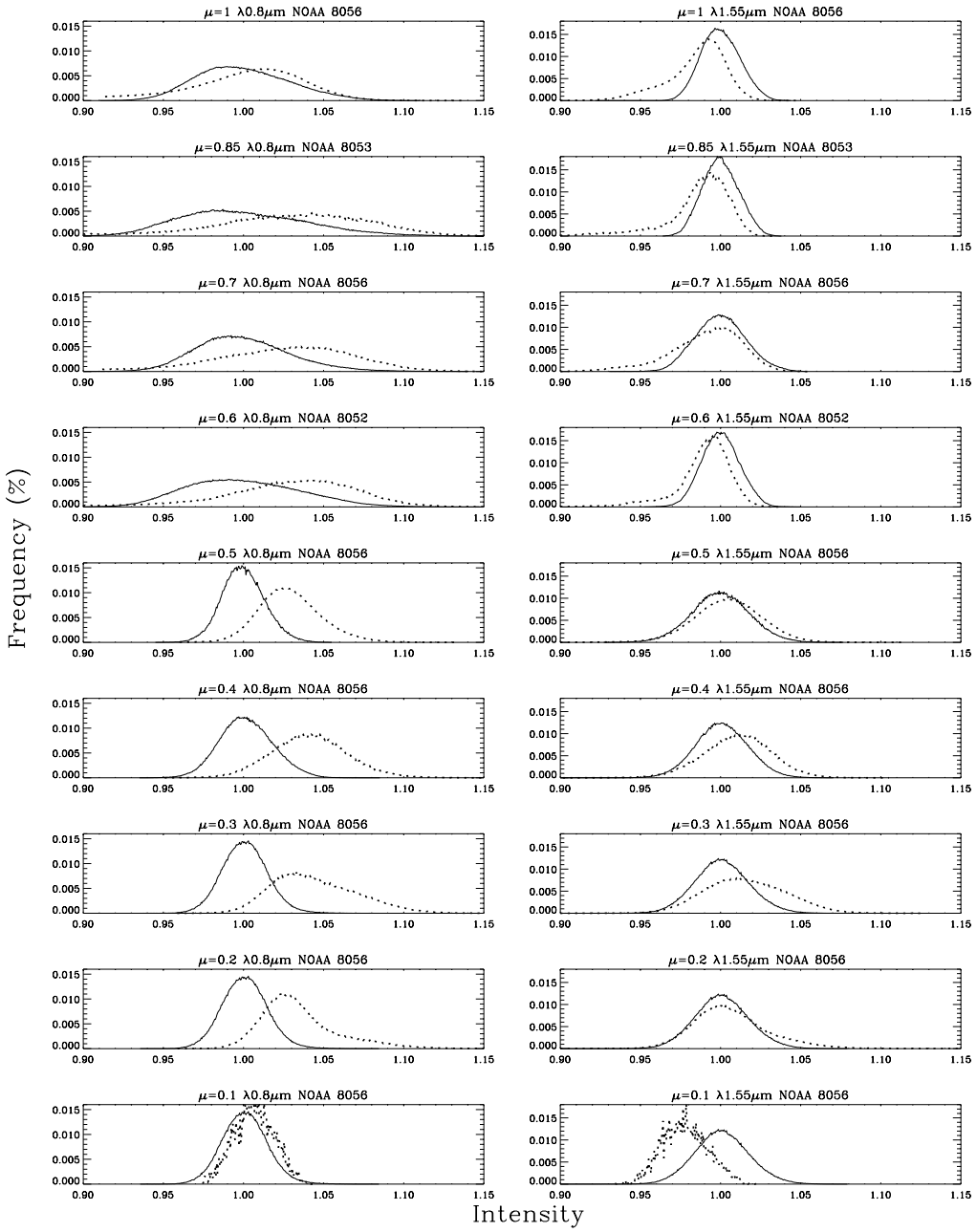

FIGURE 4.6— Intensity histograms of quiet regions (solid lines) and faculae (dotted lines) computed for $\lambda 0.8\mu$m and $\lambda 1.55\mu$m images (left and right panels respectively) for the observed heliocentric angles of regions NOAA 8056, NOAA 8053 and NOAA 8052. Pores are not included in the computations.

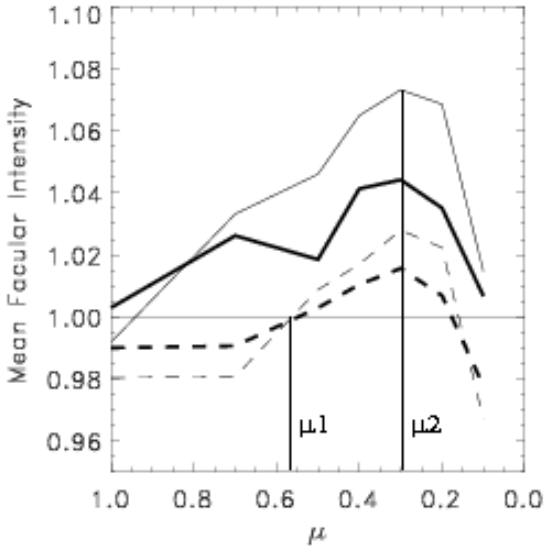

FIGURE 4.7— Center to limb variation of the mean facular intensity at $\lambda 0.8\mu$m (solid lines) and $\lambda 1.55\mu$m (dashed lines). Thick lines are obtained taking $g = 1.5$ in equation (3) and thin ones by setting $g = 3$.

generally an intensity deficit. As discussed below, in the present work we find that the facular brightness depends on the photometric definition of faculae. In the $\lambda 0.8\mu$m images, faculae can have a brightness excess or deficit depending on the g threshold parameter in Equation (4.3). In the $\lambda 1.55\mu$m images we find always a brightness deficit, whose amount depends on g. Nevertheless, the difference in the facular contrast between our two spectral ranges at disk center is the expected from the fact that we have sampled the same flux tubes at different heights in the atmosphere (see figure 4.1). At deeper layers (1.55 μm) the inhibition of convective flux is stronger than the effect of lateral heating and we see dark structures. At upper layers (0.8 μm), the contrary happens and we see bright contrasts. This could confirm the existence of dark faculae (see Xu & Wang, 2001 for a different view).

As seen in Figure (4.6), the faculae show at $\lambda 1.55$ μm a decreasing intensity deficit from μ=1 to $\mu = 0.5$ followed by an increasing intensity excess up to $\mu = 0.3$, while for $\lambda 0.8$ μm they develop an increasing intensity excess from the center to μ=0.3. From μ=0.3 to the limb the tendency for the intensity of faculae at both wavelengths is to decrease.

In order to perform a quantitative study of the different histograms the

mean intensity of faculae at each disk position has been plotted in Figure (4.7). Solid thick lines show the mean intensity at $\lambda 0.8$ μm and thick-dashed lines the mean intensity at $\lambda 1.55$ μm. The thinner lines represent the mean facular intensity if in equation (4.3) the g threshold is set to 3 instead of 1.5. The threshold affects the absolute values of the mean intensity of faculae at each μ though it does not affect the disk position at which the turnover from an increasing facular intensity to a decreasing one does occur (μ=0.3). Inspection of the morphology and of the intensity distribution in faculae show that the effect of changing g from 1.5 to 3 in the determination of the facular regions is to exclude the outermost parts of faculae when the g threshold is raised. Additionally, several small faculae are excluded when g=3.

The difference in the curves corresponding to $g = 3$ and $g = 1.5$ in figure (4.7) can be explained as a combination of two effects: on one hand, small faculae have an almost constant intensity for every disk position, which is higher than the intensity of large faculae at the disk center but smaller than their intensity near the limb (see section 4.4.2, Figure (4.9)). On the other hand, the innermost part of each facula seems to suffer a stronger center-to-limb change in its intensity than the outermost part. As expected, the absolute facular brightness excess or deficit depends on the photometric definition of faculae.

Nevertheless, we find that both, the disk position at which the facular brightness at $\lambda 1.55 \mu$m changes from a deficit to an excess (i.e. from dark to bright faculae), which we name μ_1, and the μ at which the facular mean intensity peaks, which we name μ_2, remain constant independently of the threshold value g. The μ_1 in $\lambda 1.55 \mu$m images is observed between μ=0.5 and μ=0.6. It is interesting to compare the values of μ_1 and μ_2 obtained in the present work with those obtained by other authors. Table (4.3) summarizes the observational results related with the determination of μ_1 and μ_2. Note that for the authors who find an increase of the facular intensity up to the very limb and no dark facula at disk center columns 3 and 4 appear empty. The results shown in Table (4.3) coincide in determining μ_1 around $\mu = 0.6$ and μ_2 around $\mu = 0.3$, in good agreement with the present study.

In order to test to what extent the results are affected by the fact that solar acoustic waves were not filtered out for disk positions with $\mu < 0.5$, the above computations were repeated without filtering the p-modes in any disk position. The obtained mean facular intensity also changes from a deficit to an excess at the same disk position and the mean facular intensity also peaks at $\mu = 0.3$. In addition, the values of the mean intensity change by less than 0.01 units normalized to the mean of the quiet regions. Thus, we can conclude that the results are not significantly affected by not filtering the solar acoustic waves in positions near the limb where the p-modes in intensity fluctuations have less

TABLE 4.3— Facular intensity values as measured by several authors

	Wavelength	μ_1	μ_2	Remarks
Chapman & Klabunde (1982)	5250 Å	-	-	Limb faculae
Lawrence & Chapman (1988)	6264 Å	-	0.4	Active facula
Aufret & Muller (1991)	5750 Å	-	0.3	Bright network points
Lin & Kuhn (1992)	5000	-	-	Quiet and active
	6500	-	-	region network
Wang et al (1998)	1.6 μm	0.5 - 0.7		
Ahern & Chapman (2000)	4706 Å	-	0.25	
	6723 Å	-	-	
Our work	8000 Å	-	0.3	Active facula
Our work	1.6 μm	0.6	0.3	

power.

4.4.2 Facular size-dependent properties

Our study, described in the previous section, is a statistical determination of the average properties of faculae over a large sample, which is useful for comparison with the predictions of the theoretical models. In the present section, taking advantage of the high spatial resolution of the photometrical data that we use in the differential photometry techniques, the dependence of these properties on the facular size is investigated.

The study of the CLV of the size distribution of facula and of the size dependence on facular intensity has great implications in the determination of the total solar irradiance variations with the solar cycle. In addition, the investigation of the CLV of these parameters gives information about the change of the facular size with height in the photosphere. Figure (4.8) shows the size histograms, in log-log scale, of faculae for the different studied disk positions of region NOAA 8056. The facular sizes have been computed by counting the pixels belonging to each unconnected region identified photometrically as a facula (see equation (4.3)). The correction for the foreshortening has been performed by dividing each facular area by μ. With the method used here, the facular areas are equal for λ 0.8 μm and λ 1.55 μm images. As seen in the figure, the smallest observable faculae have a dominant presence for all the studied disk positions. Note that the minimum facular size observable at each μ increases with the heliocentric angle due to the foreshortening correction. The dominance of the smallest observable faculae for every disk position indicates that probably the smallest facular sizes are still under the resolution limit of the present observations (we resolve structures as small as 0.5 arcsec^2). Harvey & Zwaan (1993) performed a statistical study of the size distribution of emerging bipolar

active regions. They found that the shape of the characteristic size distribution of active regions is a fundamental invariant property of solar magnetic activity and that this function decreases with increasing size, in qualitative agreement with the distributions found in the present work.

In Figure (4.8) it can be seen that, for increasing heliocentric angles, the amount of large faculae decreases. In principle, the mere fanning out of the flux tubes with height in the photosphere should produce the opposite effect, this is, an increase of the facular size for increasing heliocentric angles. Nevertheless, two different facts could influence this expected behavior. On the one hand, the observed region was decaying during its passage from the center to the limb, which causes the facular area to decrease also. On the other hand, as mentioned in section 4.4.1, the difference images are more sensitive to the magnetic structures at disk center than near the limb. Since facular areas are defined by means of a photometric threshold in the difference images, their areas are found to be smaller at large heliocentric angles.

In order to study the size dependence on the facular intensity, the different faculae have been grouped into size bins. Figure (4.9) shows the CLV of the mean facular intensity for the different bins. Upper panels represent the intensity of faculae at $\lambda 0.8$ μm and lower ones at $\lambda 1.55$ μm. The straight solid line is the mean intensity of the quiet photosphere, normalized to unity. The general trend observed is in agreement with the work of Ortiz et al. (2002).

It can be seen in Figure (4.9) that, near the disk center, the facular intensity is smaller for increasing facular sizes. As mentioned in section 4.4.1, in $\lambda 1.55 \mu$m images this facula can be identified as the 'dark faculae' observed in infrared by Foukal et al. (1989) and Foukal et al. (1990). The decrease of facular intensity with facular size near disk center is in agreement with the model predictions, since the lateral radiative heating becomes more efficient for smaller flux tubes (Spruit 1976; Knölker & Schüssler 1988). Nevertheless, some authors present a different approach to this phenomena. Deinzer et al. (1984), modeling stationary magnetic flux elements, found the formation of a cool ring around the flux tube. They claim that faculae are seen dark at disk center as a consequence of this cooling around the magnetic structure, and that an additional heating mechanism is required to reproduce the observed CLV of facular contrast. Actually, they found that the 'wall' around the magnetic structure is significantly cooler than the undisturbed atmosphere at the same geometrical depth. The observations performed in the present work can not support neither rule out this model. Nevertheless, they offer observational constraints which models must reproduce.

In Figure (4.9) it can be seen that for positions near to the solar limb the facular intensity increases, peaking at positions the closer to the limb the larger

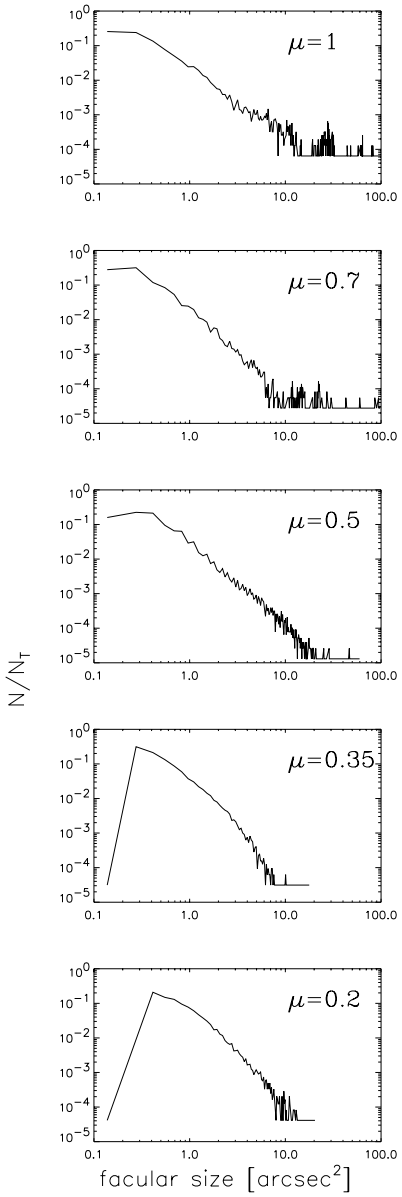

FIGURE 4.8— Facular size histograms (number of facula at each size, N, over total number of faculae, $N_{\rm T}$) for different heliocentric angles

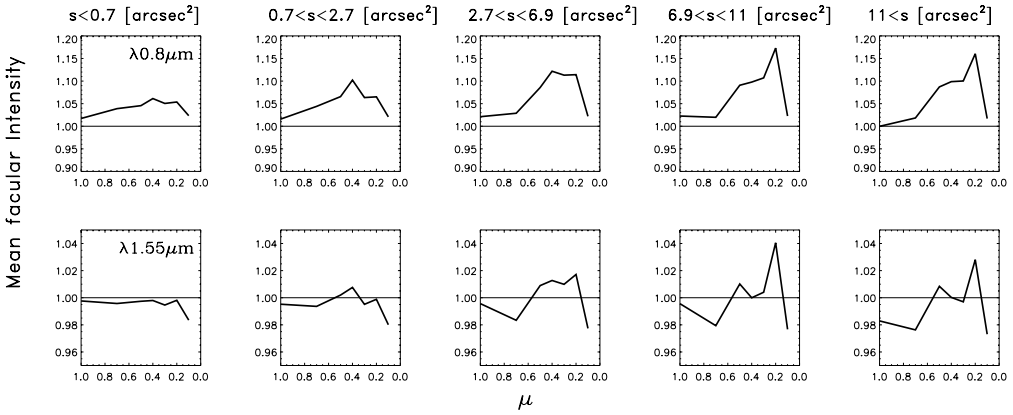

FIGURE 4.9— Center to limb variation of the mean facular intensity for different bins of facular sizes (s).

the facular structure is (i.e. for larger facular structures μ_2 decreases). Figure (4.9) also shows that, at the intensity peak, the brightness excess increases with facular area up to a certain facular size. For still larger faculae (s $>$ 11 arcsec^2) the intensity excess remains roughly constant. This is, for s $<$ 11 arcsec^2 the intensity at μ_2 increases with facular size.

Spruit (1976), Knölker & Schüssler (1988) and Topka et al (1997) have calculated the CLV of the facular contrast based on the hot wall model. Although differing in some computational approaches, all they show how the magnetic flux (or its proxy, the tube diameter D), and the Wilson depression, z_W, are the parameters defining the shape of the CLV. It is an open matter wether or not the z_W depends of the facular size. A question difficult to know from observations, although the constancy of magnetic field strength with facular size is a good support for the first option (Solanki, 1999). Lawrence & Chapman (1988) proposed the relation $\mu_2 = (1 + \mathrm{D}^2/z_W^2)^{-1/2}$.

We have no direct information about the z_W. Nevertheless, in order to explain the observational results obtained in the present work a nearly constant Wilson depression for every flux tube is the best assumption. For simple geometrical reasons, the larger faculaes' cool floor remains visible up to larger heliocentric angles if the z_W is constant. This causes the facular intensity to increase at larger heliocentric angles the larger the faculae are, producing the observed dependence of μ_2 on the facular size. Besides, the increase of the brightness excess at intensity peak (at μ_2) can be understood by taking into account that the temperature of the wall increases with height in the atmosphere (Spruit, 1976), and that for larger flux tubes (with a constant Wilson depression) the wall remains visible up to larger heliocentric angles. Topka,

Tarbell & Title (1997) found that the Wilson depression is of about 100 km, independently of the facular diameter, in agreement with the present work.

We should also consider the influence of the environment on the physical properties of the facular structures. Zayer et al. (1990) and Solanki et al. (1992) have shown how the thermal structure depends on the magnetic filling factor of the facular region. In the present work we find that the FFF decreases for $\mu = 0.7$ and $\mu = 0.35$ (see Figure 4.3), positions at which the facular intensity decreases too, specially for large faculae and $\lambda 1.55$ μm. This correlation is in agreement with the behaviour found in other works, where the decrease of the filling factor causes μ_1 to move closer to disk center and the brightness excess at μ_2 to be smaller (Topka et al., 1997).

A third order polynomial function of μ has been fitted to each of the facular contrast curves (C_{fac}) presented in figure 4.9. This is:

$$C_{fac} = a + b\mu + c\mu^2 \tag{4.4}$$

The obtained coefficients for each facular size bin are presented in table 4.4.

TABLE 4.4— Coefficients of the polynomial fit to the facular contrast

Facular size [arcsec^2]	Wavelength [μ m]	a	b	c
s $\leq$ 0.7	0.8	0.999962	0.369507	-0.703735
0.7 $\leq$ s $\leq$ 2.7	0.8	0.963112	0.738342	-1.36841
2.7 $\leq$ s $\leq$ 6.9	0.8	0.934158	1.23975	-2.55554
6.9 $\leq$ s $\leq$ 11	0.8	0.941650	1.35974	-2.98376
11 $\leq$ s	0.8	0.952713	1.20044	-2.54065
s $\leq$ 0.7	1.55	0.972099	0.158630	-0.286865
0.7 $\leq$ s $\leq$ 2.7	1.55	0.957153	0.287476	-0.527832
2.7 $\leq$ s $\leq$ 6.9	1.55	0.947632	0.462219	-0.948975
6.9 $\leq$ s $\leq$ 11	1.55	0.960297	0.411316	-0.915039
11 $\leq$ s	1.55	0.950615	0.415710	-0.876465

4.4.3 Brightness Temperature

As mentioned in section 4.4.1, the dark structures appearing in the difference images at the disk center are caused by a systematic change in the value of the vertical temperature gradient ($\delta T/\delta\tau$) between the faculae and the photosphere.

In order to study with deeper insight the temperature structure of our images, the brightness temperatures have been computed.

The brightness temperature T_b is defined according to Planck's law:

$$T_b(\lambda) = \frac{c_2}{\lambda \ln\left[c_1/(\lambda^5 I^{\rm abs}(\lambda)) + 1\right]} \ , \tag{4.5}$$

where c_1 and c_2 are the constants of the Planck formula. The normalized intensities are transformed to absolute intensities (in physical units). At disk center this transformation is performed by means of the calibration factors $I^{\rm abs}_{\rm phot}(0.80) = 0.196\,{\rm W\,cm^{-2}\,ster^{-1}\,\AA^{-1}}$ (Neckel & Labs 1984) and $I^{\rm abs}_{\rm phot}(1.55) = 0.043\,{\rm W\,cm^{-2}\,ster^{-1}\,\AA^{-1}}$ (Makarova, Roshchina, & Sarychev 1994). At other disk positions these factors have been corrected for the CLV of the quiet Sun intensity using the tabulated values of Pierce & Slaughter (1977).

The brightness temperatures $T_b(0.80)$ and $T_b(1.55)$ were computed for every pixel of the best images at each observed disk position. Then, the points corresponding to quiet regions (QR), faculae, and pores were separated following the criteria described in section 4.4.1. Table (4.5) presents the obtained mean values of $T_b(0.80)$ and $T_b(1.55)$ for the different disk positions. The last column presents the brightness temperature difference $\Delta T_b = T_b(1.55) - T_b(0.80)$, which is an important parameter that gives information about temperature stratifications in different photospheric structures. Note that different active regions (NOAA 8056, NOAA 8053 and NOAA 8052) have been included in the table. Though the obtained T_b values might be influenced by the scattered light, it can be assumed that this influence doesn't affect qualitatively the results presented in this section (see paper I for a detailed discussion).

As seen in Table (4.5), the brightness temperature of the quiet photosphere decreases for larger heliocentric angles at both wavelengths. This is logical since, as shown in Table (4.2), radiation seen at higher heliocentric angles comes from layers higher in the atmosphere. Last column of Table (4.5) shows that ΔT_b in QR increases from disk center up to $\mu = 0.6$ and then it decreases. This is due to the decrease of the temperature gradient with atmospheric height (see Figure 4.4). Since at larger heliocentric angles the formation heights,$z_{\rm c}$, are higher, even though $\Delta z_{\rm c}$ increases, the resulting temperature difference decreases.

Faculae also have, at both wavelengths, decreasing mean T_b for positions nearer to the solar limb: As seen in Figure (4.4), the facular temperature also decreases with height. But when observing faculae from a certain heliocentric angle on, we see the 'hot wall'. This hot wall increases the brightness temperature to higher values than those of QR at the same heliocentric angle. Therefore the faculae appear bright from a certain disk position up to the limb.

TABLE 4.5— Average brightness temperatures T_b (K)

μ	Region	$T_b(0.80\,\mu\text{m})$	$T_b(1.55\,\mu\text{m})$	ΔT_b
1	Quiet (reference)	6049	6614	565
	Faculae	6030	6520	490
	Pores	5080	5790	710
0.85	Quiet (reference)	5954	6552	598
	Faculae	6017	6505	488
	Pores	5273	5986	714
0.7	Quiet (reference)	5857	6463	606
	Faculae	5915	6430	515
	Pores	5359	5982	623
0.6	Quiet (reference)	5730	6339	609
	Faculae	5786	6290	504
	Pores	5228	5873	645
0.5	Quiet (reference)	5620	6228	609
	Faculae	5696	6264	568
	Pores	5445	5860	415
0.35	Quiet (reference)	5470	6068	598
	Faculae	5533	6101	568
	Pores	5265	5742	478
0.2	Quiet (reference)	5245	5793	548
	Faculae	5336	5861	525
	Pores	5090	5511	421

Pores, on the other hand, have an increasing $T_b(0.80\,\mu\text{m})$ up to $\mu = 0.5$ and a decreasing $T_b(0.80\,\mu\text{m})$ from $\mu = 0.5$ to the limb. The discrepancy with this trend at $\mu = 0.6$ can be due to the fact that at $\mu = 0.6$ we observe another active region, NOAA 8052, which can have a different magnetic configuration. In $\lambda 1.55$ μm pores show a similar behavior but their temperature peaks around $\mu = 0.7$ (the data on $\mu = 0.85$ belong to active region NOAA 8053, which could also have a different magnetic configuration). These trends of the mean T_b are easy to understand. When we observe pores near the disk center, we are seeing the cool floor. For increasing heliocentric angles, a larger portion of the 'hot wall' becomes visible. Pores have much cooler atmospheres than QR and, therefore, the appearance of the hot wall in the observed field of view raises significantly the T_b of the pore. For increasing heliocentric angles, the contrast (and thus the temperature brightness) decreases due to the dependence of the visibility of both the pore's cool floor and the hot wall on the angle of view.

Figure (4.10) shows scatter plots of the $T_b(0.80\,\mu\text{m})$ versus $T_b(1.55\,\mu\text{m})$ for

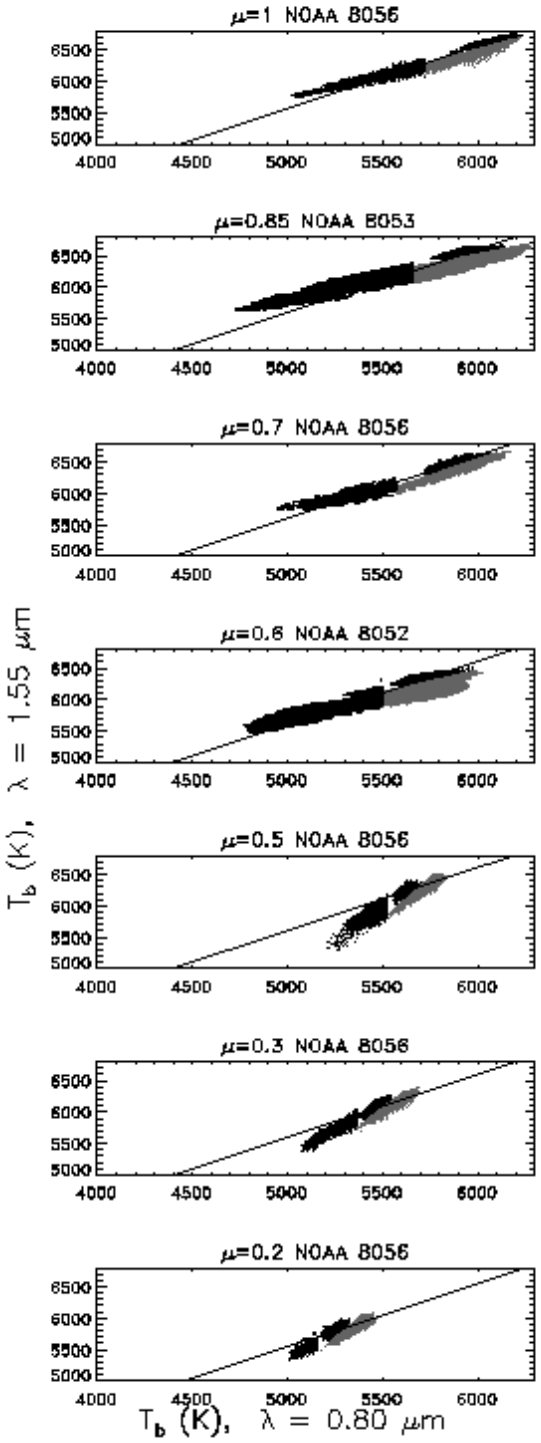

FIGURE 4.10— Scatter plots of brightness temperatures for 1.55μm versus 0.8μm images at different disk positions.At disk ceneter, elements of quiet regions (black) are located top right, facular elements(gray) are below them; elements of pores (black)continue in the trend of faculae. The color code keeps for all the disk positions. The straight line represents the constant temperature difference corresponding to the mean quiet region at each heliocentric angle.

the studied structures at the different disk positions. The straight line represents the constant temperature difference corresponding to the mean quiet region at each heliocentric angle. Gray points stand for facular regions while pores are displayed by black points with lower T_b. Black points standing around the straight line with higher T_b belong to quiet regions. At disk center, the faculae are located slightly below the straight line which means that they have temperature differences a bit smaller than quiet regions. As discussed above, this is due to the lower temperature gradient in facular atmospheres than in quiet photosphere. Pores are located above and below the straight line (i.e. have larger and smaller temperature differences), extending smoothly the cloud of points corresponding to facular regions. This means that facula and pores share the same physical mechanism (inhibition of convection and lateral heating), which changes its contribution as a function of the size of the structure. Cooler pores present larger temperature differences (they are higher above the straight line). This is a consequence of the decrease of the opacity with the decrease of the mean atmospheric temperature.

As we move towards the limb, the faculae are found to decrease their brightness temperature, but less than the T_b(QR) decreases. Thus, many facular points have higher temperatures than the QR. This is due to the appearance of the 'hot wall' in the observer's field of view, as mentioned above. Facular ΔT_b is similar to ΔT_b in QR for hot faculae, and smaller for cold ones. Pores, similarly, extend the facular cloud of points to smaller ΔT_b the cooler the pores are. This is the opposite to what happened at disk center where cooler structures had larger ΔT_b. It must be noted that two different factors are influencing the presently analyzed results. On the one hand, the region NOAA 8056 was a decaying region and therefore we assume that was loosing magnetic flux as approaching to the limb. On the other hand, the region is observed at higher layers in the atmosphere for larger heliocentric angles. The changes due to the evolution of the region can not be disentangled from those due to the change in disk position. At disk center the difference in formation heights between $\lambda 1.55\mu$m and $\lambda 0.8\mu$m, $\Delta z_{\rm c}$, of the HSRA atmosphere is much smaller than $\Delta z_{\rm c}$ of a small spot atmosphere (see table 4.2). Since the temperature gradients of these two atmospheres at the observed layers do not differ significantly, the temperature difference is larger for pores than for the quiet regions. On the contrary, near the limb the $\Delta z_{\rm c}$ of the HSRA atmosphere and of a small spot are similar. Since at those layers the temperature gradient of the atmospheres are still similar, the temperature difference, ΔT_b, of quiet regions and pores tends to be similar. In parallel, assuming that the decay of the active region observed causes the filling factor and the magnetic strength (flux) to decrease, the radiative heating would become more efficient at the upper layers of the flux

tubes making the opacity increase and thus ΔT_b decrease. The combination of the effect caused by the change in heliocentric angle and the decay of the active region observed causes the ΔT_b of pores to be smaller in pores than in quiet regions near the limb.

4.4.4 Maps of temperature differences

To study the spatial distribution of ΔT_b, the best images of each heliocentric angle have been selected and their resulting temperature difference maps are shown in the fourth column of panels in Figure (4.2). Dark areas correspond to $\Delta T_b < \Delta T_b(\mathrm{QR})$ and bright ones to $\Delta T_b > \Delta T_b(\mathrm{QR})$. As explained in the previous section, faculae have ΔT_b smaller than $\Delta T_b(\mathrm{QR})$ at disk center, but for larger heliocentric angles this difference gets smaller or it even disappears. Therefore faculae in the temperature difference maps are almost invisible close to the limb. On the contrary, pores have a $\Delta T_b > \Delta T_b(\mathrm{QR})$ at disk center and $\Delta T_b < \Delta T_b(\mathrm{QR})$ near to the limb, thus appearing bright at disk center and dark near to the limb.

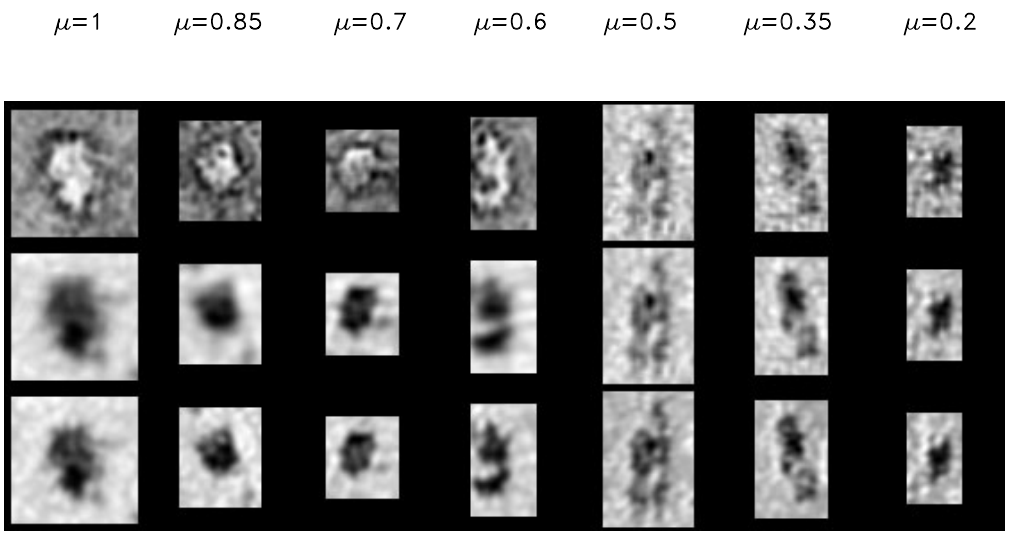

FIGURE 4.11— Composite figure showing the center to limb evolution of the largest pores in the temperature difference images (upper panels), $T_b(1.55)$ (midle panels) and $T_b(0.8)$ (lower panels).

In Sobotka et al. (2000) was shown that in most cases the pores are surrounded at disk center by "rings" of dark faculae. These rings were identified as the continuum signature of clumps of less densely packed flux tubes around the more compact magnetic structures of the pores. These more diffuse and bright flux tubes around the pore would be linked to the same magnetic structure and belong to the same trunk as the pore (Martínez Pillet, 1997). In order to study the center to limb variation of these "dark rings", we show in Figure (4.11) a composite picture with zooms of the pores at the different studied heliocentric angles. Lower panels show the $T_b(0.80)$, middle panels the $T_b(1.55)$ and upper panels ΔT_b. As seen in the upper panels of the figure, these dark rings disappear at $\mu = 0.5$, like faculae do in the temperature difference images. In contrast, no structures are visible around the pores in the T_b images (lower panels) at disk center but for positions nearer to the solar limb a "bright ring" appears. This supports the finding that the pores are surrounded by thinner facular-like magnetic flux tubes (Keppens & Martínez Pillet 1996; Skumanich 1999), and confirms that the "magnetic radii" of pores (and sunspots) are larger than their "brightness radii".

The spatial resolution of our observations allows to resolve the inner structure of the pores analyzed. As seen in Figure (4.11) several umbral dots (UDs) (or clumps of them) can be distinguished in the pores displayed. Near disk center the UDs appear as dark structures in the temperature difference images, like faculae do. On the contrary, for positions near the limb, the UDs appear bright in the temperature difference images, opposite to faculae that appear also dark near the limb. This shows that the atmospheres of pores, UDs and faculae are different.

4.5 Conclusions

We have studied the CLV of facular regions and pores at two different spectral ranges, placed at the extremes of the distribution of continuum opacity with the wavelength. In other words, we have compared information coming from different heights in the solar photosphre. In order to estimate from which layers comes the information analyzed we have calculated the respective response functions to the temperature(see Section 4.2).

Studies of center-to-limb variation are inevitably contamined by the intrinsic evolution of the active region while crossing the disk. In facular regions this is manifested in changes in the magnetic filling factor. Moreover, the different spatial resolution between the two working wavelengths must also be considered. With this constraints in mind, we have applied the differential technique used in Sobotka et al. (2000) to study the CLV of facular brightness.

We found that, at disk center, faculae have on average no contrast in $\lambda 0.8$ μm and appear as dark structures in $\lambda 1.55$ μm. The absolute values of the facular intensity depend on the photometric definition of a facula. Nevertheless, general trends remain independently of the threshold g used in the definition (see equation (3)). We have observed the change from dark to bright facula in $\lambda 1.55$ μm at μ=0.5-0.6. On average, for both observed wavelength channels the facular intensity is observed to increase with heliocentric angle up to μ=0.3. For larger heliocentric angles the facular intensity decreases.

Studies on the size dependence of facular intensity have revealed that large faculae have lower intensities at disk center, but higher near the limb, than small faculae. In addition, for large faculae the intensity peaks at positions nearer to the solar limb. The facular size distribution has also been computed and the smaller facular sizes are found to be the most frequent.

All the observed properties described above fit qualitatively with the predictions derived from a 'hot wall' model of faculae (see the introduction for a description). According to this model, the facular intensity peaks somewhere between the center of the disk and the limb. The μ_2 at which this peak occurs is strongly dependent on the Wilson depression and on the horizontal size of the modeled flux tubes (Spruit, 1976). In the present work, the observed dependence of the facular intensity CLV on the facular size points to the existence of a small range of Wilson depressions in the facular flux tubes. This is in agreement with the work of Topka et al. (1997) who also found that the Wilson depression is of about 100 km independently of the facular size.

The average CLV of facular intensity has also been computed, obtaining a CLV curve which peaks at μ_2=0.3. The simulations of flux tubes assuming a hot wall model obtain a peak at μ_2=0.15 (e.g. Spruit, 1976; Knölker & Schüssler 1988) in contradiction to our observations. This contradiction can be understood if we take into account that most flux tube computations model isolated flux tubes of different sizes, Wilson depression, etc. but, in active regions, flux tubes are not isolated. Some works predict that the increase of the filling factor causes the overall convective energy transport to be distributed through densely packed magnetic structures, so that the surrounding of the flux elements are cooler than for an isolated flux tube. This reduces the efficiency of radiative heating and leads to cooler structures with a different thermal structure (e.g. Grossmann-Doerth et al., 1994).

In addition, in active regions flux tubes of different sizes are present, each having its own CLV. The average CLV of facular intensity depends on the size distribution of the facular flux tubes. Therefore, it is of crucial importance to determine this distribution. We have computed the size histograms of the faculae, obtaining a distribution that increases with decreasing size. Some

models reproduce the observations with an unique flux tube size (Grossmann-Doerth et al. 1994). However, our observations require flux tubes of different sizes in order to explain the size dependence of the observed CLV of facular intensity.

Brightness temperature maps have been computed for $\lambda 0.8$ μm and $\lambda 1.55$ μm. The obtained values in the two wavelengths channels are compared, pixel by pixel, in scatter plots shown in Figure (4.10). Faculae show temperature differences smaller than quiet regions at disk center. This difference decreases and almost disappears as approaching to the limb. On the other hand, pores show larger temperature differences than quiet regions at disk center, but smaller near the limb. We interpret this fact as a consequence of the combination of two effects: the change of the FFF of region NOAA 8056 during its passage from the center to the limb, and the variation of the difference of formation heights between pores and quiet regions at disk center and near the limb. Pores show brightness temperatures that extend smoothly the cloud of points corresponding to facular regions. This means that both facula and pores share the same physical mechanism (lateral heating and inhibition of convection), simply changing its contribution as a function of the size of the structure.

Maps of temperature differences have also been computed. We observe around pores a ring like structure that has small temperature difference at disk center. However, as approaching the limb, this ring-like structure disappears in the temperature difference image, appearing a bright ring in the temperature maps instead. We interpret this as a signature of the less densely packed flux tubes around the densely packed pore suggested by Martínez Pillet (1997). This thin facular-like magnetic flux tubes would belong to the same trunk as the pore.

5

Numerical simulations of the solar granulation

In the present chapter we study the agreement of the observables derived from different theoretical and semi-empirical models of the solar granulation with the observables derived from the observed data used in the present thesis. To that aim, radiative transfer codes are applied to different model atmospheres of quiet granulation. Besides, the influence of the instrumental and atmospheric factors that affect solar observations on the CLV curves of the ΔI_{rms} is investigated. Finally, it is tested how sensible are these curves to changes in granular area and temperature fluctuation stratification.

5.1 Method

The basic idea of the method used is to compare the observed center to limb variation of the granular properties and the synthetic one by applying a radiative transfer code to a 3D box of data that simulates the solar atmosphere. The input data for the code can be directly a snapshot of the output of a theoretical hidrodynamical code or of semi-empirical models. In the later case, models of a mean granular and intergranular atmosphere are required. Then, a geometrical model must be assumed in order to reproduce the horizontal variation of the physical quantities at each given depth layer. The different geometries and atmospheres studied are described below, together with a brief overview of the principles of the radiative transfer codes used.

5.1.1 Atmospheric models

As mentioned above, atmospheres obtained in two different manners can be used for the purposes of the present chapter. The advantage of using both, theoretical and semi-empirical atmospheres, is that one method can be confronted to the other, looking to the similarities and the differences in the obtained results.

Theoretical atmospheres

The atmospheres that result from a 3D hydrodynamical code offer the possibility to check the fit to observations of granular contrast, granular filling factor, granular power spectra, etc. Therefore, this kind of data is suitable to check to what extent do the theoretical models reproduce the properties of the granulation.

In the present thesis we have used a snapshot of the synthetic granulation computed by Stein & Nordlund (2000). These data result from a model of solar convection obtained by using a 3D, compressible, MHD code that integrates the conservation equations of mass, momentum and internal energy, and induction equation for the vector potential. Three dimensional LTE radiative transfer is included in this model. The authors claim that these computations contain enough detailed physics to realistically model convection near the solar surface and the overlaying photosphere.

2-D models of solar granulation are also found in the literature. Even though three dimensional models are more realistic, the 2D models require less computational effort and, therefore, some physical details can be treated in deeper insight. Thus, it is interesting to compare the observables predicted by 2D models with those of our observations, in order to test the differences between 2D and 3D models and the agreement of 2D models with the observed granulation. We have used in the present chapter a set of 2D solar granulation models based on a complete system of hydrodynamic equations for a compressible, radiatively coupled and gravitationally stratified medium (Gadun, 1995; Gadun & Pavlenko, 1997; Gadun et al. 1999). We have two different temporal series of models, each with different boundary conditions and spatial dimensions, that we name 35KM model and 15KM model, according to their spatial resolution (both in the z and x axis). In Table 5.1 we present a summary of some properties of these 2D models studied. They were computed with a temporal resolution of 0.3 s. However, the study that will be presented below only takes into account models every 30 s.

In figure 5.1 we present the space averaged mean stratification of the different physical quantities in the models of Stein & Nordlund (2000) and, in figure 5.2, the time and space averaged mean stratification in the models of Gadun

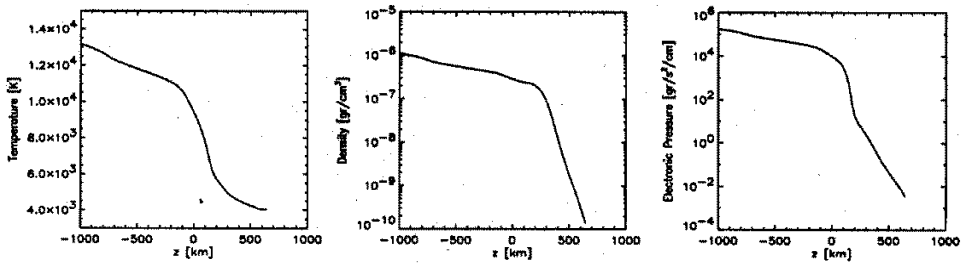

FIGURE 5.1— Stratification of temperature, density and electronic pressure in the models of Stein & Nordlund (2000)

TABLE 5.1— Bidimensional models

MODELS	Points in the computational grid [Hor x Ver]	Spatial resolution [km]	Lateral boundary conditions
35KM	112 x 58	35	simetric
15KM	112 x 58	15	periodic

(1995) (solid line–35KM models, dotted–15KM models). Below, in section 5.1.6 figure 5.8, we present the part of the atmospheres where the emergent radiation comes from and where granules and intergranules can be distinguished for the model of Stein & Nordlund (2000). In figure 5.9 we plot the mean model atmosphere for the 35KM and the 15KM models in the layers where the radiation that we observe comes from.

The definition of the point where z=0 in the mean atmosphere is somewhat arbitrary. It is common to fix it at $\log(\tau_{5000})$=1, or at the height where the gas pressure coincides with the gas pressure of the HSRA atmosphere at z=0. In order to unify criteria and to be able to compare the results obtained in the next sections, we have placed z=0 in all the models used, both theoretical and semi-empirical, at the height where the gas pressure coincides with that of the HSRA atmosphere at z=0.

Semi-empirical atmospheres

Semi-empirical atmospheres are obtained from the inversion of observational data. This means that, by definition, these atmospheres reproduce the obser-

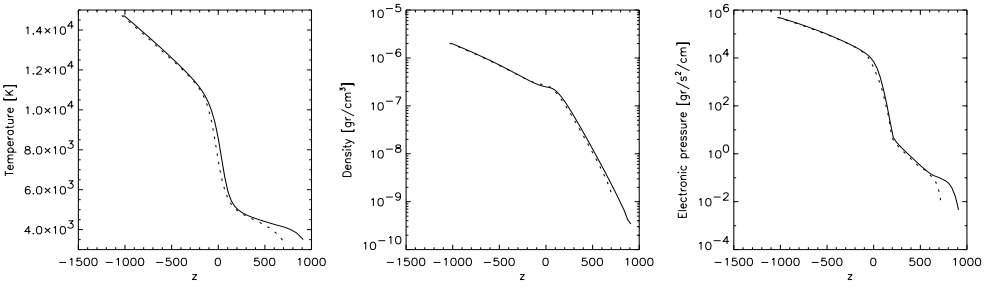

FIGURE 5.2— Stratification of temperature, density and electronic pressure in the 35KM models (solid line) and 15KM models (dotted line) of Gadun (1995).

vations to which the inversion procedure was applied. However, it would be interesting to see to what extent do they also match other observations performed independently.

Besides, the semi-empirical atmospheres we are interested in give a mean granular atmosphere and a mean intergranular atmosphere. Therefore, to apply the 3D code it is necessary to assume a certain geometry. The variations introduced in the simulated geometry allow us to study how do the observables depend on the details of the granular sizes, granule-intergranule transition, granular shape, etc, which will be explained in the following subsection. Here the atmospheres used are described.

Rodríguez Hidalgo et al. (1995) analyzed spectroscopic two dimensional data of a quiet region at disk center, which were obtained by scanning the solar surface with a step of 0".4. Two spectral regions were simultaneously observed: Fe I 5576 AA and Fe I 6301,6302 Å. The images were not corrected for terrestrial atmospheric degradation. They applied the inversion code developed by Ruiz Cobo & del Toro Iniesta (1992) to the spectrum of each spatial point, thus obtaining the stratification of temperature, line of sight velocity, pressure and density. For this computations, local thermal equilibrium (LTE) and hydrostatic equilibrium were assumed in each line of vision. By averaging the obtained atmospheric models for the different granules (hot upflows) and intergranules (cold downflows), the mean granular and intergranular models were obtained.

Figure 5.3 presents the stratification of the different physical quantities obtained for this model. Solid lines stand for granular structures and dashed lines for intergranular lanes. Note that the inversion methods only allow to obtain information of the layers of the atmosphere from which the emergent intensity

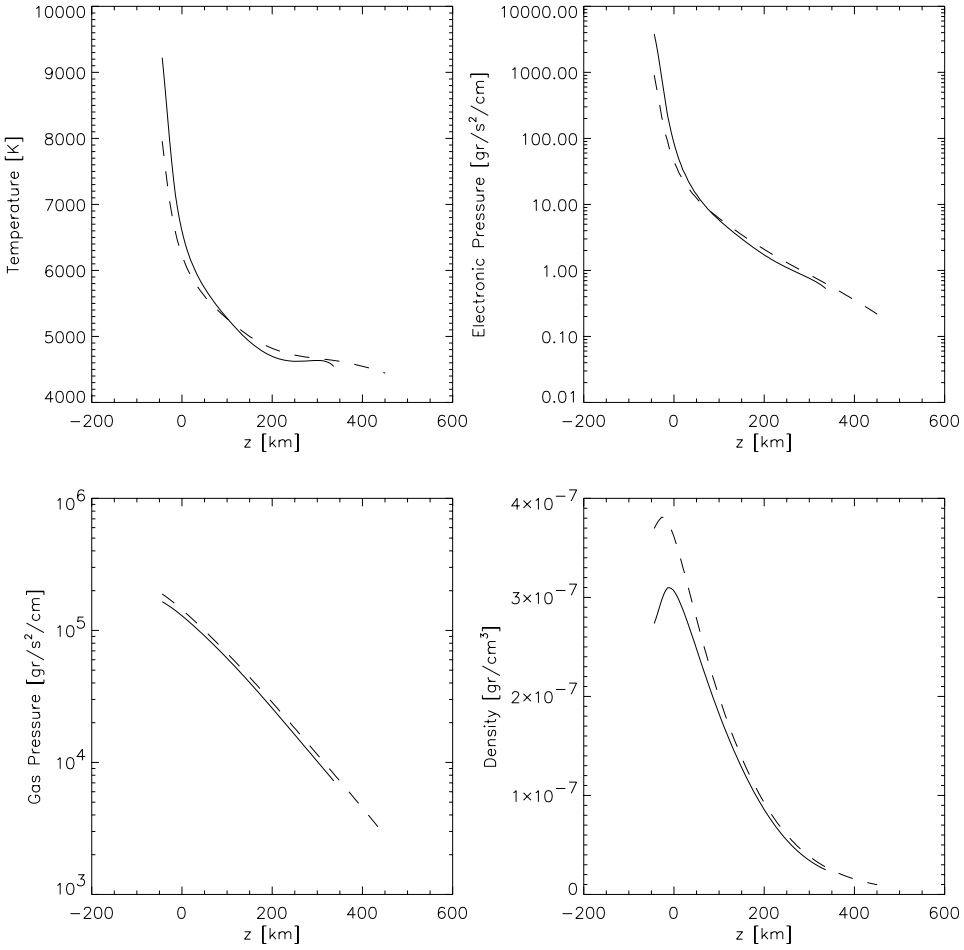

FIGURE 5.3— Stratification of Temperature, Electronic pressure, Gas Pressure and Density in the semi-empirical models of Rodríguez Hidalgo et al. (1995) for granules (solid lines) and intergranules (dashed lines).

comes from. Therefore the range of height points is smaller for semi-empirical than for theoretical atmospheres.

5.1.2 Geometries

As mentioned above, in order to apply the radiative transfer code to a given semi-empirical two component model of the solar photosphere, it is necessary to assume a certain geometry. We aim to construct a geometry that reproduces, as accurate as possible, the granular pattern on the Sun. However, several questions arise when constructing this geometry, namely: how does the granular size distribution affect the resulting granular parameters?; how does the specific shape of the granules affect?; how does the granule-intergranule transition influence the obtained results? It is important to answer this questions by varying the geometries and checking the obtained observables in order to decide which kind of geometry will be used.

We have performed tests on how does the granular cell size distribution affect the resulting CLV of the granular contrast, obtaining that it is a fundamental parameter, since the shape of the CLV curve depends critically on it. Therefore, we have decided to use a realistic granular cell size distribution like the one we observed at λ 6708 Å (chapter 2, figure 2.11, upper curve). In section 5.2.5, a study of the influence of granular areas on the CLV curve of the granular contrast is presented.

For a given granular cell size distribution we have studied how does the CLV of the granular contrast depend on the specific shape of each granule. We used different shapes such as boxes, sinusoids, random polygonal shapes, etc. We concluded that the specific shape of the granules does not affect the contrast in any significative manner.

Tests on the influence of the granule-intergranule transition shape on the resulting CLV of the contrast have shown that this parameter does influence the obtained results only marginally. This effect is less significant than the effects of a convolution with a PSF or other factors affecting solar observations that will be shown in further sections. We have not found in the literature any statistical study on how does this transition occur in an average granular cell. Therefore, we have chosen a transition which visually fits the outfit of real solar granulation.

Schrijver et al. (1997) performed a study of the granulation and supergranulation patterns and concluded that they can be adequately reproduced by using a generalized Voronoi tessellation method. This method generates randomly a series of 'generator points' that are supposed to correspond to the strongest up-flows of each granule. Then, in a classical Voronoi tessellation, the plane is

segmented into non-overlapping sets of points closer to some so-called generator point than to any other such point in the plane (see Okabe, Boots & Sugihara 1992). The formal representation of the Voronoi regions $V(p_i)$ based on a set of distinct generator points x_i can be written as:

$$V(p_i) = \left\{ x \,\middle|\, \frac{1}{||x - x_i||} \geq \frac{1}{||x - x_j||},\ for\, j \neq i, j \in [1, ..., n] \right\}, \tag{5.1}$$

where $P = p_1, ..., p_n$ is the set of points in the Euclidean plane that is being segmented. However, this kind of tessellation is not able to reproduce the size distribution of granules. A generalized Voronoi tessellation is more suitable for this purpose. Its formal representation is:

$$V(p_i) = \left\{ x \,\middle|\, \frac{w_i}{||x - x_i||^p} \geq \frac{w_j}{||x - x_j||^p},\ for\, j \neq i, j \in [1, ..., n] \right\}, \tag{5.2}$$

In this so-called 'generalized multiplicatively weighted Voronoi tessellation' different weights $w_i > 0$ are associated to the generator points. The linear distance used in the classical Voronoi segmentation is replaced by some function of distance, here taken to be a power law with index p. We have performed tests on which p index best fits the observed granular pattern, concluding that the best choice is $p = 1$. The weights w_i have been extracted from the observed histogram of the granular cell size distribution which ensures that the synthetic pattern will follow the observed cell size distribution. To generate the geometry, a number N of granules and a box size are fixed. Then, N weights w_i proportional to the observed cell size distribution are associated to the generator points, and the Voronoi cells are produced in the Euclidian plane that is being segmented. By matching the cell size distribution obtained in the computing box with the observed one, the pixel size is calibrated.

Once the surface is segmented, a function must be assumed inside each granular cell to reproduce the variation of the physical quantities from the granule to the intergranular lane. This transition is done in an exponential way in our approach, with a tunable index that regulates the steepness of this decrease:

$$G = 1 - e^{-g*A}, \tag{5.3}$$

where A is the tunable parameter, G is the resulting geometry and g is a working geometry in which the values vary between 1 at the granular cell centers

and 0 at granular cell borders. The g geometry is constructed by assuming the center of each granular cell at the centroid of each Voronoi cell and setting a value to each point of the cell that decreases linearly with the distance to this center down to a value of 0 at the borders. The points with maximum intensity will coincide with the cell centers. We have not chosen as the maximum intensity points the 'generator points' of the Voronoi tessellation because in the Sun most cells show a maximum intensity near their centers.

The geometry G will be converted into physical quantities. Therefore, it must fluctuate in such a way that the mean granular (intergranular) values of a given physical quantity have a variation with depth that coincides with the mean granular (intergranular) atmosphere given by the semi-empirical model. This is achieved by a separate normalization of the granular areas and the intergranular lanes to a mean value of $+1$ and -1 respectively, thus obtaining a normalized geometry $\overline{G}$. The discrimination of granular and intergranular areas is performed by means of a threshold in the G geometry.

Then, $\overline{G}$ is converted into physical quantities for each given depth by applying the following equation:

$$P(x,y,z) = P_c(z) + \overline{G(x,y)} * \Delta P(z), \tag{5.4}$$

where $P(x,y,z)$ is the horizontal distribution at a given depth of some physical quantity (specifically: temperature, gas pressure, electronic pressure or density). $\overline{G(x,y)}$ is the geometry assumed, $P_c(z)$ is the central value of the physical quantity at this depth (this is $(P_g(z) + P_i(z))/2$ i.e., the mean value of the granular and intergranular components) and $\Delta P(z)$ is the fluctuation of this quantity at this depth (this is $(P_g(z) - P_i(z))/2$).

As mentioned above, several A parameters have been used in order to test the influence of the granule-intergranule transition on the obtained results. In Figure 5.4, geometries produced by setting $A = 1.5$ (left panel) and A=5.5 (right panel) are presented. The value chosen for further computations was A=5.5.

5.1.3 3D Radiative transfer code

We have used the three dimensional radiative transfer code developed at the Instituto de Astrofísica de Canarias by Fabiani Bendicho & Trujillo Bueno (1999). This code performs radiative transfer computations by means of solving parallely the equations of populations of atomic levels in complex atomic models with many levels and the equations of radiative transfer for three dimensions. The metals that are included in the code to compute the absorption coefficient of

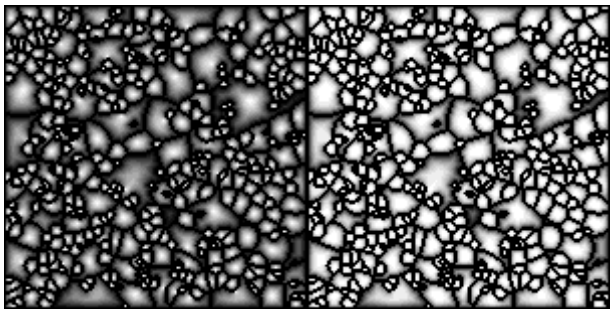

FIGURE 5.4— Synthetic geometry of the granular pattern for $A = 1.5$ (left panel) and $A = 5.5$ (right panel).

the continuum are: Si, C, Mg, Al, Fe. The code assumes Local Termodynamic Equilibrium (LTE).

Introducing the parameters that describe an atmosphere for each point of the computational grid (x, y, z), the code gives as an output the emergent intensity in all the computational surface (x, y) in the wavelength required. For each depth point the boundary conditions are periodic in x and y.

The code is based in the Short Characteristic Method, with parabolic integration of the source function and parabolic interpolation of the upwind intensity. In order to avoid the numerical errors produced by the high order interpolation, it uses the "slope testing" method (Fabiani Bendicho, 2002).

This code allows to obtain the emergent intensity for different angles with the x and y axis, enabling to study the radiative effects produced by an oblique vision angle.

5.1.4 2D Radiative transfer code

In order to analyze the emergent intensity of the theoretical 2D hydrodynamical code of Gadun (1995) we have used a 2D radiative transfer code developed by this author. In this code the radiative transfer equations were treated in 2D, including the wavelength dependence of the monochromatic opacity of the continuum. The radiative transfer in the spectral lines was computed by using the tabulation of Kurucz ODF (Kurucz, 1979) of standard solar abundances. More details on this code can be found in Gadun (1995).

5.1.5 Response Functions

In order to be able to analyze properly the obtained results it is necessary to know from which layers of the atmosphere does the information that we

receive comes from. This information is given by the response functions to the temperature.

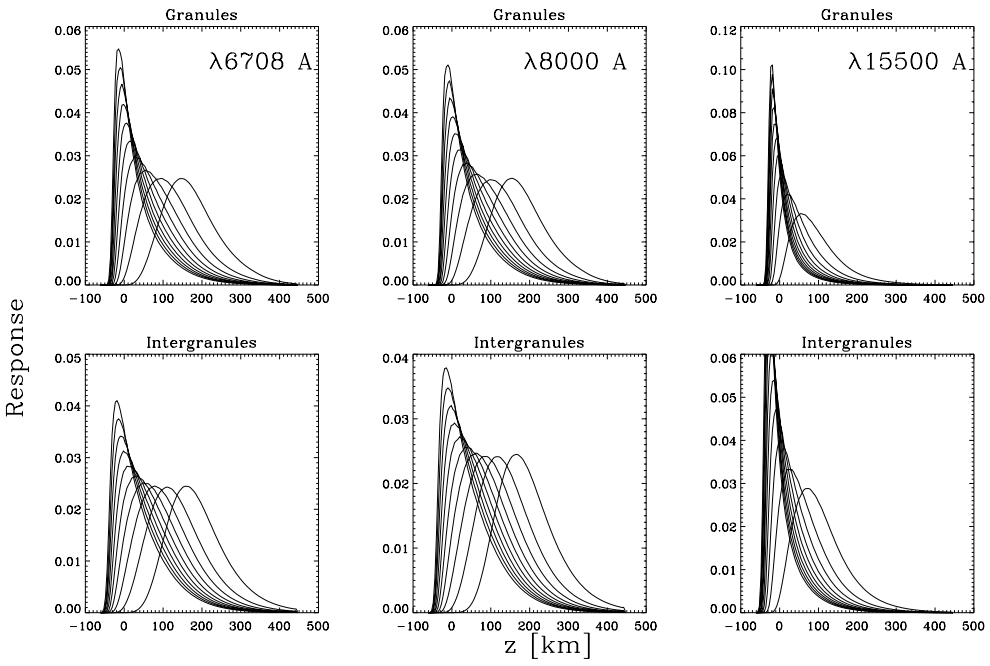

FIGURE 5.5— Response functions to the temperature of the semi-empirical models of granule (upper panels) and intergranular lanes (lower panels) of Rodríguez Hidalgo et al. (1995) at λ6708 Å (left panels), λ8000 Å (middle panels) and λ15500 Å (right panels) for μ=1., 0.9, 0.8, 0.7, 0.6, 0.5, 0.4, 0.3, 0.2, 0.1, going to higher layers.

Semi-empirical models

Figure 5.5 presents the response functions to the temperature of the semi-empirical model of a mean granule (upper panels) and a mean intergranular lane (lower panels) of Rodríguez Hidalgo et al. (1995) at λ6708 Å (left panels), λ8000 Å (middle panels) and λ15500 Å (right panels) for μ=1., 0.9, 0.8, 0.7, 0.6, 0.5, 0.4, 0.3, 0.2, 0.1. The curves with larger contributions in higher layers of the atmosphere stand for positions nearer to the limb. Intergranular lanes have larger contributions in deeper layers than the granules, and for λ15500 Å the information comes from deeper layers in the atmosphere than for λ8000 Å and λ6708 Å. Moreover, for λ15500 Å the response functions at different heliocentric angles have contributions in a narrower vertical region than for the smaller wavelengths, where the contributions come from more separated layers.

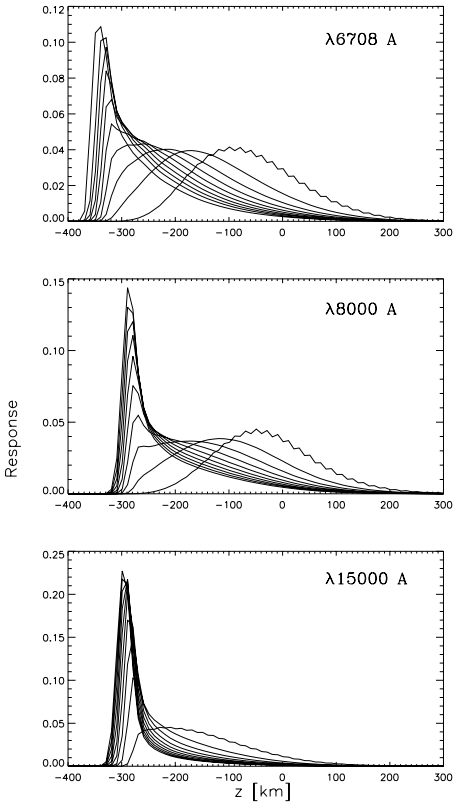

FIGURE 5.6— Response functions to the temperature of the mean atmosphere of the theoretical model of Stein & Nordlund (2000) at λ6708 Å (upper panel), λ8000 Å (middle panel) and λ15500 Å (lower panel) for μ=1, 0.9, 0.8, 0.7, 0.6, 0.5, 0.4, 0.3, 0.2, 0.1.

Theoretical models

Figure 5.6 presents the response functions of the mean atmosphere of the numerical simulations of Stein & Nordlund (2000) for different wavelengths (upper panel λ6708 Å, middle panel λ8000 Å and lower panel λ15500 Å) and heliocentric angles (μ=1, 0.9, 0.8, 0.7, 0.6, 0.5, 0.4, 0.3, 0.2, 0.1.). Note also that the height range represented in this figure is reduced to bottom at -400 km and top at 300 km. The rest of the height computational domain of the models of Stein & Nordlund (2000) has been excluded since the radiation that we observe does not come from these layers. This is clearly seen in the response functions which have zero values there. The geometrical heights from which the radiation that is observed comes from for this model is lower than in the

semi-empirical ones. This is due to a different gas pressure stratification in this theoretical model than in the HSRA atmosphere.

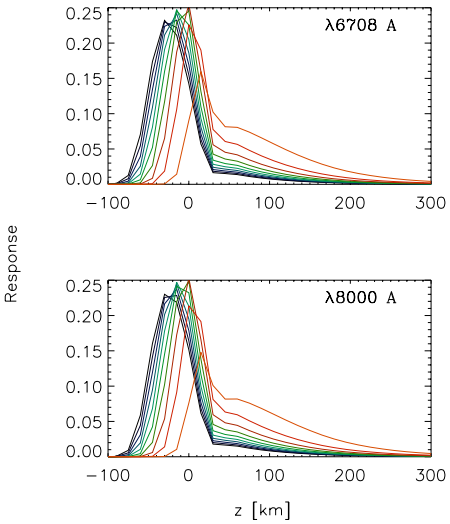

FIGURE 5.7— Response functions to the temperature of the mean 15KM model atmosphere of Gadun (1995) at λ6708 Å (upper panel) and λ8000 Å (lower panel) for μ=1, 0.9, 0.8, 0.7, 0.6, 0.5, 0.4, 0.3, 0.2, 0.1. Hotter colors stand for larger heliocentric angles.

The response functions of the 15KM and 35KM models have also been computed. The obtained curves of the 15KM models are presented in figure 5.7 (upper panels λ6708 Å, lower panels λ8000 Å). Hotter colors stand for larger heliocentric angles. The emergent intensity for these 2D models was not computed at λ15500 Å since the 2D radiative transfer code developed by Gadun is not prepared for this long infrared wavelength. Therefore, the analysis concerning the 2D models will only be performed at λ6708 Å and λ8000 Å. The curves corresponding to the 35KM are very similar to those of the 15KM model and therefore they are not plotted in figure 5.7.

Theoretical models simulate a large range of heights in the atmosphere. This allows to study layers of the Sun which are not accessible by direct observations. However, as mentioned above, the radiation that we observe comes from a smaller range of geometrical depths in the atmosphere. Therefore, it is interesting to make a plot of the stratification of the physical quantities in the theoretical models for these layers. There it is possible to make a distinction between granules and intergranules by means of a photometric criteria applied to the emergent intensity computed with the radiative transfer codes. We have

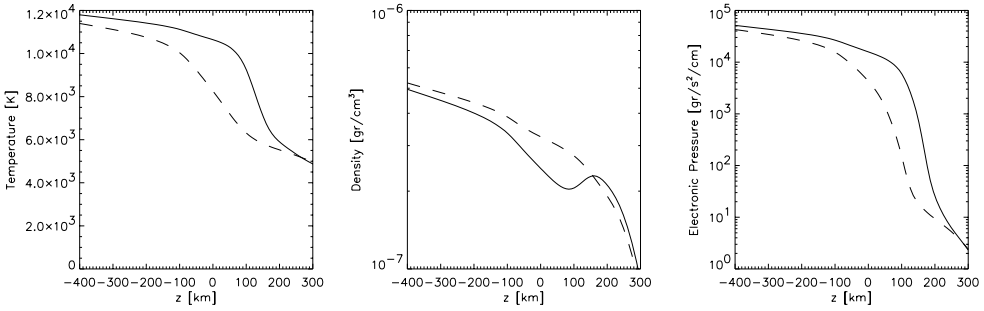

FIGURE 5.8— Stratification of Temperature, Density and Electronic Pressure in the models of Stein & Nordlund (2000) for granules (solid line) and intergranular lanes (dashed line) for the atmospheric layers where the observed radiation comes from.

used a threshold criterion as described in Section 2.3.3 chapter 2. Figure 5.8 presents the mean stratification for granules (solid line) and intergranular lanes (dashed line) of the physical parameters in the models of Stein & Nordlund (2000). When comparing this figure with figure 5.3 we see that the semi-empirical models have different gradients in the stratification of the physical quantities, and distinct absolute values than the 3D theoretical model we use. The theoretical model presents higher temperatures, smaller gradients of the temperature with height in the atmosphere and smaller densities. How do these differences influence the obtained parameters characterizing the granulation will be checked in the following sections.

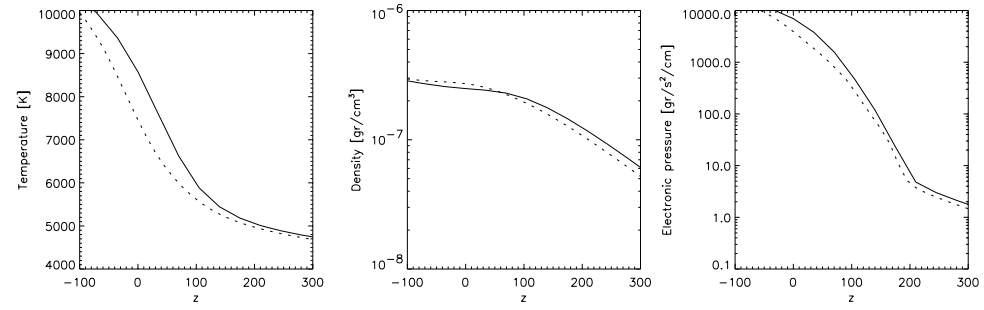

FIGURE 5.9— Mean stratification of Temperature, Density and Electronic Pressure in the mean 35KM model (solid line) and 15KM model (dotted line) for the atmospheric layers where the observed radiation comes from.

In figure 5.9 we show the stratification of the physical quantities in the mean 35KM model (solid line) and 15KM model (dotted line) for the layers where the radiation comes from.

5.1.6 Output of the radiative transfer codes

Limitations of the computations

When constructing the geometry as explained in section 5.1.2, it must be taken into account that, in order to be able to compare directly observations to simulations, both should have a similar spatial resolution. Furthermore, the cell size histogram should also be correctly reproduced. Therefore, enough granules must be put in the computing surface so that the histogram of granular cell sizes is sufficiently well represented statistically (otherwise, the CLV would be biased by the specific granules in the box), but less enough so that the pixel size is comparable to that of the observations. Besides, the size of the computing box can not be increased as much as desired because the available computers can only run the radiative transfer code in a limited box size. Therefore, a compromise must be reached.

In the present study, two kind of computations have been performed by assuming different conditions of the geometries used. On the one hand, a box has been constructed with as many granules as necessary to make sure that the cell size histogram has enough elements of population to be adequately represented. In this model the spatial resolution is not as high as desirable (pixel size–0.31 arcsec, field of the box–46.5 $\times$ 46.5 arcsec). Besides, models with high spatial resolution (pixel size–0.09 arcsec, field of the box–13.5 $\times$ 13.5 arcsec) but with less population elements in the histogram of granular cell sizes have also been computed. This spatial resolution was chosen because it is equal to the one used in our observations at λ8000 Å, although we are aware that this small pixel size produces an oversampling, since it is smaller than the diffraction limit of the telescope in all the observations performed in the present thesis.

Then, these geometries are applied to the model atmospheres following equation 5.4. For the sake of conciseness the different models (theoretical and semi-empirical) and geometries have been renamed as described in Table 5.2. This table also presents the pixelsize of the models, their field of view and their Nyquist frequencies according the particular sampling in each case.

Application to semi-empirical models

Figure 5.10 presents the raw emergent intensity of the RHL model for μ=1, 0.9, 0.8, 0.7, 0.6, 0.5, 0.4, 0.3, 0.2, 0.1. at λ 6708 Å. Figure 5.11 presents the emergent intensity at the same wavelength and heliocentric angles for the

TABLE 5.2— Models of granulation

Model	Name	Pixelsize [arcsec]	Field	$\nu_{Nyquist}$ [arcsec^{-1}]
Rodríguez Hidalgo et al. (1995) + Low spatial resolution geometry	RHL	0.″31	46.″5 × 46.″5	1.61
Rodríguez Hidalgo et al. (1995) + High spatial resolution geometry	RHH	0.″09	13.″5 × 13.″5	5.56
Stein & Nordlund (2000)	SN	0.″16	8.″14 × 8.″14	3.13
15KM Gadun (1995)	15KM	0.″02	2.″3	25.0
35KM Gadun (1995)	35KM	0.″04	4.″6	12.5

RHH model. In both figures, and also in those presented below with emergent intensities, the solar limb is on the right y-axis of each panel (i.e., of each disk position).

Note that the radiative effects due to a oblique line of sight are present in the figures, although the foreshortening observed in the Sun due to the perspective effect is not. For further analysis this effect will have to be artificially introduced by means of rebinning the images to the desired sizes in order to make them comparable with the real observations.

In figures 5.11 and 5.10 for μ=0.1, an inversion of the contrast occurs. When looking to the response functions presented in figure 5.5, section 5.1.5 for the semi-empirical model of Rodríguez Hidalgo et al. (1995) at λ6708 Å this can be easily understood. The main contribution for this heliocentric angle comes from z$\sim$170 km, where the temperatures of granules and intergranules in this model cross (see figure 5.3), and an inversion occurs from there upwards. When looking to the velocities in the model of Rodríguez Hidalgo et al. (1995) it can be found that, for z larger than 170 km up-flows are colder than down-flows.

Application to theoretical models

The 3D models of Stein & Nordlund (2000) produce time series of the granulation with a field of view of 8.14 x 8.14 arcsec^2 (see Table 5.2). We only have a single snapshot, and therefore certain statistical analysis on the morphological properties of granulation will not be performed due to the lack of statistical significance. However, a lot of information can be obtained from this model.

In figure 5.12 the emergent intensity of the SN model at λ6708 Å, for μ=1,

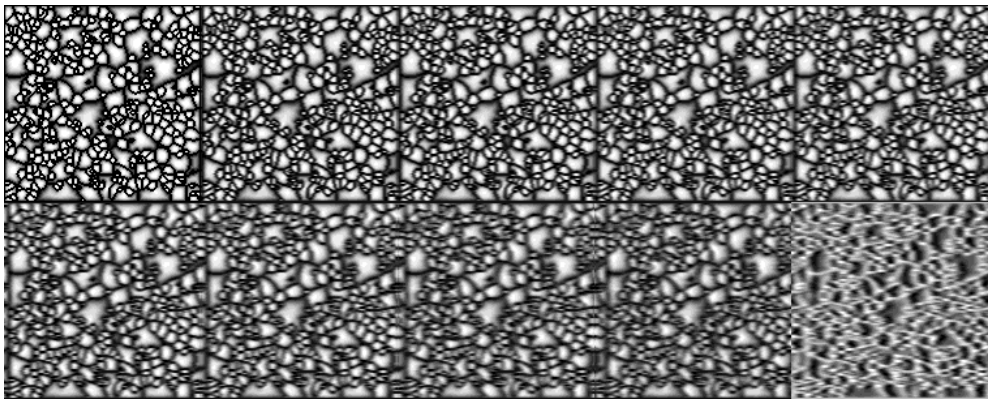

FIGURE 5.10— Synthetic emergent intensity of the RHL model at λ6708 Å for μ=1., 0.9, 0.8, 0.7, 0.6, 0.5, 0.4, 0.3, 0.2, 0.1 (panels from left to right and from top to bottom).

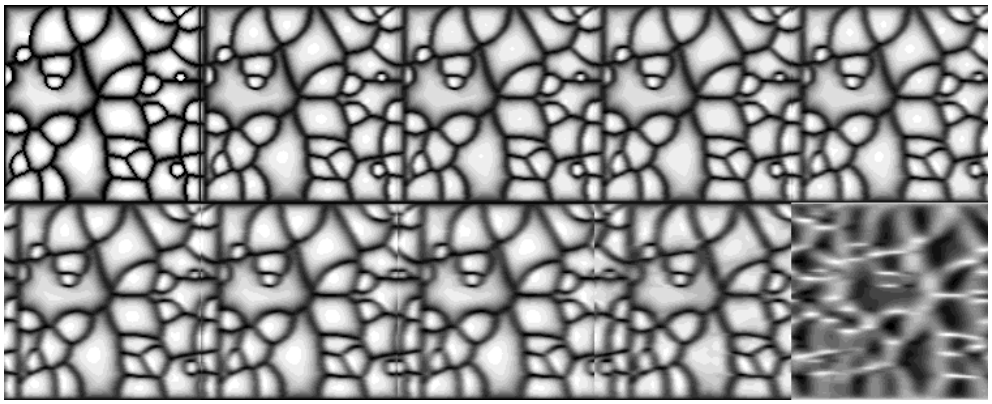

FIGURE 5.11— Synthetic emergent intensity of the RHH model at λ6708 Å for μ=1., 0.9, 0.8, 0.7, 0.6, 0.5, 0.4, 0.3, 0.2, 0.1 (panels from left to right and from top to bottom)..

0.9, 0.8, 0.7, 0.6, 0.5, 0.4, 0.3, 0.2, 0.1 is presented.

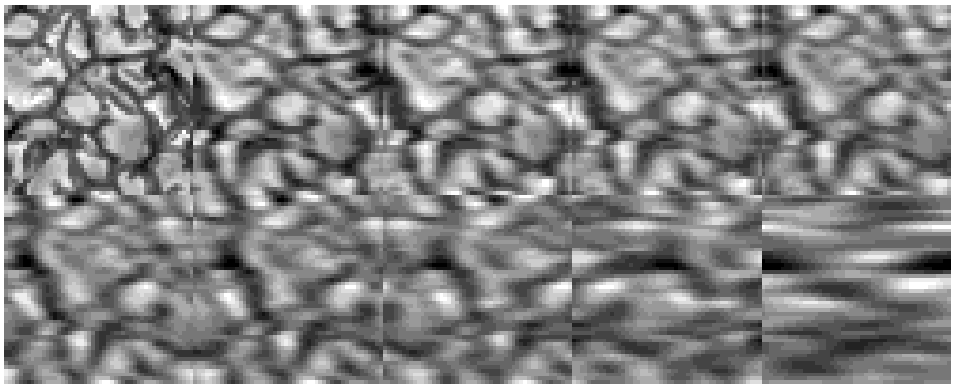

FIGURE 5.12— Synthetic emergent intensity in the 3D models of Stein & Nordlund (2000) at λ6708 Å for μ=1., 0.9, 0.8, 0.7, 0.6, 0.5, 0.4, 0.3, 0.2, 0.1 (panels from left to right and from top to bottom)..

In Figure 5.12 the radiative effects get progressively more important from the center to the limb, where the structures are very elongated and hard to recognize. As will be shown in section 5.2.5, the radiative transfer effects are more efficient at small spatial scales. The fact that in the SN model granules show internal structure which is resolved with the pixelsize of 0.16 arcsec, makes the radiative effects to be more effective in this model than in the semi-empirical ones shown in figure 5.10 and 5.11. Besides, the size distribution of the SN model differs from the one observed on the Sun. In figure 5.13 the histogram of cell areas in the SN model is presented (right panel, solid line). For the sake of comparison the cell area histogram observed (see chapter 2) is also plotted in the right panel sampled with a small amount of size bins in order to make it comparable to the cell size histogram in the SN model. Left panel presents the observed cell size histogram as shown in chapter 2. Note that the cell sizes in the SN model are smaller than those observed on the Sun which would also cause the radiative transfer effects to be more efficient in the SN models than in the semi-empirical ones.

The models of Gadun (1995) are bidimensional, however we have the whole temporal series of them which lasts 264 minutes of physical time for the 35KM models and 92 minutes for the 15KM ones. The 15KM models have a spatial field of 2.3 arcsec and a pixelsize of 0.02 arcsec and the 35KM models of 4.6 arcsec and a pixelsize of 0.04 (see Table 5.2). This means that, specially the 35KM models, have a statistical significance which allows a study on granular

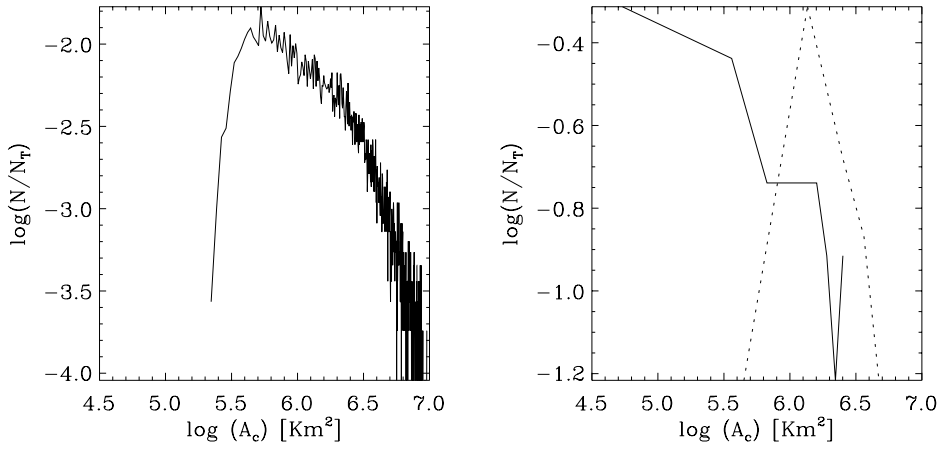

FIGURE 5.13— Histogram of cell areas observed at λ6708 Å (left panel), computed in the SN model (right panel solid line), and observed sampled with a small amount of size bins (right panel dotted line).

properties such as contrast, granular filling factor, etc. Since granulation is a stationary phenomenon and statistically isotropic, we can make the ergodic assumption which states that the statistical properties deduced from a one-dimensional cut of the granulation over time are comparable to the statistical information deduced from a two-dimensional image of granulation.

In order to compute the emergent intensity of these models we have used the 2D radiative transfer code developed by A. Gadun at the Kiev University.

In figure 5.14 the 35KM model (left panels) and 15KM model (right panels) are presented for μ=1, 0.9, 0.8, 0.7, 0.6, 0.5, 0.4, 0.3, 0.2, 0.1. at λ6708 Å. The temporal direction (horizontal axis) is constructed by plotting models every 30 s. Since the 15KM model has a smaller spatial direction, fewer granules fit in the computational domain, although their structure is sampled with greater detail.

5.2 CLV of the granular contrast

5.2.1 Influence of the factors degrading solar observations

In order to compute the CLV of the granular contrast in a way that is directly comparable to the CLV observed in the Sun, the conditions of the real observations must be reproduced as accurately as possible. The fact that we can introduce the different factors that affect granulation observations separately

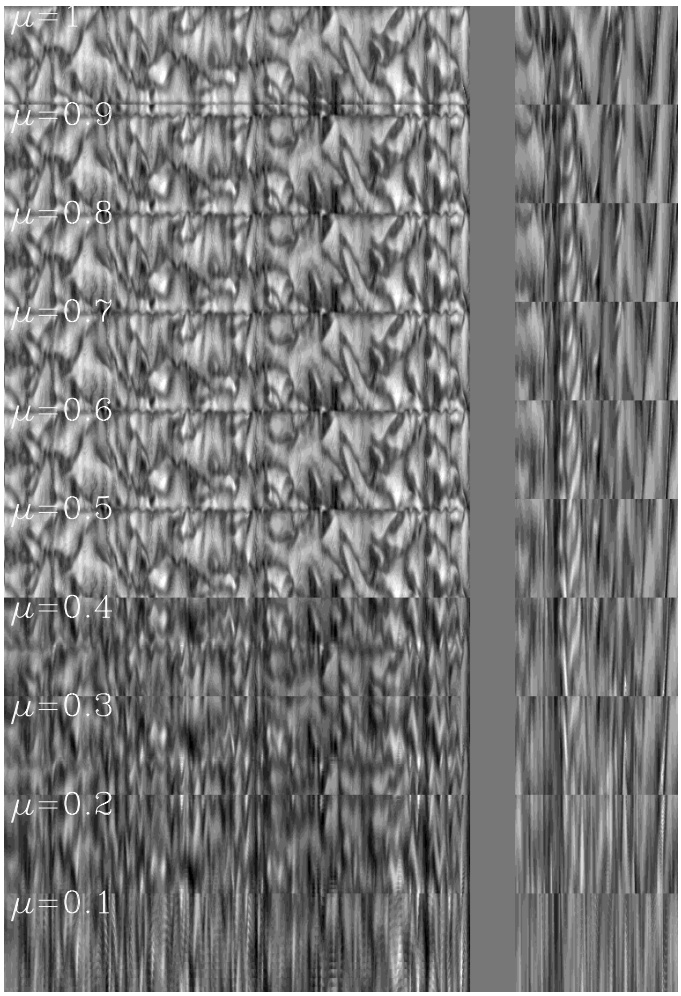

FIGURE 5.14— Synthetic emergent intensity in the 35KM models (left panels) and 15KM models (right panels) of Gadun (1995) at λ6708 Å at μ=1., 0.9, 0.8, 0.7, 0.6, 0.5, 0.4, 0.3, 0.2, 0.1. x-axis is the temporal direction, y-axis the spatial direction. Both sets of models are sparated by a broad vertical gray band.

allows also to perform a study of their effects on the observations.

On real granulation observations the images are affected by foreshortening, telescope diffraction, telescope aberrations and degradation due to the terrestrial atmosphere. After the images are acquired, they are usually corrected for the instrumental profile of the telescope (in our case 50 cm of aperture) assumed diffraction limited. Therefore, to compare synthetic granulation images with images only corrected for diffraction, the raw emergent intensity images from the models must be foreshortened and then degraded by the earth atmosphere and telescope aberrations.

The degradation caused by atmospheric turbulence and telescope aberrations has been simulated as the effect produced by a certain perfect telescope. However, it is known that the earth atmosphere influences differentially at different spectral ranges. In long-exposure images the effect of the atmospheric turbulence can be approximately represented by the degradation caused by a perfect telescope of diameter r_o (the Fried parameter) which varies with wavelength as $r_o \propto \lambda^{6/5}$. Here we use the same approximation, which considers the wavelength dependence, to reproduce the atmospheric degradation. However, it is true that our case consists of short-exposure images taken in moments of very good seeing; consequently the expected atmospheric PSF has to be much narrower than that corresponding to long-exposure. We justify the use of the model for long-exposure PSF in our simulations, simply by overestimating the value of r_o and considering that also the telescopic aberrations are included in the model. Typically, under good seeing conditions, r_o ~45 cm at λ15500 Å. Then, we will initially represent the atmospheric plus telescope aberrations in short exposure with a telescope of an aperture larger than twofold 45 cm (100 cm at λ15500 Å) which, accordingly to the law $r_o \propto \lambda^{6/5}$, gives 36.6 cm at λ6708 Åand 45.22 cm at λ8000 Å. Naturally, in simulations with $r_o \geq 50$ cm we also impose a cutoff frequency at the diffraction limit of the telescope employed in our observations (50 cm aperture). Besides, in following sections a study will also be performed on how do variable atmospheric conditions, simulated by telescopes of smaller apertures, modify the obtained granular properties. *Hereafter, images degraded simulating the effect of the earth Atmosphere and Telescope Aberrations will be refered to as degraded by ATA.*

In some cases the Modulation Transfer Function (MTF) characterizing the earth atmosphere and telescope aberration can be estimated empirically and the images restored of its effect. In these cases, to compare synthetic granulation images with images of the real Sun restored of earth atmosphere perturbations, it is necessary to rebin the synthetic images to simulate the foreshortening and simply to apply a low pass band filter with cutoff at the diffraction limit of the telescope to simulate the irrecoverably lost frequencies. Table 5.3 presents the

TABLE 5.3— 50 cm telescope cutoff frequencies

Wavelength [Å]	ν_{cutoff}[arcsec^{-1}]	k_{cutoff}[Mm^{-1}]
6708	3.62	31.37
8000	3.13	27.12
15500	1.62	14.04

cutoff frequencies and wavenumbers for the 50 cm telescope and the wavelengths used in the observations. *Hereafter, the images only degraded with this Low Pass Band Filter will be refered to as degraded by LPBF.*

Semi-empirical models

Figure 5.15 presents the CLV curves of the granulation contrast of the RHL model at λ6708 Å (upper panels), λ8000 Å (middle panels) and λ15500 Å (lower panels). An arbitrary color code has been used to facilitate comparison. The meaning of the different line styles is: Solid black line–contrast of emergent intensity, dashed magenta line– contrast of artificially foreshortened images, three dot-dashed blue line– contrast of foreshortened images and degraded by ATA, long dashed green line– contrast of the images foreshortened and degraded by LPBF. Left panels show the absolute values of the granular contrast CLV and right panels show the CLV normalized to the value at μ=0.9. Note that the CLV curves have a different slope in the drop of contrast for μ=1–0.9 than for $\mu \leq$0.9. This difference can be caused by the lack of spatial resolution in the model since, as will be shown below, the RHL and SN models show this difference while the RHH, 35KM and 15KM models do not. Therefore, all the curves are normalized to the value at μ=0.9 to enable a comparision of the CLV of the granular contrast for $\mu \leq$0.9 free of the effect of this artifact.

Even tough the Rodríguez Hidalgo et al. (1995) models have been computed without correcting for the degradation due to earth atmosphere, in this section they are degraded by ATA and by LPBF to check the effects that these degradations produce qualitatively in the CLV curves. However, for further comparison with the observational CLV curves only the foreshortened and degraded with LPBF images will be used.

The obtained absolute contrast for the RHL model at disk center is of 8.2% (λ6708 Å), 6.7% (λ8000 Å) and 3.7% (λ15500 Å) in the raw emergent intensity images. This values are in reasonable agreement with our observations: 9.6% at λ6708 Å (images corrected from telescope and earth atmosphere degradation), 6.1% at λ8000 Å and 2.9% at λ15500 Å(both corrected for the MTF of the

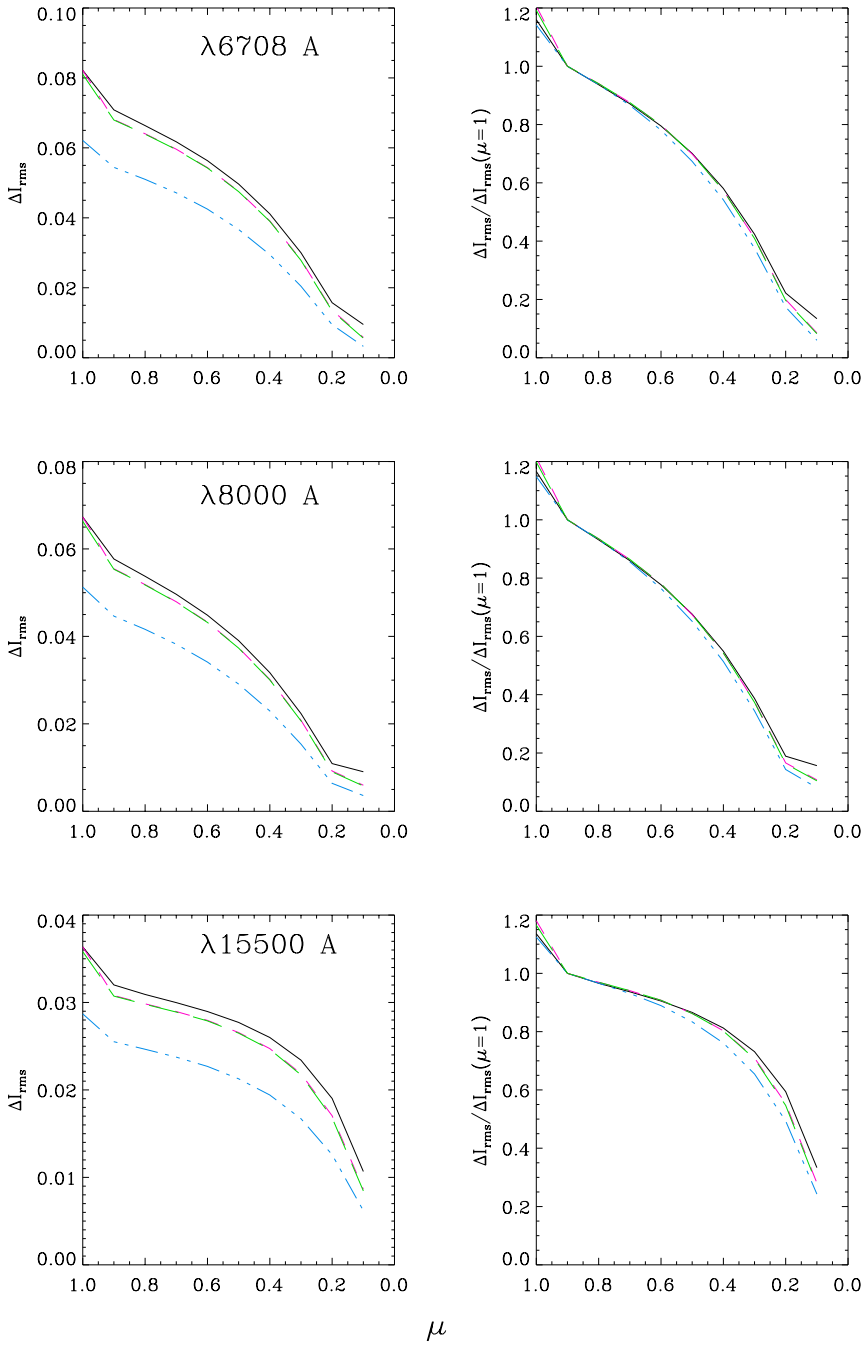

FIGURE 5.15— CLV of granulation contrast computed in the RHL model at λ6708 Å (upper panels), λ8000 Å (middle panels) and λ15500 Å (lower panels). Solid black line–contrast of emergent intensity, dashed magenta line– contrast of artificially foreshortened images, three dot-dashed blue line– contrast of foreshortened images and degraded by ATA, long dashed green line– contrast of the images foreshortened and degraded by LPBF. Left panels show the absolute values of the granular contrast CLV and right panels show the CLV normalized to the value at μ=0.9.

telescope assumed diffraction limited).

One secondary effect of rebinning the images to the correct size to simulate the foreshortening observed on the Sun is to reduce a little the absolute contrast, but the shape of the CLV curve is not modified significantly. When, in addition, the images are degraded by ATA a larger loss of absolute contrast is found. However, at λ6708 Å the cutoff frequency of the telescope simulating degradation due to the terrestrial atmosphere (Ø36.6 cm) is larger than the Nyquist frequency of the RHL model and therefore the loss of contrast is not so significative as expected. Similarly, at λ8000 Å (ATA with Ø45.22) the same effect takes place. At λ15500 Å in order to simulate the loss of high frequencies caused by the diffraction limit of the telescope used in the observations, the cutoff frequency is given by the observing telescope of 50 cm aperture and not by the diameter used to simulate ATA (Ø100 cm). In this case, the cutoff frequency and the Nyquist frequency are very similar, which causes the relative loss of absolute contrast to be more significant. On the other hand, the comparison of the Nyquist frequency in the RHL model and the cutoff at the different wavelengths of the telescope used for observations (see tables 5.2 and 5.3) justifies why foreshortened images degraded by LPBF do coincide with the only foreshortened raw intensity images and therefore the long dashed and the dashed line in figure 5.15 to be equal.

For all the studied wavelengths the effect of foreshortening and degradation by LPBF or by ATA does not change in a significant manner the shape of the CLV curve at λ6708 Å and λ8000 Å (this is due, as explained above, to the cutoff frequencies of the telescope at these wavelengths, which are larger than the Nyquist frequency). But at λ15500 Å the foreshortening and degradation by LPBF increases slightly the gradient of the normalized contrast decrease. Foreshortening and degradation by ATA causes the normalized contrast drop to be steeper for large heliocentric angles than in the raw emergent intensity images.

In the CLV curves at λ6708 Å and λ8000 Å the decrease of contrast tends to stabilize at μ=0.2. This can be understood by looking to the response functions to the temperature of the model of Rodríguez Hidalgo et al. (1995), section 5.1.5. They show for these wavelengths and for μ=0.2–0.1 their maximum contributions near z=150 km, where a crossing point between the temperature of granules and intergranular lanes occurs.

Theoretical models

In figure 5.16 the CLV of the granular contrast of the SN model for different degradations is presented, with left and right panels and line styles and colors

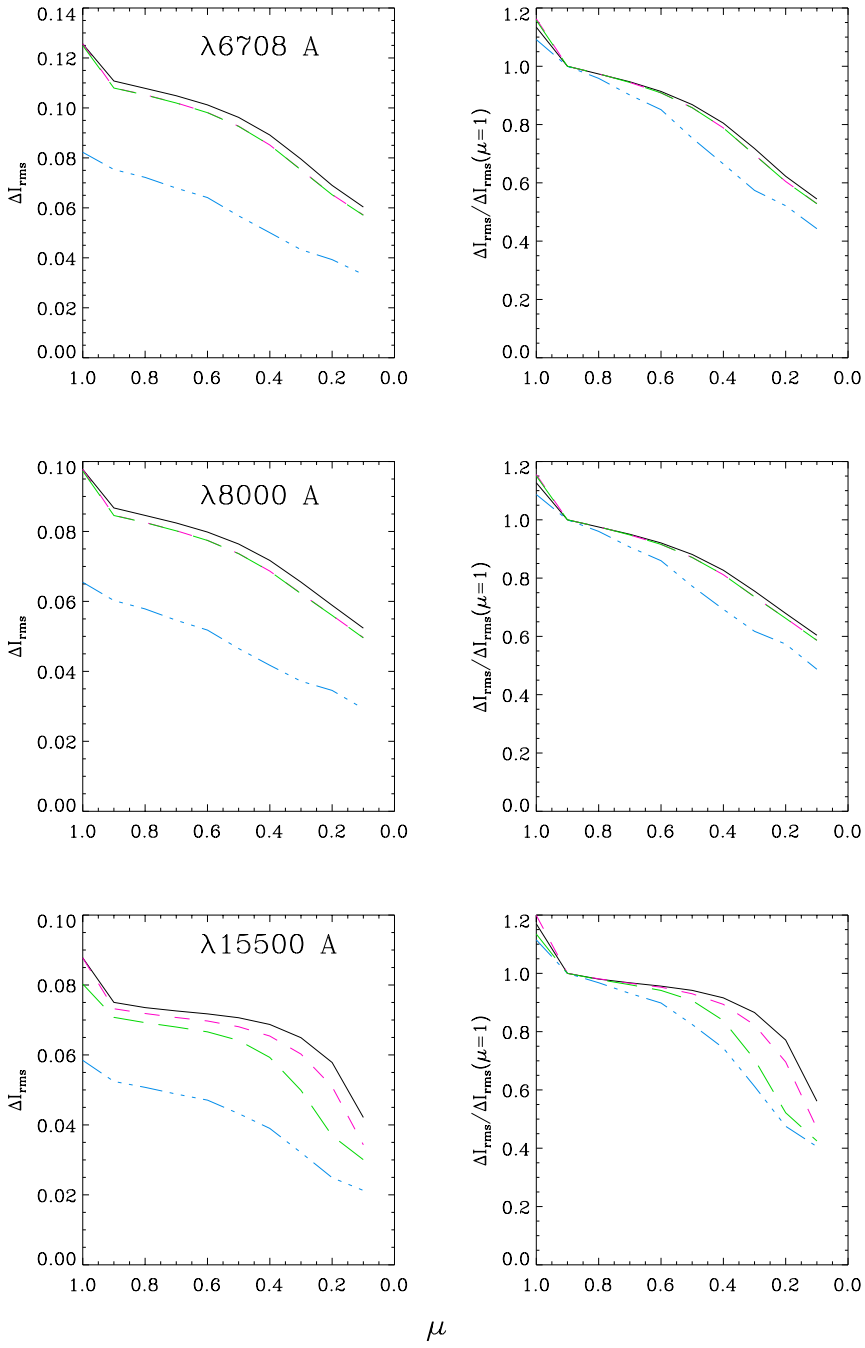

FIGURE 5.16— CLV of synthetic granulation contrast in the SN model at λ6708 Å (upper panels), λ8000 Å (middle panels) and λ15500 Å (lower panels). Solid black line–contrast of emergent intensity, dashed magenta line– contrast of artificially foreshortened images, three dot-dashed blue line– contrast of foreshortened images and degraded by ATA, long dashed green line– contrast of the images foreshortened and degraded by LPBF. Left panels show the absolute values of the granular contrast CLV and right panels show the CLV normalized to the value at μ=0.9.

with the same meaning as in figure 5.15. Note in the upper and middle panels that the long-dashed lines coincide with the dashed ones. In the case of λ6708 Å this is due to the fact that the Nyquist frequency of the SN model is smaller than the telescope cutoff frequency at this wavelength, while at λ8000 Å they are similar (see Table 5.2 and 5.3). This implies that there is no significant loss of power at frequencies higher than the telescope cutoff. However, at λ15500 Å there is a significative loss of contrast in high frequencies since the Nyquist frequency is larger than the telescope cutoff.

The absolute values obtained in the raw emergent synthetic granulation contrast at disk center are 12.5% (λ6708 Å), 10% (λ8000 Å) and 9% (λ15500 Å). When the images are degraded by ATA the values of the contrast are 8.2% (λ6708 Å), 6.5% (λ8000 Å) and 5.8% (λ15500 Å). This values are smaller at short wavelengths and larger at large wavelengths than in our observations: 9.6% at λ6708 Å (images corrected for telescope and earth atmosphere degradation), 6.1% at λ8000 Å and 2.9% at λ15500 Å(both corrected for the MTF of the telescope assumed diffraction limited).

As seen in the figure 5.16, the effect of applying foreshortening to the emergent intensity images is to decrease slightly the absolute values of the contrast, altough no significant change in the shape of the CLV curve is introduced. However, when both foreshortening and degradation by ATA are included, the normalized contrast decreases in the steepest way. In general, the different factors that influence solar observations affect this model in the same way as in figure 5.15 for the semi-empirical model.

The shape of the CLV curve is similar in the RHL model and in the SN one. Nevertheless, surprisingly, in the SN model the normalized contrast does not decrease so significantly from the center to the limb as in the semi-empirical models. This can probably be attributed to the increase of the temperature fluctuations between granules and intergranular lanes with height in the photosphere in the SN model for a large portion of the range where the observed radiation comes from (see figure 5.8, left panel).

The CLV of the granulation contrast has also been computed for the 2D models of Gadun (1995). Figure 5.17 presents the obtained CLV of the granulation contrast computed for the 15KM models and for the 35KM models. The meaning of the linestyles, colors and left and right panels is the same as in figure 5.16.

The values of contrast at disk center for raw intensity images in the models of Gadun are of 13% (λ6708Å) and 10.5 % (λ8000 Å) in the 15KM models and 15% (λ6708Å) and 12 % (λ8000 Å) in the 35KM models. When the images are degraded by ATA the contrast decreases to 10.2% (λ6708Å) and 8.1% (λ8000 Å) in the 15KM models and to 12.5% (λ6708Å) and 10% (λ8000 Å) in the 35KM

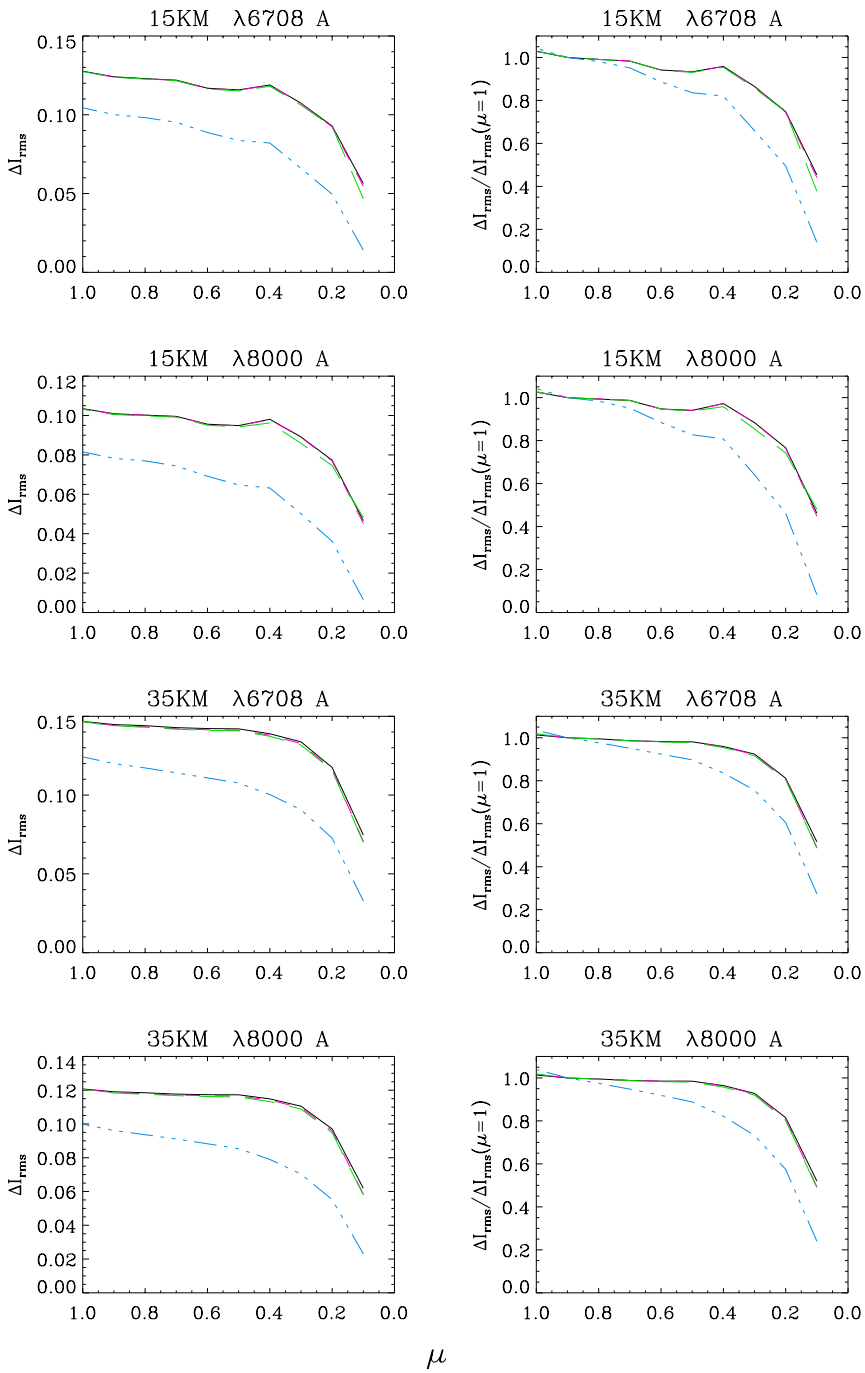

FIGURE 5.17— CLV of synthetic granulation contrast in the 15KM models at λ6708 Å , and λ8000 Å and in the 35KM models at λ6708 Å , and λ8000 Å . Left panels show the absolute values of the contrast, right panels the contrasts normalized to the value at μ=0.9. Solid black line–contrast of emergent intensity, dashed magenta line– contrast of artificially foreshortened images, three dot-dashed blue line– contrast of foreshortened images and degraded by ATA, long dashed green line– contrast of the images foreshortened and degraded by LPBF.

models. The contrasts of the 15KM models fit better our observed values than those of the 35KM models. However, it must be noted that the 15KM model has less statistical significance than the 35KM model since its time series is shorter and its field of view is of only 2.3 arcsec, and the contrast is mainly a statistical parameter.

Note that the contrast of the raw emergent intensity of the 15KM models decreases, for both wavelengths, very smoothly from the center to μ=0.4, with a stronger decrease for $\mu \leq$0.4, while for the 35KM model the contrast decreases smoothly up to μ=0.3, and more steeply for $\mu \leq$0.3. When the images are rebinned to simulate foreshortening, the shape of the CLV stays mainly unchanged. When foreshortening and degradation by ATA are included, the steepest decay is obtained in both models. This tendency is the same as the one shown by the SN and semi-empirical models studied above and, therefore, we could conclude that, independently of the model atmosphere or geometry used for the computations, the effect of including the foreshortening and the degradation in the raw emergent intensity images is to cause a steeper decrease of the normalized contrast. Independently of the CLV obtained from the raw emergent intensity images, after applying the conditions of the observations (i.e., foreshortening and degradation by ATA) it is detected as a steeper decrease.

5.2.2 Influence of the working wavelength range

The wavelength dependence of the different factors that influence granular observations has also been studied.

It has been obtained for the RHL model that the λ15500 Å CLV presents smaller slopes than the other wavelengths up to $\mu \sim$0.2–0.3, and the λ8000 Å a slightly steeper decrease than the λ6708 Å. These characteristics keep constant independently of the effect applied on the images to simulate the real observations conditions. In chapter 3 it was shown that the effect of mere foreshortening and telescope cutoff caused the CLV curves to decrease more steeply for longer wavelengths (section 3.2.1). Therefore, the tendency observed must be caused by the stratification of the model atmosphere of Rodríguez Hidalgo et al. (1995) together with the radiative transfer effects and is not caused by perturbative observational factors. The effect of foreshortening and degradation by ATA is to reduce the differences between the CLV curves at the various studied wavelengths as compared to the differences between different λ of the curves computed on the raw emergent intensity images.

The CLV of synthetic granulation contrast in the SN model decreases steeper up to $\mu \sim$0.2–0.3 for shorter wavelengths in the raw emergent intensity images, and the effect of foreshortening is to keep this trend. However, when both

foreshortening and degradation by ATA are included together, the tendency is modified, this is, for λ15500 Å the decrease of contrast is the steepest while for λ6708 Å the contrast decreases slightly steeper than for λ8000 Å.

For the 35KM models, there is essentially no difference between the CLV curves at λ6708 Å and λ8000 Å neither in the raw emergent intensity images nor when the factors affecting solar observations are taken into account. The 15KM models show steeper decreases at λ6708 Å than at λ8000 Å for the raw emergent intensity images. However, when the effect of foreshortening and degradation by ATA is introduced the tendency is inverted. This is similar to what happened in the SN models where the curve at λ15500 Å had the same trend.

Comparing the obtained trends we can conclude that the wavelength dependence of the slope of the decrease of the granulation contrast from disk center to the limb is dependent on the specific stratification of the physical parameters in the model atmospheres used. And, even though the effect of foreshortening and degradation by LPBF is to cause a larger contrast decrease for longer wavelengths, the specific stratification and geometry of the atmosphere together with the radiative effects have a more important role which is very sensitive to the details of the distribution. Therefore, no common pattern can be deduced. Moreover, intending to find a common trend, like in table 2.2 of chapter 2, is a difficult task, since the differences in the statistical significance of the different observations, spatial resolutions, observing methods and image treatment methods modify in a very significative manner the wavelength dependence of the CLV curves of granular contrast.

5.2.3 Influence of the geometry model

In figure 5.18 we present the same curves as in figure 5.15 but computed for the RHH model. Note that the shape of the CLV curves is remarkably similar to those shown in figure 5.15. This is due to the fact that, even though the high resolution geometry has less elements of population in the granulation cell size histogram, the total distribution is essentially the same.

However several differences are visible between figure 5.18 and 5.15. On the one hand the absolute values of the granulation contrast are slightly smaller at disk center (7.8% at λ6708 Å, 6.4% at λ8000 Å and 3.4% at λ15500 Å) . These marginal differences in the contrast values can be due to the specific granules included in this box which have less statistical significance in the RHH than in the RHL model. . On the other hand, the variation of the slope of the contrast drop between μ=1–0.9 and $\mu \leq$0.9 is not present in the RHH model, which can be probably attributed to the higher spatial resolution of this model

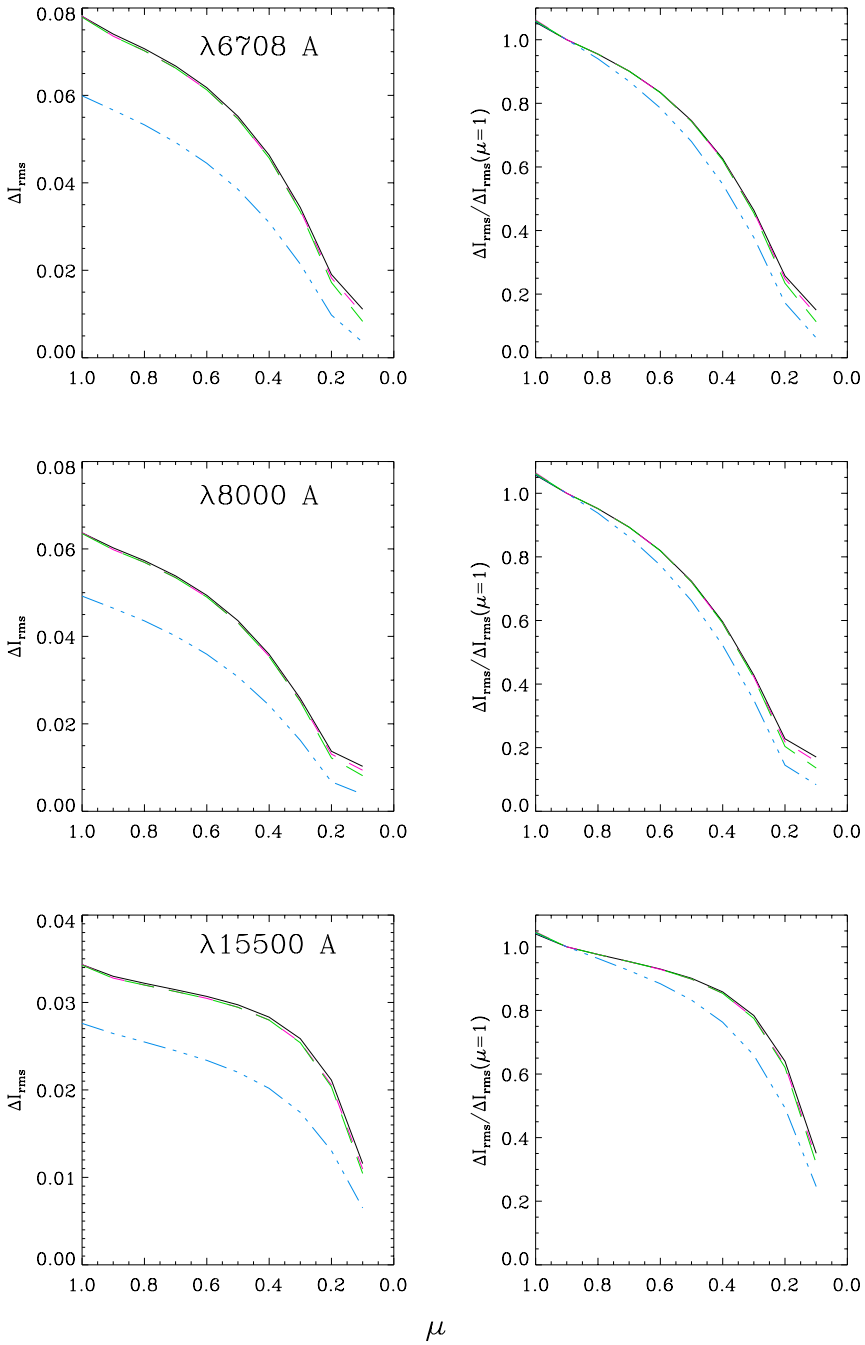

FIGURE 5.18— CLV of granulation contrast computed in the RHH model at λ6708 Å (upper panels), λ8000 Å (middle panels) and λ15500 Å (lower panels). Solid black line–contrast of emergent intensity, dashed magenta line– contrast of artificially foreshortened images, three dot-dashed blue line– contrast of foreshortened images and degraded by ATA, long dashed green line– contrast of the images foreshortened and degraded by LPBF. Left panels show the absolute values of the granular contrast CLV and right panels show the CLV normalized to the value at μ=0.9.

In the RHH model the effect of applying foreshortening to the raw emergent intensity images does not change the obtained CLV curves. This could be due to the high spatial resolution, which causes the large structures that contribute mainly to the contrast to remain visible up to large heliocentric angles. In the low spatial resolution geometry these structures occupied less pixels and, therefore, resizing to simulate foreshortening produced mixing of information due to the averaging performed in the rebinning process.

The effect of foreshortening and degrading the emergent intensity images by LPBF does not change the CLV curves at λ6708 Å and λ8000 Å, although the Nyquist frequencies of this model at these wavelengths are larger than the telescope cutoff frequencies. In section 5.3. the power spectra of the RHH model are studied. In the foreshortened images the power drops to noise level at $\nu \sim 30$ Mm^{-1}, wich approximately corresponds to 3 arcsec^{-1}. This frequency is very similar to the cutoff frequency of the telescope at λ6000 Å and λ8000 Å. Therefore, the degradation by LPBF does not affect significantly the CLV curves at these wavelengths in figure 5.18. The power spectra of the RHH model drops to noise level at 3 arcsec^{-1} due to the lack of inner granular structures in this model. Furthermore, a small amount of granules is generated in the high resolution geometry computing box, which causes very less granular cells of small scales to be included in the model.

As seen in figure 5.18 the effect of applying foreshortening and degrading by ATA is to produce a steeper decrease of the contrast at all heliocentric angles.

Comparing figure 5.15 and 5.18 we can conclude that the specific shape of the CLV curve does not change very significatively if the high or low spatial resolution model geometry is used. The most significative change is the different slope of the contrast drop between μ=1–0.9 and $\mu \leq 0.9$ observed in the low resolution models which does not appear in the high resolution ones. Note also that the effect of foreshortening and degrading by ATA affects in the same manner the CLV curves independently of the resolution of the model atmosphere used. The effect of applying the different factors that affect solar granulation observations does not change in any dramatic way the shape of the CLV curve. Essentially they introduce a steeper decay of the contrast from the center to the limb and make the CLV curves to be more similar between the different wavelengths in the degraded than in the raw emergent intensity images.

5.2.4 Influence of different atmospheric conditions

Semi-empirical models

It is interesting to study how do the differences in image quality or spatial resolution affect the obtained CLV curves. We have simulated it by using the

images obtained from the RHH model. These images are foreshortened and degraded by ATA simulated by MTFs of telescopes with different diameters. Three diferent atmospheric conditions have been chosen, each characterized by a telescope diameter of 100 cm, 75 cm and 50 cm at λ15500 Å, respectively. The aperture of the telescope at the other studied wavelengths has been obtained by means of the relation $r_o \propto \lambda^{6/5}$. In figure 5.19 we present the obtained CLV curves, noramlized to the value at μ=0.9, created by degrading with the MTF of a 100 cm (solid line), 75 cm (dotted line) and 50 cm (dashed line) diameter telescope at λ15500 Å. Left panel present the curves at λ6708 Å, middle panel at λ8000 Å and rigth panel at λ15500 Å. It can be seen in the figure that the effect of augmenting the ATA is to increase the steepness of the CLV curve as the telescope diameters used for the simulation become smaller. When the same test is applied to the low spatial resolution model geometry a similar trend is found.

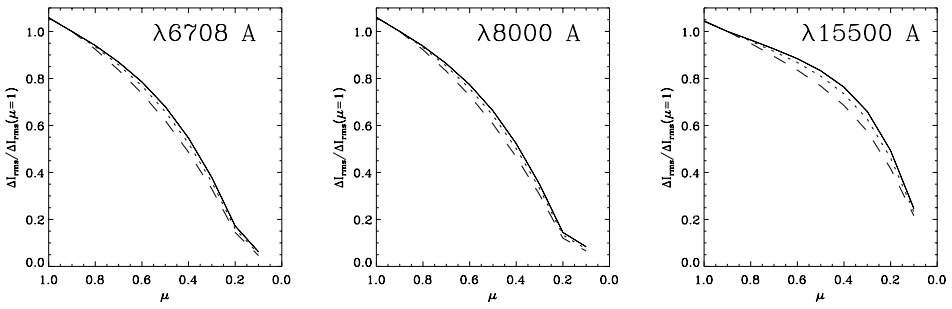

FIGURE 5.19— CLV of the synthetic granulation contrast of the RHH model normalized to the value at μ=0.9 at λ6708 Å (left panel), λ8000 Å (middle panel) and λ15500 Å (right panels) degraded with a theoretical MTF of a 100 cm (solid line), 75 cm (dotted line) and 50 cm (dashed line) diameter telescope at λ15500 Å.

In general, we can conclude that for these semi-empirical models the change of atmospheric conditions affects less the shape of the CLV curve than the simulation of the factors that influence solar observations such as foreshortening and degradation by ATA. This is, the shape of the CLV curves is more similar in case of two images degraded with a 100 cm and a 50 cm ATA at λ15500 Å than in the case of the raw emergent intensity images and those degraded with a 100 cm ATA at λ15500 Å.

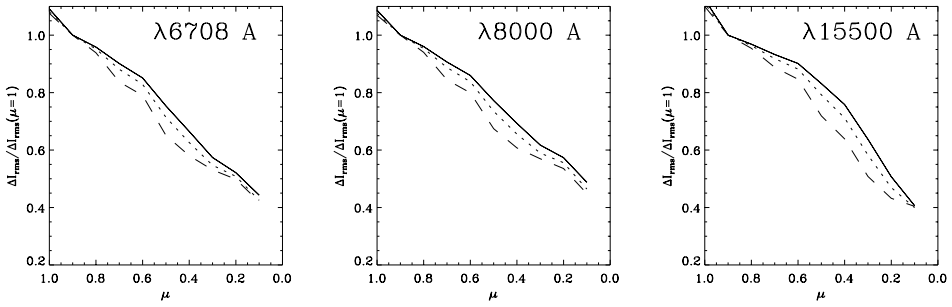

FIGURE 5.20— CLV of the synthetic granulation contrast of the SN model normalized to the value at μ=0.9 at λ6708 Å (left panel), λ8000 Å (middle panel) and λ15500 Å (right panels) degraded with a theoretical MTF of a 100 cm (solid line), 75 cm (dotted line) and 50 cm (dashed line) diameter telescope at λ15500 Å.

Theoretical models

Following the same procedure, the influence of different atmospheric conditions on the theoretical models has been tested. Figure 5.20 shows the computed CLV curves for the SN model. The meaning of the different linestyles is the same as in figure 5.19. We obtain that, for smaller telescope diameters simulating different conditions of ATA, the contrast decreases more steeper.

The influence of different atmospheric conditions on the 2D models is shown in figure 5.21. The images are degraded with telescopes of different diameters as in figure 5.20, and the meaning of the different line styles is the same as in that figure. Note that for the 15KM models a similar trend as the one found for the SN and RHH models is obtained: for every disk position the slope of the contrast drop increases for smaller telescope diameters.

5.2.5 Influence of the distribution of granular areas

It is known that the radiative effects are more effective at shorter spatial scales than at larger ones. It is interesting to make a simple exercise to illustrate qualitatively how a general decrease of the granular areas affects the resulting CLV curve of the granular contrast. The radiative transfer code has been applied to a box of simulated granulation constructed following the method described in section 5.1.2 with the model atmosphere of Rodríguez Hidalgo et al. (1995). In various computational runs, different pixel sizes of different values have been assumed for this box, which is equivalent to shift the granular cell size histogram to smaller or larger granular cell areas. This produces computing

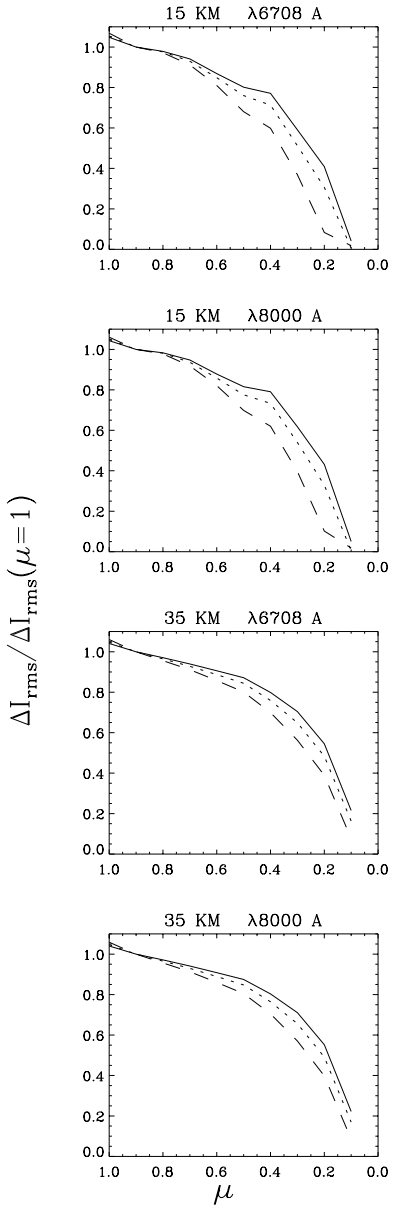

FIGURE 5.21— CLV of the synthetic granulation contrast of the 15KM models at λ6708 Å , λ8000 Å and the 35KM models at λ6708 Å, λ8000 Å (lower panels) degraded with a MTF of diffraction limited telescope of different diameters at λ15500 Å: 100 cm (solid line), 75 cm (dotted line) and 50 cm (dashed line).

boxes of various fields of view. This experiment has been performed for a range of pixel sizes. Here we present only two extreme cases (very large granules, and very small ones) together with the real granular sizes with the aim to illustrate the obtained trends. The computed emergent intensities are shown in figure 5.22. The pixel sizes in each panel are: a) 2.8 arcsec, b) 0.28 arcsec, c) 0.028 arcsec. The pixel size of panel b) corresponds to the real size histogram observed on the Sun, but with a small amount of elements of population in the histogram, due to the few granules included in the box. For each panel the radiative transfer computations have been performed at μ=1., 0.9, 0.8, 0.7, 0.6, 0.5, 0.4, 0.3, 0.2, 0.1 (from left to right, and top to bottom) at λ6708 Å.

In Figure 5.22 it can be clearly appreciated that, for oblique lines of sight, the radiative effects get progressively more effective for smaller pixel sizes. However, for μ=1 all the images have a similar emergent intensity. To understand this point it must be taken into account that the horizontal spatial dimension of the box has been changed but the vertical one not. Besides, the geometry is the same for every geometrical depth, and the radiative transfer computations assume LTE. Therefore, at μ=1 no cancellations are produced by a light ray crossing several structures. However, for larger heliocentric angles this effect gets progressively more important.

The CLV curves of the granulation contrast for the models presented in figure 5.22 have been computed. In figure 5.23 the obtained curves are presented. The fact that for every pixel size the contrast amounts the same value at disk center can be explained by the same effect which caused in figure 5.22 the emergent intensities at μ=1 to be equal for every panel. From μ=1 to μ=0.9 a strong decrease of the contrast is obtained for the models with small pixel sizes. This is due to the radiative effects produced by light rays crossing several small granular and intergranular structures, which suggest cancellations. For larger heliocentric angles the decrease is smoother. The total loss of contrast from the center to the limb is larger for decreasing pixel sizes.

5.2.6 Influence of the temperature stratification

Temperature is the physical quantity most directly related to the granular contrast. The study of the CLV curves of the granular contrast allows to infer information about the temperature stratification in the solar photosphere. In order to be able to interpret the obtained curves, tests have been performed on the influence of different temperature stratifications on the CLV curves. To that aim, the semi-empirical models of a mean granule and intergranule of Rodríguez Hidalgo et al. (1995) have been modified with a linear perturbation to obtain temperature stratifications of different characteristics. In order

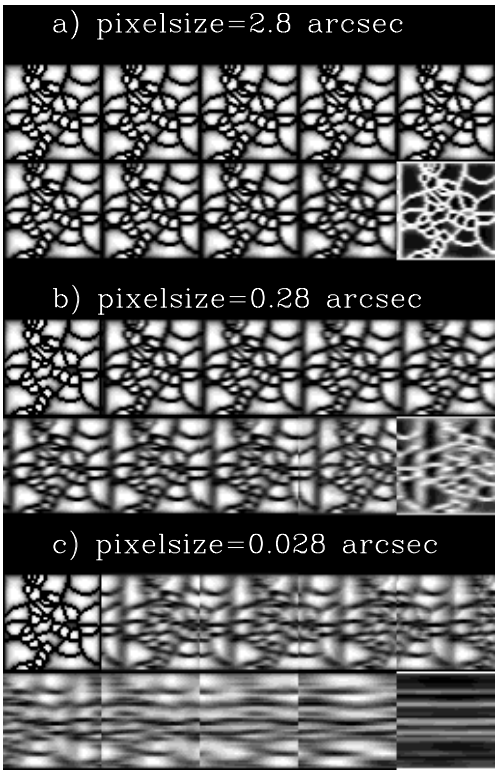

FIGURE 5.22— CLV of the synthetic emergent intesity applied to the same geometry varying the pixel size: panel a)– pixelsize of 2.8 arcsec, panel b)– pixelsize of 0.28 arcsec, panel c)– pixelsize of 0.028 arcsec. Each panel contains, from left to right and from top to bottom computations at μ=1., 0.9, 0.8, 0.7, 0.6, 0.5, 0.4, 0.3, 0.2, 0.1 at λ6708 Å.

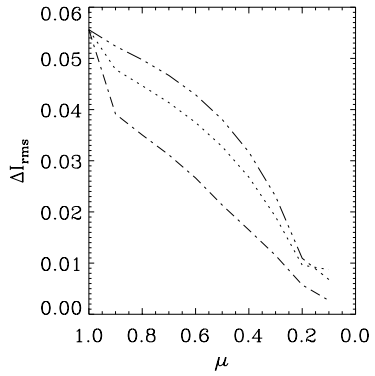

FIGURE 5.23— CLV of the granular contrast at λ6708 Å computed on the synthetic emergent intesity of the geometries presented in figure 5.22: three dotted dashed– pixelsize of 2.8 arcsec, dotted– pixelsize of 0.28 arcsec, dotted dashed – pixelsize of 0.028 arcsec.

to preserve physical consistency it is necessary to recompute the Hydrostatic Equilibrium equations for the new temperature stratification in order to have all the physical quantities in equilibrium.

These new atmospheric models computed by perturbing the Rodríguez Hidalgo et al.(1995) model have been applied to the high spatial resolution geometry described in section 5.1.6. Then, the CLV curves of the granular contrast have been obtained.

Different temperature stratifications have been constructed in order to test separately the effect of the different features characterizing the model atmospheres on the CLV curve.

Gradient of the temperature fluctuations

Many works have shown that the temperature fluctuations (ΔT) causing the granulation pattern must decrease rapidly with height (i.e. Kneer 1984). However, how steep is the gradient of this decrease and at which height do the temperature fluctuations associated with the granulation disappear is still a matter of controversy.

Here we intend to check the influence on the CLV curve of various ΔT stratifications which decrease with geometrical height at different rates. However, in order to isolate the effect of the ΔT gradient from the other factors characterizing the temperature stratification the same mean atmosphere has been considered for all the models studied and the point at which granular and in-

tergranular temperatures merge has also been preserved constant. These have been chosen to coincide with the semi-empirical model of Rodríguez Hidalgo et al. (1995).

The temperatures of the atmospheric models considered are shown in figure 5.24, left panel. Solid lines stand for granular models and dotted for intergranular lanes. Right panel shows the associated temperature fluctuations using the same color code.

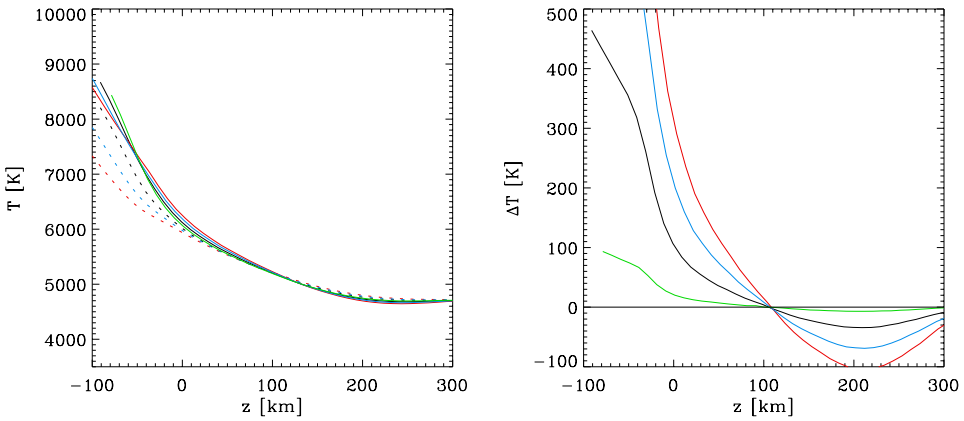

FIGURE 5.24— Temperature stratification (left panels) and temperature fluctuations (right panel)

These temperature stratifications have been applied, as explained above, to the high spatial resolution geometry presented in section 5.1.6. The 3D radiative transfer code has been used to obtain the emergent intensity of these cubes of data at the three studied wavelengths. Then, the contrast has been computed from the raw emergent intensity images. No simulation of the degradation due to earth atmosphere, foreshortening, etc. has been performed here, since the objective of this section is just to evaluate qualitatively the effect of the temperature stratification on the CLV curves, and the effect of the factors affecting solar observations has already been studied in section 5.2.1. The CLV curves obtained are presented in figure 5.25. The color code is the same as in figure 5.24. Upper panels stand for λ6708 Å, middle for λ8000 Å and lower for λ15500 Å. Left panels present the absolute values of the contrast and right panels the contrasts normalized to the value at disk center.

In figure 5.25 it can be seen that steeper gradients of ΔT produce larger values of the granulation contrast at all disk positions. However, when the CLV

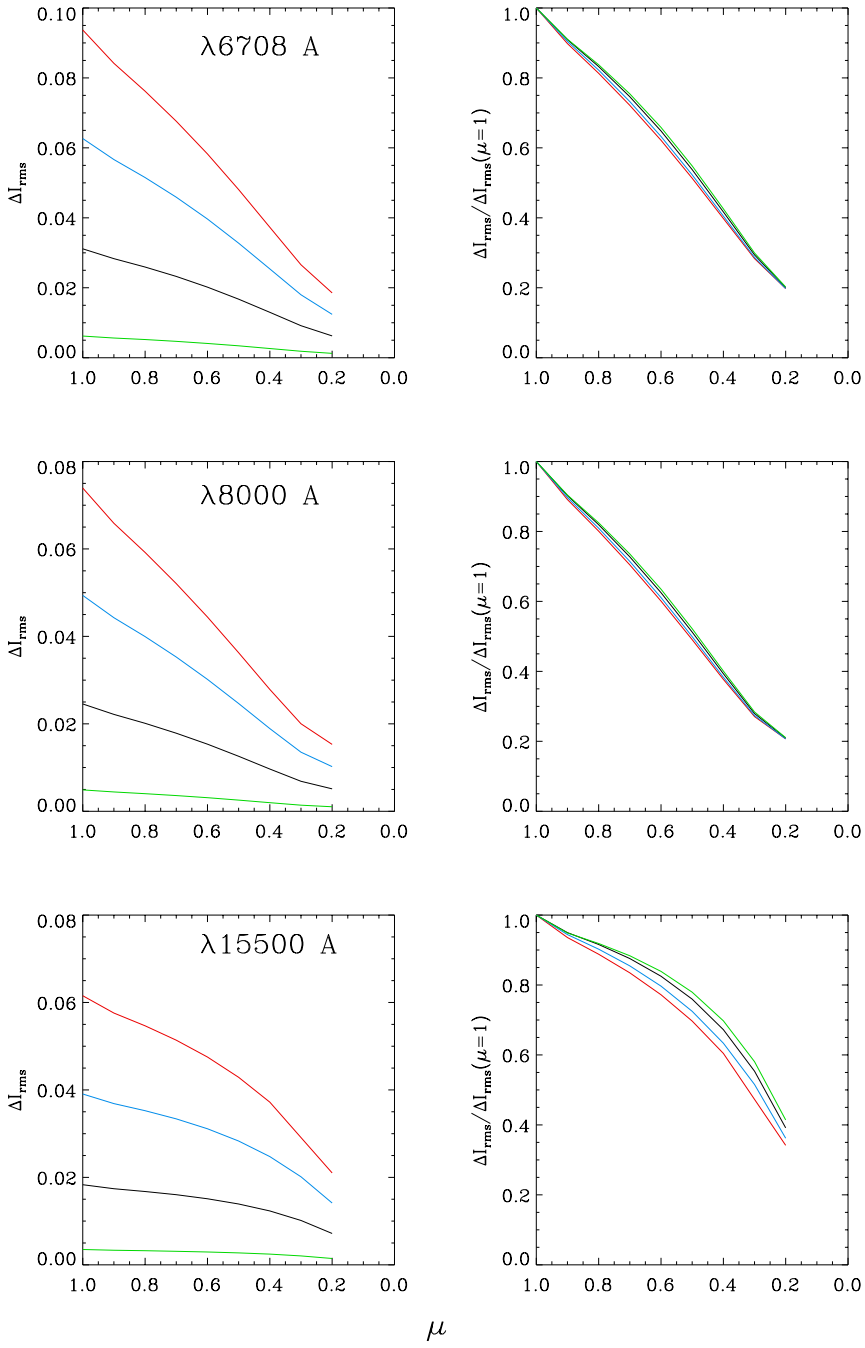

FIGURE 5.25— CLV curves of granular contrast of the models shown in fig 5.24 presented with the same color code at λ6708 Å (upper panels), λ8000 Å (middle panels) and λ15500 Å (lower panels). In left panels the absolute values of the contrast are presented, on the right panels the contrasts normalized to the value at disk center.

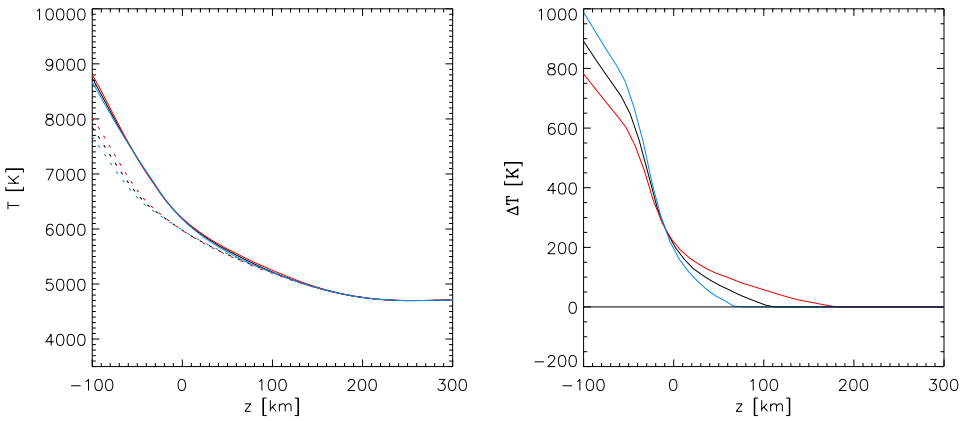

FIGURE 5.26— Temperature stratification (left panels) and temperature fluctuations (right panel).

curves are normalized to the value at disk center the differences between the shapes of the different ΔT stratifications are very small, beeing slightly steeper the curves corresponding to stronger decreases of ΔT with height in the solar photosphere. The differences in the shape of the CLV curves are larger at λ15500 Å than at λ8000 Å and λ6708 Å.

Penetration of the temperature fluctuations

A controversial matter is the height at which the temperature fluctuations associated to the granulation penetrate in the photosphere.

In order to test how does the penetration height of the granules influence the CLV curves of granular contrast, several atmospheres with temperature fluctuations that vanish at z$\sim$60 km, z$\sim$100 km and z$\sim$180 km have been constructed. Their temperature stratification is shown in left panel of figure 5.26 and their temperature fluctuations in the right panel. Solid lines stand for granules and dotted for intergranular lanes.

The CLV curves computed for these models are shown in figure 5.27 with the same color code as figure 5.26. The curves with temperature fluctuations that vanish deeper in the photosphere present a steeper decrease of the contrast from the center to the limb. However, the values of the contrast at disk center do not differe very significantly for the different studied models, exept for λ15500 Å.

Thus, we can conclude that the absolute values of the granulation contrast

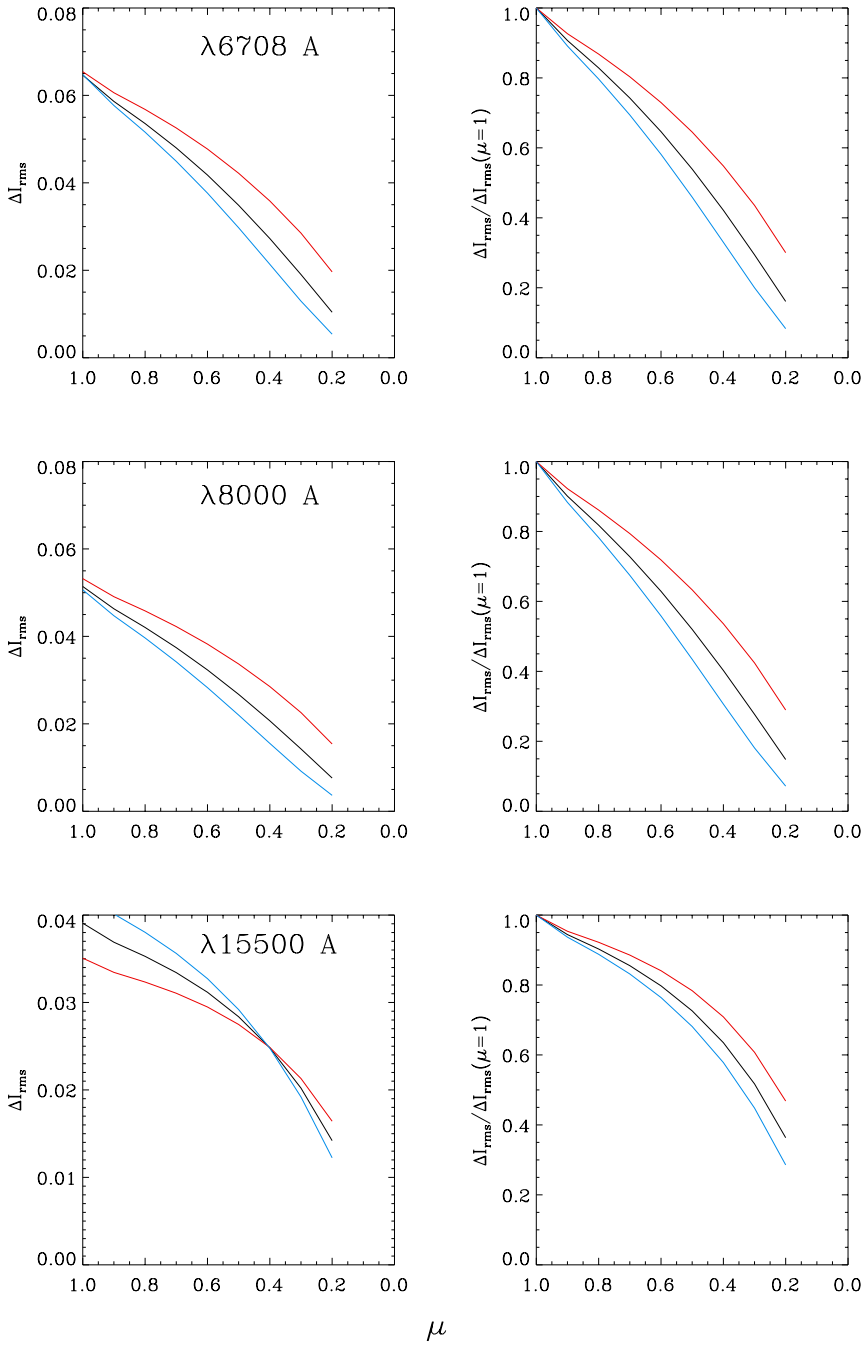

FIGURE 5.27— CLV curves of granular contrast of the models shown in fig 5.26 presented with the same color code at the three studied wavelengths. In left panels the absolute values of the contrast are presented, on the right panels the contrasts normalized to the value at disk center.

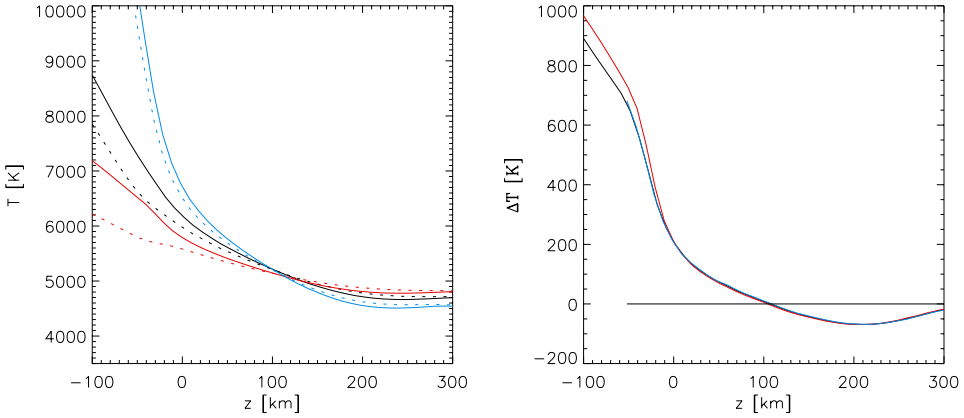

FIGURE 5.28— Temperature stratification (left panels) and temperature fluctuations (right panel)

mainly depend on the gradient of the ΔT decrease with height in the photosphere. However, the shape of the CLV curve depends mainly on the height at which the temperature fluctuations vanish. We wish to stress that for the studied models no CLV curve shows a tendency of the contrast to peak somewhere between disk center and the limb. Probably a much higher efficiency of granules in penetrating higher up in the photosphere would be required.

Gradient of the mean temperature

In order to test to what extent does the mean temperature stratification affect the resulting CLV curves, several atmospheres with similar temperature fluctuations but with different mean temperature stratifications have been constructed. The temperature stratifications are shown in left panels of figure 5.28. Solid lines stand for granular structures and dotted for intergranular ones. The right panel shows the associated temperature fluctuations with the same color code.

The CLV curves of the granular contrast for these models are presented in figure 5.29 with the same color code as figure 5.28.

The curves with larger temperature gradients have smaller contrasts at disk center and present CLV curves which decrease less steeply from the center to the limb. The shape of the CLV curve and the values of the contrast at disk center are very dependent on the mean temperature stratification. Therefore we can conclude that, eventough the granular structures are usually associated to

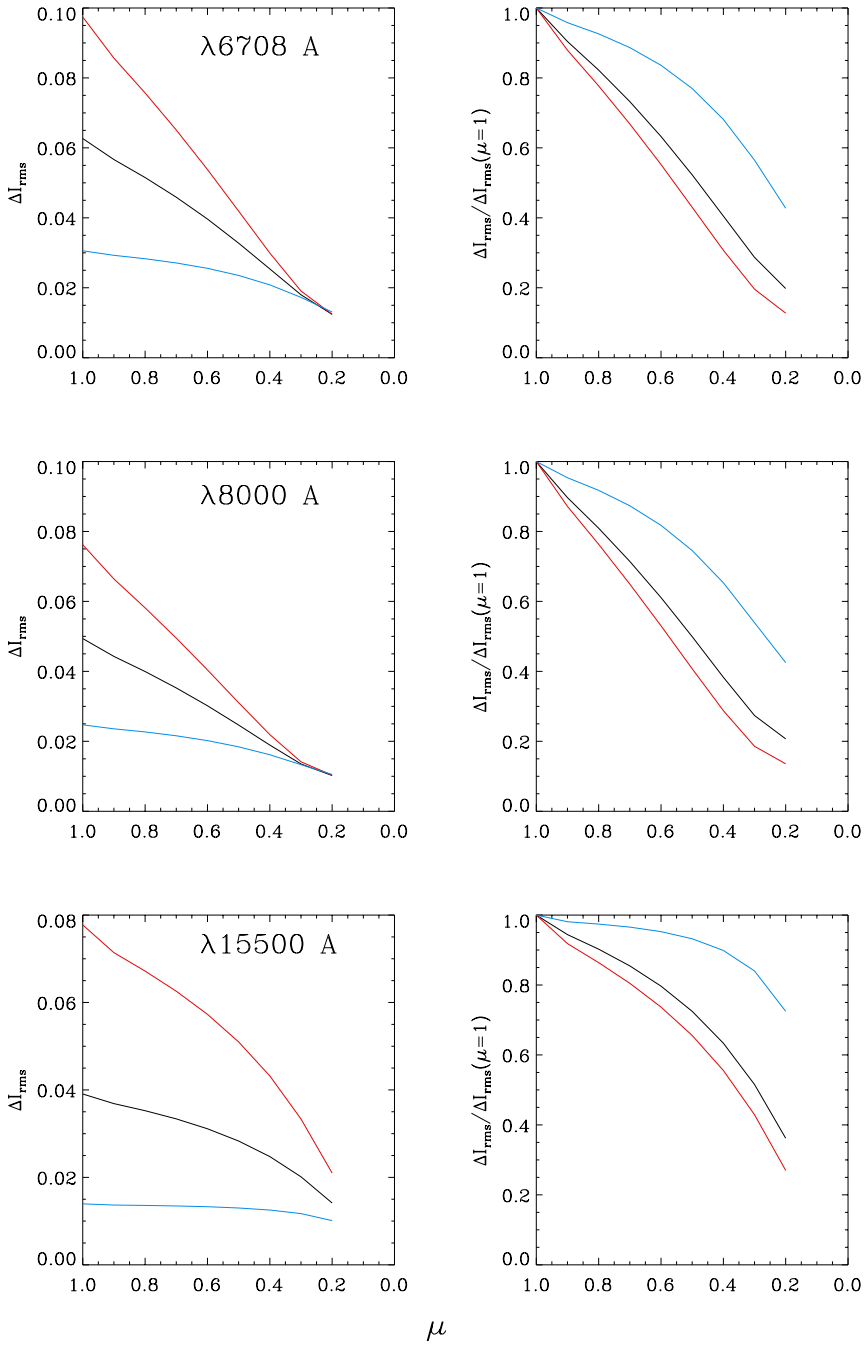

FIGURE 5.29— CLV curves of granular contrast of the models shown in fig 5.28 presented with the same color code at λ6708 Å (upper panels), λ8000 Å (middle panels) and λ15500 Å (lower panels). In left panels the absolute values of the contrast are presented, on the right panels the contrasts normalized to the value at disk center.

the temperature fluctuations in the photosphere, the mean temperature stratification has an important role in the constructuion of the granulation contrast pattern. Therefore, in order to characterize correctly the solar granulation it is necessary to determine both, the mean temperature and the ΔT stratification.

Limitations of the previous numerical experiments

In the three numerical experiments presented above we have tried to treat separately the influence of the temperature fluctuations and of the mean temperature stratification. However, as the reader may have noticed, the recomputation of the hydrostatic equilibrium for each of the linearly perturbated temperature stratifications causes small changes in them. This causes the mean T or ΔT stratifications not to be exactly equal in the experiments where we have tried to isolate their influence.

Here we present together all the curves used in the three previous experiments to emphasize that, eventhough small differences appear in the studied temperature stratifications, in all the cases the effect which is beeing studied is the predominant one.

Figure 5.30 presents all the studied mean temperature stratifications (upper panel) and temperature fluctuations (lower panel). The thick lines stand for the curves used for studying the influence of the gradient of the mean temperature. As seen in the figure, the differences in the mean temperature stratification are much more significative for the thick lines than for the thin ones. Similarly, in the lower panel it can be appreciated that, eventhough small differences occur between the ΔT of the thick lines, they are much less significative than for the thin ones.

Therefore, we can conclude that the predominant effect on each one of the performed experimets is the desired one.

5.2.7 Comparison with observations

All the tests performed above show that there are a lot of factors which influence both the shape of the center-to-limb variation and its absolute values. In the previous analysis we have tried to clarify how does each of this effects affect the obtained curves in order to be able to analyze qualitatively the real observations. Here, we compare the theoretical and semi-empirical models with the real observations in order to obtain information of the fit of these models to observations, and to infer information of the temperature stratification that our observations point to.

In figure 5.31 we present the observed CLV curves of the granulation contrast (solid thick lines) at λ6708 Å (upper panels), λ8000 Å (middle panels) and

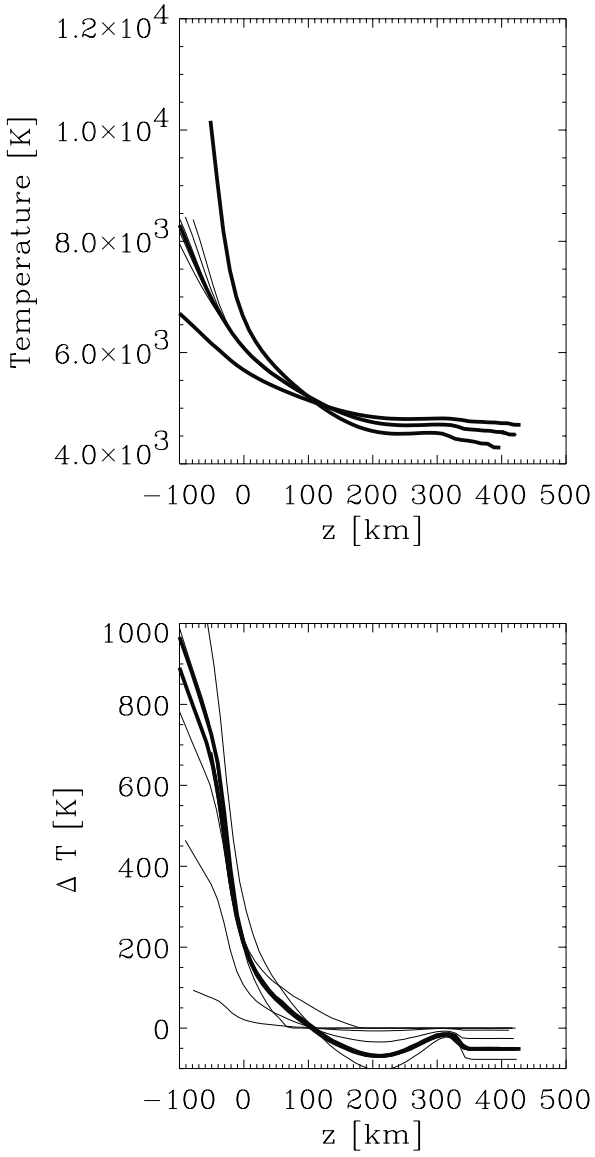

FIGURE 5.30— Mean temperature stratification (upper panel) and temperature fluctuations (lower panel) for all the studied temperature stratifications. Thick lines stand for those belonging to the experiment on the influence of the mean temperature gradient.

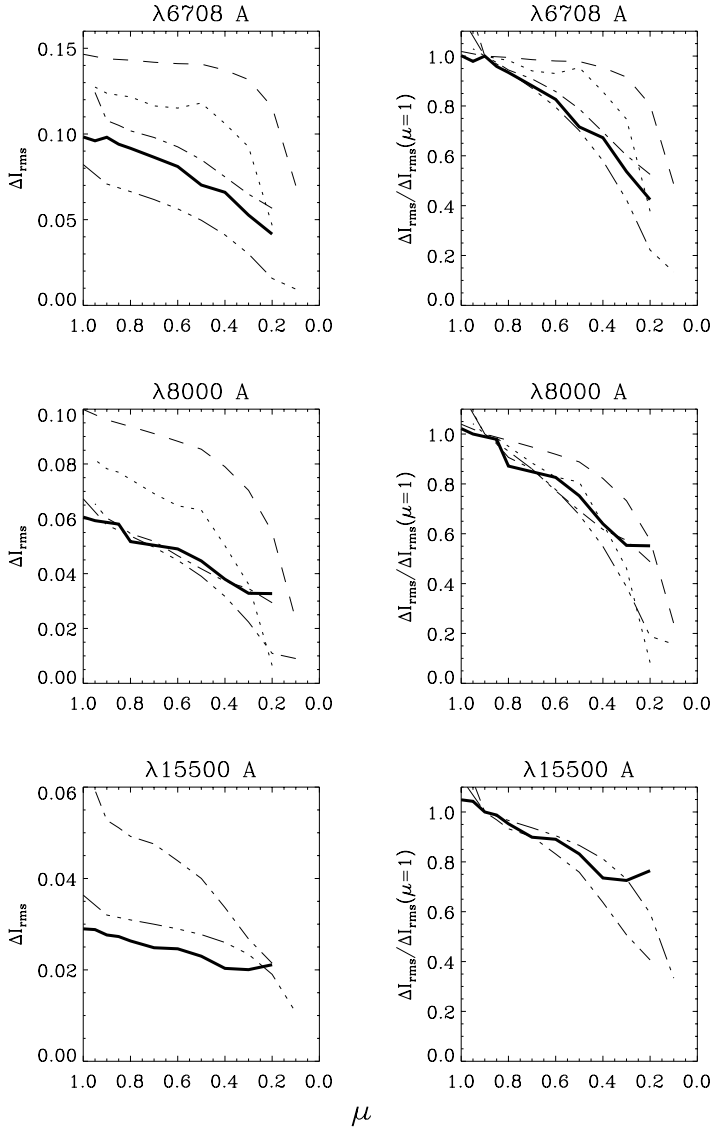

FIGURE 5.31— CLV of granular contrast at λ6708 Å (upper panels),λ8000 Å (middle panles) and λ15500 Å (lower panels). Absolute values of the contrast (left panels) and normalized to the value at μ=0.9 (right panels) are shown. Solid thick line–observed contrast, dotted line–15KM model contrast, dashed line–35KM model contrast, dotted-dashed line–SN model contrast, three dots-dashed line– RHL model contrast.

λ15500 Å (lower panels). As explained in chapter 2, the observations at λ6708 Å were performed during a partial solar eclipse and the images were restored of both, telescope and earth atmosphere degradation. Therefore, together with the observed curve the upper panels present the CLV curves obtained from the SN model (doted-dashed line), from the 15KM model (dotted line), from the 35KM model (dashed line) and from the RHL model (three dotted-dashed), all foreshortened and degraded by LPBF. Middle panels show the same models with the same linestyles but in this case foreshortened and degraded by ATA. The RHL model has not been degraded by ATA since the Rodríguez Hidalgo et al. (1995) atmosphere was obtained by inverting data uncorrected for the degradation due to earth atmosphere, and its effect is included in the model. Lower panels show the observed curves together with the ones derived from the SN model and the semi-empirical ones also foreshortened and degraded by ATA (exept in the case of the RHL model). Left panels show the absolute vales of the contrast and right panels the contrasts normalized to the value at μ=0.9.

No perfect agreement between any of the models at all the studied wavelengths and the observations is found. The models which show the best concordance with the observed absolute values of the contrast are the SN and RHL.

For λ6708 Å the RHL model has qualitatively the same shape as the observed one at least up to μ=0.4, and the SN model shows a very good agreement with our observations. The 15KM model has the same relative amount of contrast loss from the center to the limb but in a different manner. For λ8000 Å there is again a very good agreement of the curve derived from the SN model and the observations. The RHL model also shows a close trend to the one observed at this wavelength. The curve of the 15KM model of Gadun also agrees in its steepness in a reasonable way for $\mu \geq$0.4, but for smaller μ's it has a too large slope of the contrast decrease. For λ15500 Å the best agreement is found with the curve of the RHL model for $\mu \geq$0.4. For larger heliocentric angles the observed curve shows a tendency of the contrast to stabilize, while the semi-empirical models have a steep decrease.

The RHL model presents a reasonable agreement of the absolute values of the contrast with the observed ones. However, its decrease from the center to the limb is too steep. From the studies performed in the previous section we can conclude that a temperature stratification with approximately the same slope as the one of the RHL model but with a reversal height of granular and intergranular temperatures upper in the photosphere would agree better with our observations. This would produce similar values of the contrast but with smoother decreases from the center to the limb. The RHL model has the merging point around z=150 km, so it can be stated that our observations point to a merging point higher up in the photosphere.

The SN model also shows a reasonable agreement in the absolute values of its contrast with our observations at λ8000 Å and at λ6708 Å (specially if the change of slope between μ1–0.9 and $\mu \leq 0.9$ would not be present) . However for λ15500 Å it shows a too high granular contrast at disk center. The slope of the contrast decrease for this model from the center to the limb matches very well our observations at λ6708 Å and at λ8000 Å , but at λ15500 Å it is too steep for $\mu \leq 0.7$. The slope of the temperature decrease at the deep layers of the range where the information comes from is small for this model. As shown in section 5.2.6, this produces high values of the granulation contrast with steep decreases of the granulation contrast from the center to the limb. This could explain the lack of agreement found for this model at λ15500 Å. A steeper mean temperature stratification would produce a better agreement of this model with our observations. A merging point of the granular and intergranular temperature higher up in the photosphere would also produce curves more similar to our observations. However, this is not likely in this case since the merging point in the SN model occures in the highest layers of the atmosphere where the information comes from.

The 15KM and 35 KM models present too high values of the contrast and too smooth decreases from the center to the limb. This can be caused by a too steep decrease of the temperature fluctuations with height in the photosphere, together with a too steep stratification of the mean temperature fluctuations for this model.

5.3 CLV of granular power spectrum

In chapter 2 we performed a study on how does the power spectra (hereafter PS) of granulation change with heliocentric angle. It is interesting to perform also this study on the theoretical and semi-empirical models in order to check the agreement between the predictions derived from the models and the observations, and in addition, to see the influence of the different geometries in the resulting PS parameters.

In chapter 2, the PS of the restored images of solar granulation was studied in detail. It was found that the section of the PS parallel to the solar limb showed an excess of power as compared to the expected just from mere foreshortening for high spatial wavenumbers. This was interpreted as a sign of small granular structures penetrating higher in the atmosphere. It is interesting to repeat this analysis on the semi-empirical models constructed by assuming a known geometry created as described in section 5.1.2. This allows to check the origin of the observed structures and to interpret them.

5.3.1 Semi-empirical model

The PS of the foreshortened and degraded by LPBF images produced by applying the radiative transfer code to the RHH model has been computed. In figure 5.32 the sections parallel (solid thick) and perpendicular (solid thin) to the solar limb of this PS are presented, smoothed in logarithmic scale with a 5 points running box to reduce noise. The dotted lines correspond to the azimuthally averaged PS at disk center (lower line in each panel) and the expected power if equation 2.7 is fulfilled, this is, if the change of power is only due to the foreshortening effect (upper dotted line in each panel). The sections of the PS are computed for the three studied wavelengths.

Even though the high spatial resolution models do not have as many population elements in the granulation cell size histogram as the low resolution models, we have chosen them for this section because it is important to have information in the high frequency range. The differences of the PS of low and high spatial resolution geometries have been checked finding that they are essentially the same up to $k \sim 15$ Mm^{-1}. For higher frequencies the low resolution model shows no power, so they have been excluded from this analysis.

The PSs have been computed on the images foreshortened and degraded by LPBF because these are the ones directly comparable to the observations at λ6708 Å, which were restored from the degradation due to the earth atmosphere. Although the other observed wavelengths were not restored for the terrestrial atmosphere degradation, the PS computations in the simulations at λ8000 Å and λ15500 Å have also been performed in order to study the influence of different wavelengths on the PS.

For all spatial frequencies less power than expected from equation 2.7 is found for heliocentric positions different than μ=1. This is equivalent, by virtue of the Parseval's theorem, to the loss of contrast from the center to the limb studied in section 5.2. For increasing heliocentric angles, a more efficient transfer of contrast from low to middle and high frequencies is found in the direction perpendicular to the solar limb, due to the foreshortening effect. In the direction parallel to the solar limb a decrease of power is also found from the center to the limb, but no excess of power at high frequencies is found as compared to the expected just from foreshortening. This is logical since the geometry used has no vertical variation, and therefore, no higher efficiency of small granules in penetrating in the atmosphere can be inferred from the observables derived from the simulations. This points to the result that the excess of power observed in chapter 2 was due to a real penetration of small granules in the Sun's atmosphere and not to mere radiative effects.

The described tendency of the granular PS keeps for all the studied wave-

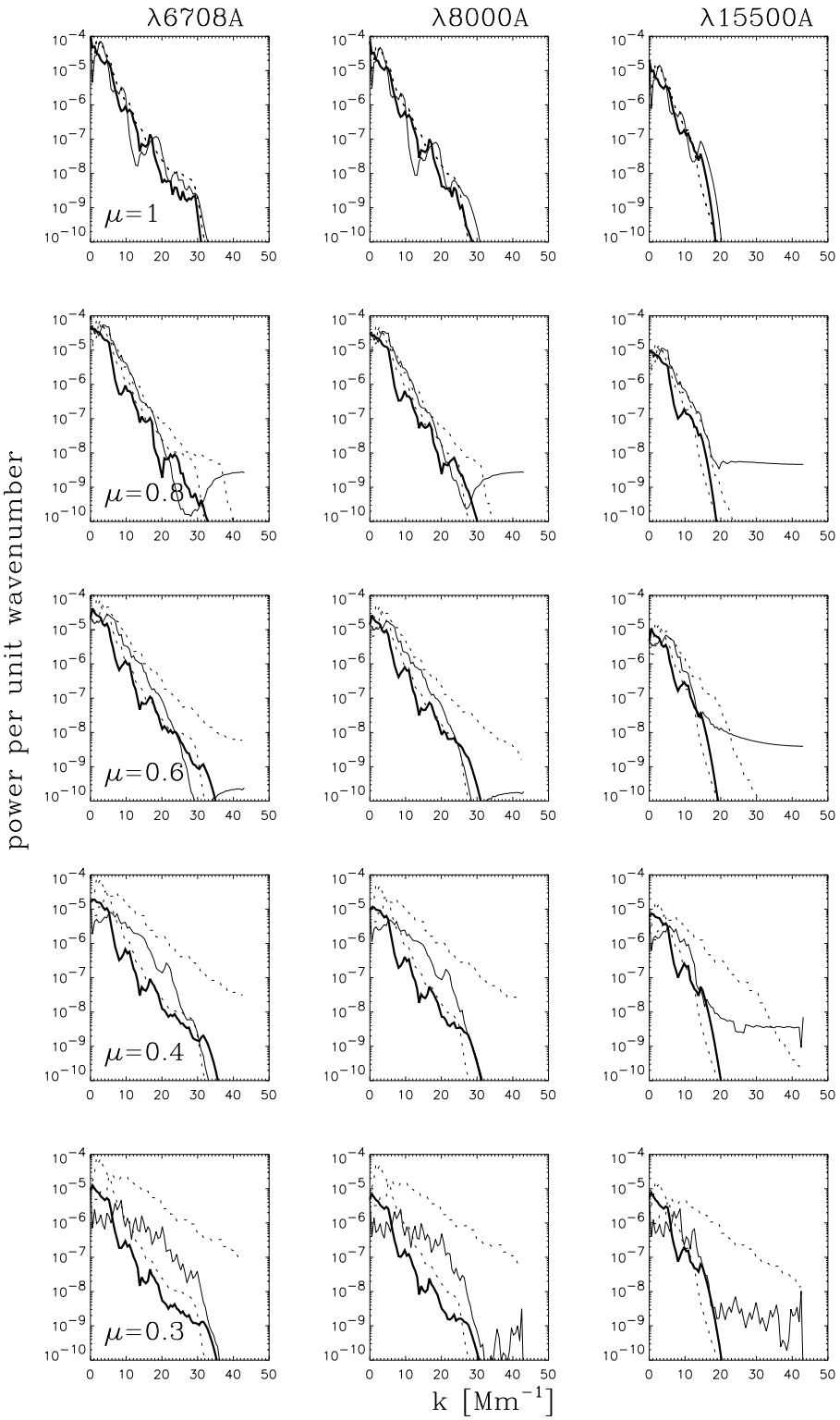

FIGURE 5.32— Mean smoothed power spectra along the axis parallel (thick solid line) and perpendicular (thin solid line) to the solar limb of the PS of the RHH model images for μ=1, 0.8, 0.6, 0.4, 0.2. The azimutally averaged PS at μ=1 is represented with lower dotted line in each panel. Upper dotted lines in each panel are derived from the power at μ=1 under the assumption of only prespective foreshortening. Left panels–λ6708 Å, middle panels–λ8000Å, right panels–λ15500 Å

lengths. The only difference is that, at λ15500 Å, the power decreases to noise level for k ~20 Mm^{-1}, while in the other wavelengths it does at k ~30 Mm^{-1} (see table 5.3). This difference is due to the different telescope cutoffs for the different wavelengths. The observed noise in the PS at high wavenumbers beyond the cutoff can be atributed to numerical noise in the calculation of the Fourier Transform.

As explained in chapter 2, the isotropy of the granular structures justifies the integration of the two-dimensional PS over ellipses of ellipticity ϵ_μ. A one-dimensional PS is obtained which represents the average power for each wavenumber at the different disk positions. Hereafter this one-dimensional azimutally averaged PS is refered to as PS$_{az}$. In chapter 2 it was obtained a peak of power of the PS$_{az}$ which moved to lower spatial frequencies for larger heliocentric angles. This was interpreted as a sign of the predominance of larger granular structures for higher layers, which is logical due to the expansion of the structures with height.

In the semi-empirical models such expansion is not present since, as mentioned before, for every geometrical height the horizontal fluctuation of the physical parameters is the same. However, studies on the PS$_{az}$ in the semi-empirical models are performed to see if just the pure radiative transfer effects do change its shape or the results obtained in chapter 2 can be completely attributed to a physical expansion of granules with height in the solar atmosphere.

In figure 5.33 the PS$_{az}$ obtained from the RHH model at the three studied wavelengths for μ=1., 0.8, 0.6, 0.4, 0.3 are presented. The curves with less power correspond to higher heliocentric angles. The PS$_{az}$ for $\mu \leq$0.2 is not presented since the lack of statistical significance at these large heliocentric angles makes the curves too noisy.

The parameters usually chosen to characterize PS$_{az}$ are the wavenumber with maximum power, k_{max}, and the mean wavenumber $\overline{k}$. In figure 5.34 the CLV of $\overline{k}$ for the RHH model is presented at λ6708 Å (solid line), λ8000 Å (dashed line) and λ15500 Å (dashed dotted line). k_{max} keeps constant with a value of 3.45 Mm^{-1} for every disk position, therefore we have not presented it in this graphic. On the contrary, the $\overline{k}$ shows a decrease from the center to the limb. The $\overline{k}$ varies approximately from 4.7 Mm^{-1} at disk center to 4.1Mm^{-1} for μ=0.3 at λ6708 Å and λ8000 Å, and from 4.5 Mm^{-1} to 3.7 Mm^{-1} at λ15500 Å. When comparing these values with the ones obtained in chapter 2 it can be seen that the observational ones correspond to smaller mean granular structures, but the absolute amount of decrease from the center to the limb is larger for the observations than for these simulations. The fact that the $\overline{k}$ differ in their absolute values between observations and simulations can be due

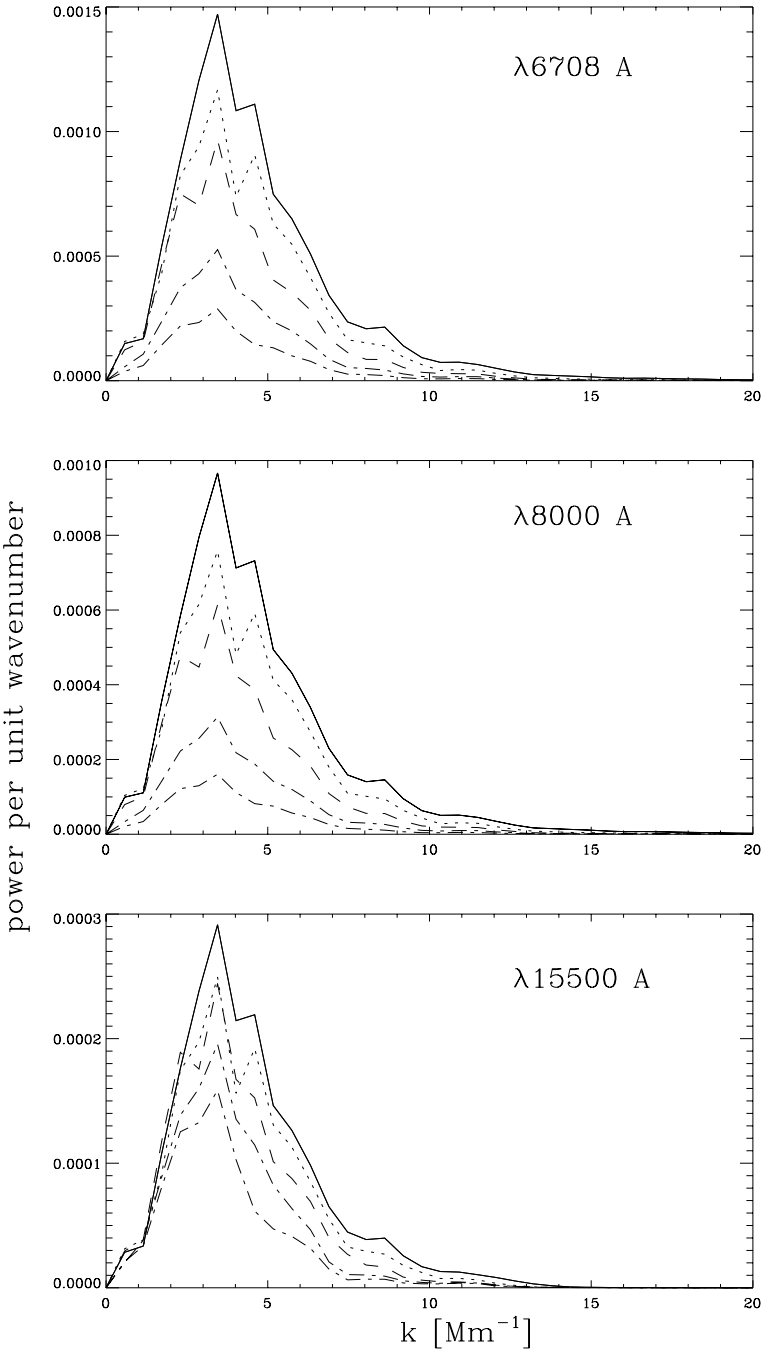

FIGURE 5.33— PS_{az} of the RHH model for μ=1, 0.8, 0.6, 0.4, 0.3. Curves with less power stand for positions nearer to the solar limb.

to the use of the high spatial resolution geometry, which has a small amount of elements of population in the cell size histogram. Therefore, differences can appear in the average scale of granulation.

The fact that the absolute values of $\overline{k}$ are lower for λ15500 Å than for the other wavelengths points to the radiative effects causing the mean scale of granulation to be larger at larger wavelengths. However this does not reflect a physical situation where the granules have larger mean sizes at deeper layers of the atmosphere. On the contrary, this is purely a radiative effect since this studied model has a geometry that keeps constant for every depth of the solar photosphere.

The decrease of $\overline{k}$ with the heliocentric angle in these simulations means that the radiative effects produce, for this model atmosphere, an apparent increase of the mean spatial scale of the solar granulation which is not correlated with a physical expansion of the granules. However, the amount of the decrease of $\overline{k}$ in the observations of chapter 2 was larger than the amount obtained from the simulations. It could be interpreted that the difference in decrease of $\overline{k}$ between simulations and observations is really due to an increase of the granular sizes with height.

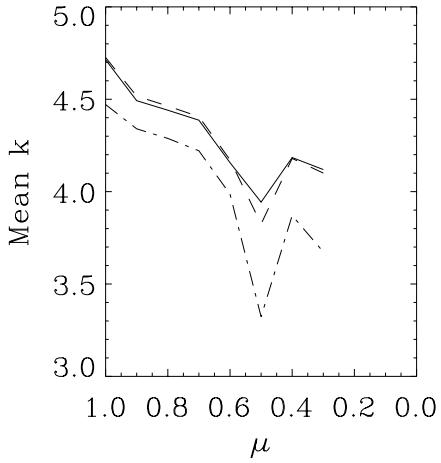

FIGURE 5.34— $\overline{k}$ of the PS_{az} of the RHH model at λ6708 Å (solid line), λ8000 Å (dashed line) and λ15500 Å (dashed dotted line).

5.3.2 Theoretical models

The same studies have been performed with the PS of the SN model. On the models of Gadun (1995) such studies have no sense since the PS is modified by the fact that the models are two dimensional, thus, missing the information of the direction parallel to the solar limb.

In figure 5.35 the smoothed with a 5 points running box in logarithmic scale sections parallel and perpendicular to the limb and those derived from the foreshortening law expressed in equation 2.7 are presented. The meaning of the different line styles is the same as in figure 5.32. Note that at λ6708 Å and λ8000 Å for $\mu \leq$0.8 the cuts parallel to the Sun limb show an excess of power at high frequencies as compared to the predictions derived from a pure foreshortening law as expressed in equation 2.7. This result was interpreted in chapter 2 as a sign of the higher penetration in the atmosphere of the smaller granules. However, for λ15500 Å this power excess is not observed, on the contrary, a deficit of power at high frequencies is obtained, which can be interpreated as a decrease of the power to noise level. This is due to the degradation by LPBF which, at λ15500 Å, has a cutoff frequency of 1.62 arcsec^{-1} that corresponds to $\sim$15 Mm^{-1}.

In figure 5.36 the azimuthally averaged PS of the synthetic granulation is presented at λ6708 Å (upper panels), λ8000 Å (middle panels) and λ15500 Å (lower panels) for μ=1.,0.8,0.6,0.4,0.3. The curves with less power stand for positions closer to the limb. Note that the lack of statistical significance, which increases towards the limb, causes the noisy aspect of the curves. However, a clear trend of the maximum of the PS$_{az}$ to move to lower wavenumbers for higher heliocentric angles can be observed.

Figure 5.37 is useful for studying in greater detail the trends of the PS$_{az}$. In left panel the CLV of the $\overline{k}$ is shown at λ6708 Å (solid line), λ8000 Å (dashed line) and λ15500 Å (dotted-dashed). Right panels show the CLV of the k_{max} for the same wavelengths represented with the same line styles. For low heliocentric angles the k_{max} keeps constant and then decreases for larger ones. The lines at λ6708 Å and at λ8000 Å are overlapped in the plot since the k_{max} coincides for these two wavelengths.

Left panel of figure 5.37 shows that, for λ15500 Å the absolute values of $\overline{k}$ are systematically lower than for the other wavelengths, and in λ8000 Å they are essentially similar to the ones in λ6708 Å. It has been shown above that this should be due, at least partially, to a radiative transfer effect.

In figure 5.37 it can also be seen that for all the wavelengths $\overline{k}$ tends to decrease for low heliocentric angles. For $\mu \leq$ 0.6 at λ6708 Å and λ8000 Å and for $\mu \leq$0.4 at λ15500 Å $\overline{k}$ increases again. This could be interpreted

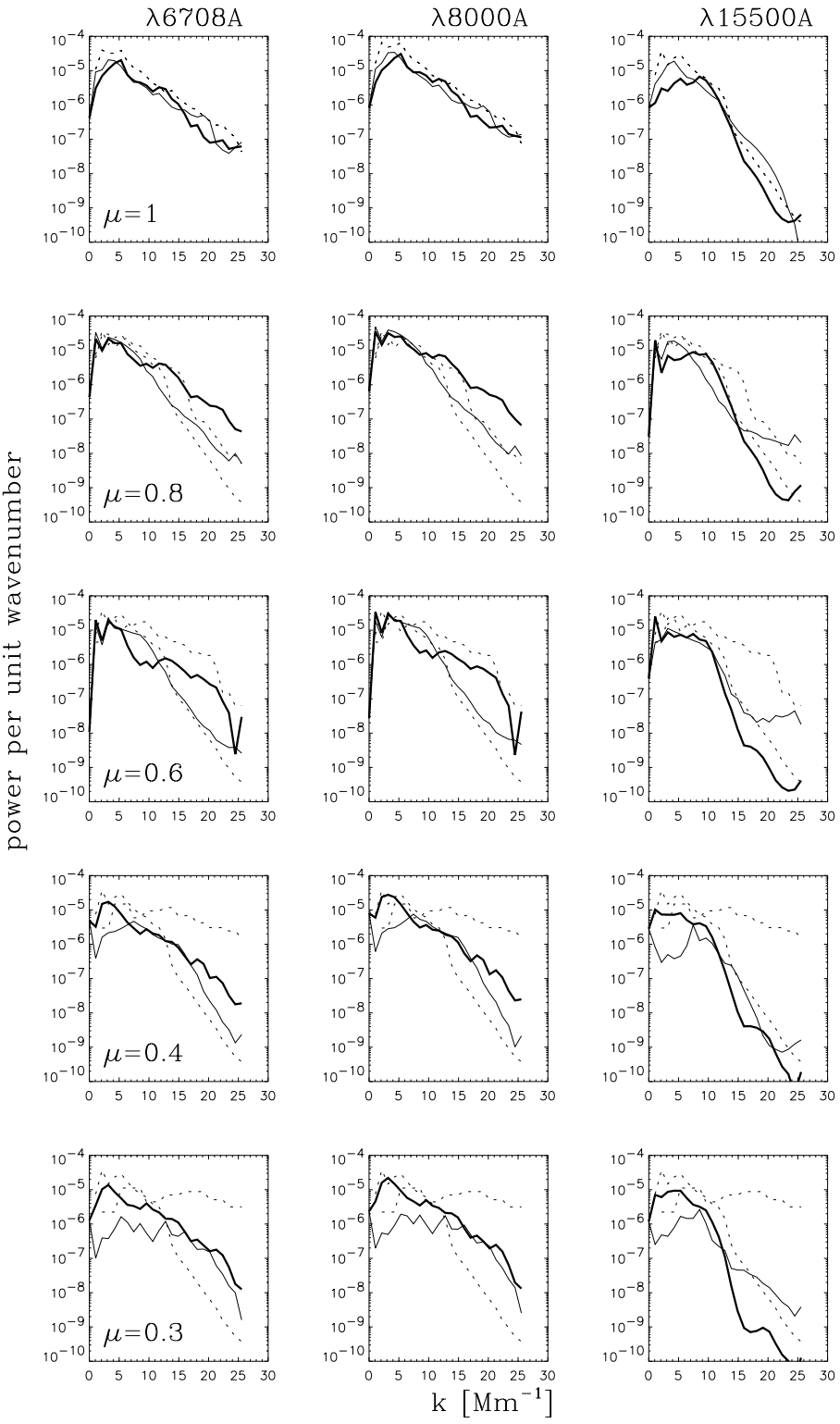

FIGURE 5.35— Mean smoothed power spectra along the axis parallel (thick solid line) and perpendicular (thin solid line) to the solar limb of the PS of the SN model images for μ=1, 0.8, 0.6, 0.4, 0.3. The azimutally averaged PS at μ=1 is represented with lower dotted line in each panel. Upper dotted lines in each panel are derived from the power at μ=1 under the assumption of only prespective foreshortening. Left panels–λ6708 Å, middle panels–λ8000Å, right panels–λ15500 Å

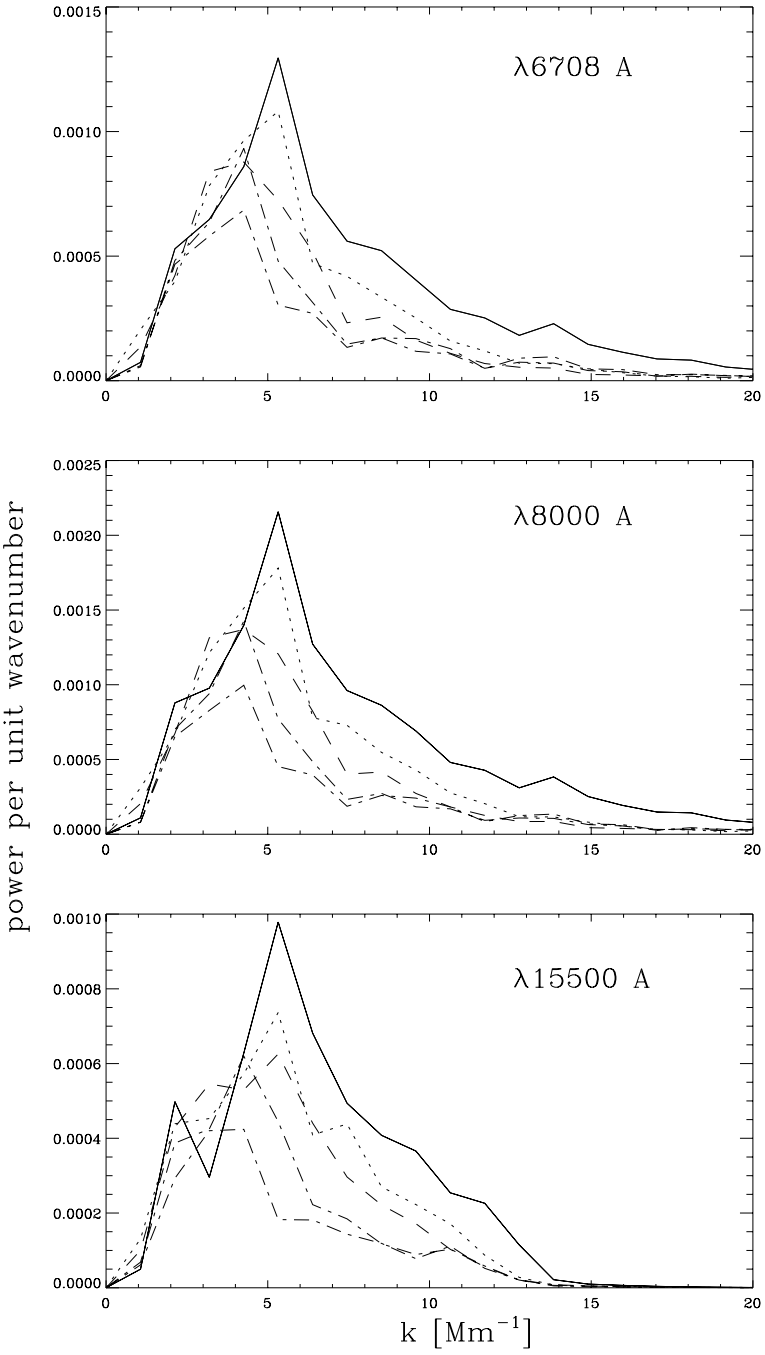

FIGURE 5.36— PS_{az} of the SN model for μ=1, 0.8, 0.6, 0.4, 0.3. Curves with less power stand for positions nearer to the solar limb.

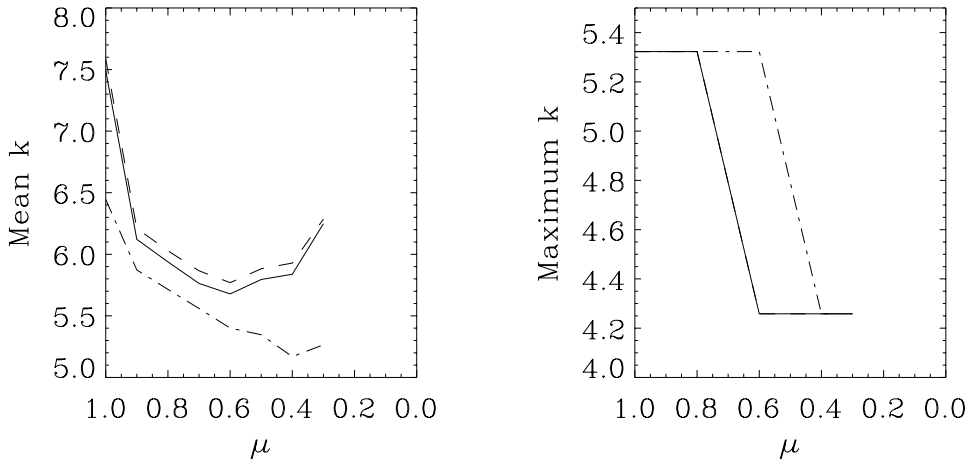

FIGURE 5.37— $\overline{k}$ (left panel) and k_{max} (right panel of the PS_{az} of the SN model at λ6708 Å (solid line), λ8000Å (dashed line) and λ15500Å (dashed dotted line).

as an increase of the characteristic size of granulation with height in the solar atmosphere up to a certain geometrical height, and for upper layers a decrease of this characteristic size. This would cause the reversal from a decreasing $\overline{k}$ to an increasing one to be visible at smaller μ's in smaller wavelengths since they show information coming from higher layers in the atmosphere. The results found in figure 5.35 of a more efficient penetration in upper layers of the atmosphere of small granules fit with the findings in figure 5.37. The increase of the mean size of granulation at low heliocentric angles found in figure 5.37 can be interpreted as the expansion of granules with height in the atmosphere. The decrease of the mean size of granulation for large heliocentric angles, this is, for high layers in the atmosphere, can be interpreated as the effect produced by a higher efficiency of small granules in penetrating into upper layers of the atmosphere.

However, when comparing the results obtained for this theoretical model with the observations presented in chapter 2, only a partial agreement is found. Actually, the higher efficiency of small granules in penetrating high into the photosphere is found in our observations. However, the absolute values of $\overline{k}$ are too high in the model. This can be due to a different size distribution of granules for this model with respect to our observations. The trend for large heliocentric angles of the mean size of granulation to decrease is not found either in chapter 2.

5.4 CLV of granular filling factor

In chapters 2 and 3 it was found that the granular filling factor (GFF) decreases with heliocentric angle down to a certain μ and then it increases again. It is of interest to check which influence play in this trend the pure radiative effects, the factors affecting solar observations and the horizontal fluctuations of the solar atmosphere. To that aim, the CLV of the GFF has been studied for the semi-empirical and theoretical models.

5.4.1 Semi-empirical models

The CLV of the GFF in the RHL model has been computed. The low spatial resolution geometry model has been chosen because its histogram of granular cell sizes is dense enough, and the GFF is specially sensitive to the granular cell size distribution. The results are presented in figure 5.38. We want to stress that in this simulations the geometry has no vertical structure, which means that the observed trends of the GFF can be entirely attributed to the factors degrading solar observations together with radiative transfer effects.

The values of the GFF at disk center are, from the raw emergent intensity images, 0.49 (λ6708 Å), 0.495 (λ8000Å) and 0.48 (λ15500Å). When the images are degraded by ATA the values are 0.475 (λ6708 Å and λ8000Å) and 0.425 (λ15500Å). These values are too high as compared to our observations where the GFF is 0.442 (λ6708 Å), 0.441 (λ8000Å) and 0.345 (λ15500Å). It can be seen in the figure that for the raw emergent intensity images and the foreshortened ones the GFF at λ6708 Å and λ8000 Å essentially diminishes from disk center to μ=0.8 and then keeps constant. On the contrary, at λ15500Å the GFF increases from μ=0.5 to the limb. However, the effect of foreshortening and degrading by ATA or by LPBF is to make the GFF increase from a disk position between disk center and the limb towards the limb. Even though the turning point from a decreasing GFF to an increasing one found in this case do not agree with the ones found in chapter 2 and 3, we can conclude from this model that the increase in GFF can be caused by the atmosphere together with the foreshortening, even if the increase is not intrinsic to the solar atmosphere.

5.4.2 Theoretical models

The same kind of computations have been repeated for the theoretical models, which do have a vertical structure in the morphology of granulation. In figure 5.39 the obtained results for the SN model are presented. The meaning of the different panels and linestyles is the same as in figure 5.38.

The absolute values of the GFF at disk center are 0.46 (λ6708 Å and λ8000Å) and 0.51 (λ15500Å). When the images are foreshortened and degraded

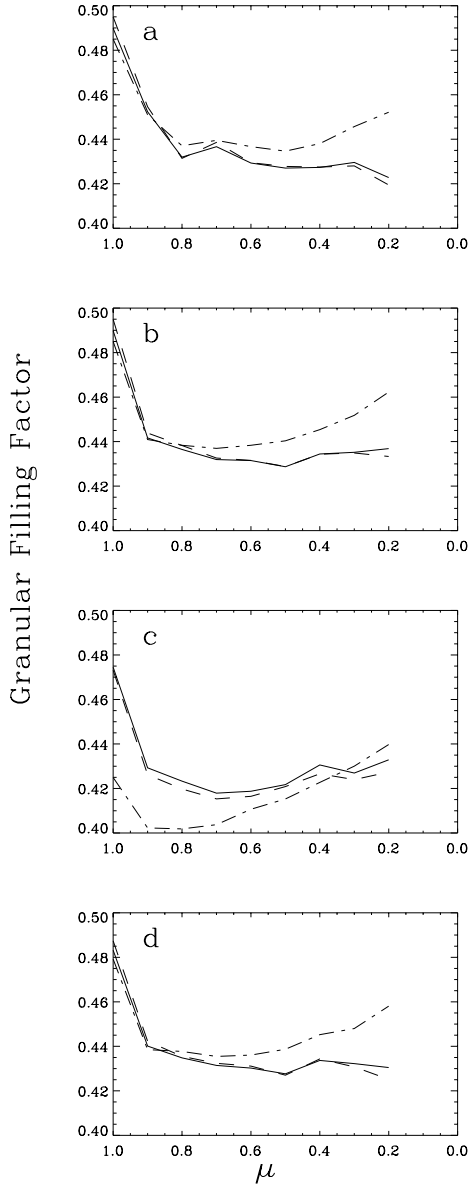

FIGURE 5.38— CLV of the GFF in the RHL model at λ6708 Å (solid line), λ8000 Å (dashed line) and λ15500 Å (dot-dashed line). a) GFF computed directly on the emergent intensity images, b) GFF computed on the foreshortened emergent images, c) GFF computed on the foreshortened and degraded by ATA images, d) GFF computed on the foreshortened and degraded by LPBF images.

by ATA the obtained values are 0.46 (λ6708 Å and λ8000Å) and 0.47 (λ15500Å). Note that in this model the larger wavelength has the highest value of the GFF. This is the contrary to what it is observed in chapter 2 and 3 and to the trends of the semi-empirical models. However, these values of the GFF fit better our observations than the ones obtained with the semi-empirical models.

In panel a) it can be seen that, for the raw emergent intensity images, the GFF shows a very smooth decrease from the center to the limb at λ6708 Å and λ8000 Å, but at λ15500 Å it shows a more strong decrease. The effect of foreshortening and degrading by ATA does not change the trends with heliocentric angle of the GFF at λ6708 Å and λ8000 Å, but at λ15500 Å it produces an increase of the GFF from disk center to μ=0.3. Foreshortening and degradation with LPBF produces a slight increase of the GFF from the center to the limb at λ6708 Å and λ8000 Å, and from μ=1 to μ=0.6 at λ15500 Å with a decrease for larger heliocentric angles.

The same kind of computations have also been performed on the 2D theoretical models of Gadun (1995). The obtained results are shown in figure 5.40 for 15KM models at λ6708 Å (black solid line) and λ8000 Å (magenta dashed line) and 35KM models at λ6708 Å (red dotted-dashed line) and λ8000 Å (blue three dot-dashed line). The meaning of the different panels is the same as in figure 5.39.

The values of the GFF obtained at disk center are 0.48 for both wavelengths in the 15KM models and 0.47 in the 35KM ones, which again are too large as compared to our observations.

As seen in the figure the shape of the CLV of the GFF does not vary very significatively when the different factors that affect solar observations are introduced. In the 15KM models the general trend is a decrease of the GFF from the center to the limb. For the 35KM models a similar trend is found with an increase at μ=0.1, which can not be considered as real due to the lack of statistical significance at this large heliocentric angle.

In summary we can conclude that the trends observed for the GFF on the solar surface can be caused by radiative transfer effects combined with the effects of different factors degrading solar observations. Foreshortening and degradation by ATA or by LPBF can cause an increase of the GFF from the center to the limb even if in the raw emergent intensity images a decrease is observed.

The theoretical models do reproduce approximately the value of the GFF at disk center. However, the observed variation with heliocentric angle and with wavelength is not reproduced. This suggests that some detail of the physical stratification on the granulation is not accurately enough reproduced by the theoretical models.

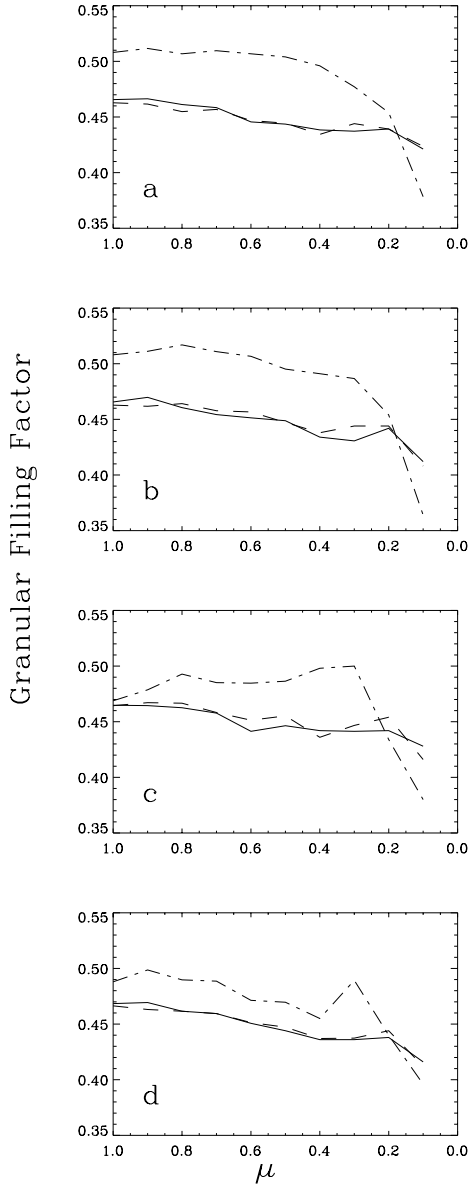

FIGURE 5.39— CLV of granular filling factor in the SN model at λ6708 Å (solid line), λ8000 Å (dashed line) and λ15500 Å (dot-dashed line). a) GFF computed directly on the emergent intensity images, b) GFF computed on the foreshortened emergent images, c) GFF computed on the foreshortened and degraded by ATA images, d) GFF computed on the foreshortened and degraded by LPBF images.

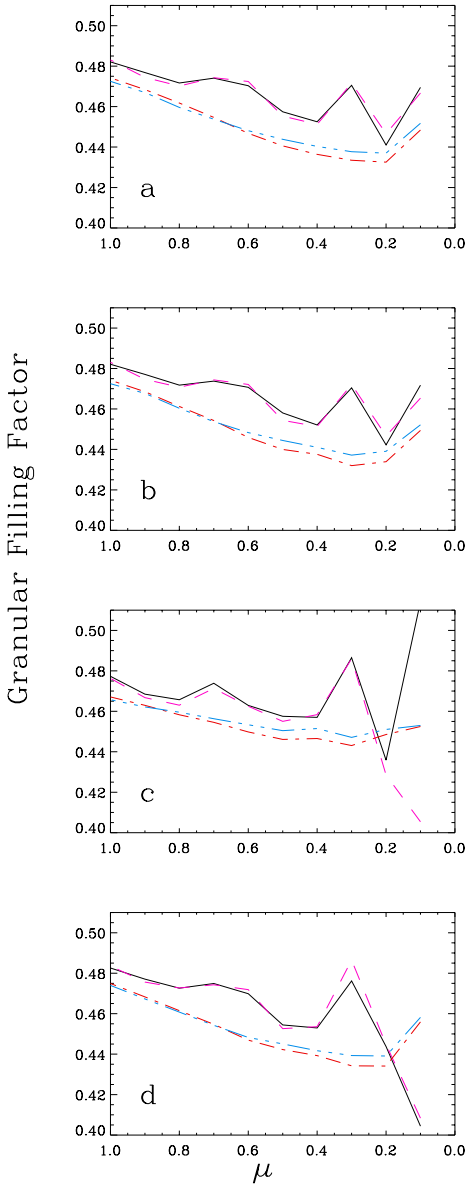

FIGURE 5.40— CLV of granular filling factor in the 15KM models at λ6708 Å (black solid line) and λ8000 Å (magenta dashed line) and 35KM models at λ6708 Å (red dotted-dashed line) and λ8000 Å (blue three dot-dashed line). The meaning of the different panels is the same as in figure 5.39.

5.5 Conclusions

Radiative transfer codes have been applied to different model atmospheres and the obtained granular parameters have been analyzed. Semi-empirical and theoretical models have been used.

The influence of the granular contrast of the different factors affecting solar observations on the CLV has been tested. Foreshortening and degradation by ATA of the emergent intensity images produces a decrease of the contrast from the center to the limb, even if in the raw emergent intensity images the constrast keeps constant for a large μ range (like in the 35 KM models).

The wavelength dependence of the CLV curves is highly related to the details of the model atmosphere used for the computations. Besides, the foreshortening and degradation by ATA can change the trend. By assuming that the granules radiate like a black body, the Wien approximation can be used to calculate the expected variation of the granular contrast with wavelength ($\Delta I_{rms} \propto \lambda^{-1}$). This should be valid for all the μ-positions. However, the formation heights are not a linear function of λ, changing according to the variation of physical parameters like the continuum opacity. This fact, combined with the decreasing values of ΔT with height, complicates the first simple expectation.

As a first approximation the Wien law is frequently used to obtain the dependence of the granulation contrast with λ. However, the formation heights change for different heliocentric angles, and this change is distinct for different λ. Since the temperature fluctuations decrease with height in the photosphere, the CLV curves are expected to have a wavelength dependence that changes for different temperature stratifications.

The pooreness of atmospheric conditions causes the CLV curves to decrease moore steeply from the center to the limb. However, the change in the CLV curve is smaller between good and bad atmospheric conditions than between raw emergent intensity images and those foreshortened and degraded by ATA.

The influence of the granular areas on the CLV curve has also been checked. Smaller sizes produce larger decrease of the contrast from the center to the limb. This confirms that radiative transfer effects are more efficient at small spatial scales.

The granulation contrast and its center to limb variation are mainy relatated to the temperature stratification in the solar photosphere. The influence of different stratifications on the CLV curves has been investigated. Steeper decreases of ΔT with height in the photosphere produce larger values of the contrast but the shape of the CLV curve does not depend very significantly on the steepness of the ΔT decay. On the contraty, a change in the height at which the temperature fluctuations associated to the granulation disappear produces different

shapes of the CLV curves but similar values of the granulation contrast. A vanishing point higher up in the photosphere produces smoother CLV curves, confirming previous results by Kneer (1984). The mean temperature stratification of the atmosphere does affect in a significant manner the values of the contrast and their center-to-limb variation. Smaller gradients of the mean temperature produce larger values of the contrast at disk center and steepest decays from the center to the limb.

The agreement of the CLV produced by the different theoretical and semi-empirical models to our observations has also been tested.

The Rodríguez Hidalgo et al. (1995) semi-empirical model atmosphere reproduces reasonably the observed center to limb variation curve of the granular contrast. However, a merging point of the granular and intergranular temperatures placed higher up in the photosphere would produce a better agreement with our observations.

The theoretical 3D model of Stein & Nordlund (2000) does reproduce the observed CLV curve in a reasonable way, although the contrasts is larger and presents a steeper decrease than our observations at λ15500 Å. This can be probably attributed to a too smooth mean temperature stratification in the deep photospheric layers of this model.

The 2D models of Gadun (1995) present higher values of the contrast and smoother decreases from the center to the limb than our observations. This can be caused by a too steep decrease of the ΔT with height in the photosphere, together with a too large gradient of the mean temperature fluctuations stratification for these models.

The power spectra of the different models have been investigated. The PS of the SN model resproduces reasonably the observed trends. However, in our study the use of only one box could be limiting the statistical significance even near disk center. A statistical parameter like the granular cell area histogram is not reproduced. However, it can not be discarded that a full time series of the model would produce a different histogram in better agreement with our observations.

The role of radiative transfer effects in the construction of the observed intensity pattern of solar granulation has been studied. It has been found that they produce apparent larger mean sizes of granulation for longer wavelengths and an increase of the observed mean granular size with heliocentric angle. Thus, the $\overline{k}$ shows a tendency to decrease with wavelength and with heliocentric angle which is not correlated with a change of granular areas with height in the atmosphere.

The GFF shows a dependence with μ wich varies for different model atmospheres but is not correlated with a relative change of granular-intergranular

areas with geometrical height. The values of the GFF for the SN model at disk center match approximately the observed ones, although the GFF variation from the center to the limb is not reproduced. The values of the GFF in the 15KM and 35KM models are too large as compared to observations. However it must be taken into account that in 2D models the GFF can be biased by the dimensions of the model.

6

A first step towards a simulation of solar facular regions

The term facula (from the latin expression for torche) has been traditionally used in the literature to describe bright structures observed in the photosphere close to the limb and associated spatially to sunspots. In the last decades these structures have been observed at the disk center by means of narrow-band imaging but the name facula, or facular points, has been kept.

The development of the techniques for measuring the light polarization has allowed to describe the faculae as concentrations of magnetic field, the so-called flux tubes. A facular structure as observed in image like ours in chapter 5, could be composed by different tubes varying in size until a spatial limit which is still a matter of current debate. Only a fraction of the observed area in faculae is composed by flux tubes which are embedded in quiet photosphere. The filling factor is the percentage of facular area occupied by the flux tubes. The lower limit of the sizes directly observed for flux tubes is fixed by the resolution limit of the telescope and/or the Nyquist frequencies imposed by the pixel size in the images. However, a good approach to the filling factor value can be mainly derived from the Q, U and V stokes parameters and in less extend from the I profile, the parameter used in our obsevations.

For this reason and in a first phase of development of our simulations of facular regions, we will simulate the facula as an isolated atmosphere, with the geometry of a tube, and with a different thermal structure in the surroundings. As a logical consequence we will use indiscriminately the names facula or flux tube. The extension of the code to a geometry allowing for facular elements of variable size and thermal properties and occupying different fractions of

the observed area is planned for the future, depending mainly on the memory capabilities of the available computers.

As in the previous chapter, the main aim of the simulations is to get a tool for a better understanding of the results emerging from the analysis of the observations, including the study of the different factors (solar, terrestrial and instrumental) affecting them.

6.1 Method

The 3D radiative transfer code described in the previous chapter offers the possibility to use an irregular grid for the x and y axis of the computational domain. In the present chapter this possibility has been exploited and a geometry of a flux tube has been constructed. If a regular grid would be used to construct the geometry of a flux tube and the sorrounding granular cell, a very small spatial step would be needed in order to resolve the expansion of the flux tube with height in the atmosphere. Since the flux tubes of the facular regions are smaller than the granular cells, this would lead to a very big computational box. Nowadays computers available in our institution do not have enough memory to run the radiative transfer code in such big computational boxes. Therefore, an irregular grid is needed. The spacing in x and y has been set to a small spatial step in the part of the grid where the flux tube is placed, to fully resolve its structure. For the outer atmosphere a greater spatial step has been chosen in order to include a large portion of the surrounding quiet photosphere (i.e. a granular cell).

Some works point to the existence of an atmosphere cooler than the intergranular one in the immediate surroundings of a flux tube (e.g. Bellot Rubio et al. 2000b, Deinzer et al. 1984). Tests on the influence of this atmosphere have also been performed, and a cool region around the flux tube has optionally been implemented in the geometry used. This cold region will be hereafter referred to as the "cool wall".

6.1.1 Geometry

A geometry has been constructed to simulate a flux tube and its surrounding atmosphere as shown in figure 6.1. In this representation the irregular grid of the computing box has been interpolated to a regular one for the sake of clarity, and a zoom of the magnetic region at two depths in the atmosphere, together with a portion of the quiet Sun are presented. The structure of the quiet Sun in the geometry is presented below in figure 6.2; in figure 6.1 it is not shown. Left panel stands for bottom layer at the model in the atmosphere, and right panel for upper one. The dark-gray area corresponds to the quiet Sun, the innermost

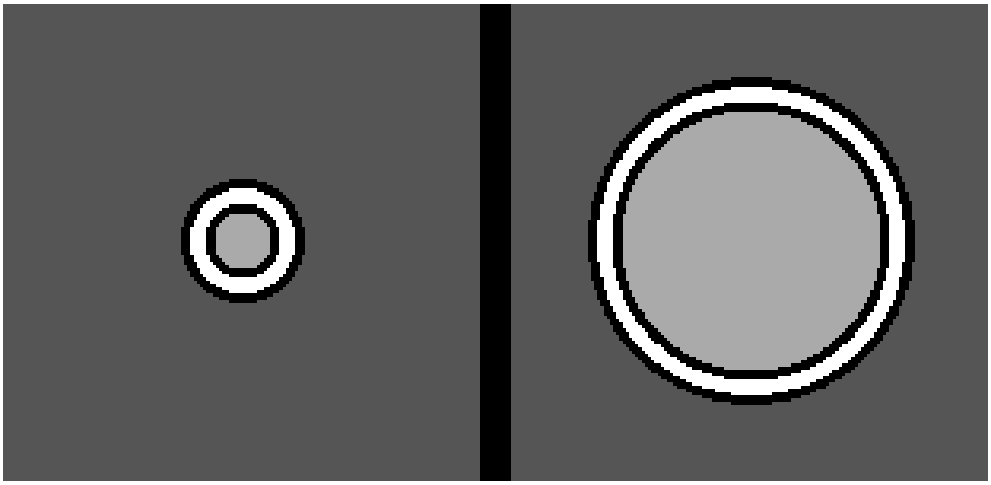

FIGURE 6.1— Geometry used to simulate a flux tube, left panel–bottom layer, right panel–upper layer of the model. Innermost light gray circle–flux tube, black rings–transition areas where linear interpolation between the different atmospheres is performed, white ring– region where the cool wall is placed.

light gray area corresponds to the magnetic flux tube, and the white ring around it to the area where the cool wall is placed. The black rings correspond to the transition areas where linear interpolation is performed between the different atmospheres in order to avoid discontinuities. When no surrounding cool wall is considered, the geometry used looks like that of figure 6.1 but without the outer black and white ring around the magnetic flux tube. The difference in diameter of the magnetic structure in the different layers reflects the expansion of the magnetic structure (the outward bending of the lines of force) with height producing the so-called "canopy".

The expansion with height of a given magnetic structure is computed by assuming a constant magnetic flux for all the heights and a constant magnetic field across the flux tube at each geometrical height . The magnetic flux is expressed as:

$$\Phi = \pi r(z)^2 B(z) = cte., \tag{6.1}$$

Therefore, the expansion of the walls of the magnetic flux tube can be written:

$$r(z) = \sqrt{\frac{\Phi}{\pi B(z)}}, \tag{6.2}$$

Thus, by fixing the value of the flux tube radius at a given height, the radius at other layers can be derived as a function of the magnetic filed model $B(z)$. For the sake of simplicity, it has been assumed that the thickness of the cool wall adjacent to the magnetic flux tube does not change with height, neither do the transition regions.

Our aim is to study the observable parameters derived from small magnetic structures which are embedded in a surrounding quiet Sun atmosphere. It is of interest to test if magnetic flux tubes are observable at different disk positions and what contrasts do they show. In the geometry of the quiet Sun, granules and intergranules are considered and flux tubes are placed in the intergranular lanes. A sinusoidal transition from granules to intergranules has been assumed. A unique granular structure is included in the computing box, distributed as shown in figure 6.2. The black circle stands for the region where the flux tube, cool wall and transition regions are placed at a given height in the atmosphere, white areas correspond to granular regions and grey ones to intergranular lanes. This geometry keeps costant at every height for granules and intergranular lanes, while the magnetic flux tube is assumed to expand with height at the expenses of the intergranular space.

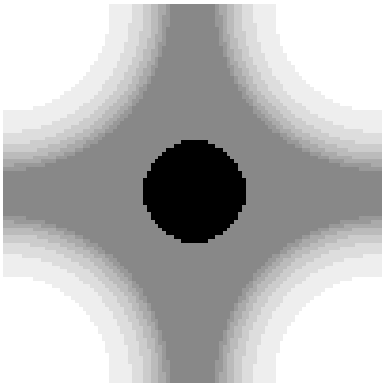

FIGURE 6.2— Geometry used to simulate the quiet photosphere surrounding a flux tube

This geometry is applied to atmospheres of magnetic elements, surrounding cool wall, granules and intergranules.

6.1.2 Atmospheric models

The information received when observing magnetic structures comes from deeper layers in the solar atmosphere than when observing the quiet Sun. This is due to the inhibition of convection by the magnetic field, which causes the magnetic structures to be cooler, and the photons to have a longer mean free path within them. Therefore, the semi-empirical atmospheres obtained with an inversion procedure applied to data of a magnetic structure include information on deeper layers in the Sun as compared to the semi-empirical atmospheres obtained by applying an inversion procedure to data of quiet regions.

But the cube of data supplied as the input of the 3D radiative transfer code has to contain information on the deeper layers in the whole 3D computational grid. Various prolongations of the quiet Sun atmospheric model have been essayed in the deeper region of the computational domain, realizing that the emergent relative intensity of faculae changes only by less than 0.01 % . This can easily be understood taking into account that the radiative transfer code used assumes LTE, i.e. there is no cross-talking between two adjacent points. Besides, in quiet regions the radiation observed comes from upper layers. Thus it can be concluded that these deep layers have no relevant influence in the emergent continuum radiation obtained.

Quiet atmospheres

In the present chapter the semi-empirical quiet atmosphere obtained by Rodríguez Hidalgo et al. (1995) described in chapter 5 is used.

The HSRA is a one component mean atmosphere. To obtain separated granular and intergranular stratifications it has been assumed a mean HSRA atmosphere with granular-intergranular mean fluctuations equal in percentage to those in the Rodríguez Hidalgo et al. (1995) model. This modified HSRA model, hereafter referred to as HSRAm, has also been used for some purposes in our computations.

It must be noted that each magnetic semi-empirical atmosphere is surrounded by a certain quiet atmosphere. However, care must be taken to do this in a full consistent manner. To that aim, it must be checked that the total pressure inside the magnetic region and outside it is the same. This has been tested between each pair of atmospheres used in the computations presented in the following sections.

Magnetic atmospheres

The semi-empirical atmosphere of Bellot Rubio et al. (2000b) was obtained by applying an inversion procedure to spatially averaged Stokes I and V profiles of

the Fe 6301.5 and 6302.5 Å lines in plage regions near disk center. The average profiles were constructed by summation of the spectra in all facular points with a degree of polarization, integrated over thea 6302.5 Å line, greater than 0.4 %. Therefore, they are more representative of strong magnetic fields and/or high filling factor regions. The Stokes profiles were derived from spectra of a facular region in the NOAA group 7197, observed with the Advanced Stokes Polarimeter at the Sacramento Peak VTT (U.S.A.) on June 18, 1992. They obtained semi-empirical tube models representing the internal atmosphere and the external medium, which is cooler than the intergranular lanes. They used the inversion code described in Bellot Rubio et al. (2000a) that computes in a self-consistent mode the atmospheric quantities, assuming the "thin flux tube approximation". The expansion of the flux tube with height was taken into account to perform the inversion. That code gives as an output the stratification of the magnetic field and of the flux tube radius among other physical quantities. The obtained values at z=0 are 1384 G and 50 km respectively. The estimated Wilson depression was 73 km.

Figure 6.3 shows the temperature stratification of the magnetic interior of this model and the external atmosphere. For comparison purposes, the intergranular atmosphere by Rodríguez Hidalgo et al. (1995) is also included in the figure (dashed line).

Representing a pore, the "hot model" of Collados et al. (1994) is also used in this chapter. It was obtained by using the SIR inversion code described in the previous chapter (Ruiz Cobo & del Toro Iniesta 1992). This inversion procedure gives the stratification of the atmospheric parameters inside the flux tube including magnetic field, but no surrounding medium is considered. This hot model resulted from the inversion of the Stokes V profile of a small spot. The value of the magnetic field at z=0 is 2300 G. The temperature stratification of this model is shown in Figure 4.4, chapter 4.

6.1.3 Combined quiet-magnetic models

The model atmospheres described above have been applied to geometries of flux tubes of different sizes. In table 6.1 a summary of the models used in this chapter is presented together with the names used to refere to them. The parameters characterizing each model are shown, namely: radius of the granular cell included in the computational box, radius of the flux tube at z=0 and inclusion or not of the cool wall. The stratification of the magnetic field and the Wilson depression are assumed to remain unchanged independently of the flux tube radius. The size of the granular cell has been set to the mean value derived from the observations in chapter 2, that is, 1.36 Mm^2. The width of

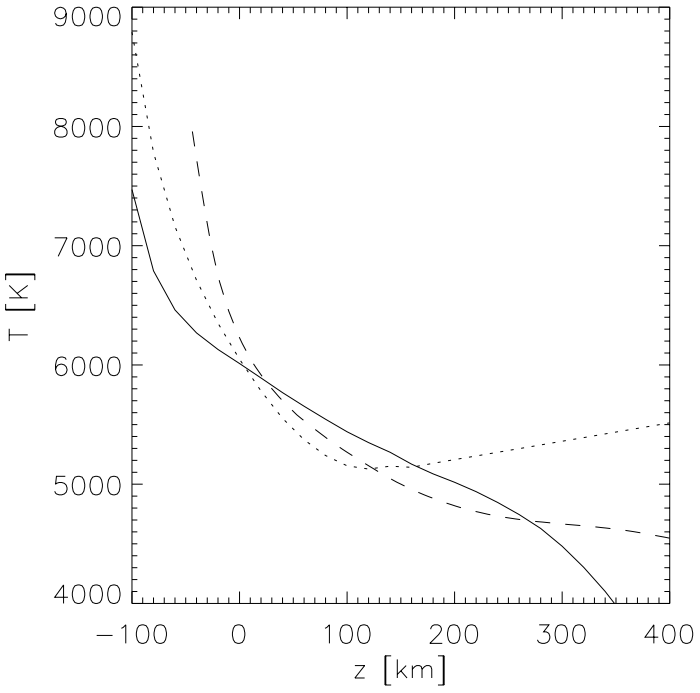

FIGURE 6.3— Temperature stratification of the Bellot Rubio et al. (2000b) model of magnetic interior (solid line) and cool wall (dotted line). For comparison purposes the intergranular atmosphere by Rodríguez Hidalgo et al. (1995) is also plotted (dashed line)

the cool wall around it, if any, has been set to 20 % of the flux tube radius at z=0. Test have been performed on how various widths of the cool wall affect the derived observables, obtaining no significant change. Therefore, as a first approximation, we have assumed a width of 20 % the radius of the flux tube at z=0.

All the models described in table 6.1 correspond to facular structures except the SPHT model which corresponds to a pore.

6.1.4 Response functions

As explained in previous chapters, the response functions to the temperature (RFT) are useful to interpret the obtained results. In figure 6.4 the normalized RFT of the facular model of Bellot Rubio et al. (2000 b) are presented together with those of the cool wall at λ8000 Å and λ15500 Å . In each panel the RFT's

TABLE 6.1— Models of granulation

QS atmosphere	Magnetic atmosphere	Name	Granular cell radius [km]	Magnetic radius at z=0 [km]	Cool wall
Rodríguez Hidalgo et al. (1995)	Bellot Rubio et al. (2000 b)	RB1	1200	62	YES
Rodríguez Hidalgo et al. (1995)	Bellot Rubio et al. (2000 b)	RB2	1200	124	YES
Rodríguez Hidalgo et al. (1995)	Bellot Rubio et al. (2000 b)	RB3	1200	310	YES
Rodríguez Hidalgo et al. (1995)	Bellot Rubio et al. (2000 b)	RB4	1200	434	YES
Rodríguez Hidalgo et al. (1995)	Bellot Rubio et al. (2000 b)	RB5	1200	620	YES
Rodríguez Hidalgo et al. (1995)	Bellot Rubio et al. (2000 b)	RBNC1	1200	62	NO
Rodríguez Hidalgo et al. (1995)	Bellot Rubio et al. (2000 b)	RBNC2	1200	124	NO
Rodríguez Hidalgo et al. (1995)	Bellot Rubio et al. (2000 b)	RBNC3	1200	310	NO
Rodríguez Hidalgo et al. (1995)	Bellot Rubio et al. (2000 b)	RBNC4	1200	434	NO
Rodríguez Hidalgo et al. (1995)	Bellot Rubio et al. (2000 b)	RBNC5	1200	620	NO
HSRAm	Collados et al. et al. (1994)	SPHT	1200	5400	NO

for μ=1, 0.9, 0.8, 0.7, 0.6, 0.5, 0.4, 0.3, 0.2, 0.1. are shown. Curves with larger contributions in higher layers stand for positions nearer to the solar limb.

This figure complements with figures 4.5 and 5.5 which show the RFT computed for the pore mean atmosphere of Collados et al. (1994), for the HSRA quiet atmosphere (Gingerich et al. 1971) and for the granular and an intergranular mean atmosphere of the Rodríguez Hidalgo et al. (1995). Note that the radiation observed comes progressively from deeper layers in the sequence: granules, intergranular lanes, cool wall, faculae and pores.

6.1.5 Emergent intensities

In this section we present the emergent intensities for some models (the extreme cases: the largest and the smallest flux tubes) to let the reader visualize the output of the radiative transfer code.

In figure 6.5 the emergent intensity of the RB1 model at λ8000 Å is presented for μ=1., 0.9, 0.8, 0.7, 0.6, 0.5, 0.4, 0.3, 0.2, 0.1. In this figure, and in all the other figures where emergent intensities are presented, the solar limb is placed towards the right y-axis of each panel.

The fact that faculae appear bright in the raw emergent intensity images at μ=1 reflects the observations inverted to obtain this facular atmospheric model, in which an intensity excess was detected for faculae at disk center. Note that in the figure the foreshortening due to the perspective effect is not included. In

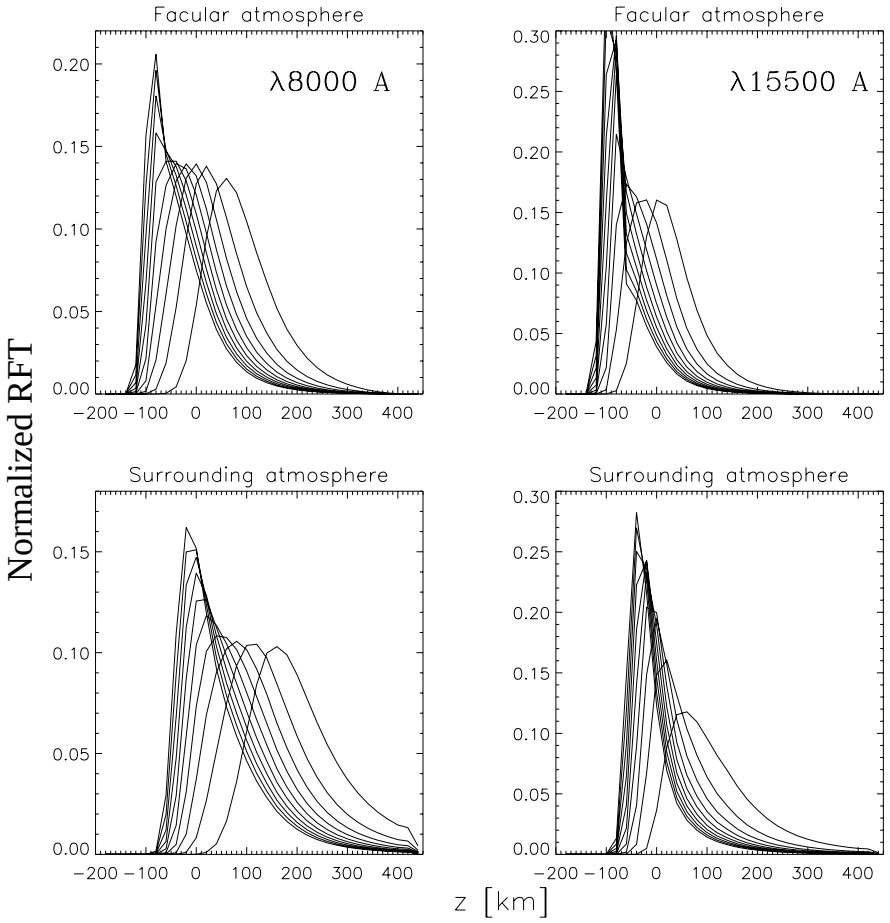

FIGURE 6.4— Normalized RFT's of the facular model by Bellot Rubio et al. (upper panels) and of the cool surrounding atmosphere (lower panels) at λ8000 Å (left panels) and λ15500 Å (right panels) for μ=1, 0.9, 0.8, 0.7, 0.6, 0.5, 0.4, 0.3, 0.2, 0.1.

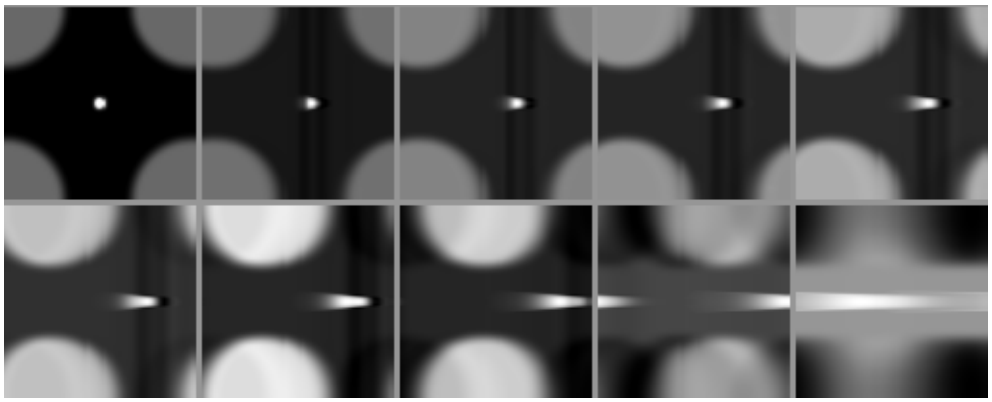

FIGURE 6.5— Emergent intensity of the RB1 model at λ8000 Å for μ=1., 0.9, 0.8, 0.7, 0.6, 0.5, 0.4, 0.3, 0.2, 0.1 (from left to right and from top to bottom).

order to analyze this data, it will have to be artificially introduced by rebinning the images to the desired size at each heliocentric angle. However, the radiative effects are already apparent. The facula elongates with increasing heliocentric angles. Due to the rebinning performed to resize the emergent intensity images to a regular grid, a vertical dark band appears in the central region of each image as an artifact. Note that on the right hand side of the facula for μ 0.9–0.3, a dark structure appears. This is caused by the cool wall surrounding the magnetic flux tube.

The emergent intensity of the RBNC1 model presents visually no difference with the RB1 model. Therefore, its emergent intensities are not presented. Eventhough the cool wall does not significantly change the outfit of the images, in further sections its effect on the mean facular intensity will be studied. The dark structure appearing on the right hand side of the facula for μ 0.9–0.3, is caused in this case by the intergranular lane sorrounding the magnetic flux tube.

The emergent intensity for the RBNC5 model model is presented in figure 6.6. For μ=1–0.5 a dark circle inside the facular structure is visible in the raw emergent intensity images. However, when the images are convolved with PSFs to simulate the degradation due to telescope and terrestrial atmosphere the circle is not observable. This dark circle is caused by the temperature stratification of the flux tube and the surrounding intergranular atmosphere in combination with the magnetic canopie of the flux tube.

Because of the relative high intensity of the facular structure, the granular cell in figures 6.5 and 6.6, is represented by a short dynamical range in the gray

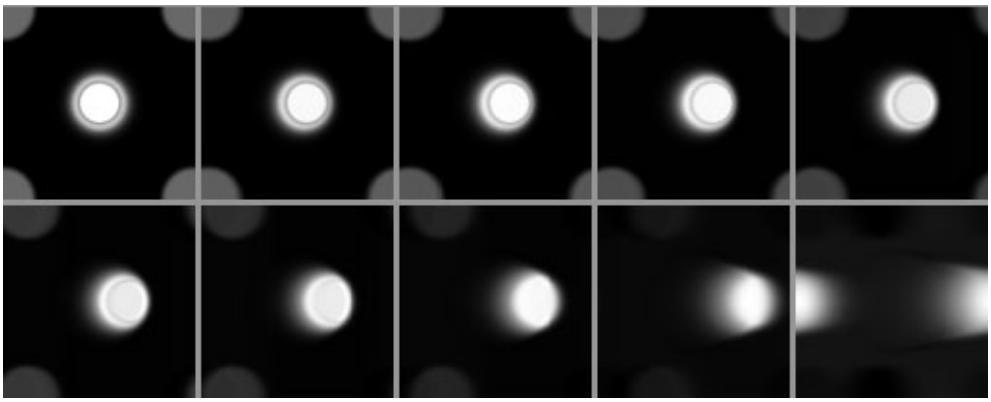

FIGURE 6.6— Emergent intensity of the RBNC5 model at λ8000 Å for μ=1., 0.9, 0.8, 0.7, 0.6, 0.5, 0.4, 0.3, 0.2, 0.1 (from left to right and from up down).

scale and consequently the gradual transition granule-intergranule exhibited in figure 6.2 is not evident here.

6.2 CLV of facular contrast

The procedure described in section 4.4.1 of chapter 4 has been used to identify faculae. The images of emergent intensity at λ8000 Å and λ15500 Å have been rebinned to the desired size in order to simulate the foreshortening due to the perspective effect on the solar surface. Then, they have been degraded with a low passband filter (LPBF) with the cutoff frequency of a 50 cm telescope diffraction limited at λ15500 Å. This procedure simulates, on the one hand, the loss of high frequencies due to the cutoff of the telescope, and on the other hand the degradation described in section 4.4.1 of the λ8000 Å images to the λ15500 Å resolution. Afterwards, images are degraded, as in chapter 5, with a MTF to simulate the effect of the earth atmosphere by means of a telescope assumed diffraction limited. Then difference images will be computed. It is necessary to do good simulations of the real observing conditions in order to make comparable the images depending on the wavelength. It is known that the earth atmosphere influences differentially at different spectral ranges. We have introduced this effect into our simulations by degrading the images at λ8000 Å and λ15500 Å with telescopes of different apertures. It has been assumed that the telescope aperture, D, varies with wavelength as the Fried parameter does: $D = r_o \propto \lambda^{6/5}$ (see chapter 5, section 5.2.1). Finally, the images are normalized to the mean value at quiet regions and the difference images are

computed following equation 4.1.

In figure 6.7, the difference image of the RBNC1 model at μ=1 with a pixel size of 0.08 arcsec, equal to that of our observations at $\lambda 0.8\mu$m, is presented. As described in chapter 5, the radiative effects produce apparent larger granular sizes at λ15500 Å than at λ8000 Å, which causes the bright and dark rings in the difference image around the granular structures at the borders of the computing box. As explained in chapter 4, the facula appears dark in the difference image due to its different temperature stratification as compared to the quiet Sun.

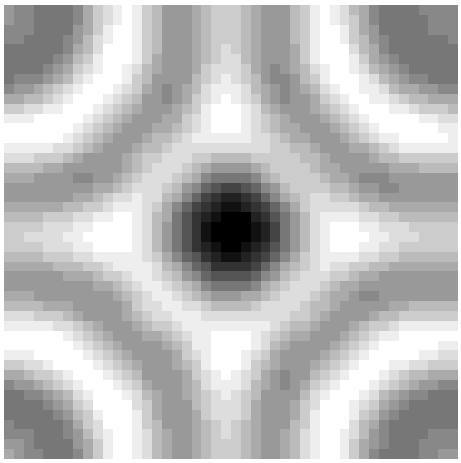

FIGURE 6.7— Difference image of the RBNC1 model at μ=1 with a pixelsize of 0.08 arcsec.

Note that the radiative transfer computations have been performed with an irregular grid that completely resolved the structure of the flux tube. However, in real observations the diffraction limit of the telescope impedes the resolution of structures smaller than the telescope cutoff which makes senseless the use of too small pixelsizes. In the present study the images must be rebinned to a correct pixel size which is comparable to that of the observations. However, too large pixel sizes can not be used since the field of view of the computational box is not very large and, therefore, big pixel sizes produce boxes with a small amount of pixels, where no study can be performed.

6.2.1 Influence of facular size

The threshold criteria expressed in equation 4.3 has been used to identify facular regions. The g parameter has been set to 1.5. Then the mean facular intensity has been computed for the λ8000 Å and λ15500 Å images.

In figure 6.8 the CLV of mean facular intensity for the RB1, RB2, RB3, RB4 and RB5 models at λ8000 Å (upper panels) and λ15500 Å (lower panels) are presented. The straight line at a constant facular contrast of 1 stands for the mean value of the intensity of the quiet Sun. A pixel size of 0.″08 has been chosen for this computations. A study has been performed on how do different pixel sizes in the range 0.″05-0.″5 influence the obtained CLV curve of the mean facular intensity, obtaining that the curve does not significantl change with this parameter.

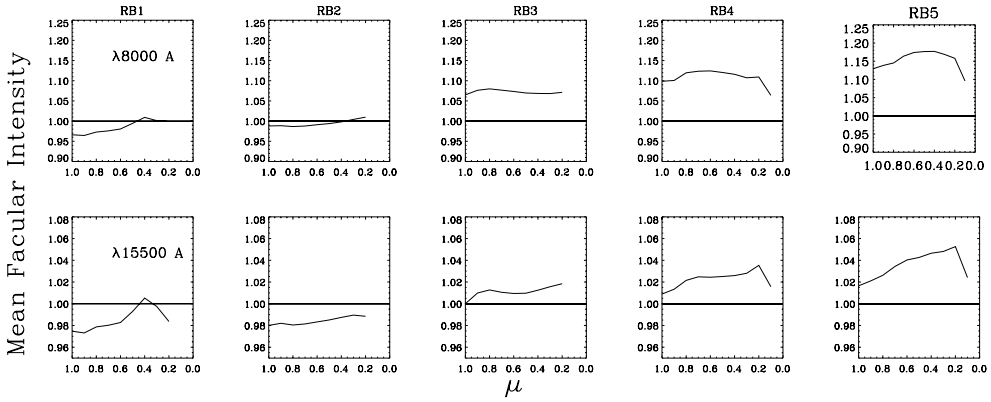

FIGURE 6.8— CLV of mean facular intensity for the RB1, RB2, RB3, RB4 and RB5 models at λ8000 Å (upper panels) and λ15500 Å (lower panels).

In figure 6.8 the small faculae at λ15500 Å and λ8000 Å are slightly darker than the mean quiet photosphere, increasing their intensit brightness to values near that oclose to the quiet Sun intensity for large heliocentric angles. For larger facular sizes the value of the mean facular intensity at disk center augments. At λ8000 Å, medium and large size faculae show an increase of the relative contrast from disk center to a certain heliocentric angle and then a decrease further on. As defined in chapter 4, the heliocentric angle where the mean facular intensity peaks is referred to as μ_2. For increasing facular sizes the peak occurs at a smaller μ_2, and it has greater mean facular intensity. At λ15500 Å, medium and small faculae present an increase of the mean facular intensity from the disk center to the limb when a pixel size of 0.″08 is used. Large facula show a peak of the mean facular intensity at μ_2=0.2.

The described CLV of the contrast dependence on the facular size is similar to that observed in chapter 4 at large heliocentric angles, but different for small ones. For comparison purposes, the observed CLV of the mean facular intensity for different bins of facular sizes described in chapter 4 is presented in figure

6.9. In the figure, faculae show a decreasing value of the facular contrast at disk center for increasing facular sizes. This was interpreted in terms of an increasing convection inhibition for larger facular sizes, i.e. for larger magnetic fields. However, in the simulations analyzed here the same facular atmosphere with the same stratification of magnetic field is considered for every facular size. Therefore, a decrease of the facular contrast with facular area is not expected at disk center. Rather an increase is found. This is due to the better resolution of faculae for increasing facular sizes. As mentioned above, for small faculae the information of the magnetic structure is mixed with the surrounding cool atmosphere and intergranular lane.

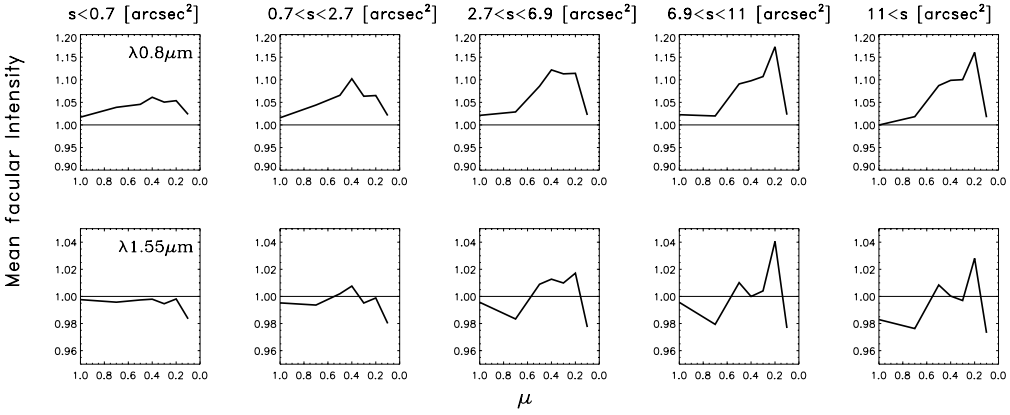

FIGURE 6.9— Observed center to limb variation of the mean facular intensity for different bins of facular sizes (see chapter 4, section 4.4.2).

The facular contrast at disk center is larger at λ8000 Å than at λ15500 Å for medium and large faculae. This can be understood by looking to figures 6.4 and 6.3. The regions where the observed radiation comes from are higher in the photosphere at λ8000 Å than at λ15500 Å. Since around $z = 0$ km a crossing point of the facular and quiet Sun temperature occurs, with a subsequent relative increase of the facular one, a larger facular contrast is observed at λ8000 Å than at λ15500 Å. However, at $z \sim 150$ km a second crossing point occurs between the temperature of the cool surrounding atmosphere and the magnetic atmosphere, and at $z \sim 270$ km between the intergranular and the facular one. This produces the mean facular intensity to decrease for large heliocentric angles at λ8000 Å , because at this wavelength the observed radiation comes from these high layers. At λ15500 Å the decrease of the mean facular intensity for large heliocentric angles is not found because the observed radiation comes from deeper layers.

For increasing heliocentric angles one wall of the flux tube blocks the other

one, due to a pure perspective effect. Since in the present simulations the Wilson depression is assumed to be the same for every facular size, the hot facular atmosphere remains visible up to larger heliocentric angles for increasing facular sizes. This explains the μ_2 to move to smaller μ's for increasing facular sizes.

In chapter 4 the hot wall model was used to explain the observed trends of the mean facular intensity. This model explains the brightening of the faculae from the center to the limb of the solar disk as a consequence of the entrance in the observers field of view of the 'hot wall' behind the evacuated flux tube. From a certain heliocentric angle onwards, only a fraction of the hot wall is visible and therefore the contrast decreases. From pressure equilibrium the temperature is expected to be smaller inside the facular flux tube than in its quiet surrounding. However, the lateral radiative heating produced by the hot wall makes the temperature increase inside the facula and produces a radiative cooling around it. This effect explains why in the range z ~0–180km the facula appear hotter than the external atmosphere in the Bellot Rubio et al. (2000b) model, and why does the surrounding external atmosphere have smaller temperatures than the intergranules. Deinzer et al. (1984), modeling stationary magnetic flux elements, found the formation of a cool wall around the flux tube. They claim that faculae are seen dark at disk center as a consequence of this cooling around the magnetic structure, and that an additional heating mechanism is required to reproduce the observed CLV of facular contrast. Note that the Bellot Rubio et al. (2000b) facular model has been computed applying an inversion process to data at disk center and therefore the geometric effects due to a lateral line of sight have not been taken into account in the computations. However, when the CLV curve of the mean facular intensity is calculated the observed trends of the facular contrast near the limb, and the dependence of μ_2 with facular size are properly reproduced.

The same curves as presented in figure 6.8 but now computed for the RBNC1, RBNC2, RBNC3, RBNC4 and RBNC5 models are shown in figure 6.10.

The observed trends are the same as in figure 6.8. The only difference caused by not including the cool wall around the facular flux tube is to produce slightly larger values of the mean facular intensity. Also not significant differences are found in the pixel size dependence of the CLV curves of the mean facular intensity.

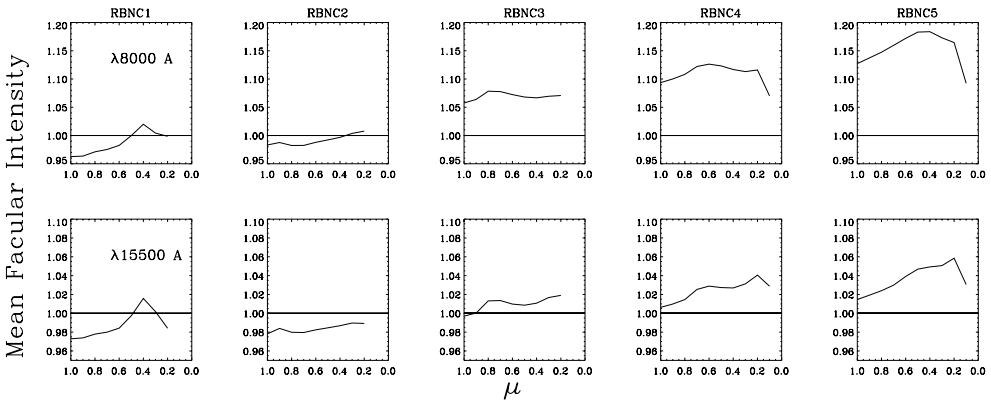

FIGURE 6.10— CLV of mean facular intensity for the RBNC1, RBNC2, RBNC3, RBNC4 and RBNC5 models at λ8000 Å (upper panels) and λ15500 Å (lower panels).

6.2.2 Degradation by Earth's atmosphere

The CLV of mean facular intensity presented above have been computed by assuming a fixed terrestrial atmospheric turbulence the contribution of which was simulated with a telescope of diameters varying with wavelength as $D = r_o \propto \lambda^{6/5}$. A study on how do different atmospheric conditions influence the results obtained has also been performed. To that aim, the earth degradation has been simulated with telescopes of 100 cm, 75 cm and 50 cm diameters at λ15500 Å(see chapter 5, section 5.2.1). Figure 6.11 presents the obtained CLV of mean facular intensity for the RBNC1 and RBNC5 models at λ8000 Å (upper panels) and λ15500 Å (lower panels). The same kind of computations have also been performed on the RB1, RB5 models obtaining the same results. Therefore their CLV curves are not presented in figure 6.11.

As seen in the figure the effect of poor atmospheric conditions is not very significative for small facular sizes (left panels). However, for large faculae (right panels) it produces a decrease of the mean facular intensity at all the heliocentric angles.

6.3 CLV of facular area

In Chapter 4 it was found that studied faculae were less conspicuous in the difference images near the solar limb than near disk center. Two different possible interpretations were given for this fact. On the one hand, the decay of the active region during its transit from the center to the limb produced a decrease of the filling factor which, in general, produces smaller magnetic

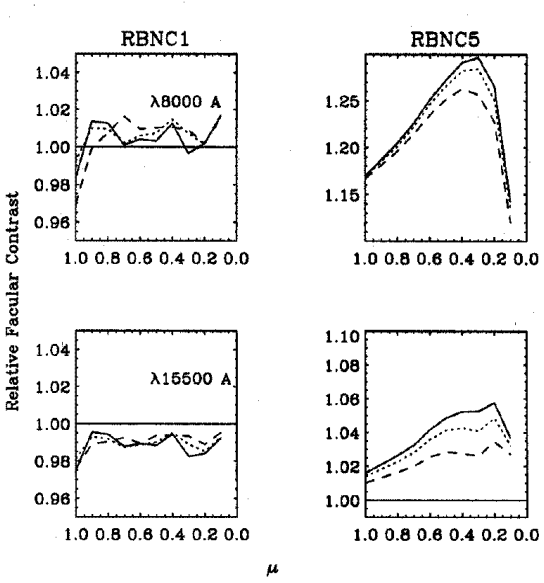

FIGURE 6.11— CLV of mean facular intensity for the RBNC1 and RBNC5 models at λ8000 Å (upper panels) and λ15500 Å (lower panels). The degradation due to earth atmosphere is simulated at λ15500 Åwith a diffraction limited telescope of 100 cm (solid line), 75 cm (dotted line) and 50 cm (dashed line) diameter. The corresponding telescope diameters at λ8000 Å are computed according to the law $D \propto \lambda^{6/5}$.

structures, together with the limited resolution of the observations. On the other hand, the different change of the response functions with heliocentric angle for the magnetic and non-magnetic atmospheres and their different temperature stratifications.

The simulations performed in this chapter offer the possibility to study how does the appearance of faculae in the difference images change with heliocentric angle. This can be used to validate one of the two possible explanations mentioned above. Besides, the CLV of facular area can also be determined.

The facular sizes are computed on the degraded images used in the previous section to obtain the CLV of the mean facular intensity. Areas are determined by counting the pixels belonging to the regions identified photometrically as a facula by means of equation 4.3. The correction for foreshortening has been performed by dividing each facular area by μ.

In figure 6.12 the CLV of facular area for the RBNC1, RBNC2, RBNC3, RBNC4 and RBNC5 models is presented.

From the expansion of the magnetic flux tubes with height, an increase of

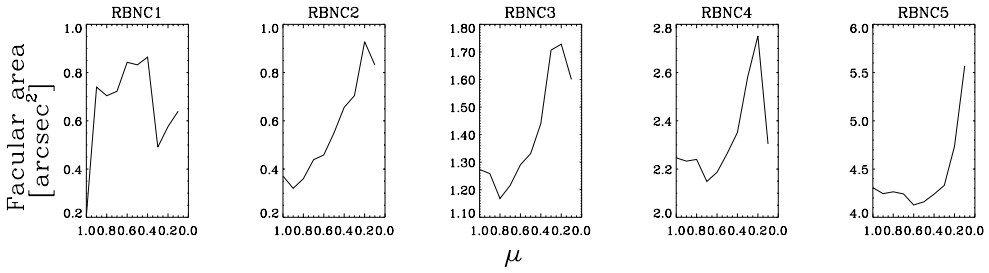

FIGURE 6.12— CLV of facular area for the RBNC1, RBNC2, RBNC3, RBNC4 and RBNC5 models.

the facular area with heliocentric angle is expected. In figure 6.12 this increase is observed although at $\mu \sim 0.1$ a decrease is obtained in some panels. However, at this large heliocentric angle the structures are not properly resolved due to the foreshortening effect. Thus, we can conclude from figure 6.12 that facula have an apparent size which increases from the center to the limb, and that this increase amounts approximately 0.8-1 arcsec^2.

This result rules out the explanation presented above of facula being less conspicuous in the difference images near the limb due to the different change of the response functions with heliocentric angle for the magnetic and non-magnetic atmospheres and to their different temperature stratifications. It can be stated that in chapter 4 the faculae were less apparent in the difference images near the limb due to the decay of the active region.

6.4 CLV of pore brightness

In Section 4.4.4 the CLV of maps of brightness temperature differences were studied. It was found that near disk center a ring like structure with small temperature difference appeared around pores. For larger heliocentric angles, this ring-like structure disappeared in the temperature difference images, appearing a bright ring instead. This was interpreted as a signature of the less densely packed flux tubes around the pore suggested by Martínez Pillet (1997). This thin facular-like magnetic flux tubes would belong to the same trunk as the pore.

The CLV of the brightness temperature difference maps obtained from synthetic images of a pore are studied. To that aim, the emergent intensity images of the SPHT model are computed at λ8000 Å and λ15500 Å. The same procedure applied to the synthetic images of faculae prior to computation of the difference images is applied here. Then, applying equation 4.4

the brightness temperatures are obtained, and the difference maps computed ($\Delta T_b = T_b(1.55) - T_b(0.80)$). In figure 6.13 a composite figure showing the center to limb variation of the SPHT model in the temperature difference images (upper panels), $T_b(1.55)$ (middle panels) and $T_b(0.8)$ (lower panels) at μ=1.,0.8,0.6,0.4,0.2 (from left to right) is shown.

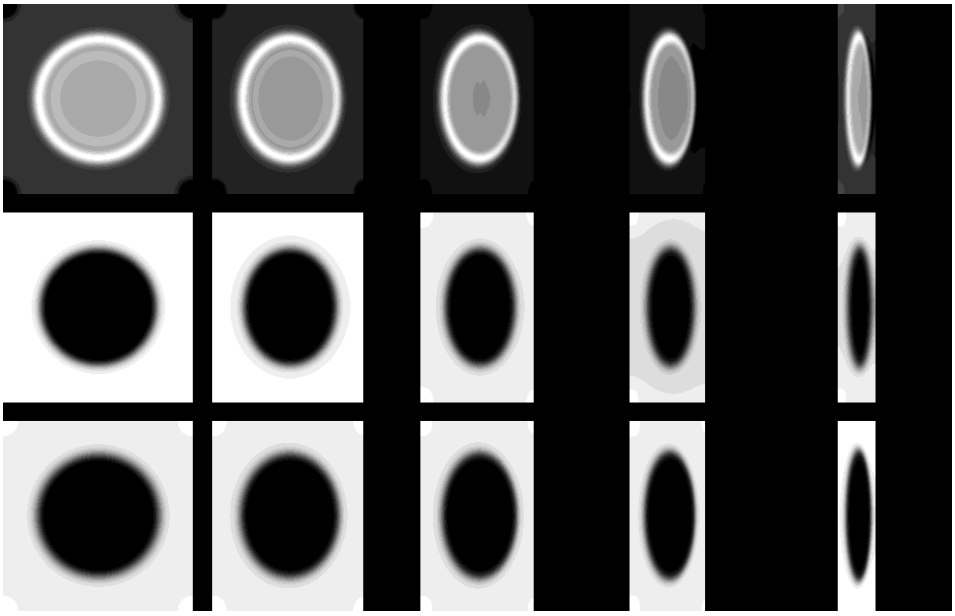

FIGURE 6.13— Composite figure showing the center to limb variation of the SPHT model in the temperature difference images (upper panels), $T_b(1.55)$ (middle panels) and $T_b(0.8)$ (lower panels) at μ=1.,0.8,0.6,0.4,0.2 (from left to right).

No dark rings appears in the temperature difference maps around the pore. Instead a bright ring is found which is visible for every heliocentric angle. Due to the expansion of the flux tube with height the pore is seen larger at λ8000 Å than at λ15500 Å. Since pores are colder than the surrounding quiet photosphere, a ring of larger temperature appears around the pore in the temperature difference maps. It was not expected to find in this simulation a dark ring since no facular-like structures are included around the pore in the SPHT model, as suggested by Martínez Pillet (1997). However, the fact that the bright ring is seen shows that really some atmosphere different than the granulation must surround the pore in order to compensate the magnetic canopy effect on the temperature difference map and produce a dark ring as shown in chapter 4.

6.5 Conclusions

A three dimensional radiative transfer code has been applied to different geometries of a flux tube simulating faculae and pores. By means of differential photometry faculae have been identified.

The influence of the cool wall on the mean facular intensity has been tested obtaining that it produces a slight decrease of its absolute value, although no qualitative difference in its CLV.

The mean facular intensity has been obtained for faculae of different sizes with an equal magnetic field stratification. The mean facular intensity is found to increase with facular size at disk center due to the better resolution of the magnetic flux tube. The facular contrast peaks at a disk position (μ_2) between disk center and limb at λ8000 Å and at λ15500 Å.

For increasing facular sizes the mean facular intensity peak occurs at smaller μ_2 and has larger mean facular intensity. This can be explained in terms of the 'hot wall' model together with the constant Wilson depression assumed in the present simulations for every facular size. Note that the facular atmospheric model used was obtained by applying an inversion method to data at disk center. Therefore, the geometrical effects due to the perspective produced by a change in heliocentric angle have not been included in the computation of the atmospheric model. However, it reproduces the observed trends near the limb.

The influence of different terrestrial atmospheric conditions has also been tested. For small facular structures poorer atmospheric conditions produce no significant change in the values of the mean facular intensity at different μ's. For large faculae the mean facular intensity decreases as the seeing gets worse.

Simulated facula present an apparent size which increases from the center to the limb. This increase amounts approximately 0.8-1 arcsec^2 independently of the facular size. This is due to the assumptions used for computing the variation of the flux tube radius with geometrical height (see equation 6.2).

The brightness temperature difference maps of a pore have been computed. No dark ring is found surrounding the pore. On the contrary, the magnetic canopie produces the a bright ring around it. We suggest that a facular-like atmosphere sorrounding the pore should reproduce the observed feature.

7

Conclusions and future studies

In the present thesis a study of the center-to-limb variations of the photometric properties of photospheric structures (granulation and faculae) has been performed. Combining data obtained for different heliocentric angles at various observing wavelengths ($\lambda 0.67\mu$m, $\lambda 0.8\mu$m and $\lambda 1.55\mu$m) information about the vertical structure of these features has been deduced.

In a second phase of the memory the obervational results have been compared to the output of numerical simulations trying to test the influence of variable observing conditions and the goodness of different theoretical and semi-empirical models.

7.1 Conclusions

Among the main obtained results the following can be outstanded:

7.1.1 Solar Granulation

- The images obtained during a partial solar eclipse could be satisfactorily restored of the degradation due to earth's atmosphere by means of the implementation of a novel restoration filter based on the observed data themselves. The PSF was estimated from the lunar limb.

- The granular contrast obtained at the solar disk center is 9.6% at $\lambda 6708$ Å, 6.1% at $\lambda 0.8\mu$m and 2.9 % at $\lambda 1.55\mu$m. If a Wien law is assumed these contrasts can be converted to λ 5000 Å, obtaining contrast of 12.88% (images restored from the degradation caused by the earth atmosphere), 9.7% and 9.0%, respectively. This is a proof of the excellent quality of the observations used in this thesis.

- A monotonic decrease in the granular contrast toward the limb has been obtained for the three observing ranges. The steepness of the curves increases with decreasing wavelength, probably due to the different range of formation. Simulations show that the wavelength dependence of the CLV curves is highly related to the details of the model atmosphere used for the computations. Besides, the foreshortening and degradation by terrestrial atmosphere and telescope aberrations can change the trend.

  Our curve at $\lambda 6708$ Åshows one of the greatest overall slopes when compared to those obtained by other authors. In principle, this points to a steep gradient of ΔT with the height. However, the simulations indicates that the shape of the CLV curve does not depend very significantly on the steepness of the ΔT decay. Smaller gradients of the mean temperature produce larger values of the contrast at disk center and steepest decays from the center to the limb. Therefore, our results point to a steep ΔT gradient in the photosphere together with a smooth mean T stratification.

- A general increase in both granular and intergranular areas is found for positions near to the solar limb at the three observing wavelengths. For any disk position no typical granular size is found. In contrast, intergranular areas seem to have a typical size characterized by the maximum of the intergranular area histogram.

  The mean wavenumber $\overline{k}$ of the equivalent 1D power spectra obtained by azimuthally integrating the 2D spectra along ellipses of ellipticity $1-\mu$ has been obtained for different μ-positions. Its value at disk center amounts ~ 6.15 Mm^{-1} at $\lambda 6708$ Å. The CLV of $\overline{k}$ shows a monotonic decrease toward the limb, thus indicating a progressive augmentation of the mean spatial scale with increasing height in the solar photosphere. Simulations show that the radiative transfer effects produce an apparent decrease of the $\overline{k}$ with heliocentric angle not correlated with a physical expansion of the granules with height. However, the amount of the $\overline{k}$ decrease is larger in the observations than in the simulations. Therefore, we can attribute, at least partially, the decrease of $\overline{k}$ to a physical expansion of granules with height in the photosphere, in agreement with the increase of the mean granullar cell size found.

- An effective transfer of power from lower to higher wavenumbers in the dimension parallel to the solar limb is found. This fact can be interpreted as a manifestation of the presence of small granular structures which penetrate into higher photospheric layers than the large ones. The apparent contradiction of this result with the one of the previous item is solved

when we take into account that the maximum contribution to the power spectra comes from the low spatial frequencies, and that a general expansion of small and large granules with height in the photosphere would produce an increase of the mean granullar cell size, independently wether large or small granules are more effective penetrating into higher layers.

- Spatial scales of 0."53 (eclipse observations) or 0."96 ($\lambda 0.8\mu$m observations) are detectable up to the very limb. Using a simple Eddington Barbier–approximation, this means that we observe structures up to atmospheric heights of $z \approx 200$ km or z$\approx$ 220 km above $\tau = 1$, respectively. Simulations indicates that a change in the height at which the temperature fluctuations, ΔT, associated to the granulation disappear produces different shapes of the CLV curves but similar values of the granulation contrast. A vanishing point higher up in the photosphere gives place to smoother CLV curves.

- A decrease in the Granular Filling Factor (GFF) from the disk center to $\mu = 0.5$, and an increase for larger heliocentric angles is measured both at λ6708 Å and $\lambda 0.8\mu$m. In the $\lambda 1.55\mu$m images, the CLV curve of the GFF is more noisy and a clear minimum is not detected. Simulations show that the GFF presents a dependence with μ wich varies for different model atmospheres but is not correlated with a relative change of granular-intergranular areas with geometrical height.

- The mean and maximum granular intensities of small granules show a linear increase with cell area, and a constant average intensity for granules with equivalent cell diameters larger than $d_{\rm g} \sim 2\farcs0$. Intergranular mean and minimum intensities do not show these two differenced slopes in their variation with $A_{\rm c}$. The intergranular mean intensity stays constant in average for every cell size while the intergranular minimum intensity decreases almost linearly with cell size, although a larger dispersion is observed for smaller granules.

- The agreement of the CLV curves produced by the different theoretical and semi-empirical models to our observations has been tested. The Rodríguez Hidalgo et al. (1995) semi-empirical model atmosphere reproduces reasonably the observed center to limb variation curve of the granular contrast. However, a merging point of the granular and intergranular temperatures higher up in the photosphere would still produce a better agreement with our observations. The theoretical 3D model of Stein & Nordlund (1999) does reproduce also the observed CLV curve in

a reasonable way although the contrasts are larger and present a steeper decrease than our observations. The 2D models of Gadun (1995) give larger values of the contrast and smoother decreases from the center to the limb than our observations.

7.1.2 Facular regions

- The observed facular properties and the preliminary results of the simulations can be explained in terms of the 'Hot wall' model.

- At disk center, faculae have on average no contrast in $\lambda 0.8\mu$m and appear as dark structures in $\lambda 1.55\mu$m. We have observed the change from dark to bright facula in $\lambda 1.55\mu$m at μ=0.5-0.6. On average, for both observed wavelength channels, the facular intensity is observed to increase with heliocentric angle up to μ=0.3. For larger heliocentric angles the facular intensity decreases.

  Simulations using the Bellot Rubio et al. (2000) model atmosphere of a facula produce a facular contrast which peaks at a disk position (μ_2) between disk center and limb at λ8000 Å. However, at λ15500 Å the synthetic relative facular contrast increases from disk center to the limb. It must be noted that the semi-empirical facular model atmosphere of Bellot Rubio et al. (2000) was computed by applying an inversion method to data obtained at disk center and, therefore, the geometrical effects due to a oblique line of sight, which play an important role in the 'Hot Wall' model, were not included in this computations. However, in our preliminary simulations a qualitative agreement is found with our observations. This strongly supports the 'Hot Wall' model which predicts a peak of the facular contrast somewhere between disk center and the limb. We want to stress that this result has great implications for the models of the total solar irradiace variations with the solar cycle. Nowadays, most of this models assume a monotonic increase of the facular contrast from disk center to the limb. Our results point to this assumption not beeing correct.

- Studies on the size dependence of facular intensity have revealed that large faculae have lower intensities at disk center but higher near the limb than small faculae. In addition, for large faculae the facular intensity peaks at positions nearer to the solar limb. The observed dependence of the facular intensity CLV on the facular size supports the existence of a small range of Wilson depressions in the facular flux tubes.

- The facular size distribution has also been computed and the smaller facular sizes are found to be the most frequent.

- Faculae show brightness temperature differences smaller than quiet regions at disk center. This difference decreases and almost disappears as approaching to the limb. Pores show larger temperature differences than quiet regions at disk center but smaller near the limb.

  Maps of temperature differences have been computed. We observe around pores a ring like structure that has small temperature difference at disk center. However, as approaching to the limb this ring-like structure disappears in the temperature difference image, appearing a bright ring in the temperature maps instead. We interpret this as a signature of the presence of less densely packed flux tubes around the pore suggested by Martínez Pillet (1997). The simulations don't reproduce such dark ring, showing only a bright one, instead. We suggest, that a facular like atmosphere should reproduce the observed feature.

- Pores show brightness temperatures that extend smoothly the cloud of points corresponding to facular regions. This means that both facula and pores share the same physical mechanism (lateral heating and inhibition of convection), which simply changes its contribution as a function of the size of the structure.

7.2 Future studies

The results obtained in the present thesis can be complemented with future studies which will help to understand with deeper insight some open questions concerning the solar photospehere, its observational characterization and the interpretation of the results by means of numerical modelling.

- The studies of the CLV of solar granulation in the infrared have been partially limited by the low signal-to-noise ratio at large heliocentric angles. The repetition of this kind of observations with larger telescopes such as the future NSST (1 m diameter) or the GREGOR (1.5 m) will allow to increase this relation, thus enabling the characterization of the granulation at these large wavelengths.

- The adquisition of time series of the solar granulation at different heliocentric angles would allow the correct filtering of the p-modes at each disk position. This kind of data would be suitable for studying the CLV of the granular contrast and of other morphological properties characterizing the solar granulation.

- The numerical simulations of the solar granulation presented in this thesis could be extended by means of increasing the spatial resolution of the computational grid. Besides, the development of a code which would iteratively modify the model atmosphere of the granulation, compute the CLV of its contrast and match it to the observed one would allow to obtain a guess of the stratification of the physical quantities in the solar atmosphere that fits best the observations.

- The numerical simulation of small magnetic structures could be extended by means of applying the same procedure to different model atmospheres existing in the litterature and by investigating the influence of different facular size-Wilson depression ratios. Specially important should be the inclusion of flux-tubes of different size in order to study the influence of the filling factor.

8

Bibliography

- Ahern, S., Chapman, G.A. 2000, Solar Phys., 191, 71
- Aime, C. 1978, A&A 67, 1
- Akimov, L. A., Belika, I.L., Dyatel, N.P., Marchenko, G.P., 1987, Sov. Astron. 31, 64
- Allende Prieto, C., Ruiz Cobo, B., García Lopez, R. J., 1998, ApJ, 502, 951
- Altrock, R. C., Musman, S., 1976, ApJ, 203, 533
- Astroshchenko, I.N., Gadun, A.S., 1994, A&A, 291, 635
- Atkinson, R. d'E. 1951, MNRAS, 111, 448
- Auffret, H., & Muller, R. 1991, A&A, 246, 264
- Ayres, T. R., Testerman, L., & Brault, J. W., 1986, ApJ, 304, 542
- Beckers, J.M.,& Parnell, R.L. 1969, Solar Phys. 9, 39
- Beckers, J.M.,& Milkey, R.W., 1975, Sol. Phys. 43, 289
- Bellot Rubio, L. R., Ruiz Cobo, B.,& Collados, M., 2000 a, ApJ, 535, 475
- Bellot Rubio, L. R., Ruiz Cobo, B.,& Collados, M., 2000 b, ApJ, 535, 489
- Bendlin, C., Volkmer, R., 1993, A&A, 111, L1
- Berrilli, F., Florio, A., Consolini, G., Bavassano, B.,Briand, C., Bruno, R., Caccin, B., Carbone, V., Ceppatelli, G., Egidi, A., Ermolli, I., Mainella, G., Pietropaolo, E., 1999, A&A, 344, L29
- de Boer, C.R., Kneer, F., Nesis, A., 1992, A&A, 257, L4
- de Boer, C.R., Stellmacher, G., Wiehr, E., 1997, A&A, 324, 1179
- Bonet, J. A., Ponz, J. D., & Vázquez, M. 1982, Solar Phys. 77, 69
- Bonet, J. A., Sobotka, M., & Vázquez, M. 1995, A&A, 296, 241
- Bonet, J. A. 1999, in *Motions in the Solar Atmosphere*, ed. A. Hanslmeier & M. Messerotti, (Dordrecht: Kluwer), 1

- Brandt, P. N.,Greimel, R., Guenther, E., & Mattig, W. 1991, en *Applying Fractals in Astronomy* (Berlin: Springer), 77
- Brault, J. W., & White, O. R. 1971, A&A, 13, 169
- Bray, R.J., Loughhead, R.E., Durrant, C.J., 1984, *The Solar Granulation*, 2nd edition, Cambridge University Press.
- Brünnow, F. 1881, Lehrbuch der Sphärischen Astronomie, 4. Aufl., Dümmler, Berlin, Abschnitt 3.I
- Caccin, B., Gómez, M.T., Marmolino, C., & Severino, G., 1977, A&A, 54, 227
- Caccin, B., & Severino, G., 1979, ApJ, 232, 297
- Canfield, R.C., Mehltretter, J.P., 1973, Solar Phys., 33, 33
- Cattaneo, F., Brummell, N.H., Toomre, J., Malagoli, A., Hurlburt, N.E., 1991, ApJ, 370, 282
- Chapman, G.A., 1970, Solar Phys., 1970, 14, 315
- Chapman, G. A., & Ingersoll, A. P. 1972, ApJ, 175, 819
- Chapman, G. A., 1977, ApJ Suppl. Ser., 33, 35
- Chapman, G. A., 1979, ApJ, 232, 923
- Chapman, G. A., & Klabunde, D. P. 1982, ApJ, 261, 387
- Chapman, G. A., & Gingell, T.A., 1984, Solar Phys. 91, 243
- Chevalier, S., 1908, ApJ, 27, 12
- Collados, M., & Vázquez, M. 1987, A&A, 180, 223
- Collados, M., Martínez Pillet, V., Ruiz Cobo, B., del Toro Iniesta, J. C., & Vázquez, M. 1994, A&A, 291, 622
- Collados, M., Joven, E., Fuentes, F. J., Díaz, J. J., González Escalera, V., Bonet, J. A., & Vázquez, M. 1997, in ASP Conf. Series, Vol. 118, Advances in the Physics of Sunspots, ed. B. Schmieder, J. C. del Toro Iniesta, & M. Vázquez (San Francisco, ASP), 361
- Cooley, J. W., Lewis, P. A. W., & Welch, P. D. 1970, J. Sound Vib., 12 (3), 339
- Dahlquist G., & Björck Å. 1974, Numerical Methods (Englewood Cliff: Prentice–Hall), 395
- Darvann, T.A., Kusoffsky, U., 1989, in *Solar and Stellar granulation*, R.J. Rutten and G. Severino (eds.) Kluwer, Dordrecht, 173
- Dawes,W.R., 1864, MNRAS, 24, 161
- Deinzer, W., Hensler, G., Schüssler, M., & Weisshaar, E. 1984, A&A, 139, 435
- Denker, C., Johannesson, A., Marquette, W., Goode, P. R., Wang, H., Zirin, H., 1999, Solar Phys., 184, 87
- Deubner, F. L., & Mattig, W. 1975, A&A, 45, 167
- Druesne, P., Borgnino, J., Martin, F., Ricort, G., & Aime, C. 1989, A&A,

217, 229
- Durrant C. J., Mattig, W., & Nesis, A. 1983, A&A, 123, 319
- Eckert, W. J., Jones, R., & Clark, H. K. 1954, *Improved Lunar Ephemeris 1952-1959, a Joint Supplement to the American Ephemeris and the (British) Nautical Almanac* (Washington, D. C.: U. S. Government Printing Office), 283
- Edmonds, F. N. 1960, ApJ, 131, 57
- Edmonds, F.N.,& Hinkle, K.H. 1977, Solar Phys. 51, 273
- Espagnet, O., Muller, R., Roudier, Th., Mein, N., Mein, P., 1995, A&A Suppl. Ser., 109, 79
- Espenak, F., & Anderson, J. 1993, Annular Solar Eclipse of 10 may 1994, NASA RP–1301
- Fabiani Bendicho, P., & Trujillo Bueno, J. 1999, in Proc. 2nd Solar Polarization Workshop: *Solar Polarization*, ed. K. N. Nagendra & J. O. Stenflo, (Dordrecht: Kluwer), 219
- Fabiani Bendicho, P., 2002, in *Workshop on Stellar Atmosphere Modeling, Abstracts from a conference held 8-12 April 2002 in Tuebingen, Germany.* Editors: I. Hubeny, D. Mihalas, K. Werner. To be published in the ASP Conference Series, 2003.
- Ferrari, A., Massaglia, S., Kalkofen, W., Rosner, R., Bodo., G., 1985, ApJ, 298, 181
- Fontenla, J. M., Avrett, E. H., & Loeser, R., 1993, ApJ, 406, 319
- Foukal, P., Duvall, T., Gillespie, B., 1981, ApJ, 249, 394
- Foukal, P., & Duvall, T. 1985, ApJ, 296, 739
- Foukal, P., Little, R., & Mooney, J. 1989, ApJ, 336, L33
- Foukal, P., Little, R., Graves, J., Rabin, D., & Lynch, D. 1990, ApJ, 353, 712
- Foukal, P. 1998, in *From the Sun, Auroras, Magnetic Storms, Solar Flares, Cosmic Rays* ed. Steven T. Suess & Bruce T. Tsurutani. (Washington, D. C.: American Geophysical Union), 103
- Fraizer, E.N., 1971, Solar. Phys. 21,42
- Frutiger, C., Solanki, S. K., Fligge, M., Bruls, J. H. M. J., 2000, A & A, 358, 1109
- Fröhlich, C., Lean, J., 1998, Geophys. Res. Letters, 25, 4377
- Gadun, A.S., 1995, Kinemat. i Fiz. Nebesn. Tel 11, no. 3, 54
- Gadun, A.S., Pikalov, K.N., 1996, Solar. Phys., 166, 43
- Gadun, A.S., Pavlenko, Ya.V., 1997, A&A, 324, 281
- Gadun, A.S., Hanslmeier, A., Pikalov, K.N., Ploner, S.R.O., Puschmann, K.G., Solanki, S.K., 2000, A&A Supl. Ser., 146, 267
- Gingerich, O., Noyes, R. W., Kalkofen, W., & Cuny, Y. 1971, Solar Phys.,

18, 347
- Grossmann-Doerth, U.,,Schüssler, M., & Solanki,S.K., 1989, A&A, 221, 338
- Grossmann-Doerth, U.,Knölker, M.,Schüssler, M., & Solanki, S. K. 1994, A&A, 285, 648
- Hansky, A., 1908, *Mitteilungen des Astronomischen Hauptobservatoriums Pulkovo*, 3, 1
- Hanslmeier, A., Nesis, A., Mattig, W., 1991, A&A, 251, 307
- Hanslmeier, A., Nesis, A., Mattig, W., 1993, A&A, 270, 516
- Harvey, K., & Zwaan, C. 1993, Solar Phys., 148, 85
- Herschel, W.,1801, *Philosophical Transactions of the Royal Society*, Part1, p.265
- Hirzberger, J., Vázquez, M., Bonet, J.A., Hanselmeier, A., Sobotka, M., 1997, ApJ, 480, 406
- Janssen,J., 1896, *Annales de l'Observatoire d'Astronomie Physique de Paris sis Parc de Meudon (Seine-et-Oise)*, 1, 91
- Kalkofen, W., Rosner, R., Ferrari, A., Massaglia, S., 1986, ApJ, 304, 519
- Kandal, R., & Keil, S. 1973, Solar Phys. 33, 3
- Karpinsky, V. N., & Pravdjuk, L. M. 1972, Soln. Dannye No. 10, 79
- Keil, S. L. 1977, Solar Phys., 53, 359
- Keil, S.L., Canfield, R.C., 1978, A&A, 70, 169
- Keil, S.L., 1980, ApJ, 237, 1035
- Keil, S. L., Kuhn, J., Lin, H., Reardon, K., 1994, in *Infrared solar physics: proceedings of the 154th Symposium of the International Astronomical Union* ed. D.M.Rabin, John T. Jefferies, and C. Lindsey., International Astronomical Union. Symposium no. 154, p. 251
- Keller, C.U., 1992, Nature, 359, 307
- Keller, C.U., Koutchmy, S., 1991, ApJ, 379, 751
- Keppens, R., & Martínez Pillet, V. 1996, A&A, 316, 229
- Kneer, F.J., Mattig, W., Nesis, A., Werner, W., 1981, Solar Phys., 68, 31
- Kneer, F. 1984, in *Small-Scale Dynamical Processes in Quiet Stellar Atmospheres*, Sac Peak Obs. workshop, ed. S. L. Keil , 110
- Knölker, M, Schüssler, M. & Weisshaar, E., 1985, in *Theoretical Problems in High Resolution Solar Physics*, ed. H.U. Scmidt, Max-Plank-Institut für Astrophysik, Munich, p.195
- Knölker, M., & Schüssler, M. 1988, A&A, 202, 275
- Knölker, M., Grössman Doerth, U., Schüssler, M., Weisshaar, E., 1990, Adv. Space Res., 11, 285
- Köppen, J. 1975, Solar Phys., 42, 325
- Komm, R., Mattig, W., Nesis, A., 1990, A&A, 239, 340

- Koutchmy, S., 1977, A & A, 61, 397
- Koutchmy, S., Stellmacher, G., 1978, A&A, 67, 93
- Koutchmy, S., Lebecq, C., 1986, A&A, 169, 323
- Koutchmy, S., 1990, in *Solar Photosphere: Structure, Convection, and Magnetic Fields*, ed. Jan Olof Stenflo. International Astronomical Union. Symposium no. 138, 81
- Koutchmy, S., 1994, in *Infrared solar physics: proceedings of the 154th Symposium of the International Astronomical Union* ed. D.M.Rabin, John T. Jefferies, and C. Lindsey., International Astronomical Union. Symposium no. 154, p. 239
- Krat, V. A., Karpinsky, V. N.,& Sobolev, V. M., 1973, Space Research 12, vol. 2, 1713
- Krieg, J., Wunnenberg, M., Kneer, F., Koschinsky, M., Ritter, C., 1999, A&A, 343, 983
- Kurucz, R.L., 1979, ApJSS, 40, no.1, 1
- Lawrence, J. K., & Chapman, G. A. 1988, Solar Phys., 335, 996
- Lawrence, J. K., Chapman, G. A., & Herzog, A. D. 1988, ApJ, 324, 1184
- Leighton, R.B., 1963, Ann. Rev. Astron. Astrophys., 1, 19
- Lèvy, M. 1971, A&A, 14, 15
- Libbrecht, K. G., & Kuhn, J. R. 1984, ApJ, 277, 889
- Libbrecht, K. G., & Kuhn, J. R. 1985, ApJ, 299, 1047
- Lin, H., & Kuhn, J.R. 1992, Solar Phys., 141, 1
- Lovejoy, S. 1982 Science, 216, 185
- Löfdahl, M.G., Scharmer, G.B.,1994, A&A Suppl. Ser., 107, 243
- Makarova, E. A., Roshchina, E. M., & Sarychev, A. P. 1994, Solar Phys., 152, 47
- Malagoli, A., Cattaneo, F., Brummel, N.H., 1990, ApJ Lett., 361, L33
- Maltby, P. 1971, Solar Phys. 18, 3
- Maltby, P., & Staveland, L. 1971, Solar Phys., 18,3
- Mandelbrot, B. B. 1975, J. Fluid Mech., 72, 401
- Mandelbrot, B. B. 1977, *The fractal geometry of nature*, (New York: W. H. Freeman and Company), 15
- Martínez Pillet, V. 1997, in ASP Conf. Series, Vol. 118, *Advances in the Physics of sunspots*, ed. B. Schmieder, J.C. del Toro Iniesta, & M. Vázquez (San Francisco: ASP), 212
- Mattig, W. 1971, Solar Phys., 18, 434
- Meeus,J. 1991, Astronomical Algorithms (Richmond: Willmann-Bell), chap. 24
- Mehltretter, J. P. 1971a, Solar Phys., 16, 253
- Mehltretter, J. P. 1971b, Solar Phys., 19, 32

- Mein, P., 1977, Solar Phys. 54, 45
- Montenbruck, O. 1985, Grundlagen der Ephemeridenrechnung, 2. Aufl. (München: Verlag Sterne und Weltraum), Kap. IV
- Moran, T., Foukal., P., Rabin, D., 1992, Solar Phys., 142, 35
- Muller, R., & Keil, S.L., 1983, Solar Phys., 87, 243
- Muller, R. 1990, *New Windows to the Universe*, Vol. 1, ed. F. Sánchez & M. Vázquez, (Cambridge: Cambridge University Press), 1
- Muller, R., 1999, en *Motions in the Solar Atmosphere*, ed. A. Hanslmeier & M. Messerotti, (Dordrecht: Kluwer), 35
- Namba, O., Diemel, W.E., 1969, Solar Phys., 7, 167
- Nasmyth, J., 1862, *Memoirs of the Literary and Philosophical Society of Manchester*, Series 3, 1,p.407
- Neckel, H., & Labs, D. 1984, Solar Phys., 90, 205
- Nelson, G. 1978, Solar Phys., 60, 5
- Nesis, A., Hanslmeier, A., Hammer, R., Komm, R., Mattig, W., Staiger, J., 1992, A&A, 253, 561
- Nesis, A., Hanslmeier, A., Hammer, R., Komm, R., Mattig, W., Staiger, J., 1993, A&A, 279, 599
- Nesis, A., Hammer, R., Schleicher, H., 1996, AASM, 188
- Nordlund, Å, 1984, en *Small-Scale Dynamical Processes in Quiet Stellar Atmospheres*, Sunspot, Sac. Peak Observ., 181
- Nordlund, Å, 1985, Sol. Phys., 100, 209
- Nordlund, Å, Stein, R.F., 1990, Comput. Phys. Commun, 59, 119
- Nordlund, Å, Spruit, H.C., Ludwig, H.-G., Trampedach, R., 1997, A&A, 328, 229
- Nordlund, Å, Stein, R.F., 1999, en *Theory and tests of Convective Energy Transport* A. Gimemez, E. Guinan, B. Montesinos (Eds.) ASP Conf. Series Vol. 173, 91
- Okabe, A., Boots, B., & Sugihara, K., 1992, *Spatial Tessellations: Concepts and Aplications of Voronoi Diagrams* (Chichester: Wiley)
- Ortiz, A., Solanki, S.K., Domingo, V., Fligge, M., Sanahuja, B., 2002, A&A, 388, 1036
- Pierce, A. K., & Slaughter, C. D. 1977, Solar Phys., 52, 179
- Pravdjuk, L. M., Karpinsky, V. N., & Andreiko, A. V. 1974, Soln. Dannye No.2, 70
- Rao, Chang-Hui, Jiang, Wen-Han, Ling, Ning, Beckers, J. M., 2001, Ch A& A, 25, 439
- Rast, M.P., 1995, ApJ, 443, 863
- Richardson, R. S. 1933, ApJ, 78, 359
- Richardson, R.S.,Schwarzchild, B., 1950, ApJ, 111, 351

- Ricort, G., & Aime, C. 1979, A&A, 76, 324
- Ricort, G., Aime, C., Deubner, F., & Mattig, W. 1981, A&A, 97, 114
- Roddier, F. 1981, Progress in Optics XIX, ed. E. Wolf North-Holland, Amsterdam, p. 281-376.
- Rodríguez Hidalgo, I., Collados, M., & Vázquez, M. 1992a, A&A, 254, 371
- Rodríguez Hidalgo, I., Collados, M., & Vázquez, M. 1992b, A&A, 264, 661
- Rodríguez Hidalgo, I., Ruiz Cobo, B., del Toro Iniesta, J.C., Collados, M., Sanchez-Almeida, J., 1995, en *JOSO Annual report 1995*, M. Saniga (ed.), 162
- Rogerson, J. B. 1961, ApJ 134, 331
- Roudier, Th, Muller, R., 1987, Solar Phys, 107, 11
- Ruiz Cobo, B., del Toro Iniesta, J.C., Rodríguez Hidalgo, I., Collados, M., Sánchez Almeida, J., 1996, in *Cool Stars Stellar Systems, and the Sun, 9th Cambridge workshop*, eds. R. Pallavicini & A.K. Dupree, ASP Conf. Ser., 109, 155
- Ruiz Cobo, B., del Toro Iniesta, J.C., 1992, ApJ, 398, 375
- Sanchez Almeida, J., 1997, ApJ, 491, 993
- Sánchez Cuberes, M., Bonet, J.A., Vázquez, M., Wittmann, A., 2000, ApJ, 538, 940
- Sánchez Cuberes, M., Bonet, J.A., Vázquez, M., Wittmann, A., 1999, *High resolution Solar Physics: theory, observations, and techniques*, ASP Conf. Series vol. 183, 515
- Sánchez Cuberes, M., Vázquez, M., Bonet, J.A., Sobotka, M., 2002, ApJ, 570, 886
- Sánchez Cuberes, M., Vázquez, M., Bonet, J.A., Sobotka, M., 2002, A&A, in press
- Salucci, G., Bertello, L., Cavillini, F., Cepatelli, G., Righini, A., 1994, A&A, 285, 322
- Scharmer, G. B., Brown, D. S., Pettersson, L., & Rehn, J. 1985, Appl. Opt., 24, 2558
- Schmahl, G. 1967, Zeitschrift für Astrophysik, 66, 81
- Schmidt, W., Deubner, F. L., Mattig, W., & Mehltretter, J. P. 1979, A&A, 75, 223
- Schmidt, W., Knölker, M. T. F., & Schröter, E. H. 1981, Solar Phys., 73, 217
- Schmidt, W., Stix, M., & Wöhl, H. 1999, A&A, 346, 633
- Schrijver, C.J., Hagenaar, H.J., Title, A.M., 1997, ApJ, 475, 328
- Schüssler, M., 1987, in *The Role of Fine-scale Magnetic Fields on the*

Structure of the Solar Atmosphere, E.-H. Schröter, M. Vázquez, A.A.Wyller (Eds.) Cambridge University Press, p. 223

- Siedentopf, H., 1933,*Astronomische Nachrichten*, 247, 297
- Simon, G., & Weiss, N. O., 1968, Zeitschrift für Astrophysik, 69, 435
- Skumanich, A., 1955, ApJ, 121, 404
- Skumanich, A. 1999 ApJ, 512, 975
- Skumanich, A., Lites, B. W. 1987, ApJ, 322, 473
- Sobotka, M., Bonet, J.A., & Vázquez, M. 1993,ApJ, 415, 832
- Sobotka, M., Vázquez, M., Sánchez Cuberes, M., Bonet, J. A., & Hanslmeier, A. 2000, ApJ, 544, 1155
- Sobotka, M., Sütterlin,P., 2001, A&A, 380, 714
- Socas-Navarro, H., Ruiz Cobo, B., Trujillo Bueno, J. 1998, ApJ, 507, 470
- Solanki, S. K., & Stenflo, J.O., 1985 A&A, 148, 123
- Solanki, S. K., & Steenbock, W. 1988, A&A, 189, 243
- Solanki, S. K., Ruedi, I., & Livingston, W. 1992, A&A, 263, 339
- Solanki, S. K., Brigljevíc, V., 1992, Solar Phys., 262, L29
- Solanki, S.K., Rüedi, I., Bianda, M., Steffen, M., 1996, A&A, 308, 623
- Solanki, S. K. 1999, in ASP Conf. Ser., Vol. 158, *Solar and Stellar Activity: Similarities and differences*, ed. C. J. Buttler & J.S. Doyle (San Francisco: ASP), 109
- Solanki, S. K., & Fligge, M., 2000, in *The Solar Cycle and Terrestrial Climate*, ed. A. Wilson, ESA SP-463, 51
- Spruit, H. C. 1976, Solar Phys., 50, 269
- Spruit, H. C. 1977, Solar Phys., 55, 3
- Spruit, H.C., Nordlund, Å, Title, A.M., 1990, ARA&A, 28, 263
- Spruit, H.C., 1997, Mem. Soc. Astron. Italiana, 68, 397
- Sreenivasan, K.R., Meneveau, C., 1986, J. Fluid Mech. 173, 357
- Steffen, M., Ludwig, H.-G., Krüss, A., 1989, A&A, 213, 371
- Steffen, M., Freytag, B., Holweger H., 1994, *Solar Magnetic Fields*, M. Schüssler and W. Schmidt (eds.), Cambridge Univ. Press, 298
- Stein, R.F., Nordlund,A., 1989, ApJ, 342, L95
- Stein, R.F., Nordlund,A., 1994, IAU Symp. 154, *Infrared Solar Physics*, ed. D. Rabin, J.Jefferies, C. Lindsey, (Dordrecht:Kluwer), 225
- Stein, R.F., Nordlund, Å, 1998, ApJ, 499, 914
- Stein, R.F., Nordlund, 2000, Solar Phys, 192, 91
- Steinegger, M., Vázquez, M., Bonet, J. A., & Brandt, P. N. 1996, ApJ, 461, 478
- Steiner, O., 1990, Ph.D Thesis, No 9292, ETH-Zürich
- Steiner, O., & Stenflo, J.O., 1990, in *Solar Photosphere: Structure, Convection and Magnetic Fields*, J.O. Stenflo (Ed.), Kluwer, Dordrecht, IAU

Symp, 138, 181
- Stellmacher, G., Wiehr, E., 1973, A&A, 29, 13
- Stellmacher, G., Wiehr, E., 1979, A&A, 75, 263
- Stix, M., & Wöhl, H. 1974, Solar Phys., 37, 63
- Strebel, H., 1933, *Zeitschrift für Astrophysik*, 6, 313
- Sütterlin, P., Wiehr, E., Stellmacher, G., 1999, Solar Phys., 189, 57
- Ten Bruggencate, P., 1940, Z. Astrophys., 19, 59
- Title, A., Tarbell, T.D., Topka, K.P., Ferguson, S.H., Shine, R.A., 1989, ApJ, 336, 475
- Title, A., Topka, K. P., Tarbell, T.D., Schmidt, W., balke, C., Scharmer, G., 1992, ApJ, 393, 782
- Topka, K. P., Tarbell, T. D., & Title, A. 1992, ApJ, 396,351
- Topka, K. P., Tarbell, T. D., & Title, A. 1997, ApJ, 484, 479
- del Toro Iniesta, J. C., Collados, M., Sánchez Almeida, J., 1990, A & A, 227, 591
- Turon, P. J., Lna, P., 1973, Solar Phys., 30, 3
- Uberoi, M. S., 1955, ApJ, 122, 466
- Unruh, Y. C., Solanki, S. K., & Fligge, M. 1999, A&A, 345, 635
- Unsöld, A., 1930, *Zeitschrift für Astrophysik*, 1, 138
- Vázquez, M. 1999, in Astrophys. Sp. Sci. Lib., Vol. 239, *Motions in the Solar Atmosphere*, ed. Arnold Hanslmeier & Mauro Messerotti (Dordrecht: Kluwer), 169
- von der Lühe, O., & Dunn, R. B. 1987, A&A, 177, 265
- von der Lühe, O., & Dunn, R. B. 1987, A&A, 177, 265
- Waldmeier, M., 1940, Helv. Phys., Acta 13, 13
- Walton, S.R., 1987, ApJ, 312, 909
- Wang, H., & Zirin, H., 1987, Solar Phys., 110, 281
- Wang, H. 1994, Chin. Astron. Astrophys., 18, 97
- Wang, H., Spirock, T., Goode, P. R., Lee, C., Zirin, H., & Kosonocky, W. 1998, ApJ, 495, 957
- Watts, C. B. 1963, *The Marginal Zone of the Moon*, in Astronomical Papers prepared for the Use of the American Ephemeris and Nautical Almanac Vol. XVII (Washington, D. C.: Nautical Almanac Office), 1
- Wiehr, E., Kneer, F., 1988, A&A, 195, 310
- Wiesmeier, A., & Durrant, C. J. 1981, A&A, 104, 207
- Wilken, V., de Boer, C., Denker, C., & Kneer, F. 1997, A&A, 325, 819
- Willson, R. C., Gulkis, S., Janssen, M., Hudson, H. S., Chapman, G. A., 1981, Science, 211, 700
- Willson, R.C., 1982, A&A, 87. 4319
- Willson, R.C., Hudson, H. S., Frohlich, C., Brusa, R. W., 1986, Science,

234, 1114
- Wittmann, A. D., & Mehltretter, J. P. 1977, A&A, 61, 75
- Wittmann, A. D. 1979, *Small Scale Motions on the Sun*, Mitteilungen aus dem Kiepenheuer–Institut Nr.179, Freiburg., 29
- Wittmann, A. D. 1984, Mitt. Astron. Ges., 62, 201
- Wittmann, A. D. 1997, Astron. Nachr., 318, 305
- Worden, S.P., 1975, Solar Phys., 45, 521
- Wöhl, H., & Nordlund, Å, 1985, Solar Phys. 97, 213
- Xu, Y., & Wang, H. 2001, American Geophysical Union, Spring Meeting 2001, abstract SP21A-02
- Zayer, I., Stenflo, J. O., Keller, C. U., Solanki, S. K. 1990, A&A, 239, 356
- Zirker, J.B., Solar Phys., 1993, 147, 47